Towards Scalable Si and Ge Spin Qubit Architectures : Highlights from Modelling

Biel Martinez Diaz

THÈSE

Pour obtenir le grade de

DOCTEUR DE L'UNIVERSITÉ GRENOBLE ALPES

École doctorale : PHYS - Physique
Spécialité : Physique de la Matière Condensée et du Rayonnement
Unité de recherche : Modélisation et Exploration des Matériaux

Modélisation d'architectures de BITS quantiques SI et GE pour l'intégration à grande échelle

Towards Scalable Si and Ge Spin Qubit Architectures: Highlights from Modelling

Présentée par :

Biel MARTINEZ DIAZ

Direction de thèse :

Yann-Michel NIQUET — Directeur de thèse
Université Grenoble Alpes

Rapporteurs :

MARIA JOSE CALDERON
Chargé de recherche, Instituto de Ciencia de Materiales
MATHIEU LUISIER
Professeur, Ecole Polytechnique Fédérale de Zurich

Thèse soutenue publiquement le **8 novembre 2022**, devant le jury composé de :

MARIA JOSE CALDERON Chargé de recherche, Instituto de Ciencia de Materiales	Rapporteure
MATHIEU LUISIER Professeur, Ecole Polytechnique Fédérale de Zurich	Rapporteur
CHRISTOPHE DELERUE Directeur de recherche, CNRS DELEGATION HAUTS-DE-FRANCE	Examinateur
DAVID FERRAND Professeur des Universités, UNIVERSITE GRENOBLE ALPES	Président

History of Physics:

Aristotle said a bunch of stuff that was wrong.
Galileo and Newton fixed things up. Then Einstein broke everything again.
Now, we've basically got it all worked out, except for small stuff, big stuff,
hot stuff, cold stuff, fast stuff, heavy stuff, dark stuff, turbulence,
and the concept of time.

Zach Weinersmith

Abstract

Quantum computers rely on quantum two-level systems as memory units, the so-called qubits, and it is their quantum character what brings the unique attributes that should enable to solve unaffordable problems with nowadays best classical computers. To this end, millions of qubits are required, and consequently large-scale quantum architectures capable of hosting and individually controlling them. Many quantum two-level systems have been proposed as qubits. Superconducting circuits have taken the lead, and platforms with tens of qubits are already available at present. However, their scalability beyond a few hundreds is challenging. In this respect, quantum-dot-based spin qubits are among the latest to join the race, yet they seem to gather most of the requirements of an ideal quantum processor. Current experiments deal with a few spin qubits at most, and one of the issues they may encounter when scaling up is variability. Spin qubits are sensible to their electrical environment, and defects in the surrounding materials may scatter their properties and yield to processors made of very heterogeneous qubits.

This thesis addresses the challenges that spin qubits may face in the near future, both by understanding their impact and by proposing improved device candidates. We numerically quantify the variability for two of the most promising platforms for spin qubits: electrons and holes in Si MOS devices, and holes in Ge/SiGe heterostructures. We simulate their main sources of disorder, and discuss the repercussion on the realization of one- and two-qubit operations. We find that variability in Si MOS devices is a major challenge for scalability. We also evidence that for Ge/SiGe heterostructures, while smaller than for Si MOS, it still considerably impacts the properties of individual qubits, and we propose a novel gate layout for Ge/SiGe-based processors that palliates its issues. Finally, we discuss how many-body interactions can reshape the physics of quantum dots, and how this must be accounted for in the design of spin qubit arrays.

Résumé

Les ordinateurs quantiques utilisent des systèmes à deux niveaux comme unités de mémoire, les bits quantiques, et c'est leur caractère quantique ce que leur apportent des attributs uniques qui devraient permettre de résoudre des problèmes inabordables par les meilleurs ordinateurs classiques d'aujourd'hui. Pour que ce soit une réalité, des millions de qubits sont nécessaires, et par conséquent des architectures quantiques à grande échelle capables de les héberger et de les contrôler individuellement. De nombreux systèmes quantiques à deux niveaux ont été proposés comme bits quantiques. Les circuits supraconducteurs ont pris la tête et des plates-formes avec des dizaines de bits quantiques sont déjà disponibles. Cependant, sa croissance au-delà de quelques centaines présente des défis. À cet égard, les bits quantiques de spin basés sur des boîtes quantiques sont parmi les derniers à rejoindre la course, mais ils semblent rassembler la plupart des prérequis d'un processeur quantique idéal. Les expériences actuelles ont quelques qubits de spin au maximum, et l'un des problèmes qu'ils peuvent rencontrer lors de leur développement est la variabilité. Les qubits de spin sont sensibles à leur environnement électrique, et les défauts dans les matériaux environnants peuvent modifier leurs propriétés et laisser des processeurs très hétérogènes.

Cette thèse aborde les défis auxquels les bits quantiques de spin pourraient faire face dans un proche avenir, à la fois en comprenant son impact et en proposant des dispositifs améliorés. Nous quantifions numériquement la variabilité pour deux des plates-formes les plus prometteuses pour les bits quantiques de spin : les électrons et les trous dans les dispositifs Si MOS, et les trous dans les hétérostructures Ge/SiGe. Nous simulons leurs principales sources de désordre, et discutons ses répercussions sur la réalisation des opérations à un et deux qubits. Nous constatons que la variabilité des appareils Si MOS est un gros défi pour l'extensibilité de cette plate-forme. Nous constatons également que dans les hétérostructures Ge/SiGe, bien que plus petite que pour Si MOS, elle modifie toujours les propriétés des qubits individuels ; et on propose un nouveau grillage pour les processeurs basés sur Ge/SiGe qui pallie ses problèmes. Enfin, nous discutons comment les interactions entre particules peuvent modifier la physique des boîtes quantiques, et comment cela doit être considéré dans la conception des systèmes de boîtes quantiques de spin.

Acknowledgments

Time flies. It seems like yesterday when a younger version of myself packed all his belongings in his car and headed north full of excitement and nervousness in equal weights. But it was already three years ago, and what a turbulent time! Covid decided to show up six months after the start of my PhD, and it triggered quite a few lockdowns (I lost count at some point) and a great dose of teleworking (with which I have had a troublesome love-hate relationship). But I cannot think on a better place to spend, both personally and professionally, such tough times. I was lucky enough to fill the countless hours confined at home with exciting work, and the nature surrounding Grenoble enabled me to breath and disconnect during those brief outings we were allowed to do. Even though all the unexpected events, I have learned and grown as I could not have imagined.

The day to write these lines finally came. I will thank here everyone who helped me in one way or another. First, I want to thank Yann-Michel for always having an answer to all of my questions, and for finding time for me despite the difficult circumstances. I extend the acknowledgment to everyone who has been part of the group during my PhD: Benjamin, Jing, Vincent, José, Michele, and Esteban. I have learned a lot from all our discussions. I want also to thank everyone I have collaborated with in the last three years: the fabrication team at LETI, all the members from Lateqs, and Bernhard, Victor, and Matias from Institut Néel.

On the personal side, I must thank Marc and Júlia for becoming a pillar of my life in Grenoble. Also David, for his endless strength and for being always ready for whichever plan we come up with. Not to forget my hometown friends: Arnau, Enric, Guillem, Jaume. Your visits and the (virtual) company during the pandemic have been priceless. Finally, a special mention to my family for their unconditional support.

I am deeply thankful to everyone mentioned (and to those I may have forgotten) for doing their bit to make this project successful.

Contents

List of Acronyms

Chapter 1

Introduction

Contents

Like classical computing at its time, the emergence of quantum computing, together with its countless promising advantages, have gathered huge amounts of economical and human resources worldwide. In this Chapter, we review the story and the current status of quantum computing in general, and of spin qubits in particular.

1.1 Timeline of quantum computing

It is certainly difficult to set an initial date for the birth of a new research field such as quantum computing, since it is a collection of small contributions brought through the years that yielded to quantum computing as we understand it nowadays. Relevant preliminary work carried out during the seventies set the stage for the first proposal of a computer operating under the laws of quantum mechanics, published by Paul Benioff in 1980 [1]. One year later, Richard Feynman introduced the idea of a quantum simulator, arguing that the simulation of quantum phenomena in a quantum system would be more efficient than trying to do it on a classical computer [2]; but it was not until 1988 when the first physical realization of a quantum computer was theoretically proposed in a mixed atomic-photonic quantum system [3]. The nineties finally triggered the bloom of the field, and in 1994 and 1996 Peter Shor and Lov Grover, respectively, described the two paradigmatic algorithms of quantum computing, the firsts showing a quantum advantage. Shor's algorithm enables the factorization of large numbers, inaccessible by classical computers and crucial for nowadays cryptosecurity [4]; and Grover's algorithm is an unstructured search quantum algorithm whose cost scales as $O(\sqrt{N})$, improving the typical $O(N)$ scaling of its classical counterparts [5].

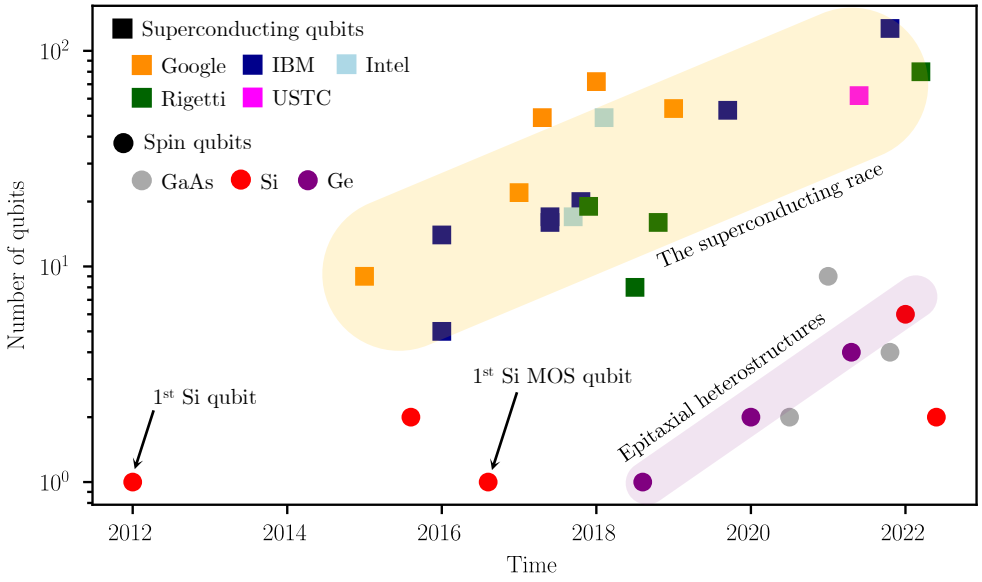

Figure 1.1: Evolution of the number of qubits with time in the last few years. A few selected quantum processors are shown for superconducting qubits at Google [10, 11], IBM, Intel, Rigetti, and USTC [12]; and for spin qubits in Si [13–17], GaAs [18–20], and Ge [21–23].

Also in 1996, DiVincezo sketched his first thoughts about the requirements to build a quantum computer [6], and later in the year 2000, he further developed them to set what is known as the DiVincenzo criteria [7]. It was the first time someone highlighted the importance of the quality of the employed qubits and the scalability of the chosen hardware. In 1997, together with Daniel Loss, they proposed an electronic spin in a Quantum Dot (QD) as unit of information, showing that such system formally fulfills all the requisites for a quantum processor [8]. One year later, Bruce Kane went one step further and gave concrete details on a feasible experimental setup [9]. He proposed to use nuclear spins of individual Phosphorous atoms hosted in Silicon, and he introduced the concept of metallic gates as control knobs for the qubits. These two proposals set the basis of the semiconductor spin qubits.

The first few-qubit experiments were based on Nuclear Magnetic Resonance (NMR) computing [24–26], and it was not until 1999 when the first superconducting qubit was realized [27]. Since then, the number of qubits per processor based on this technology has continuously increased, see Figure 1.1. The largest quantum processor to date belongs to IBM and is made of 127 superconducting qubits. Moreover, they have prospects of releasing a 433 qubits quantum processor in 2022. Reaching such number of qubits allowed to perform the first computations [10, 11, 28, 29]. In 2016, Martinis group in Google were able to simulate the Hydrogen molecule in a 9-qubit processor [10]. Also Google, in 2019, claimed reaching quantum supremacy for the first time with a 53-qubit quantum processor by performing a task that they claimed could not be simulated in a classical computer [11].[1] Unfortunately, superconducting qubits are large (of

[1]It is in fact a source of debate whether the experiment indeed demonstrated quantum supremacy or not [30].

the order of 0.1 mm^2 each) [31], which hinders their scalability due to the need to operate them at very low temperatures. Also, their lifetimes are short (at the order of the μs), which limits the number of operations that can be realized with the quantum processor. Consequently, their large-scale integration, beyond hundreds of qubits, may be complex.

The first semiconductor spin qubits were realized in 2005 [32, 33]. These were based on gate-defined QDs in GaAs/AlGaAs heterostructures. Such heterostructures were a valuable playground for the first proof-of-concept experiments, yet it was soon realized that the nuclear spins of Ga and As isotopes are strongly limiting the lifetimes of the qubits due to the hyperfine interaction. In this context, Silicon appeared as a much more appealing material, since it only contains 5% of ^{29}Si, its only stable isotope with non-zero spin. Indeed, the spin qubit community started to turn its interest towards Si after the first demonstration of a Si spin qubit in 2012 [13]. Since then, the quantity and quality of Si spin qubits has been steadily increasing. Together with spin qubits in Ge, the lasts to join the race [21], they make spin qubits one of the most promising platforms to achieve large-scale quantum computers.

In the early days of modern computing, efforts were put on building larger and larger computers based on vacuum tubes, known as the first generation of classical computers. The volume of these vacuum tubes was a few cm^3, and they were frequently damaged. History changed when the first transistor was built in BELL labs in 1947, and the second generation of classical computers based on this technology took over. The possibility to integrate millions of transistors on a much smaller volume, as well as its robustness, were crucial aspects. Time will tell whether the second generation of quantum computers is based on spin qubits, and whether they become to superconducting qubits what transistors were to vacuum tubes.

1.2 The quantum bit

In a quantum computer the information is stored in a quantum two-level system, the quantum bit (or qubit); and it is its quantum nature that brings all the advantages over its classical counterparts. A classical bit, also being a two-state system, is digital, in the sense that it can either take the value of 0 (no current through a transistor) or 1 (current through a transistor). In a qubit, however, not only the quantum states $|0\rangle$ and $|1\rangle$ are available, but also any superposition of the two: $\Psi = \alpha\,|0\rangle + \beta\,|1\rangle$, with $\alpha, \beta \in \mathbb{C}$. Without any loss of generality, we can express the state coefficients as a function of two angles θ and ϕ,

$$\Psi = \cos\frac{\theta}{2}\,|0\rangle + e^{i\phi}\sin\frac{\theta}{2}\,|1\rangle\,, \tag{1.1}$$

which in fact define the sphere shown in Figure 1.2, called the Bloch sphere. The state of the quantum bit can be represented as a vector of module 1 that can point to any direction in this sphere. Any quantum operation on a qubit can be seen as a rotation of the state Ψ within the sphere, and the continuous evolution of Ψ from its initial to its final state is what gives quantum computing its analog character. The classical operation of switching from 0 to 1 is a π rotation over the Bloch sphere in quantum computing.

The quantum advantage arises from state superposition when the number of qubits increases. If we now consider the case of two qubits, the quantum state can be on any superposition of the states $|00\rangle$, $|01\rangle$, $|10\rangle$, $|11\rangle$,

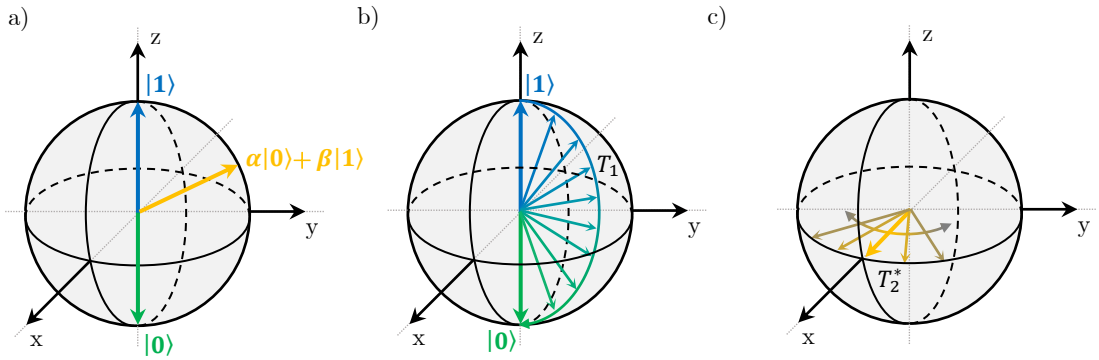

Figure 1.2: Bloch sphere representation of a qubit. a) The quantum bit may be on the ground state $|0\rangle$, the excited state $|1\rangle$, or any linear combination of the two. Since the coefficients can be complex, the state of a qubit can be represented as a vector that can point to any position around the Bloch sphere. b) Representation of the relaxation mechanism, where the excited state $|1\rangle$ relaxes to $|0\rangle$ in a characteristic timescale T_1. c) Representation of the dephasing mechanism, where a mixed state $\alpha\,|0\rangle + \beta\,|1\rangle$ changes its precession speed around z due to fluctuations on the environment and breaks the coherence of its free evolution on a timescale T_2^*.

$$\Psi = \alpha\,|00\rangle + \beta\,|01\rangle + \gamma\,|10\rangle + \delta\,|11\rangle\,, \tag{1.2}$$

with $|\alpha|^2 + |\beta|^2 + |\gamma|^2 + |\delta|^2 = 1$. From the previous expression it is already clear that in general $\Psi \neq \psi_1 \otimes \psi_2$, where ψ_1 and ψ_2 are the states of qubit 1 and qubit 2. Consequently, the Hilbert space grows faster with the number of qubits than with the number of classical bits, and so does the amount of information that they can store. In the two-qubit case, the system is described by a four-parameter space, whereas in the two-bits case the system is characterized by two parameters. More generally, while the space of an ensemble of classical bits grows as the number of bits N, in a quantum computer it grows as 2^N. As an illustration, the memory required on a classical computer to store the coefficients of a 64-qubit state in double precision is roughly $1.5 \cdot 10^8$ TB. It is clear, then, that qubits have the potential to store and process much more information than the classical bits.

We can also benefit from quantum superposition to achieve what has been named as quantum parallelism. In quantum mechanics, a unitary operator $\mathcal{M}$ applied to a state $\Psi = \sum_i \alpha_i \psi_i$ fulfills the distributive property, $\mathcal{M}\Psi = \sum_i \alpha_i \mathcal{M}\psi_i$. Translated to qubits, this implies that by applying an operation $\mathcal{M}$ to a superposition of states, we are in fact doing so for all the superposed states at once,

$$\mathcal{M}\Psi = \alpha\mathcal{M}\,|00\rangle + \beta\mathcal{M}\,|01\rangle + \gamma\mathcal{M}\,|10\rangle + \delta\mathcal{M}\,|11\rangle\,. \tag{1.3}$$

The same task on a classical computer would require as many operations as superposed states in Ψ. Even though we cannot directly benefit from this parallelization, as the readout of the state in equation 1.3 would project Ψ onto one of the basis states, quantum algorithms such as Grover's algorithm make use of quantum parallelism to reduce the scaling of certain tasks with

respect to the classical solution [5].

Probably the main obstacle to deal with in a quantum computation is decoherence (loss of quantum coherence), which provokes the loss of information. Quantum information is fragile, and it is very difficult to isolate a quantum system. It is the interaction with the environment that triggers decoherence, and the two mechanisms involved are relaxation and dephasing. Relaxation occurs due to the excited nature of the $|1\rangle$ state, which tends to relax to the ground state with characteristic timescale T_1. The representation of a relaxation event in the Bloch sphere is illustrated in Figure 1.2b.

Dephasing finds its origin in the free evolution of quantum states driven by the Time-Dependent Schrödinger Equation (TDSE), $\Psi(t) = e^{-iHt/\hbar}\Psi(0)$, where H is the system Hamiltonian, and t is the time. Ψ acquires a time-dependent phase $e^{-iHt/\hbar}$ that results in rotations along the z axis of the Bloch sphere. These are *a priori* harmless as we can represent the system in a rotating frame in which the state does not precess. All the illustrations in Figure 1.2 are actually drawn in this rotating frame. The speed of this precession is proportional to the energy splitting between the $|0\rangle$ and $|1\rangle$ states, which becomes a problem when environment fluctuations reshape them, and consequently modify the rotation speed. Having a precession speed that is not constant over time leads to non-reproducibility of the quantum operations, and to a loss of the quantum information stored in the coefficients of the quantum states, with typical timescale T_2^*.

The analog character of a quantum bit also poses some drawbacks, since the fact that operations involve a continuous transformation of the states opens the door to errors. Unlike in classical computing, where a $0 \rightarrow 1$ transition either happens or not, a qubit may suffer from imperfections in operations, yielding, for example, to a $|0\rangle \rightarrow |1\rangle + \delta\,|0\rangle$ (non-perfect π rotation). These small errors may pile-up with the number of consecutive operations, becoming another source of information loss. Overall, a computation using quantum bits must be fast enough to avoid dephasing and relaxation, and the qubit operations must be good enough to avoid the aforementioned loss of information due to the analog character. Quantum error correction codes are being developed to cope with these errors, at the cost of a considerable increase in the number of physical qubits to encode a single, resilient "logical" qubit in a quantum register [34].

In quantum computing, the building blocks of a quantum algorithm are called quantum logic gates. For a quantum computer to be universal, it must have a complete set of quantum gates allowing to perform any arbitrary task. This includes single- and multi-qubit gates. At the single-qubit level, having a two-axis control over the Bloch sphere enables the reconstruction of any quantum state. The elementary operations can be rotations along $\boldsymbol{x}$, $\boldsymbol{y}$, and $\boldsymbol{z}$. To complete the set of quantum gates, as in classical computing with logic gates, we need two-qubit operations. Two-qubit gates allow to create entangled states. An example of a two-qubit operation is the Controlled-NOT (CNOT) gate (classical X-OR gate), which conditionally switches the state of one qubit depending on the state of another. Any arbitrary gate can be decomposed as a combination of CNOT and single qubit gates, which enables the implementation of any quantum algorithm. Yet, the above discussed set is not unique, and other sets of quantum gates (combinations of those discussed above) may be used as elementary operations for a quantum algorithm depending on the hardware. Any candidate platform to host a quantum processor must demonstrate the ability to achieve a complete set of quantum gates so as to be considered a potential universal quantum computer.

1.3 Quantum dot spin qubits

QD spin qubits are a promising platform to achieve all the requisites mentioned in the previous section. They are based on the formation of gate-defined QDs with an odd number of carriers (electrons or holes) under a non-zero magnetic field B. The particle is trapped in a semiconductor material thanks to the interplay between electrical and structural confinements. The latter results from *e.g.* the finite thickness of the host material, whereas a set of metallic gates introduce vertical and in-plane electric fields that ultimately trap the particle in a finite volume, forming a QD. The electrons or holes are fed to the QDs by "reservoirs", which are device areas with an excess of carriers that set the chemical potential $\overline{\mu}$. The proper alignment of the QD levels and $\overline{\mu}$ provides a tight control over the number of charges in the QD. This enables to achieve a charge occupancy with an odd number of carriers, thus an unpaired spin.

The finite magnetic field splits the energy of the $|\uparrow\rangle\,(S = 1/2)$ and $|\downarrow\rangle\,(S = -1/2)$ spin states of the trapped particle and defines the Larmor frequency $f_L = \Delta E = g\mu_B B$, where g is its gyromagnetic factor and μ_B is the Bohr magneton. This creates a quantum two-level system, in which the information is encoded in the state of the unpaired spin. With Larmor frequencies typically in the few GHz range, temperatures well below the 1 K are required to discriminate the two energy levels and avoid thermal population.

With the QDs hosted in a solid-state material, decoherence mechanisms appear due to the interaction with the environment. The spin is surrounded by possible defects, a set of metallic gates, and by a nuclear environment. If the nuclei of the host material are not spin-less, hyperfine interaction may be an important source of decoherence [35]. In addition, the metal gates are responsible for electrical Johnson-Nyquist noise [36, 37]. The presence of charge traps in the material stack brings another source of electrical noise, labeled as charge noise, which is in many cases the dominant contribution to dephasing [38–40]. With the host semiconductor being a crystalline, phonons are typically an important source of relaxation even at cryogenic temperatures [41, 42].

The main materials used in the semiconductor spin qubits community are GaAs, Si, and Ge. An overview of the devices built with such materials is given in Figure 1.3. As mentioned previously, GaAs/AlGaAs was the first material in which spin qubits were demonstrated thanks to the very clean epitaxial interface between the two materials, yet the nuclear spin $S = 3/2$ of the stable isotopes of both Ga and As soon limited T_2^* to ≈ 10 ns [43]. Silicon, in this respect, is a much more appealing material. Natural Silicon contains 95% of spin-free ^{28}Si, and only 5% of $S = 1/2$ ^{29}Si, which can even be eliminated [44]. Silicon has been widely used both in Si/SiGe heterostructures, and in Si Metal-Oxide-Semiconductor (MOS) devices. Similarly, Germanium, which is used in Ge/SiGe heterostructures, has mostly spin-free stable isotopes, and it only contains a 8% of $S = 9/2$ ^{73}Ge.

In the operation of a quantum processor there are three distinct stages one must be able to realize: the qubits must be initialized in their ground state, then they need to be manipulated to perform the desired task, and finally one must be able to read the result. In the following we review how these operations are achieved in semiconductor spin qubits.

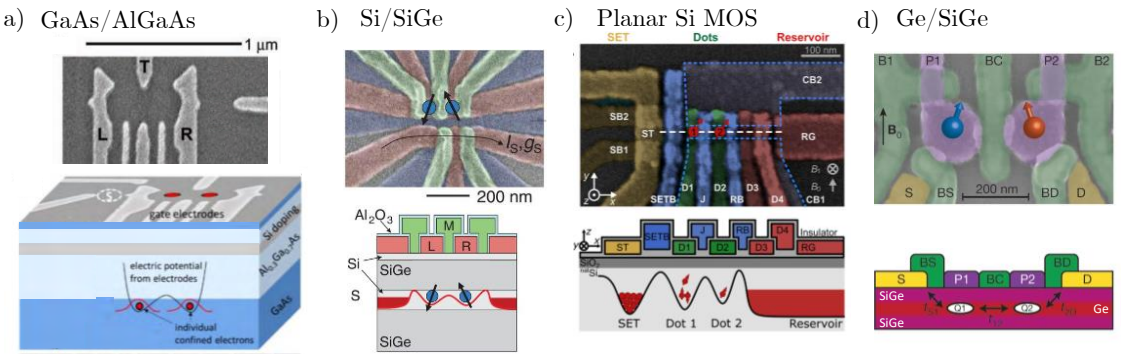

Figure 1.3: Examples of the existing quantum dot spin qubits platforms. a) Scanning electron micrograph of a GaAs/AlGaAs device, and representation of the different material layers. Adapted from Refs. [32, 45]. b) Same for a double quantum dot device on a Si/SiGe heterostructure, adapted from Ref. [46]. c) Same for a planar Si MOS device, where the active Si layer is embedded in SiO_2. Adapted from Ref. [47]. d) Same for a hole two-qubit device on a Ge/SiGe heterostructure. Adapted from Ref. [22].

1.3.1 Initialization

As illustrated in Figure 1.4a, we may rely on relaxation to initialize a quantum dot spin qubit. To do so, the $|\uparrow\rangle$ and $|\downarrow\rangle$ states of the QD, split by the finite B, are electrically tuned with the front gate voltage V_{fg} so as to bring them below the chemical potential $\overline{\mu}$. As a consequence, an electron is loaded in one of the two states indistinctively. If the electron is loaded in the $|\uparrow\rangle$ state, it relaxes on a typical time T_1. By waiting a longer time, one makes sure that relaxation has occurred and that the initial state is $|\downarrow\rangle$ no matter which state was initially loaded. Alternatively, one may also attempt to selectively load a $|\downarrow\rangle$ spin by placing the chemical potential $\overline{\mu}$ in between the $|\uparrow\rangle$ and $|\downarrow\rangle$ energy levels.

1.3.2 Manipulation

To manipulate a single qubit, we need to provide the system with a source of energy matching f_L. Spins naturally couple to magnetic fields, so *a priori* only a Radio Frequency (RF) oscillatory magnetic field $\boldsymbol{B}_{RF} = \boldsymbol{A}\cos(2\pi f_L t + \phi)$ (where $\boldsymbol{A}$ is the amplitude of the magnetic drive and ϕ is an arbitrary phase) can drive coherent oscillations between the $|\uparrow\rangle$ and $|\downarrow\rangle$ states. Such driving mechanism, known as Electron Spin Resonance (ESR), was first demonstrated in Si in 2012 [13], and although it is effective in a single-qubit experiment, the difficulties to deliver magnetic fields locally in many-qubits systems was soon identified as a major drawback. This technique has not been discarded though, and there is still ongoing work on making ESR compatible with large-scale quantum processors [47].

The most used driving mechanism, however, relies on an electrical driving of the spin: the Electric Dipole Spin Resonance (EDSR). It has better scalability perspectives, since a RF electric field can be delivered individually through the metallic gates to the qubits as $\delta V = V_{ac}\cos(2\pi f_L t + \phi)$. We need, however, a mechanism coupling the spin to an electric field. Spin Orbit Coupling (SOC) is a relativistic effect that indeed couples the orbit of the carrier (sensible to electric fields) with its spin. In a semiconductor, the electron (or hole) moves in a lattice

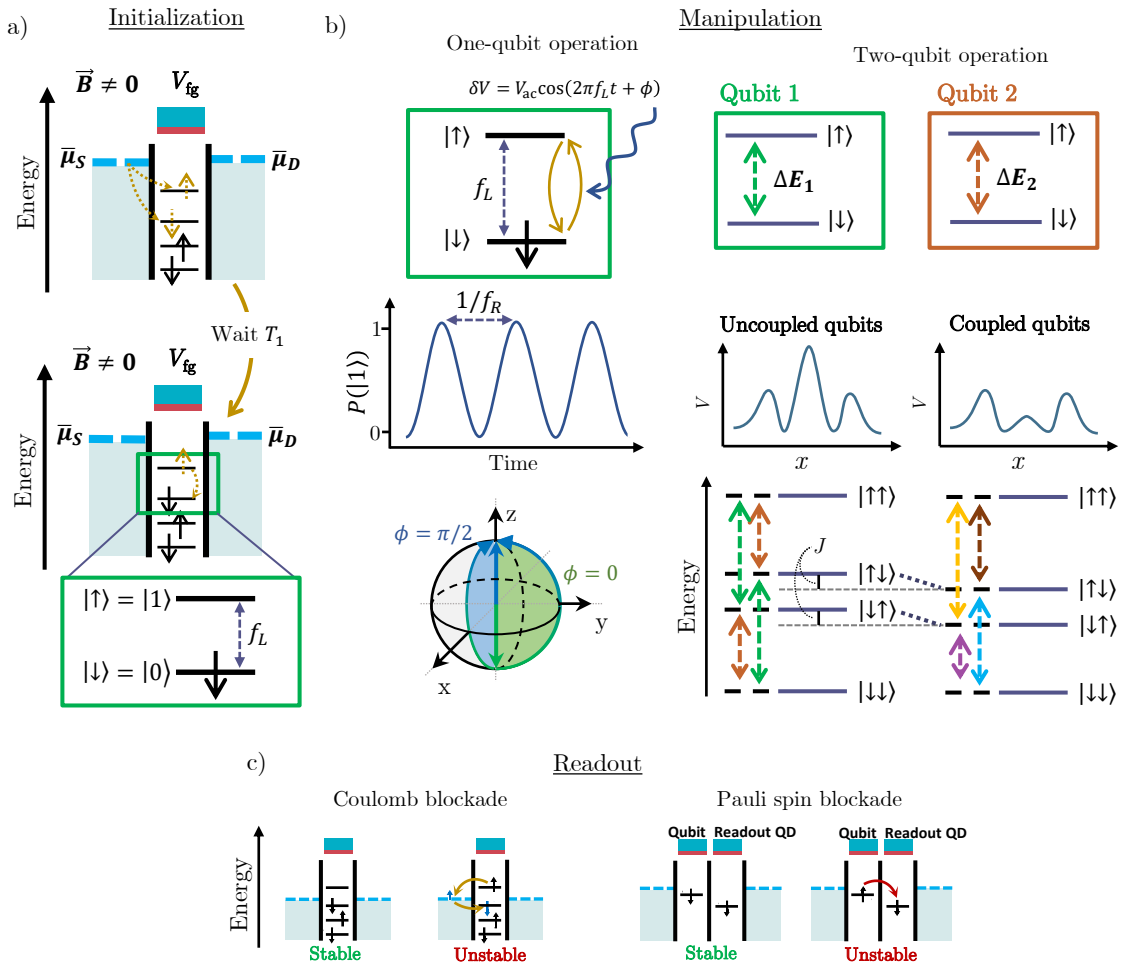

Figure 1.4: Schematic representation of the techniques used to initialize, manipulate, and readout a quantum dot spin qubit. a) For the initialization, a finite magnetic field splits the energy of the spin-up and spin-down states. The energy levels are tuned with V_{fg} so as to bring both levels below the chemical potential of the reservoirs. Consequently, one of the two states is indistinctly populated. Upon a waiting time larger than T_1, the qubit relaxes to the $|\downarrow\rangle$ ground state. Therefore, the initialization is complete. b) For one-qubit operations: A RF electric field matching f_L is applied to manipulate the spin, which rotates at frequency f_R. The rotations around the Bloch sphere can be achieved along two perpendicular directions by applying RF signals with a $\pi/2$ shift in their phase ϕ. For two-qubit operations: Illustration of the impact of the coupling between qubits on their energy spectrum. The $|\uparrow\downarrow\rangle$ and $|\downarrow\uparrow\rangle$ states of two qubits with distinct Zeeman splitting decrease their energy by J due to the interaction, giving rise to four distinct energy gaps for the possible transitions. c) To readout the spin, one can rely on Pauli spin blockade or Coulomb blockade with an energy-selective spin transition to convert the spin state into a charge signal.

of charged nuclei. In the frame of the carrier, the charged nuclei are those spinning around, creating an effective time-dependent magnetic field that acts on the spin. For holes, intrinsic

SOC is large enough to enable EDSR [15, 21]. For electrons, however, the intrinsic SOC is very weak, and artificial sources need to be engineered. In practice, a Micro-Magnet (MM) is placed on top of electron devices to introduce a magnetic field gradient that transforms the spatial motion of the QD (induced by the electric drive) into an effective time-dependent magnetic field in the frame of the carrier. This enables EDSR for electrons despite the very weak intrinsic SOC.

The control over a second axis is achieved simply by changing the phase (ϕ) of the EDSR pulse. In the Bloch-sphere representation of the two-level system, a $\pi/2$ shift on ϕ translates into a $\pi/2$ rotation around z of the transition pathway between the $|\downarrow\rangle$ and $|\uparrow\rangle$ states. This is illustrated in Figure 1.4b. Alternative ways to achieve a two-axis control without the need of any drive make use entirely of a combination of adiabatic and diabatic Direct Current (DC) pulses, but they rely on double (or triple) quantum dots for each qubit. These are the singlet-triplet [32], and the exchange-only qubits [48].

The implementation of two-qubit gates in QD spin qubits relies on the control of the interaction between qubit pairs. In the following, we present a possible implementation of a CNOT gate [46], which consists in the conditional rotation of a spin depending on the state of a second spin. If the control qubit is in the $|\uparrow\rangle$ state, the spin of a target qubit is flipped. Otherwise, the spin of the target qubit remains in its initial state.

In a single-particle picture, one can label the states of a two-qubit system as a function of the orientation of the two spins as $|\downarrow\downarrow\rangle, |\downarrow\uparrow\rangle, |\uparrow\downarrow\rangle, |\uparrow\uparrow\rangle$. These four states, degenerate at $B = 0$ T, split in energy under a finite magnetic field. The $|\downarrow\downarrow\rangle$ ($|\uparrow\uparrow\rangle$) state decreases (increases) in energy, while the pair of $|\downarrow\uparrow\rangle, |\uparrow\downarrow\rangle$ states should remain invariant in absence of SOC. However, SOC induces differences between the energy of $|\downarrow\uparrow\rangle, |\uparrow\downarrow\rangle$ due to different gyromagnetic factors between qubits (for holes), or due to the magnetic field gradients created by the MMs (for electrons), which yields to different Zeeman splitting for the individual qubits ($\Delta E_1 \neq \Delta E_2$). The energy diagram of the two-qubit system has therefore two distinct energies, as shown in Figure 1.4b. The coupling between the qubits, tuned by electrically controlling the energy barrier between them, acts as an extra $H_{\text{eff}} = -J\boldsymbol{S_1} \cdot \boldsymbol{S_2}$ term as a result of a competition between tunneling and Coulomb interactions, where J is the so-called exchange, and $\boldsymbol{S_1}, \boldsymbol{S_2}$ are the spin operators. When the Zeeman splitting is larger than J, such term brings an energy shift of the $|\downarrow\uparrow\rangle, |\uparrow\downarrow\rangle$ states, which yields to four transitions with four distinct excitation energies *i.e.* the energy needed to rotate one of the qubits depends on the state of the other. Consequently, by applying a RF drive with frequency equal to the energy of the transition of interest, we can drive conditional rotations of the spin. Additionally, by controlling the coupling between qubits we can switch from an isolated regime with minimal J, where single-qubit operations can be made; to a coupled regime, where a large J enables two-qubit operations. The origin of the exchange interaction is discussed in more detail in section 2.5.2.

1.3.3 Readout

The detection of spins is not an easy task. Therefore, most of the readout techniques of spin states in QDs rely on the so-called spin-to-charge conversion. The goal is to discern between a spin-up and spin-down state through a charge detection, and this is done in practice by relying either on Coulomb blockade or on Pauli Spin Blockade (PSB), see Figure 1.4c.

Readout techniques relying on Coulomb blockade place the chemical potential of the reservoir

in between that of the $|\uparrow\rangle$ and $|\downarrow\rangle$ states. If the carrier is in its spin down state, the system is stable. If it is in the spin up state, however, it will eventually leave the QD, and another spin-down electron will be loaded in the $|\downarrow\rangle$ state. This charge movement can be detected through different charge sensing techniques, and the presence (absence) of a charge signal determines the spin-up (spin-down) character of the state. Such technique is called Elzerman readout after its demonstration back in 2004 [49], and it is illustrated in Figure 1.4c.

An alternative readout technique relies on Pauli spin blockade, the fact that two electrons cannot fill the same orbital state if they have the same spin. Using an auxiliary QD initialized with a spin down, the spin-to-charge conversion in this case consists in probing the (1,1) $\rightarrow$ (2,0) charge transition. This transition is only allowed if the two spins are anti-parallel. Therefore, tracking changes in the charge occupancy of the auxiliary QD through gate reflectometry allows to distinguish between spin states in the qubit [50–53].

All the discussion of two-qubit operations and readout has been done a single-particle model. However, such processes involve two-particles. Although useful for simple explanations, the single-particle picture must be substituted by a two-particle model in order to have a proper description of the system. The discussion of a double-QD system in a two-particle picture is given in section 2.5.2.

1.4 The Silicon route in Grenoble

The uniqueness of quantum computing in Grenoble lies on the gathering of all expertises needed in the different steps of the project: from the design and fabrication of the devices to the characterization and modelling. The device design and fabrication are driven by the CEA-LETI, which has industrial fabrication clean room facilities and a vast experience in classical microelectronics. The physics experiments are carried out both at CEA-IRIG and at Institut Néel at CNRS. Modelling is mainly done by the L_Sim group at CEA-IRIG.

The spin qubits in Grenoble are made with Silicon as the semiconductor host material. As discussed above, Silicon is a very appealing choice for semiconductor spin qubits due to the small number of spin-carrying nuclei it contains, with the ultimately possibility to be purified to a completely atomic spin-free material. This greatly enhances the coherence times of the qubits, since the hyperfine interaction is suppressed. On top of this, the similarities between a semiconductor spin qubit and a classical transistor allowed to adapt the well-established transistor fabrication processes at CEA-LETI to produce Si MOS devices for quantum computing purposes in the same industrial facilities, and integrate them on standard 300 mm Si wafers. This enables the fabrication of a very large number of samples with respect to the handmade fabrications in academic clean rooms, with much better reproducibility and scalability perspectives. CEA was the only player in the Si spin qubits community working with samples fabricated in a 300 mm semiconductor facilities, yet Intel, in collaboration with TU Delft, recently published results on industrially-compatible Fin Field-Effect Transistor (FET) devices [54], which stresses the importance that having scalable architectures is starting to have in the design roadmap of the different players in the field.

A Si MOS spin qubit device at LETI is essentially a transistor at cryogenic temperatures, see Figure 1.5. Its fabrication starts from a Silicon On Insulator (SOI) wafer, consisting in a Si substrate with a Buried Oxide (BOX) layer that may range in between 25 nm (for thin-BOX

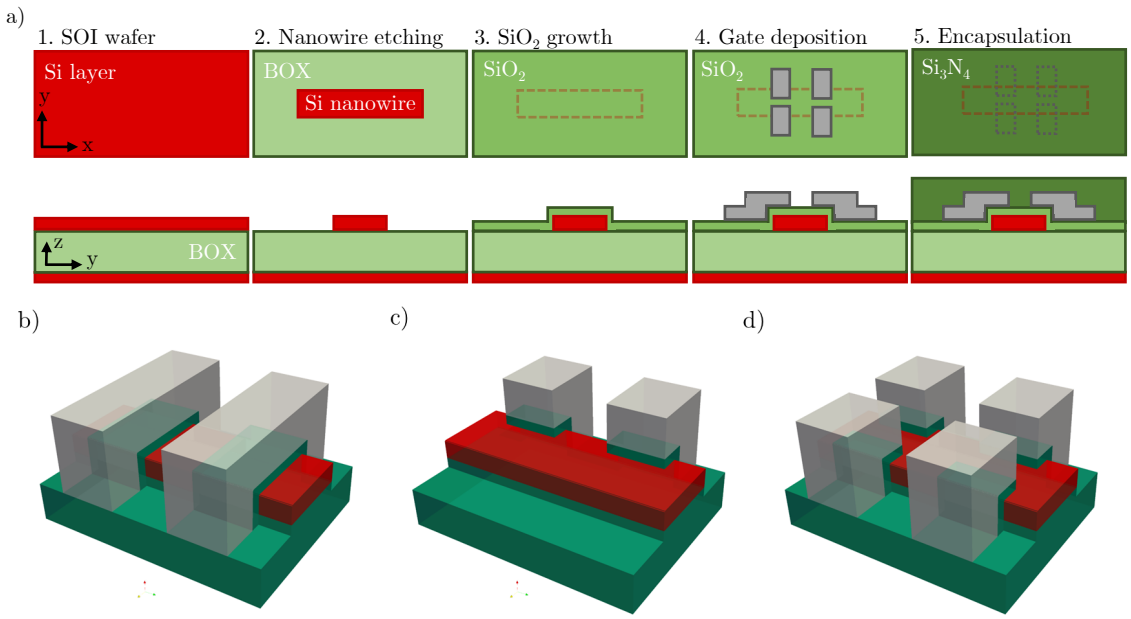

Figure 1.5: a) Schematic representation of the fabrication process of LETI devices. b) Illustration of a pump gates device. The BOX and SiO_2 are shown in green, the Si nanowire in red, and the gates in grey. The oxide covering the nanowire and the Si_3N_4 are not shown for clarity. c) Illustration of a device with partly-overlapping gates. d) Illustration of a device with face-to-face gates.

devices) and 150 nm (for thick-BOX devices). On top of it, there is a Silicon layer, that upon an etching process, becomes the nanowire of the device. Its thickness is typically around 10 nm, while its width ranges from 30 nm to 100 nm. The nanowire is next embedded in a few nanometers of SiO_2, and then metallic gates composed by a first layer of TiN (5 nm) and a second one of polysilicon (20-50 nm) are deposited. Typical gate layouts can be classified in three types, see Figures 1.5b, 1.5c, and 1.5d. For pump gates devices, the gates cover the full width of the nanowire, whereas partly overlapping gates cover only a portion of it. The latter can either be an array of single gates, or of face-to-face gates. As reservoirs of carriers for the QDs, two highly doped areas are formed at the edges of the nanowire, the so-called source and drain. Previous to the doping process, Si_3N_4 spacers are grown to isolate the gates and to protect the channel. The doping can be done with P (n-type doping) or B (p-type doping) atoms, which defines the type of carriers of the qubits: electrons for n-type devices, and holes for p-type devices. Finally, the full device is embedded in SiO_2 and Si_3N_4.

SiO_2 is an amorphous material, and as such it may present defective interfaces. Moreover, the nanowires resulting from the etching process and the non-uniformity of the BOX can lead to surface roughness. Such sources of disorder may strongly impact the performance of spin qubits in presence of SOC mechanisms. This impact had never been quantified experimentally nor theoretically. A question that remained open at the beginning of this thesis was, therefore, how large is variability, and how much can it compromise the scalability of such a platform.

The first qubit out of a Si MOS device fabricated at LETI was demonstrated in a p-type device in 2016 [15]. Since then, progress has been made on the optimization of both electron

and hole devices, switching for example from pump gate layouts to split face-to-face gates [55]. These optimizations allowed to improve and the quality of the qubits [56] and the understanding of their physics [53, 57]. On the theory side, great progress has been made in the understanding of the electrical manipulation of hole spin qubits [58–60], as well as on setting up realistic models for qubit relaxation and dephasing [41, 42].

At the beginning of this thesis, devices fabricated at LETI still lacked specific gates to tune the tunnel couplings between neighboring qubits, and MMs to manipulate electron spins in n-type devices. This prevented the demonstration of two-qubit gates, and focused the studies of electron devices to the optimization of charge control and readout [40, 61, 62], or to the exploration of alternative manipulation techniques relying on spin-valley-orbit coupling [42, 63]. The major challenges for the LETI devices at the end of 2019 were indeed to enable a proper control of the tunnel couplings to perform two-qubit gates, and to integrate micro-magnets in the n-type devices to allow for an electrical manipulation of electron spin qubits.

1.5 The overtake of epitaxial heterostructures

To date, only single-qubit demonstrations have been achieved with devices based on industrial Si MOS technology, while two-qubit experiments have been demonstrated on lab-made devices based on the same technology [64, 65]. Meanwhile, experiments using epitaxial Si/SiGe and Ge/SiGe heterostructures have reached remarkable breakthroughs recently. Several groups achieved two-qubit gates back in 2018 [46, 66], and apart from improving the quality of the two-qubit operation, a six-qubit quantum processor has been demonstrated recently, being the largest quantum processor based on spins [16]. In parallel, great progress has been made with hole qubits in a Ge/SiGe heterostructure. Since the first demonstration in 2018 [21], Veldhorst's group in Delft has managed to double the number of qubits almost every year, demonstrating a four-qubit quantum processor in 2021 [22, 23].

It is most probably not a coincidence that Si/SiGe and Ge/SiGe based devices show such a continuous progress. Si/SiGe and Ge/SiGe heterostructures have epitaxial interfaces, which are known to have a very low level of disorder. This contrasts with the more defective nature of the Si/SiO_2 interfaces in Si MOS devices. The evidences seem to point out to a crucial importance of the interface quality and level of disorder in the devices when trying to scale up the different platforms.

1.6 Large-scale architectures

While current experiments still deal with a very reduced number of qubits, several proposals for large-scale quantum processors based on spins have been already discussed in the literature [67–70]. Almost every research group has its own proposal, yet there are several similarities between the different prototypes. A large-scale quantum computer must be a two-dimensional array of qubits, not just to achieve a better integration, but also to enable error correction [71, 72]. In addition, all proposals insist that the number of control knobs per qubit must be largely reduced. In a quantum processor with a large number of qubits N, the number of DC lines cannot scale as N, since there would be a lack of physical space in the chip, and huge amounts of cooling power would be needed to palliate the heating effects. To tackle this issue, crossbar

gate architectures are envisioned, where a single DC line controls the full line/column of gates of the 2D array [73, 74]. Individual addressability of the qubits in the array would then require the proper tuning of a set of line and column gates.

With the decrease of the number of tuning knobs, qubit-to-qubit variability may start to become an issue. Arrays of identical qubits can be perfectly addressed with a crossbar architecture. It is unclear, however, to what extent such architectures can deal with qubits with individual "personalities".

1.7 Contents of this thesis

In the context discussed above, this thesis makes use of numerical simulations to identify, understand, and try to solve the challenges that spin qubits platforms may encounter if the number of qubits continues to increase.

- In Chapter 2, we review the existing computational methods to simulate the electronic structure of electron and hole quantum dots in a semiconductor, and we explain how to extract the relevant qubit properties from these simulations.
- In Chapter 3, we discuss the contributions made to the existing computational framework. First, we introduce a model to describe Rabi oscillations for electron spin qubits in presence of MMs, and derive the expressions needed to introduce them in the numerical simulations. Second, we discuss the implementation of the visualization of many-particle states.
- In Chapter 4, we address the variability of the single-qubit properties of electron and hole spin qubits in Si MOS devices. We quantify the expected variability due to surface roughness and charge defects at the Si/SiO_2 interface, analyze the underlying mechanisms, and discuss the implications that disorder may have for a large-scale quantum processor.
- In Chapter 5, we first design a second level of metallic gates for the Si MOS devices simulated in Chapter 4 that allows to control efficiently the tunnel coupling between qubits in 1D arrays. Then, we quantify the impact of variability on the two-qubit properties in such devices.
- In Chapter 6, we discuss the physics of hole spin qubits in Ge/SiGe heterostructures. We unveil a novel mechanism for Rabi oscillations, and quantify the impact of variability for this platform. We also propose a novel gate layout for epitaxial-based platforms that improves the figures-of-merit of variability of the current devices.
- In Chapter 7, we study the impact of many-body interactions in multi-particle QDs. We show that the appearance of molecularization effects can have critical consequences on Pauli spin blockade-based readout and on the management of exchange interactions.
- In Chapter 8, we highlight the main conclusions extracted throughout this work, and discuss the future perspectives that may follow.

Chapter 2

Theory of nanodevices modelling

Contents

Devices used in spin qubit experiments are in the nano (or even micro) scale, and their numerical modelling using quantum methods must be addressed carefully. At such scales, the simulation includes millions of atoms, which leaves the problem out of reach of the standard *ab-initio* methods. Alternatively, semi-empirical methods, with the correct parametrization, offer a great opportunity to address quantum properties in such large systems with sufficient accuracy and an affordable computational cost.

In the following, we discuss the theoretical methods to describe the electronic structure of semiconductors, and we explain how to go from the description of a bulk material to that of a QD. Then, we present TB_SIM, the computational code from CEA to model spin qubits, and finally we discuss how to extract the qubit properties from the output of a Single Particle (SP) calculation.

2.1 Electrons and holes in a semiconductor

The electronic structure of the bulk of semiconductor materials, as periodic crystals, is described by band diagrams. The valence bands of a semiconductor are completely filled, leaving a gap with the empty conduction bands. The most interesting part of the band diagram is then at the top of the valence band for holes, and at the bottom of the conduction band for electrons.

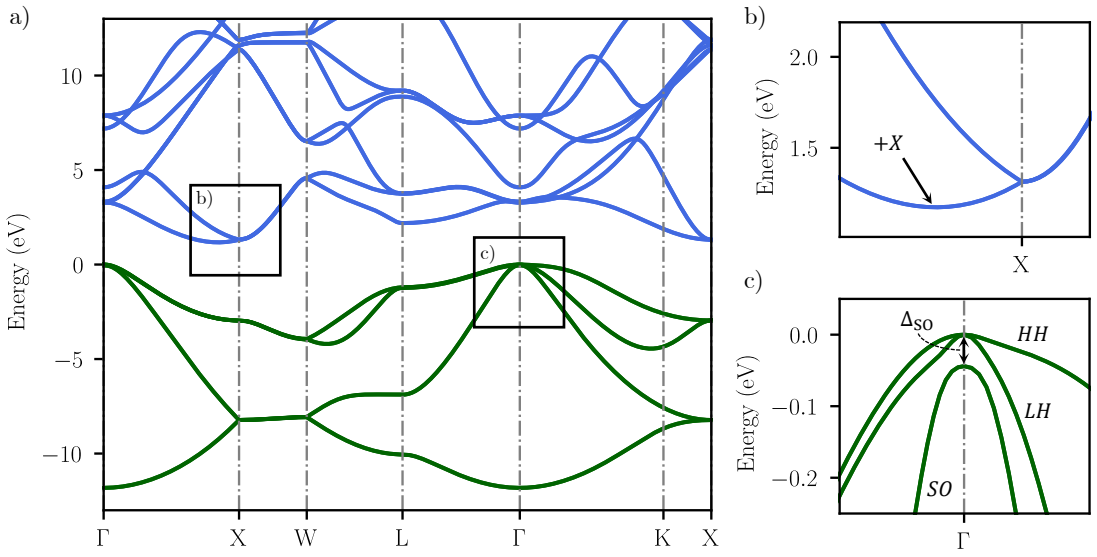

Figure 2.1: a) Band diagram of Silicon computed with a Tight-Binding calculation. b) Zoom into the bottom of the conduction band. The conduction band edge is six-fold degenerate, which gives rise to 6 conduction band valleys $\pm X$, $\pm Y$, $\pm Z$ near the X, Y, Z points of the first Brillouin zone. c) Zoom into the top of the valence band, where the heavy hole (HH) and light hole (LH) bands are split from the split-off (SO) band by Δ_{SO} due to SOC effects.

Throughout this thesis, we simulate electron spin qubits in Silicon, and hole spin qubits in Silicon and in Germanium. Silicon is an indirect band gap material, with the valence-band maximum at Γ, and the conduction-band minimum close to X, see Figure 2.1, with a band gap $E_g = 1.17$ eV at 0 K [75]. This conduction band minimum is six-fold degenerate owing to the cubic symmetry of the *fcc* diamond lattice of bulk Silicon, which gives rise to the so-called conduction band valleys, labelled $\pm X$, $\pm Y$, $\pm Z$. Note that in addition each valley state is two-fold spin degenerate. The indirect nature of the Si band gap leaves the conduction band with a very weak SOC, as it arises from the coupling between p_z, p_x, p_y orbitals, which are split in energy at large $\boldsymbol{k}$.

For holes, the qualitative structure of the band diagram is the same regardless of the semiconductor. At Γ, the states can be mapped onto $|j, m_j\rangle$ states, where $j \in [1/2, 3, 2]$ defines the total angular momentum J, and $|m_z| < j$ its projection along $\boldsymbol{z}$. The pair of $|3/2, \pm 3/2\rangle$, $|3/2, \pm 1/2\rangle$ bands (the so-called heavy hole and light hole bands) are split from the $|1/2, \pm 1/2\rangle$ (named split-off band) by an energy Δ_{SO} due to spin-orbit effects. Unlike the conduction band, SOC is important for the valence band, as in Γ the p_z, p_x, p_y orbitals are degenerate and can mix efficiently. $\Delta_{\mathrm{SO}} = 44$ meV for Si, and 290 meV for Ge [75].

The theoretical description of electrons and holes in a semiconductor can be addressed from two different perspectives. The $\mathbf{k}\cdot\mathbf{p}$ method is a continuum band model that exploits the repetitiveness of crystalline structures to simplify the problem. It gets rid of the atomistic lattice, with the consequent advantage that it does not scale with the number of atoms. Unfortunately, this approximation comes with a price, and properties strongly dependent on the atomic struc-

ture of the material may not be accounted for accurately. Alternatively, Tight-Binding (TB) approaches the problem from a microscopic perspective, and introduces an atomistic description of the semiconductor. While more expensive computationally, it captures all the effects of atomistic nature that may be missed with $\mathbf{k}\cdot\mathbf{p}$. Therefore, it enables to describe disorder at the atomistic level, dopants, etc. In the following, we review these methods and how they can be used to simulate spin qubits.

2.1.1 The k·p method

The $\mathbf{k}\cdot\mathbf{p}$ method is originally an extrapolation method for bulk band structures around a reference wave vector $\mathbf{k_0}$. The Hamiltonian of a spinless particle in the nuclei potential $V_{\mathrm{N}}(r)$ of a crystalline structure is

$$\hat{H}_0 = \frac{\hat{\mathbf{p}}^2}{2m} + V_{\mathrm{N}}(\mathbf{r}) \tag{2.1}$$

with $\hat{\mathbf{p}}$ the momentum, and m the mass of the particle. The potential V_{N} created by the nuclei in the crystalline structure follows the periodicity of the lattice. The eigenfunctions of H_0 are therefore Bloch functions $\psi_{n,\mathbf{k}} = e^{i(\mathbf{k}-\mathbf{k_0})\cdot\mathbf{r}} u_{n,\mathbf{k}}(\mathbf{r})$ (where $\mathbf{k}$ is a wave vector, and $u_{n,\mathbf{k}}(\mathbf{r})$ is also periodic over the lattice). We can then focus on the resolution of the Schrödinger equation for $u_{n,\mathbf{k}}(\mathbf{r})$,

$$\hat{H}(\mathbf{k}) u_{n,\mathbf{k}}(\mathbf{r}) = E_{n\mathbf{k}} u_{n,\mathbf{k}}, \tag{2.2}$$

with

$$\hat{H}(\mathbf{k}) = \hat{H}_0 + \frac{\hbar}{m}(\mathbf{k}-\mathbf{k_0})\cdot\hat{\mathbf{p}} + \frac{\hbar^2(\mathbf{k}-\mathbf{k_0})^2}{2m}. \tag{2.3}$$

The $\mathbf{k}\cdot\mathbf{p}$ method treats the effect of the $(\mathbf{k}-\mathbf{k_0})\cdot\hat{\mathbf{p}}$ term at $\mathbf{k}\neq\mathbf{k_0}$ in a basis set of $u_{n,\mathbf{k_0}}(\boldsymbol{r})$ at $\mathbf{k_0}$. Some of the basis states are explicitly included in the basis set, while some others (labeled as remote bands) are treated with perturbation theory. Such an approximation is accurate for $\mathbf{k}\to\mathbf{k_0}$. The subsets of explicitly-included bands differ for electrons and holes, and we review them in the following sections.

2.1.1.1 Electrons in the conduction band

A single electron in the conduction band is the simplest case one can treat with the $\mathbf{k}\cdot\mathbf{p}$ method. This is known as the Effective Mass Approximation (EMA). At $\mathbf{k_0}=\Gamma$, a perturbative treatment of the $(\mathbf{k}-\mathbf{k_0})\cdot\hat{\mathbf{p}}$ term in equation 2.3 for the remote bands yields to

$$\hat{H}_{\mathrm{EMA}}(\mathbf{k}) = E_c + \frac{\hbar^2\mathbf{k}^2}{2m^*}, \tag{2.4}$$

where E_c is the energy of the conduction band edge, and m^* is the conduction band effective mass, which accounts for the $\mathbf{k}\cdot\mathbf{p}$ coupling with the remote valence and conduction bands. In this approximation, the dispersion is therefore parabolic, and it can be generalized to the case $\mathbf{k_0}\neq\Gamma$, relevant for Silicon where the conduction band minimum is not at $\mathbf{k}=0$. If we assume that in Si[100] the different valleys are uncoupled, we can also approximate the problem to a single Z band, yet we must introduce anisotropic longitudinal and transverse effective masses

(m_l and m_t), so that

$$\hat{H}_{\mathrm{EMA}}(\mathbf{k}) = E_c + \frac{\hbar^2}{2}\left(\frac{(k_z - k_0)^2}{m_l} + \frac{k_x^2}{m_t} + \frac{k_y^2}{m_t}\right). \tag{2.5}$$

2.1.1.2 Holes in the valence band

The situation is more complex for holes. The degeneracy of the heavy- and light- hole bands at Γ and the proximity of the split-off band enlarge the minimal basis set to all the $|3/2, \pm 3/2\rangle$, $|3/2, \pm 1/2\rangle$, and $|1/2, \pm 1/2\rangle$ bands [76]. Moreover, SOC is not described by equation 2.3, yet it can be added as an extra $\hat{H}_{\mathrm{SO}}$ term [77],

$$\hat{H}_{SO} = \lambda_{SO}\mathbf{L}\cdot\mathbf{S}, \tag{2.6}$$

where λ_{SO} is a constant that quantifies the strength of the SOC, $\mathbf{L}$ is the angular momentum operator, and $\mathbf{S}$ is the spin operator.

Treating the $\mathbf{k}\cdot\hat{\mathbf{p}}$ term explicitly near Γ in the $\{|3/2,+3/2\rangle,\ |3/2,+1/2\rangle,\ |3/2,-1/2\rangle,\ |3/2,-3/2\rangle,\ |1/2,+1/2\rangle,\ |1/2,-1/2\rangle\}$ basis set [78, 79], we obtain the so called six-bands $\mathbf{k}\cdot\mathbf{p}$ (6kp) Hamiltonian, which takes the following form:

$$\hat{H}_{6\mathrm{kp}}(\mathbf{k}) = -\begin{pmatrix} P+Q & -S & R & 0 & \frac{1}{\sqrt{2}}S & -\sqrt{2}R \\ -S^* & P-Q & 0 & R & \sqrt{2}Q & -\sqrt{\frac{3}{2}}S \\ R^* & 0 & P-Q & S & -\sqrt{\frac{3}{2}}S^* & -\sqrt{2}Q \\ 0 & R^* & S^* & P+Q & \sqrt{2}R^* & \frac{1}{\sqrt{2}}S^* \\ \frac{1}{\sqrt{2}}S^* & \sqrt{2}Q & -\sqrt{\frac{3}{2}}S & \sqrt{2}R & P+\Delta_{\mathrm{SO}} & 0 \\ -\sqrt{2}R^* & -\sqrt{\frac{3}{2}}S^* & -\sqrt{2}Q & \frac{1}{\sqrt{2}}S & 0 & P+\Delta_{\mathrm{SO}} \end{pmatrix}, \tag{2.7}$$

with

$$\begin{aligned} P &= \frac{\hbar^2}{2m_0}\gamma_1\left(k_x^2 + k_y^2 + k_z^2\right) \\ Q &= \frac{\hbar^2}{2m_0}\gamma_2\left(k_x^2 + k_y^2 - 2k_z^2\right) \\ R &= \frac{\hbar^2}{2m_0}\sqrt{3}\left[-\gamma_3\left(k_x^2 - k_y^2\right) + 2i\gamma_2 k_x k_y\right] \\ S &= \frac{\hbar^2}{2m_0}2\sqrt{3}\gamma_3\left(k_x - ik_y\right)k_z, \end{aligned} \tag{2.8}$$

where k_x, k_y, k_z are the three spatial components of the wave vector $\mathbf{k}$, and γ_1, γ_2, γ_3 are the so-called Luttinger parameters, which define the hole masses (m) in the semiconductor. They

are experimentally characterized with magneto-transport measurements, and read

$$\begin{aligned} m^h_{[001]} &= \frac{m_0}{\gamma_1 - 2\gamma_2} \\ m^l_{[001]} &= \frac{m_0}{\gamma_1 + 2\gamma_2} \\ m^h_{[111]} &= \frac{m_0}{\gamma_1 - 2\gamma_3} \\ m^l_{[111]} &= \frac{m_0}{\gamma_1 + 2\gamma_3}, \end{aligned} \tag{2.9}$$

where the subscript i of m_i^j denotes the crystallographic direction, and the superscript j labels the heavy (h) or light (l) hole band. In the basis of $|j, m_j\rangle$ states, $\hat{H}_{\mathrm{SO}}$ is diagonal, and it only contributes to the split-off $|1/2, \pm 1/2\rangle$ energies in equation 2.7 with $\Delta_{\mathrm{SO}} = 3/2\lambda_{\mathrm{SO}}$. For Silicon, the split-off bands must be included due to the small Δ_{SO}. For Germanium, however, Δ_{SO} is much larger than the other energy scales of the problem, and we may disregard the pair of $|1/2, \pm 1/2\rangle$ states in equation 2.7 and work with the so-called four-bands $\mathbf{k}\cdot\mathbf{p}$ (4kp) model.

With κ, γ_1, γ_2 and γ_3 as input parameters, the band diagram can be computed upon diagonalization of equation 2.7 for different $\mathbf{k}$.

2.1.2 The Tight Binding method

The TB method faces the problem from a completely different perspective. The strategy is analogous for electrons and holes, and it is based on expressing the system wavefunction as a linear combination of orthogonal atomic orbitals $\phi_{i\alpha}$, with i labeling the atom number and α the orbital type. The system Hamiltonian is then built as

$$\hat{H}_{\mathrm{TB}} = \sum_{i\alpha} \varepsilon_{i\alpha} |\phi_{i\alpha}\rangle\langle\phi_{i\alpha}| + \sum_{i\alpha, j\beta} t_{i\alpha j\beta} |\phi_{i\alpha}\rangle\langle\phi_{j\beta}| + \hat{H}_{SO}, \tag{2.10}$$

which defines the diagonal elements $\langle\phi_{i\alpha}|\hat{H}_{\mathrm{TB}}|\phi_{i\alpha}\rangle = \varepsilon_{i\alpha}$, the energy of the orbital α in the atom i; and the off-diagonal elements $\langle\phi_{i\alpha}|\hat{H}_{\mathrm{TB}}|\phi_{j\beta}\rangle = t_{i\alpha,j\beta}$, the hopping term coupling orbital α from atom i to orbital β from atom j. As for the $\mathbf{k}\cdot\mathbf{p}$ method, the spin-orbit effects are not captured by the first two terms in the equation above, and they must be included as the same extra term $\hat{H}_{SO} = \lambda_{SO} \sum_i \mathbf{L_i} \cdot \mathbf{S}$, where $\mathbf{L_i}$ is now the angular momentum operator centered on atom i.

The lattice structure and the atomic connectivity play an important role, since they are essentially what the TB Hamiltonian emulates. A cutoff distance is set to decide the nonzero hopping terms, typically staying in the first-, second-, or even third- nearest neighbors. For pairs of atoms further than the chosen cutoff, $t_{i\alpha j\beta} = 0$. Consequently, $\hat{H}_{\mathrm{TB}}$ is sparse, and its complexity grows with the cutoff. The basis of atomic orbitals included for each atom also determines the trade-off between accuracy and complexity. For Silicon and Germanium, a complete enough basis set includes the valence s, p, and d orbitals, and an extra $s*$ orbital. The standard description of Si and Ge is thus a first-nearest-neighbors $sp^3d^5s^*$ TB model.

The advantage of TB with respect to continuum band models is the atomistic description of the material. The inclusion of defects such as dopants becomes straightforward, as it only requires setting the proper $\varepsilon_{i\alpha}$ and $t_{i\alpha j\beta}$ for the site i where the dopant is placed. The main

drawback is that the size of the basis set is proportional to the number of atoms, which makes the computations substantially more costly than a simple **k**·**p** calculation.

The TB parameters $\varepsilon_{i\alpha}$ and $t_{i\alpha j\beta}$ of semiconductor materials such as Si and Ge are typically fitted on the bulk band structures computed with *ab-initio* methods such as Density Functional Theory (DFT) or GW approximation. The application of TB to periodic lattices and the subsequent extraction of band diagrams is discussed in Ref. [80].

2.2 From bulk to a quantum dot

Up to now we have discussed the electronic structure of a bulk semiconductor and how to obtain band diagrams from **k**·**p** and TB calculations, yet in the frame of spin qubits we are interested in particles (electrons or holes) spatially confined in QDs. The QDs are generally formed by electrical and possibly also structural confinement. Electrical confinement appears when the potential landscape of the material is shaped with external electric fields so as to form a quantum well that traps the particle. This potential is typically generated with a set of metallic gates. This coexists with a structural confinement, which appears when the periodicity of a bulk material is broken in a given direction, for example, when we go from bulk to a slab. This also traps the particle in a finite space. Both type of confinements coexist, and which one dominates depends on the particular conditions of each experiment. For a given axis, we refer to an electrically-confined particle when the electrical confinement is stronger than the structural one, and to a structurally-confined particle otherwise.

The strongest (structural or electrical) confinement is typically in the "vertical" direction ($\boldsymbol{z}$) perpendicular to the active layer, owing to its finite thickness. For electrons in the conduction band of Silicon, the vertical confinement splits the $\pm Z$ valley states from $\pm X, \pm Y$ by a few meV. Moreover, the presence of sharp potentials (typically a semiconductor/dielectric interface) mixes the lowest-lying $\pm Z$ valleys and splits them by Δ_{VS}, known as the Valley Splitting (VS). Δ_{VS} can range between a few tens to a few hundreds of μeV [40], and it is extremely sensitive to the atomistic details of the interface [81]. Δ_{VS} is a clear example of a property that can be captured by TB and not easily by **k**·**p**.

The vertical confinement of a hole in the valence band breaks the degeneracy between heavy- and light-hole bands, and the in-plane confinement admixes them. This mixture depends on the confinement strength and strains, yet typically the first holes in Si and Ge are mostly heavy-hole type [60]. As for electrons, each state is two-fold (Kramers') degenerate at zero magnetic field, yet due to SOC spin is not a good quantum number anymore. For QD-based hole qubits, the computational basis is in fact made of pseudo-spin states, each of them being a combination of the pure spin envelopes.

Let us now see how can include confinement in the methods explained above. To account for electrical confinement we need to describe the potential generated by the gate layout. The way the potential spreads through the material stack depends on the dielectric constant of the different materials, and is described by Poisson's equation. The final potential landscape, $V(\mathbf{r})$, is

$$\boldsymbol{\nabla}[\varepsilon(\mathbf{r})\boldsymbol{\nabla}V(\mathbf{r})] = -4\pi\rho(\mathbf{r}), \tag{2.11}$$

which relates it to the dielectric constant $\varepsilon(\mathbf{r})$, and the charge density $\rho(\mathbf{r})$.

The resulting $V(\mathbf{r})$ can be included in the Hamiltonians of the previous models. For TB,

the Hamiltonian of the single-particle QD ($\hat{H}^{\mathrm{SP}}_{\mathrm{TB}} = \hat{H}_{\mathrm{TB}} + V(\mathbf{r})$) is computed by adding the outcome potential as a shift to the energy of each atomic orbital, $\langle\phi_{i\alpha}|\hat{H}_{\mathrm{TB}}\phi_{i\alpha}\rangle = \varepsilon_{i\alpha} + V(\mathbf{R_i})$, where $\mathbf{R_i}$ is the position in space of atom i. Moreover, structural confinement is also taken into account by breaking Periodic Boundary Conditions (PBC) in the necessary direction(s). The broken bonds at the surface of the structure are typically passivated with Hydrogen-like atoms (only one s-type orbital). We can then obtain the SP energies and wavefunctions of the particle in the QD by diagonalizing $\hat{H}^{\mathrm{SP}}_{\mathrm{TB}}$.

For the $\mathbf{k}\cdot\mathbf{p}$ Hamiltonian, the inclusion of a confining potential breaks the periodicity. We can define the Hamiltonian of a confined electron or hole as $\hat{H}^{\mathrm{SP}}_{\mathrm{kp}} = \hat{H}_{\mathrm{kp}}(\mathbf{k}) + V(\mathbf{r})$. Its eigenstates are no longer Bloch functions, but they read

$$\psi_i = \sum_k \varphi_{ik} u_k, \tag{2.12}$$

where φ_{ik} are envelope functions that spatially-confine the delocalized Bloch functions, and deliver localized states as solutions of $\hat{H}^{\mathrm{SP}}_{\mathrm{kp}}$. Note that each u_k has its own envelope, which enables them to have different spatial confinement under the same electric field. The integral of each envelope, in addition, represents the weight of each of the Bloch functions in ψ_i. Finally, the $\mathbf{k}$-dependence of $\hat{H}^{\mathrm{SP}}_{\mathrm{kp}}$ is lifted by substituting k_i terms in $\hat{H}_{\mathrm{kp}}(\mathbf{k})$ by $-i\nabla_\alpha$, with $\alpha \in [x, y, z]$.

The diagonalization of $\hat{H}^{\mathrm{SP}}_{\mathrm{6kp}}$ requires now a mapping to the real-space mesh in which $V(\mathbf{r})$ is solved. This yields to a set of coupled differential equations for the φ_i, which can be solved, and provide the $\mathbf{k}\cdot\mathbf{p}$ solutions to the SP QD problem.

2.3 Effect of a magnetic field

The methods described so far deal with a singe-particle QD in absence of magnetic field. However, spin qubits operate at finite B,[1] so we need to account for it in the modelling.

The effect of the magnetic field is two-fold. On the one hand, it breaks the degeneracy of the spin states and splits the energy levels. On the other hand, it impacts the orbital motion of the particles. In both TB and $\mathbf{k}\cdot\mathbf{p}$, the Hamiltonian describing the impact on the spin part of the wavefunctions is $\hat{H}_z = g_0\mu_B\mathbf{B}\cdot\mathbf{S}$, where g_0 is the bare Landé gyromagnetic factor and μ_B the Bohr's magneton.

In TB the effect on the orbital motion is treated by Peierls substitution [84], which replaces the hopping terms t_{ij} in $\hat{H}^{\mathrm{SP}}_{\mathrm{TB}}$ by $t_{ij}e^{\frac{-ie}{\hbar}\int_{R_i}^{R_j}\boldsymbol{A}(\mathbf{r})\cdot d\mathbf{r}}$, where $\boldsymbol{A}$ is the vector potential.[2] For $\mathbf{k}\cdot\mathbf{p}$, the situation is more complex, since the wavefunctions are products of envelope functions φ_{ik} and Bloch functions u_k, and both are affected by B. The impact on the Bloch functions is described by the Bloch Hamiltonian $\hat{H}_{\mathrm{Bloch}} = -(3\kappa+1)\mu_B\mathbf{B}\cdot\mathbf{L}$, and the effect on the envelope functions is accounted for by Peierls substitution, which in this case replaces the terms ∇_i in $\hat{H}^{\mathrm{SP}}_{\mathrm{kp}}$ by $\nabla_i - \frac{e}{\hbar}\boldsymbol{A}$.[3]

[1] Some non-standard spin qubits, like the resonant exchange qubits, do not require finite magnetic fields [82, 83].

[2] The vector potential $\boldsymbol{A}$ is the curl of the magnetic field, so $\boldsymbol{B} = \boldsymbol{\nabla}\times\boldsymbol{A}$.

[3] Once the $\mathbf{k}\cdot\mathbf{p}$ Hamiltonian is discretized on a spatial mesh, the Peierls substitution can be introduced as for TB by adding a $e^{\frac{-ie}{\hbar}\int_{R_i}^{R_j}\boldsymbol{A}(\mathbf{r})\cdot d\mathbf{r}}$ factor to the off-diagonal elements.

Consequently, the Hamiltonian describing a spin qubit at finite magnetic field is $\hat{H}_{\mathrm{TB}}^{\mathrm{SP}}$ (or $\hat{H}_{\mathrm{kp}}^{\mathrm{SP}}$), with the proper Peierls substitution (and the inclusion of $\hat{H}_{\mathrm{Bloch}}$ for $\mathbf{k}\cdot\mathbf{p}$) to account for the effects of B on the spatial part of the wavefunctions, and the addition $\hat{H}_z$ to account for the effect of B on the spin part of the wavefunctions.

2.4 Many-particle states

The systems described so far were single-particle systems, in the sense that electron-electron (ore hole-hole) interactions were not included. For spin qubits, however, the QDs are sometimes filled with more than a single carrier, and mechanisms like Pauli spin blockade or Elzerman readout are ruled by these interactions. Consequently, it is important to be able to describe them theoretically.

The computation of electron-electron interactions for spin qubits is inspired from the quantum chemistry methods. In chemistry, Coulomb repulsion is fundamental and defines the shape and properties of molecules. The number of electrons is certainly larger there than in the context of spin qubits, yet the same methods can be used. In presence of electron-electron interactions, we can write the Many Particle (MP) Hamiltonian as

$$\hat{H}^{\mathrm{MP}} = \hat{H}^{\mathrm{SP}} + W_{\mathrm{e-e}}, \tag{2.13}$$

where $\hat{H}^{\mathrm{SP}}$ is either the $\mathbf{k}\cdot\mathbf{p}$ or the TB Hamiltonian, and $W_{\mathrm{e-e}}$ is the electron-electron (or hole-hole) interaction term. This term depends on the position of the two particles, and on the dielectric constants of the materials around.[4]

The simplest antisymmetric wavefunction we can build for a many-particle system is a so-called Slater determinant. For the two-particle case, it is defined as $\Phi = |\psi_i(\mathbf{r_1})\psi_j(\mathbf{r_2})| = \psi_i(\mathbf{r_1})\psi_j(\mathbf{r_2}) - \psi_j(\mathbf{r_1})\psi_i(\mathbf{r_2})$, where ψ_i and ψ_j are two SP wavefunctions. With a single Slater determinant Coulomb interactions can be accounted for in a mean-field approximation, a widely-used method in computational chemistry, known as Hartree Fock (HF). A more accurate description can be achieved by expanding the many-body wavefunctions as linear combinations of Slater determinants, which is known as the Configuration Interaction (CI) method. For a given number of particles n and basis states N, a so-called full-CI calculation includes all possible Slater determinants, which number can be calculated as the binomial coefficient $\binom{N}{n}$. For two particles, the full-CI wavefunctions read

$$\Psi_k = \sum_{i,j>i}^{N} c_{k,ij}|\psi_i(\mathbf{r_1})\psi_j(\mathbf{r_2})| = \sum_{i,j>i}^{N} c_{k,ij}[\psi_i(\mathbf{r_1})\psi_j(\mathbf{r_2}) - \psi_j(\mathbf{r_1})\psi_i(\mathbf{r_2})]. \tag{2.14}$$

The CI Hamiltonian ($\hat{H}^{\mathrm{CI}}$) is expressed in the basis of the Slater determinants, and it is constructed from the information of the basis states composing the Slater determinants (in this case the SP states, eigenstates of $\hat{H}^{\mathrm{SP}}$) following the so-called Slater-Condon rules [85–87]. For a pair of Slater determinants Φ_a, Φ_b, the columns are swapped so they look as much alike as

[4] The interaction is repulsive, so the closer the particles are the larger the repulsion interaction is. Moreover, materials with large ε are able to smooth the propagation of the Coulomb repulsion, weakening the interaction term.

possible.[5] Then, the matrix elements $\langle\Phi_a|\hat{H}^{\mathrm{CI}}|\Phi_b\rangle$ are computed differently depending on the number of coincident basis states the determinants have. If $a = b$,

$$\langle\Phi_a|\hat{H}^{\mathrm{CI}}|\Phi_b\rangle = \sum_i \langle\psi_i|\hat{H}^{\mathrm{SP}}|\psi_i\rangle + \sum_{j<i} \langle\psi_i\psi_j|W_{\mathrm{e-e}}|\psi_i\psi_j\rangle - \langle\psi_i\psi_j|W_{\mathrm{e-e}}|\psi_j\psi_i\rangle\,. \tag{2.15}$$

If the two determinants differ only by one basis state, i.e. $\Phi_a = |....\psi_i\psi_j...|$, $\Phi_b = |....\psi_k\psi_j...|$, then

$$\langle\Phi_a|\hat{H}^{\mathrm{CI}}|\Phi_b\rangle = \langle\psi_i|\hat{H}^{\mathrm{SP}}|\psi_k\rangle + \sum_j \langle\psi_i\psi_j|W_{\mathrm{e-e}}|\psi_k\psi_j\rangle - \langle\psi_i\psi_j|W_{\mathrm{e-e}}|\psi_j\psi_k\rangle\,. \tag{2.16}$$

If the two determinants differ by two basis states, i.e. $\Phi_a = |....\psi_i\psi_j...|$, $\Phi_b = |....\psi_k\psi_l...|$, then

$$\langle\Phi_a|\hat{H}^{\mathrm{CI}}|\Phi_b\rangle = \langle\psi_i\psi_j|W_{\mathrm{e-e}}|\psi_k\psi_l\rangle - \langle\psi_i\psi_j|W_{\mathrm{e-e}}|\psi_l\psi_k\rangle\,, \tag{2.17}$$

and for all pairs of determinants that differ by more than two basis states, $\langle\Phi_a|\hat{H}^{\mathrm{CI}}|\Phi_b\rangle = 0$. In this way, the CI method allows us to describe a many-particle system with the knowledge of the non-interacting eigenstates and the interaction term W_{e-e}.

To compute the $U_{ijkl} = \langle\psi_i\psi_j|W_{\mathrm{e-e}}|\psi_k\psi_l\rangle$ terms, we can define a joint density $\rho_{jl}(\mathbf{r}) = \psi_j^*(\mathbf{r})\psi_l(\mathbf{r})$, and an associated potential $V_{jl}(\mathbf{r}) = \int \mathrm{d}^3\mathbf{r}' W_{\mathrm{e-e}}(\mathbf{r},\mathbf{r}')\rho_{jl}(\mathbf{r}')$. $V_{jl}(\mathbf{r})$ is basically the potential created by the charge density ρ_{jl}, which can be computed making use of the Poisson's solver discussed above.[6] Here, the equation to solve is

$$\boldsymbol{\nabla}[\varepsilon(\mathbf{r})\boldsymbol{\nabla}V_{jl}(\mathbf{r})] = -4\pi\rho_{jl}(\mathbf{r}). \tag{2.18}$$

With all the $U_{ijkl} = \langle\rho_{ik}|V_{jl}\rangle$ terms computed, the resolution of the problem reduces then to the diagonalization of $\hat{H}^{\mathrm{CI}}$, which provides the energy spectrum and the wavefunctions of the many-particle system.

2.5 Numerical resolution of the problem

The computational code developed at CEA Grenoble to simulate spin qubits in semiconductor QDs is called TB_Sim. It allows to analyze a wide variety of device geometries, and to extract single- and two-qubit properties through the proper post-processing of the results. It is based on the theory discussed above, and its simulation workflow is illustrated in Figure 2.2. First, a fine reproduction of the device layout is built on a 3D mesh by assigning a material to each of the elementary volumes. Then, Poisson's equation (equation 2.11) is solved numerically on the grid using a finite volumes method, which provides the potential landscape $V(\mathbf{r})$ generated by the different metallic gates.

The second step is to solve the single-particle problem. To define $\hat{H}_{\mathrm{kp}}$ for holes, the only parameters required are κ, γ_1, γ_2, γ_3, and Δ_{SO}; whereas $\hat{H}_{\mathrm{EMA}}$ for electrons requires only the

[5] For a given determinant, a swap between columns only brings a change of sign to the final result. In the two-particle case, for example, a pair of determinants $\Phi_1 = |\psi_1(\mathbf{r_1})\psi_2(\mathbf{r_2})|$ and $\Phi_2 = |\psi_2(\mathbf{r_1})\psi_3(\mathbf{r_2})|$ would be rearranged as $\Phi_1 = |\psi_1(\mathbf{r_1})\psi_2(\mathbf{r_2})|$ and $\Phi_2 = -|\psi_3(\mathbf{r_1})\psi_2(\mathbf{r_2})|$.

[6] Note that solving the U_{ijkl} terms using Poisson's equation, the results include the screening due to the dielectric constants of the different materials.

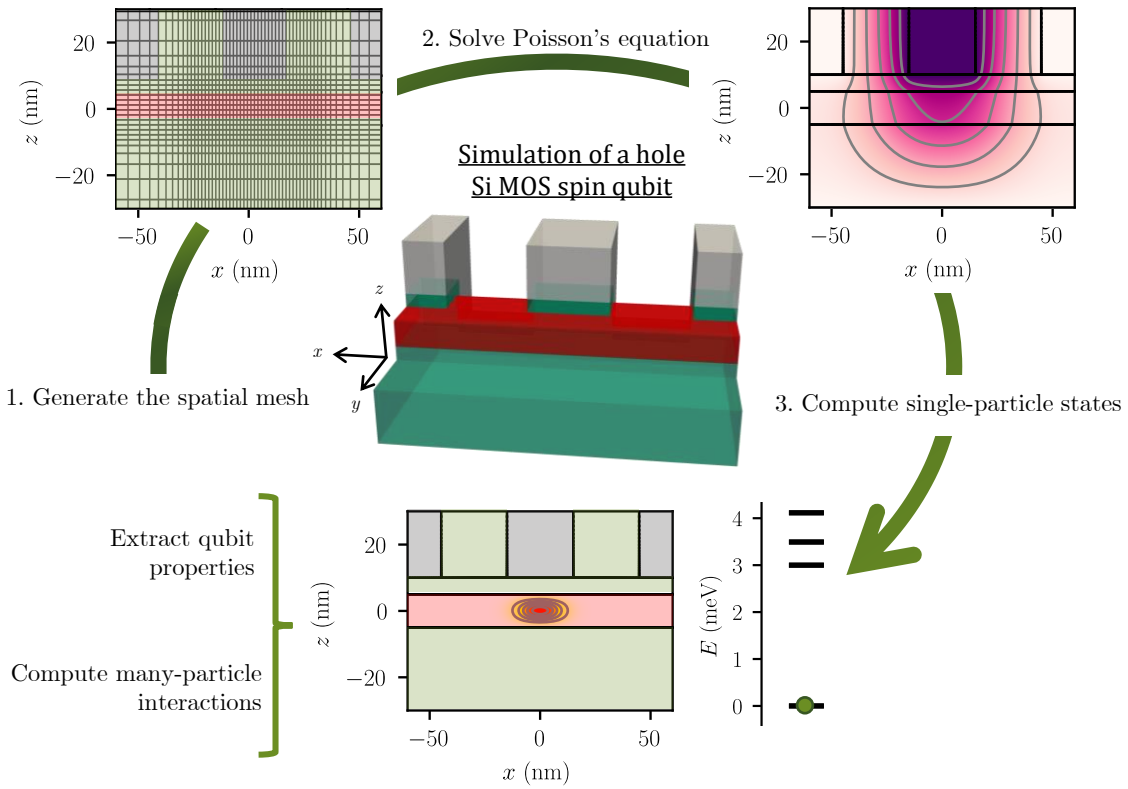

Figure 2.2: Schematic representation of the computational workflow followed to simulate a spin qubit with TB_Sim, here illustrated for a hole spin qubit in a Si MOS device. First, the device geometry is discretized on a three-dimensional mesh. Then, Poisson's equation is solved and input to the SP Hamiltonian, which is partially diagonalized to obtain the SP energies and states. With them, a CI calculation allows to account for many-body interactions. In addition, qubit properties can be extracted as explained in section 2.5.1.

effective masses $m^*_{\parallel}$ and $m^*_{\perp}$. For TB we need the ε_i and t_{ij} for the different orbitals included in the basis set, plus the parameters for the "hydrogen-like" passivation atoms. The input parameters we use throughout this thesis are given in Appendix A.2. The effect of the magnetic field is introduced in the discretized Hamiltonian as explained in section 2.3. The partial diagonalization of the Hamiltonian is performed using an iterative Jacobi-Davidson algorithm [88], which provides the lowest-lying eigenstates of the simulated qubit.

Finally, to perform a CI calculation, $\hat{H}^{\mathrm{CI}}$ is built following the rules exposed above, using as basis states those obtained in the SP calculation. All the $\langle\psi_i|\hat{H}^{\mathrm{SP}}|\psi_j\rangle$ terms are known, and the remaining inputs are the $\langle\psi_i\psi_j|W_{\mathrm{e-e}}|\psi_k\psi_l\rangle$ terms, which are computed with the Poisson solver. The diagonalization of $\hat{H}^{\mathrm{CI}}$ is also done with a Jacoby-Davidson method.

This methodology allows us to compute the electronic structure of electrostatically-trapped electrons or holes in a semiconductor material. Regardless of whether we stay at the SP level or we go for a CI calculation, the results we obtain are the energy spectrum and the wavefunctions of the simulated QD. Let us see how we can extract the qubit properties from this information.

2.5.1 Extraction of qubit properties

Once we have built and solved the single-particle (or the CI) Hamiltonian, we can easily post-process the results in order to extract relevant qubit properties. We discuss hereafter how to extract the Rabi frequency (f_R), the Larmor frequency (f_L), and the tunnel coupling between adjacent qubits.

2.5.1.1 Larmor frequency

The Larmor frequency (f_L) is the energy splitting between the two spin states encoding the quantum information, caused by the finite magnetic field. Its evaluation is therefore straightforward when the SP calculation includes $\boldsymbol{B}$, and it simply reads

$$f_L = (E_\uparrow - E_\downarrow)/h, \tag{2.19}$$

where $E_\uparrow$ and $E_\downarrow$ are the energy of the spin-up ($|\uparrow\rangle$) and spin-down ($|\downarrow\rangle$) states at finite B.

Alternatively, we can make use of the so-called "g-matrix formalism" [58], which embeds the linear response of the system to the magnetic field in a 3x3 matrix $\hat{g}$, and allows to evaluate f_L at any given $\boldsymbol{B}$ from a single calculation at $B = 0$. For that purpose, we map the two-level Hamiltonian of the spin states on the generic form

$$H(V, \boldsymbol{B}) = \frac{1}{2}\mu_B \boldsymbol{\sigma} \cdot \hat{g}(V)\boldsymbol{B}, \tag{2.20}$$

where μ_B is the Bohr magneton, and $\boldsymbol{\sigma} = (\sigma_1, \sigma_2, \sigma_3)$ is the vector of Pauli matrices. If we now expand the SP or MP Hamiltonian $H(V, \boldsymbol{B})$ in powers of B, we get

$$H(V, \boldsymbol{B}) = H_0(V) - B_x M_{1,x} - B_y M_{1,y} - B_z M_{1,z} + \mathcal{O}\left(B^2\right), \tag{2.21}$$

where $M_{1,\alpha} = -\partial H(V, \boldsymbol{B})/\partial B_\alpha$ is the first-order derivative of the Hamiltonian with respect to B_α, with α in $[x, y, z]$. The link between equations 2.20 and 2.21 yields to an expression for the $\hat{g}$ matrix as a function of $M_{1,\alpha}$ [58],

$$\hat{g}\left(V_0\right) = -\frac{2}{\mu_B}\begin{pmatrix} \mathrm{Re}\left\langle \Downarrow |M_{1,x}| \Uparrow \right\rangle & \mathrm{Re}\left\langle \Downarrow |M_{1,y}| \Uparrow \right\rangle & \mathrm{Re}\left\langle \Downarrow |M_{1,z}| \Uparrow \right\rangle \\ \mathrm{Im}\left\langle \Downarrow |M_{1,x}| \Uparrow \right\rangle & \mathrm{Im}\left\langle \Downarrow |M_{1,y}| \Uparrow \right\rangle & \mathrm{Im}\left\langle \Downarrow |M_{1,z}| \Uparrow \right\rangle \\ \left\langle \Uparrow |M_{1,x}| \Uparrow \right\rangle & \left\langle \Uparrow |M_{1,y}| \Uparrow \right\rangle & \left\langle \Uparrow |M_{1,z}| \Uparrow \right\rangle \end{pmatrix}, \tag{2.22}$$

where the $\Downarrow$ and $\Uparrow$ states are the degenerate up- and down- spin states at zero magnetic field. Due to the degeneracy, they are not uniquely defined. Consequently, $\hat{g}$ depends on the choice of $\Downarrow$ and $\Uparrow$ basis states. But the Zeeman splitting is determined by the effective g factor $g^* = |\hat{g}\left(V_0\right)\boldsymbol{B}|/|\boldsymbol{B}|$, which is actually independent of the chosen basis [58]. The Larmor frequency then reads

$$f_L = \mu_B g^* |\boldsymbol{B}|/h. \tag{2.23}$$

Numerically, we can evaluate $M_{1,\alpha}$ by finite differences including the magnetic field in H as explained in section 2.3, and easily compute $\hat{g}$. In this way, the g-matrix formalism allows to reconstruct the full anisotropy of g^* (and therefore f_L) from a single evaluation of $\hat{g}\left(V_0\right)$, whereas relying on equation 2.19 requires an individual simulation for each magnetic field orientation.

2.5.1.2 Rabi frequency

The Rabi frequency (f_R) determines the speed of rotation between the $|\downarrow\rangle$ and $|\uparrow\rangle$ spin states at finite magnetic field. As described in section 1.2, when performing EDSR the spin rotations are driven by an oscillatory Alternating Current (AC) field $\delta V_g = V_{\text{ac}}\cos(2\pi f_L t + \phi)$ applied on a gate. At first order in V_{ac}, f_R is proportional to the matrix element coupling the two spin states, and it reads

$$f_R = \frac{e}{h} V_{\text{ac}} \left| \langle \uparrow | D | \downarrow \rangle \right|, \tag{2.24}$$

with $D = \frac{\partial H}{\partial V_g} = \frac{\partial V(r)}{\partial V_g}$ the change of the total potential $V(r)$ induced by modulations of the gate potential V_g where the AC field is applied [58]. Since the electrostatics is linear,[7] we can compute D as the potential generated by 1 V on gate g with all the other gates grounded. We label this method as "direct evaluation". It is first-order in V_{ac} but all-orders in B, and H must explicitly include B as explained in section 2.3.

The direct evaluation is a useful tool to compute f_R for a fixed magnetic field orientation. If we are interested, however, in exploring multiple orientations to analyze the f_R anisotropy, relying on equation 2.24 becomes computationally costly, since we need to evaluate $\langle \uparrow | D | \downarrow \rangle$ for each orientation.[8]

We can also make use of the g-matrix formalism to evaluate f_R at any given $\boldsymbol{B}$ from a single calculation at $B = 0$. The AC field indeed modulates the g-matrix $\hat{g}(V)$. At first order in δV, we can write $\hat{g}(V) = \hat{g}(V_0) + \delta V \hat{g}'(V_0)$, which leads to the following expression for the Rabi frequency (see Ref. [58] for the demonstration),

$$f_R = \frac{\mu_B V_{\text{ac}}}{2h|\hat{g}(V_0)\boldsymbol{B}|} \left| [\hat{g}(V_0)\boldsymbol{B}] \times [\hat{g}'(V_0)\boldsymbol{B}] \right|. \tag{2.25}$$

$\hat{g}'(V_0)$ can be computed by finite differences by evaluating $\hat{g}(V_0 + V_{\text{ac}})$ and $\hat{g}(V_0 - V_{\text{ac}})$, and once we know both $\hat{g}(V_0)$ and $\hat{g}'(V_0)$ we can compute f_R at any magnetic field orientation with equation 2.25.

There are two different mechanisms that can give rise to Rabi oscillations: the so-called g-TMR and Iso-Zeeman Electric Dipole Spin Resonance (IZ-EDSR) [60]. The first one is based on the modulation of the QD confinement by the RF drive, which impacts the QD size and gives rise to a modulation of the Zeeman splitting in presence of SOC. The second one appears when the QD is displaced as a whole (typically along the direction of weakest confinement), and leaves the Zeeman splitting invariant. It typically results from Rashba-type SOI [60, 89]. Although their distinct nature, in realistic devices with complex electrostatics these mechanisms can coexist. They are both are captured by the direct evaluation and the g-matrix formalism. In Appendix A.1 we discuss possible splittings of the total f_R to disentangle the individual contributions of the different mechanisms.

2.5.2 Two-qubit interactions

The tunnel coupling (τ) between adjacent qubits is a key parameter to perform two-qubit operations, as well as to achieve fast readout. In particular, τ controls the strength of exchange

[7] The derivative $\frac{\partial V(r)}{\partial V_g}$ is constant regardless of the bias where it is evaluated.

[8] D is independent of the magnetic field, yet the $|\uparrow\rangle$ and $|\downarrow\rangle$ states do vary with B.

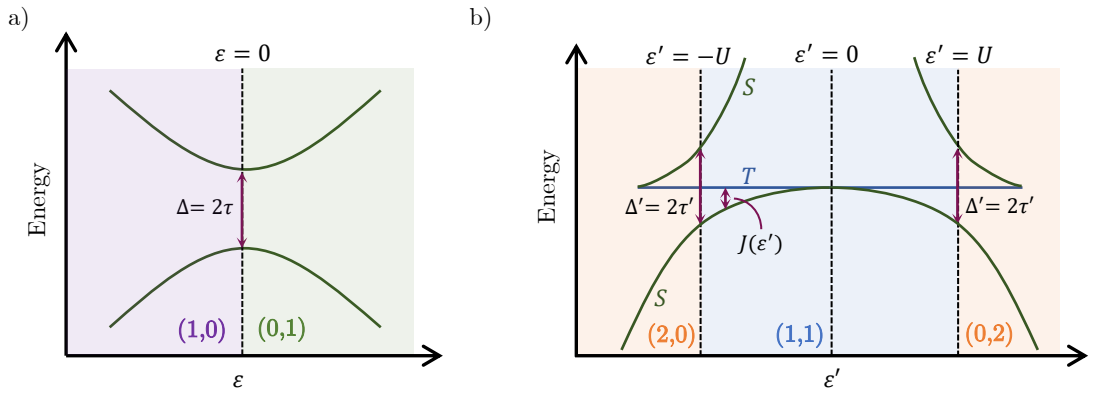

Figure 2.3: a) Schematic representation of the energy diagram of the single-particle system resulting from the diagonalization of the model Hamiltonian in equation 2.26. A SP calculation at $\varepsilon = 0$ (where the double QD is tuned) enables the extraction of τ. b) Schematic representation of the energy diagram of the two-particle system as in the model Hamiltonian of equation 2.27. A CI calculation at $\varepsilon' = \pm U$ provides an estimate of τ'.

interactions (J) between qubits, crucial to achieve two-qubit operations. Its quantification, therefore, is important to reach a proper numerical characterization and understanding of the modelled spin qubits. The evaluation of τ and J relies on mapping the results of the numerical simulation to a model Hamiltonian. For the SP case, the model Hamiltonian of a single charge in a double QD system in the minimal basis of the {(0,1),(1,0)} charge states reads

$$H = \begin{pmatrix} \varepsilon/2 & \tau \\ \tau & -\varepsilon/2 \end{pmatrix}, \tag{2.26}$$

where ε is the detuning between the two states with respect to the center of the anticrossing. At $\varepsilon = 0$, when the two QDs are tuned, the energy gap between the two charge states is $\Delta = 2\tau$. Therefore, a SP calculation of the double QD allows to map the obtained energy spectrum to the Hamiltonian above and extract τ, see Figure 2.3a.

Both PSB-based readout and two-qubit operations, however, involve at least two particles. The single-particle picture discussed in sections 1.3.2 and 1.3.3 for these mechanisms is a simplified picture. In the many-particle picture, we can label the states according to their spin quantum number as singlets (S, with total spin 0) or triplets (T, with total spin 1). At the (1,1) charge configuration, the system has three triplet states $T_-(1,1) = |\downarrow,\downarrow\rangle$, $T_+(1,1) = |\uparrow,\uparrow\rangle$, $T_0(1,1) = (|\downarrow,\uparrow\rangle + |\uparrow,\downarrow\rangle)/\sqrt{2}$, and a singlet state $S(1,1) = (|\downarrow,\uparrow\rangle - |\uparrow,\downarrow\rangle)/\sqrt{2}$. As in the single-particle picture, all these states are degenerate at $B = 0$. Moreover, in the two-particle case we have a set of four (2,0) and four (0,2) charge states, which again can be labeled as S, T_0, T_-, T_+. The $S(2,0)$ and $S(0,2)$ are the ground states of the $(2,0)$ and $(0,2)$ charge configurations, while the triplets (degenerate at $B = 0$) lie farther above in energy. The minimal basis set for the model Hamiltonian of the two-particle system at $B = 0$ includes the states $\{S(1,1), T(1,1), S(0,2), S(2,0)\}$, where $T(1,1)$ is one of the degenerate $T_0(1,1)$, $T_+(1,1)$, $T_-(1,1)$.[9] The triplet

[9]Since they are degenerate and they behave identically at $B = 0$, we can restrict the minimal basis set to one of them while keeping in mind that it is three-fold degenerate.

states for the (2,0) and (0,2) charge configurations are often not considered, as they are assumed to be much higher in energy. In this basis, the model Hamiltonian reads

$$H = \begin{pmatrix} 0 & 0 & \tau' & \tau' \\ 0 & 0 & 0 & 0 \\ \tau' & 0 & -\varepsilon' + U & 0 \\ \tau' & 0 & 0 & \varepsilon' + U \end{pmatrix}, \tag{2.27}$$

where now ε' is centered on the so-called Symmetric Operation Point (SOP), namely the center of the (1,1) region. U stands for the charging energy, and τ' is the tunnel coupling between the (1,1) and the (0,2), (2,0) charge states, here assumed equal for simplicity.

The energy diagram of the two-particle model Hamiltonian is shown in Figure 2.3b. The singlet $S(1,1)$ anticrosses with $S(2,0)$ and $S(0,2)$ with a gap $\Delta' = 2\tau'$, while the triplets $T(1,1)$ remain uncoupled.[10] At $B = 0$, the exchange interaction is in fact the energy difference between $S(1,1)$ and $T(1,1)$, see Figure 2.3b. Its dependence on the tunnel coupling appears naturally in the two-particle picture. A stronger tunnel coupling τ' opens the gap of the anticrossings, which bends the $S(1,1)$ state, and increases J. The origin of J is then found on the tunneling between $S(1,1)$ and $S(2,0)$ (and $S(0,2)$). Consequently, J increases when $|\varepsilon'| \to U$, and it can be finite at $\varepsilon' = 0$ (the SOP) for small U and large τ'.

From the simulation perspective, the energy gap for the two-particle system can be computed with a CI calculation at $\varepsilon' = \pm U$. We can then extract τ' from the energy gap (Δ'), as $\Delta' = 2\tau'$. Moreover, we can estimate the exchange interaction J, which in the (1,1) region is $J = 2\tau'^2 U/(U^2 - \varepsilon'^2)$ [90].

If we assume $\tau' = \sqrt{2}\tau$ (which neglects the swelling of the QD due to Coulomb repulsion, yet accounts for the fact that two particles can tunnel), the numerical estimation of τ already gives very useful information of the two-particle system, as we can estimate J as $J = 4\tau^2 U/(U^2 - \varepsilon'^2)$. This allows us to extract two-particle properties from single-particle calculations, much more affordable in terms of computational cost.

2.6 Chapter 2 in a nutshell

In this Chapter we have reviewed the theoretical methods to describe the electronic structure of crystalline materials, and how to go from a band diagram picture to confined electrons or holes. We have seen that for systems with the size of the spin qubit nanodevices we must rely on semi-empirical methods to perform numerical simulations, since they are too big to be treated *ab-initio*. Tight-Binding is a method in which we model the system as a set of atomic orbitals placed at the atomic position of the lattice, and we parameterize their matrix elements to greatly reduce its computational cost. Alternatively, $\mathbf{k}\cdot\mathbf{p}$ is a continuum band model that gets rid of the atomistic lattice, and can be also adapted to describe spatially-confined electrons or holes. Such methods can account for the effect of SOC and an external magnetic field upon addition of extra terms to the Hamiltonian, and provide an accurate description of the energy spectrum of singly-occupied QDs. For many-particle systems, we can rely on the CI method, which accounts for correlation effects.

[10] We assumed $T(2,0)$ and $T(0,2)$ to be far in energy, so their anticrossing with $T(1,1)$ would appear at large $|\varepsilon'|$ if they were included in the basis set.

The extraction of qubit properties from the electronic structure calculation relies on mapping the obtained results to the appropriate models. With them, we have all the ingredients for the simulation of semiconductor spin qubits. All these methods are included in TB_Sim, the computational framework developed at CEA to perform numerical simulations of spin qubits nanodevices, which has been the principal tool employed to obtain the results of this thesis.

Chapter 3

Contributions to the computational framework

Contents

The question-marks and the problems to address from the simulation side evolve with time, and so do the required computational tools to carry out these simulations. The TB_Sim platform is in constant upgrade, and new features are integrated when needed. At the beginning of this thesis, several aspects that are crucial to address the problems we have targeted were missing. First, the simulation of EDSR with MMs for electron spin qubits was not implemented. Previous studies in the group focused on TB simulations for spin-valley-mediated Rabi oscillations [42], yet the modelling of electron spin qubits in presence of MMs was still to be set up. In the first section of this chapter we derive a model for the Rabi oscillations in presence of MMs that has been integrated in TB_Sim.

In the second section of this Chapter, we derive the expressions for the many-particle wavefunctions and densities. It is of great value to be able to visualize the wavefunctions of the simulated qubits. For the SP case, this is rather simple, and it was already implemented in TB_Sim. For the CI, however, the many-particle wavefunctions are combinations of Slater determinants built with the SP states, and their visualization requires an additional post-processing step.

Additionally, we provide in Appendix B the algorithm developed to extract the tunnel coupling for defective devices. This methodology is used in Chapters 5 and 6, and the details of its derivation, implemented in TB_Sim during this thesis, are discussed in section B.1.

3.1 Micro-magnets in electron devices

The numerical simulation of EDSR relying on intrinsic SOC can be tackled using the two methodologies explained in section 2.5.1.2: direct evaluation or g-matrix formalism; yet only holes can undergo EDSR without an external source of SOC. For electrons, MMs are introduced to enable an electrical driving of the spin. TB_Sim did not have the option of including MMs in the numerical simulations of electron spin qubits. Here we describe first a model for Rabi oscillations in presence of a magnetic field gradient, and then the equations for the implementation of the MMs field directly in the single-particle calculations.

3.1.1 Model for EDSR in presence of micro-magnets

Let us assume that the g-factor of the electrons remains close to $g_0 = 2$. A general two-level Hamiltonian for such system, similar to that in equation 2.20, would then be

$$H(V, \boldsymbol{B}) = \frac{1}{2}\mu_B g_0 \boldsymbol{B} \cdot \boldsymbol{\sigma}. \tag{3.1}$$

In the presence of a micro-magnet, $\boldsymbol{B}$ is the sum of the contributions from the external magnetic field, plus the inhomogeneous magnetic field created by the MM ($\boldsymbol{B}_m(\boldsymbol{r})$),

$$\boldsymbol{B} = \boldsymbol{B}_{ext} + \boldsymbol{B}_m(\boldsymbol{r}). \tag{3.2}$$

We can approximate $\boldsymbol{B}_m(\boldsymbol{r})$ as a linear function at the scale of the QD, so we can estimate it at any $\boldsymbol{r}$ from its value and derivatives at a reference position $\boldsymbol{r_R}$,

$$\boldsymbol{B}_m = \boldsymbol{B}_m(\boldsymbol{r_R}) + G(\boldsymbol{r_R})(\boldsymbol{r} - \boldsymbol{r_R}), \tag{3.3}$$

where

$$G = \begin{pmatrix} \frac{\partial B_x}{\partial x} & \frac{\partial B_x}{\partial y} & \frac{\partial B_x}{\partial z} \\ \frac{\partial B_y}{\partial x} & \frac{\partial B_y}{\partial y} & \frac{\partial B_y}{\partial z} \\ \frac{\partial B_z}{\partial x} & \frac{\partial B_z}{\partial y} & \frac{\partial B_z}{\partial z} \end{pmatrix}. \tag{3.4}$$

Therefore, we can express the Hamiltonian in equation 3.1 as

$$H(V, \boldsymbol{B}) = \frac{1}{2}\mu_B g_0 \boldsymbol{B}(\boldsymbol{r_R}) \cdot \boldsymbol{\sigma} + \frac{1}{2}\mu_B g_0 G(\boldsymbol{r_R}) \cdot (\boldsymbol{r} - \boldsymbol{r_R}) \cdot \boldsymbol{\sigma}. \tag{3.5}$$

We can make use of the same strategy as in the g-matrix formalism [58] to estimate H in presence of the EDSR drive $\delta V(t)$. For electrons, with a constant g factor, the effect of the RF drive is reduced to the oscillatory spatial displacement of the QD,

$$\boldsymbol{r}(t) = \boldsymbol{r}_0 + \boldsymbol{r}'\delta V(t), \tag{3.6}$$

where $\boldsymbol{r}_0$ is the position of the QD in absence of driving, and $\boldsymbol{r}' = \frac{\partial \boldsymbol{r}}{\partial V_g}$ is the derivative of the QD position with respect to the gate voltage V_g. Since $\boldsymbol{B}$ is not homogeneous and the QD oscillates, an effective oscillatory magnetic field is created in the frame of the QD. Therefore, the Hamiltonian of the system when the RF signal is applied reads

$$H(V+\delta V,\boldsymbol{B}) = \frac{1}{2}\mu_B g_0 \boldsymbol{B}(\boldsymbol{r_0})\cdot\boldsymbol{\sigma} + \frac{1}{2}\mu_B g_0 G(\boldsymbol{r}_0)\boldsymbol{r}'\delta V\cdot\boldsymbol{\sigma}, \tag{3.7}$$

with $\boldsymbol{B} = \boldsymbol{B}_{ext} + \boldsymbol{B}_m(\boldsymbol{r}_0)$, and the G matrix evaluated at $\boldsymbol{r}_R = \boldsymbol{r}_0$. We can now introduce the unitary vector $\boldsymbol{b} = \boldsymbol{B}/|\boldsymbol{B}|$, and split the last term of equation 3.7 in the sum of the components parallel ($\parallel$) and a perpendicular ($\perp$) to $\boldsymbol{b}$,

$$H(V+\delta V,\boldsymbol{B}) = \frac{1}{2}\mu_B g_0 |\boldsymbol{B}+\delta V(G(\boldsymbol{r}_0)\boldsymbol{r}')\cdot\boldsymbol{b}|\boldsymbol{\sigma}_{\parallel} + \frac{1}{2}\mu_B g_0 \delta V|(G(\boldsymbol{r}_0)\boldsymbol{r}')\times\boldsymbol{b}|\boldsymbol{\sigma}_{\perp}. \tag{3.8}$$

As in the g-matrix formalism [58], we can extract the Rabi frequency f_R at resonance from the perpendicular component in equation 3.8,

$$f_R = \frac{V_{\mathrm{ac}}}{2h}\mu_B g_0 |(G(\boldsymbol{r}_0)\boldsymbol{r}')\times\boldsymbol{b}|. \tag{3.9}$$

Note the similarities between equations 3.9 and 2.25. Here, the modulations of the g tensor are substituted by the gradient of magnetic field, which acts as an artificial source of SOC. Equation 3.9 allows to estimate f_R for electrons if we know the QD polarizability $\boldsymbol{r}'$, which we can extract from single-particle calculations,[1] and the MM field and gradients. With this approach, we can evaluate different MM configurations from a single SP calculation, since the only required input is $\boldsymbol{r}'$ (which we can assume independent of $\boldsymbol{B}$ in a first approximation).

Alternatively, we could also introduce the inhomogeneous MM field into the SP simulation, and rely on the direct evaluation to get f_R. For this, as exposed in section 2.5, we would need the vector potential created by the magnet. In the following, we derive the expressions for $\boldsymbol{B}_m$, G, and $\boldsymbol{A}_m$. These were the missing elements to estimate Rabi frequencies for electrons with TB_Sim.

3.1.2 Magnetic field created by a slab of magnetic material

We consider a MM layout that can be viewed as a collection of bar magnets with all magnetizations aligned along a given external magnetic field $\boldsymbol{B} \parallel \boldsymbol{z}$. In Cartesian coordinates, the magnetic field created by a dipole magnet reads

$$\boldsymbol{B}_{\mathrm{dip}}(\boldsymbol{u}) = \frac{\mu_0}{4\pi}\frac{|\boldsymbol{m}|}{|\boldsymbol{r}|^3}\left(3\frac{\boldsymbol{r}(\boldsymbol{m}\cdot\boldsymbol{r})}{|\boldsymbol{r}|^2} - \boldsymbol{m}\right), \tag{3.10}$$

where $\boldsymbol{r} = (x,y,z)$ is the position where the magnetic field is evaluated, the dipole is centered at the origin of coordinates, and $\boldsymbol{m} = (0,0,m)$ is the magnetic moment of the dipole. The individual components of $\boldsymbol{B}_{\mathrm{dip}}$ are

$$\boldsymbol{B}_{\mathrm{dip,x}}(x,y,z) = \frac{\mu_0|\boldsymbol{m}|}{4\pi}\frac{3xz}{\left[x^2+y^2+z^2\right]^{5/2}}, \tag{3.11}$$

[1] We can evaluate $\boldsymbol{r}'$ by finite differences from the results of single-particle calculations as $\boldsymbol{r}'(V_0) = (\boldsymbol{r}(V_0 + V_{\mathrm{ac}}) - \boldsymbol{r}(V_0 - V_{\mathrm{ac}}))/2V_{\mathrm{ac}}$.

$$\boldsymbol{B}_{\mathrm{dip,y}}(x,y,z) = \frac{\mu_0|\boldsymbol{m}|}{4\pi}\frac{3yz}{\left[x^2+y^2+z^2\right]^{5/2}}, \tag{3.12}$$

$$\boldsymbol{B}_{\mathrm{dip,z}}(x,y,z) = \frac{\mu_0|\boldsymbol{m}|}{4\pi}\frac{2x^2-y^2-z^2}{\left[x^2+y^2+z^2\right]^{5/2}}. \tag{3.13}$$

The magnetic field generated by an ensemble of dipoles within a finite volume can be obtained from the integration of the previous expressions.[2] For convenience, we keep the origin of coordinates at the center of the slab, and we define the saturated magnetic polarization $J_\mathrm{s} = \mu_0|\boldsymbol{M}|$, where $\boldsymbol{M}$ is now the density of dipoles in the magnet.

$$\boldsymbol{B}_{m,i}(x,y,z) = \frac{J_\mathrm{s}}{4\pi}\int_{-\frac{L_x}{2}}^{\frac{L_x}{2}}\int_{-\frac{L_y}{2}}^{\frac{L_y}{2}}\int_{-\frac{L_z}{2}}^{\frac{L_z}{2}} \mathrm{d}x'\mathrm{d}y'\mathrm{d}z' \frac{\boldsymbol{B}_{\mathrm{dip,i}}(x-x',y-y',z-z')}{|\boldsymbol{m}|}, \tag{3.14}$$

where L_x, L_y, and L_z are the dimensions of the bar magnet in the $\boldsymbol{x}$, $\boldsymbol{y}$, and $\boldsymbol{z}$ directions, respectively; and (x', y', z') refer now to the position within the magnet. This integral can be seen as the sum of the contributions of all the infinitesimal volumes at position (x', y', z') and dipole density $\boldsymbol{M}$ of the magnet to the total magnetic field at (x, y, z).

We can rewrite equation 3.14 introducing the function F_i such that $\boldsymbol{B}_{\mathrm{dip,i}} = \frac{\partial}{\partial x'}\frac{\partial}{\partial y'}\frac{\partial}{\partial z'}\boldsymbol{F_i}$, for $i \in [x, y, z]$. The result reads

$$\boldsymbol{B}_{m,i}(x,y,z) = \frac{J_\mathrm{s}}{4\pi}\sum_{i,j,k=0}^{1}(-1)^{i+j+k}\boldsymbol{F_i}[x+(-1)^k\frac{L_x}{2}, y+(-1)^k\frac{L_y}{2}, z+(-1)^k\frac{L_z}{2}]. \tag{3.15}$$

The problem then reduces to finding the expressions for $\boldsymbol{F_i}[u, v, w]$, which have analytical solution,

$$\boldsymbol{F_x}[u,v,w] = \ln\left(\left[u^2+v^2+w^2\right]^{1/2}+v\right), \tag{3.16}$$

$$\boldsymbol{F_y}[u,v,w] = \ln\left(\left[u^2+v^2+w^2\right]^{1/2}+u\right), \tag{3.17}$$

$$\boldsymbol{F_z}[u,v,w] = -\tan^{-1}\left[\frac{uv}{w\left[u^2+v^2+w^2\right]^{1/2}}\right]. \tag{3.18}$$

The previous equations allow us to estimate the magnetic field created by the MMs ($\boldsymbol{B}_m$), but we still lack the matrix of derivatives G. Its computation simply requires the derivation of the F_i functions, *e.g.*

$$\frac{\partial \boldsymbol{B}_{m,x}}{\partial y}(x,y,z) = \frac{J_\mathrm{s}}{4\pi}\sum_{i,j,k=0}^{1}(-1)^{i+j+k}\frac{\partial \boldsymbol{F_x}}{\partial v}[x+(-1)^k\frac{L_x}{2}, y+(-1)^k\frac{L_y}{2}, z+(-1)^k\frac{L_z}{2}]. \tag{3.19}$$

Moreover, some constraints apply to the structure of G. Since $\boldsymbol{B}_m$ must fulfill Maxwell's equation

[2] The evaluation of the magnetic field with this approach is only valid outside the volume of the slab.

outside the magnet, its divergence ($\boldsymbol{\nabla}\cdot\boldsymbol{B}_{\mathrm{m}}$) and rotational ($\boldsymbol{\nabla}\times\boldsymbol{B}_{\mathrm{m}}$) must be zero. Therefore, G must be symmetric and traceless. Its full characterization, therefore, reduces to the computation of $\partial\boldsymbol{B}_{m,x}/\partial x$, $\partial\boldsymbol{B}_{m,y}/\partial y$, $\partial\boldsymbol{B}_{m,x}/\partial y$, $\partial\boldsymbol{B}_{m,x}/\partial z$, and $\partial\boldsymbol{B}_{m,y}/\partial z$. Upon derivation, we reach

$$\frac{\partial\boldsymbol{F_x}}{\partial u}[u,v,w] = -\frac{uv}{(u^2+w^2)\left[u^2+v^2+w^2\right]^{1/2}}, \tag{3.20}$$

$$\frac{\partial\boldsymbol{F_y}}{\partial v}[u,v,w] = -\frac{uv}{(v^2+w^2)\left[u^2+v^2+w^2\right]^{1/2}}, \tag{3.21}$$

$$\frac{\partial\boldsymbol{F_x}}{\partial v}[u,v,w] = \frac{1}{\left[u^2+v^2+w^2\right]^{1/2}}, \tag{3.22}$$

$$\frac{\partial\boldsymbol{F_x}}{\partial w}[u,v,w] = -\frac{vw}{(v^2+w^2)\left[u^2+v^2+w^2\right]^{1/2}}, \tag{3.23}$$

$$\frac{\partial\boldsymbol{F_y}}{\partial w}[u,v,w] = -\frac{uw}{(v^2+w^2)\left[u^2+v^2+w^2\right]^{1/2}}, \tag{3.24}$$

and due to the above-mentioned constraints, ´

$$\frac{\partial\boldsymbol{F_z}}{\partial w}[u,v,w] = -\frac{\partial\boldsymbol{F_x}}{\partial u}[u,v,w] - \frac{\partial\boldsymbol{F_y}}{\partial v}[u,v,w], \tag{3.25}$$

and

$$\frac{\partial\boldsymbol{F_y}}{\partial u}[u,v,w] = \frac{\partial\boldsymbol{F_x}}{\partial v}[u,v,w], \tag{3.26}$$

$$\frac{\partial\boldsymbol{F_z}}{\partial u}[u,v,w] = \frac{\partial\boldsymbol{F_x}}{\partial w}[u,v,w], \tag{3.27}$$

$$\frac{\partial\boldsymbol{F_z}}{\partial v}[u,v,w] = \frac{\partial\boldsymbol{F_y}}{\partial w}[u,v,w]. \tag{3.28}$$

With this set of equations, we can fully characterize the MMs magnetic field and its gradients at any $\boldsymbol{r}$, which allows to use equation 3.8 to estimate f_R. Alternatively, we could attempt a direct evaluation by explicitly introducing the inhomogeneous magnetic field in the SP calculation. However, as discussed in section 2.3, Peierls substitution requires the vector potential instead of the magnetic field. In the following, we derive the expressions of the vector potential created by a slab of magnetic material.

3.1.3 Vector potential created by a slab of magnetic material

We can use a similar strategy to extract the vector potential $\boldsymbol{A}$ created by a slab of magnetic material. The vector potential of a single magnetic dipole is

$$\boldsymbol{A}_{\mathrm{dip}}(\boldsymbol{r}) = \frac{\mu_0}{4\pi}\frac{\boldsymbol{m}\times\boldsymbol{r}}{|\boldsymbol{r}|^3}, \tag{3.29}$$

with leads to the following individual components:

$$\boldsymbol{A}_{\mathrm{dip,x}}(x,y,z) = -\frac{\mu_0|\boldsymbol{m}|}{4\pi}\frac{y}{\left[x^2+y^2+z^{2}\right]^{3/2}}, \tag{3.30}$$

$$\boldsymbol{A}_{\mathrm{dip,y}}(x,y,z) = \frac{\mu_0|\boldsymbol{m}|}{4\pi}\frac{x}{\left[x^2+y^2+z^2\right]^{3/2}}, \tag{3.31}$$

$$\boldsymbol{A}_{\mathrm{dip,z}}(x,y,z) = 0. \tag{3.32}$$

As for $\boldsymbol{B}_m$, we can express $\boldsymbol{A}_m$ as the integral of an ensemble of dipoles within the MM volume,

$$\boldsymbol{A}_m(x,y,z) = \frac{J_\mathrm{s}}{4\pi}\int_{-\frac{L_x}{2}}^{\frac{L_x}{2}}\int_{-\frac{L_y}{2}}^{\frac{L_y}{2}}\int_{-\frac{L_z}{2}}^{\frac{L_z}{2}} \mathrm{d}x'\mathrm{d}y'\mathrm{d}z'\frac{\boldsymbol{A}_{\mathrm{dip,i}}(x-x',y-y',z-z')}{|\boldsymbol{m}|}, \tag{3.33}$$

and introduce the analytical primitives Q_i, defined as $\boldsymbol{A}_{\mathrm{dip,i}} = \frac{\partial}{\partial x'}\frac{\partial}{\partial y'}\frac{\partial}{\partial z'}\boldsymbol{Q_i}$,

$$\boldsymbol{A}_i(x,y,z) = \frac{J_\mathrm{s}}{4\pi}\sum_{i,j,k=0}^{1}(-1)^{i+j+k}\boldsymbol{Q_i}[x+(-1)^k\frac{L_x}{2}, y+(-1)^k\frac{L_y}{2}, z+(-1)^k\frac{L_z}{2}]. \tag{3.34}$$

The problem again reduces to the computation of the Q_i functions, which now read

$$\begin{aligned}\boldsymbol{Q_x}[u,v,w] = &-v\tan^{-1}\left[\frac{uw}{v\left[u^2+v^2+u^2\right]}\right]\\ &+w\ln\left(\left[u^2+v^2+w^2\right]^{1/2}+u\right)+u\ln\left(\left[u^2+v^2+w^2\right]^{1/2}+w\right),\end{aligned} \tag{3.35}$$

$$\begin{aligned}\boldsymbol{Q_y}[u,v,w] = &u\tan^{-1}\left[\frac{vw}{u\left[u^2+v^2+w^2\right]}\right]\\ &-w\ln\left(\left[u^2+v^2+w^2\right]^{1/2}+v\right)-v\ln\left(\left[u^2+v^2+w^2\right]^{1/2}+w\right),\end{aligned} \tag{3.36}$$

$$\boldsymbol{Q_z}[u,v,w] = 0. \tag{3.37}$$

With the expressions above, we can sample $\boldsymbol{A}_m$ in the (x,y,z) mesh used for the single-particle calculation, and include the micro-magnet explicitly in TB_Sim. In this way, Rabi frequencies can be computed using the direct evaluation technique: $f_R = \frac{e}{h}V_\mathrm{ac}\left|\langle\uparrow|D|\downarrow\rangle\right|$. While still first order in V_ac, unlike in equation 3.8 the introduction of the explicit MM field ensures an all-order-in-B result.

3.1.4 Textbook example

Let us now illustrate an example of a calculation of the magnetic field created by a MM, and evaluate f_R using the techniques explained above. We define an isotropic 2D QD in a Si well with a circular metallic front gate, see Figure 3.1. The electron is driven with two lateral metallic gates that induce a motion $\boldsymbol{r'} \approx (\delta\langle x\rangle, 0, 0)$, with $\delta\langle x\rangle = 1.2$ Å/mV at $V_\mathrm{fg} = 40$ mV. We place two 300 nm thick semi-infinite MMs, split by 200 nm, 100 nm above the device so as to create a gradient of magnetic field. This configuration delivers a magnetic field gradient of $\partial B_z/\partial x = 2.55$ mT/nm, responsible for the spin oscillations.

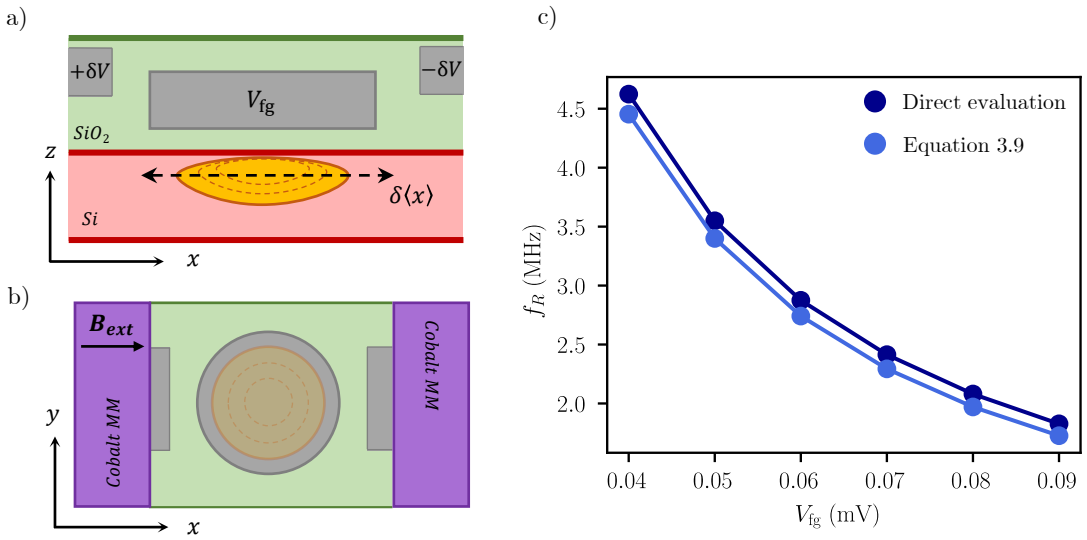

Figure 3.1: Example of Rabi oscillations for an electron spin qubit in presence of micro-magnets. a) Schematic of a longitudinal cross section of the simulated device. The QD (in orange) is formed in a Si well (in red) by a front gate voltage V_{fg} (in grey), and driven by opposite oscillatory potentials $\pm\delta V(t)$ applied on two lateral gates (also in grey), which induce a displacement of the QD along $\boldsymbol{x}$ of magnitude $\delta\langle x\rangle$. b) Schematic top view of the device. Two MMs (in purple) lay above the embedding SiO_2 (in green), and create a finite gradient $\partial B_z/\partial x$. The metallic gates and the QD are also shown although they lay below. c) Rabi frequencies dependence on V_{fg} estimated with a direct evaluation including the MMs vector potential as explained in section 3.1.3, and with the expression in equation 3.9.

Figure 3.1c shows the resultant Rabi frequencies as a function of V_{fg} for the two approximations discussed above. The direct evaluation explicitly including the MM provides slightly larger f_R than the approximation in equation 3.9. The differences come from the breakdown of the linear approximation for B_m, yet the values for both cases remain remarkably close. The decrease of f_R with V_{fg} owes to a reduction of the dot polarizability $\frac{\partial\langle x\rangle}{\partial V_{\text{fg}}}$ due to the stronger confinement.

Equation 3.9 simplifies when the QD motion and B are essentially along $\boldsymbol{x}$. Moreover, the symmetry and semi-infinite character of the MMs yields to $\partial B_z/\partial x$ being the only non-zero off-diagonal element of G. Consequently, $|\boldsymbol{b}\times G\boldsymbol{r'}|$ becomes $|\frac{\partial B_z}{\partial x}\frac{\partial\langle x\rangle}{\partial V_{\text{fg}}}|$, and $f_R = \frac{V_{\text{ac}}}{2h}\mu_B g\left|\frac{\partial B_z}{\partial x}\frac{\partial\langle x\rangle}{\partial V_{\text{fg}}}\right|$. The mechanism is therefore clear: the motion of the QD along $\boldsymbol{x}$ in the MMs gradient $\partial B_z/\partial x$ induces, in the frame of the electron, an effective oscillatory magnetic field along $\boldsymbol{z}$. It is perpendicular to the Larmor vector $g_0\boldsymbol{b}$, and consequently gives rise to Rabi oscillations. Note that decoherence processes, driven by fluctuations of f_L, are enhanced in presence of a component of $G\boldsymbol{r'}$ parallel to $\boldsymbol{b}$. In this particular case where $\boldsymbol{r'}\parallel\boldsymbol{x}$, $T_2^*\propto|\frac{\partial B_x}{\partial x}\frac{\partial\langle x\rangle}{\partial V_{\text{fg}}}|$, so the optimal MM configuration must maximize $\partial B_z/\partial x$ while minimizing $\partial B_x/\partial x$.

While the direct evaluation is more accurate, equation 3.9 allows for an easy interpretation of the mechanisms responsible for f_R, and serve as a useful tool to rationalize the MM designs. Their integration within TB_Sim, enables the numerical simulation of EDSR for electron spin

qubits with this source of artificial SOC.

3.2 Many-particle wavefunctions

The visualization of the probability of finding an electron in space is crucial when simulating QDs, since it allows to identify very easily where the dots are formed, its size, its shape, etc. Therefore, it is an excellent tool to help on the understanding and interpretation of the results, as well as to cross-check the correctness of the simulation. Here we review the expressions for the electron density for the single-particle case, and we derive it, together with the squared wavefunction, for multi-particle states. Their computation and visualization have been implemented as a post-processing step in TB_Sim for CI calculations based on $\mathbf{k}\cdot\mathbf{p}$, and it has been used in the analysis of the results of Chapter 7.

From a quantum mechanical point of view, the probability of finding an electron at a position $\boldsymbol{r}$ is the squared modulus of the wavefunction,

$$P(\boldsymbol{r}) = |\Psi(\boldsymbol{r})|^2 = \Psi^*(\boldsymbol{r}) \cdot \Psi(\boldsymbol{r}) \tag{3.38}$$

As described in section 2.2, the $\mathbf{k}\cdot\mathbf{p}$ wavefunctions of a single-particle QD are, by definition, the sum over the considered bands of the products between an envelope times a Bloch function (see equation 2.12). The envelope functions φ_{ik} are slowly varying functions, whereas the Bloch functions u_k embed the atomistic details, and satisfy periodic boundary conditions in the lattice unit cell. By construction, the u_k are orthogonal and normalized over the unit cell volume (Ω_0), such that

$$\frac{1}{\Omega_0}\int_{\Omega_0} u_k^* u_l \; dV = \delta_{kl}. \tag{3.39}$$

Obtaining the electron probabilities reduces then to the calculation of $P(\boldsymbol{r})$ as defined in equation 3.38, taking into account the relations in equations 2.12, 2.14 and 3.39.

3.2.1 Single-particle density

The single-particle case is the simplest scenario. The single carrier fills a given eigenstate i of the $\mathbf{k}\cdot\mathbf{p}$ calculation. According to equation 3.38, the carrier density $P^{\mathrm{SP}}(\boldsymbol{r})$ is just its modulus squared,

$$P^{\mathrm{SP}}(\boldsymbol{r}) = |\Psi^{\mathrm{SP}}|^2 = \psi_i^*(\boldsymbol{r})\psi_i(\boldsymbol{r}) = \sum_k \sum_{k'} \varphi_{ik}^*(\boldsymbol{r}) u_k^*(\boldsymbol{r}) \varphi_{ik'}(\boldsymbol{r}) u_{k'}(\boldsymbol{r}). \tag{3.40}$$

If we are only interested in features on the length scale of the slowly varying envelopes $\varphi(\boldsymbol{r})$, we can make use of equation 3.39 to average equation 3.40 in a unit-cell volume, which will define an approximate carrier density $\tilde{P}^{\mathrm{SP}}(\boldsymbol{r}) \approx P^{\mathrm{SP}}(\boldsymbol{r})$ that reads

$$\begin{aligned} \tilde{P}^{\mathrm{SP}}(\boldsymbol{r}) &= \frac{1}{\Omega_0}\int_{\Omega_0} \sum_k \sum_{k'} \varphi_{ik}^*(\boldsymbol{r}) u_k^*(\boldsymbol{r}) \varphi_{ik'}(\boldsymbol{r}) u_{k'}(\boldsymbol{r}) dv \\ &= \sum_k \sum_{k'} \varphi_{ik}^*(\boldsymbol{r}) \varphi_{ik'}(\boldsymbol{r}) \delta_{kk'} = \sum_k |\varphi_{ik}(\boldsymbol{r})|^2. \end{aligned} \tag{3.41}$$

We have found that, in the single-particle case, the electron probability $\tilde{P}(\boldsymbol{r})$ is the sum of the squared modulus of the envelope functions of the populated SP state. The result is no

longer the real probability, but a locally-averaged probability $\tilde{P}(\boldsymbol{r})$. It does not account for the atomistic details, but describes the properties at the length scale we are interested in.

3.2.2 The Full Configuration Interaction wavefunction and density

For a two-particle system, the full CI wavefunction is expressed in terms of the single-particle functions as a sum of Slater determinants weighted by a complex coefficient α_{ij} as shown in equation 2.14. The single-particle states used in the full CI are the result of a $\mathbf{k}\cdot\mathbf{p}$ calculation, thus they fulfill equation 2.12. Consequently, we can write

$$\begin{aligned}\Psi^{\mathrm{CI}}(\boldsymbol{r}_1,\boldsymbol{r}_2) = \sum_{i,j>i}\sum_{kl}\frac{\alpha_{ij}}{\sqrt{2}}[&\varphi_{ik}(\boldsymbol{r}_1)u_k(\boldsymbol{r}_1)\varphi_{jl}(\boldsymbol{r}_2)u_l(\boldsymbol{r}_2)\\ &-\varphi_{jl}(\boldsymbol{r}_1)u_l(\boldsymbol{r}_1)\varphi_{ik}(\boldsymbol{r}_2)u_k(\boldsymbol{r}_2)].\end{aligned} \tag{3.42}$$

The wavefunction in this case depends on the position of the two particles, $\boldsymbol{r}_1$ and $\boldsymbol{r}_2$, so does its modulus squared $|\Psi^{\mathrm{CI}}(\boldsymbol{r}_1,\boldsymbol{r}_2)|^2$. For two particles, $|\Psi^{\mathrm{CI}}(\boldsymbol{r}_1,\boldsymbol{r}_2)|^2$ gives the probability of finding an electron at $\boldsymbol{r}_1$ when the second electron is at $\boldsymbol{r}_2$. As for the SP case, we can integrate over the unit cell to get rid of the Bloch functions and obtain a locally-averaged estimate of the squared modulus of the wavefunction,

$$\begin{aligned}|\tilde{\Psi}^{\mathrm{CI}}(\boldsymbol{r}_1,\boldsymbol{r}_2)|^2 = \frac{1}{2}\sum_{i,j>i}\sum_{i',j'>i'}\sum_{kl}\alpha^*_{ij}\alpha_{i'j'}[&\varphi_{ik}(\boldsymbol{r}_1)^*\varphi_{i'k}(\boldsymbol{r}_1)\varphi_{jl}(\boldsymbol{r}_2)^*\varphi_{j'l}(\boldsymbol{r}_2)\\ &-\varphi_{ik}(\boldsymbol{r}_1)^*\varphi_{j'k}(\boldsymbol{r}_1)\varphi_{jl}(\boldsymbol{r}_2)^*\varphi_{i'l}(\boldsymbol{r}_2)\\ &-\varphi_{jl}(\boldsymbol{r}_1)^*\varphi_{i'l}(\boldsymbol{r}_1)\varphi_{ik}(\boldsymbol{r}_2)^*\varphi_{j'k}(\boldsymbol{r}_2)\\ &+\varphi_{jl}(\boldsymbol{r}_1)^*\varphi_{j'l}(\boldsymbol{r}_1)\varphi_{ik}(\boldsymbol{r}_2)^*\varphi_{i'k}(\boldsymbol{r}_2)].\end{aligned} \tag{3.43}$$

In the many-particle case, to obtain the carrier density $\tilde{P}(\boldsymbol{r})$ one must integrate over the coordinates of all particles but one. For a two-particle system,

$$\tilde{P}^{\mathrm{CI}}(\boldsymbol{r}) = 2\int_{R^3} d\boldsymbol{r_2}|\tilde{\Psi}^{\mathrm{CI}}(\boldsymbol{r}_1,\boldsymbol{r}_2)|^2. \tag{3.44}$$

The integration of equation 3.43 makes use of an extra constraint: the normalization condition of the SP states,

$$\int_{R^3} d\boldsymbol{r}\sum_k \varphi^*_{ik}(\boldsymbol{r})\varphi_{jk}(\boldsymbol{r}) = \delta_{ij}, \tag{3.45}$$

which simplifies the final expression of $\tilde{P}^{\mathrm{CI}}(\boldsymbol{r})$,

$$\begin{aligned}\tilde{P}^{\mathrm{CI}}(\boldsymbol{r}) = \sum_{ij}\sum_{i'j'}\sum_k \alpha^*_{ij}\alpha_{i'j'}\ [&\varphi_{ik}(\boldsymbol{r})^*\varphi_{i'k}(\boldsymbol{r})\delta_{jj'}\\ &-\varphi_{ik}(\boldsymbol{r})^*\varphi_{j'k}(\boldsymbol{r})\delta_{ji'}\\ &-\varphi_{jk}(\boldsymbol{r})^*\varphi_{i'k}(\boldsymbol{r})\delta_{ij'}\\ &+\varphi_{jk}(\boldsymbol{r})^*\varphi_{j'k}(\boldsymbol{r})\delta_{ii'}.\end{aligned} \tag{3.46}$$

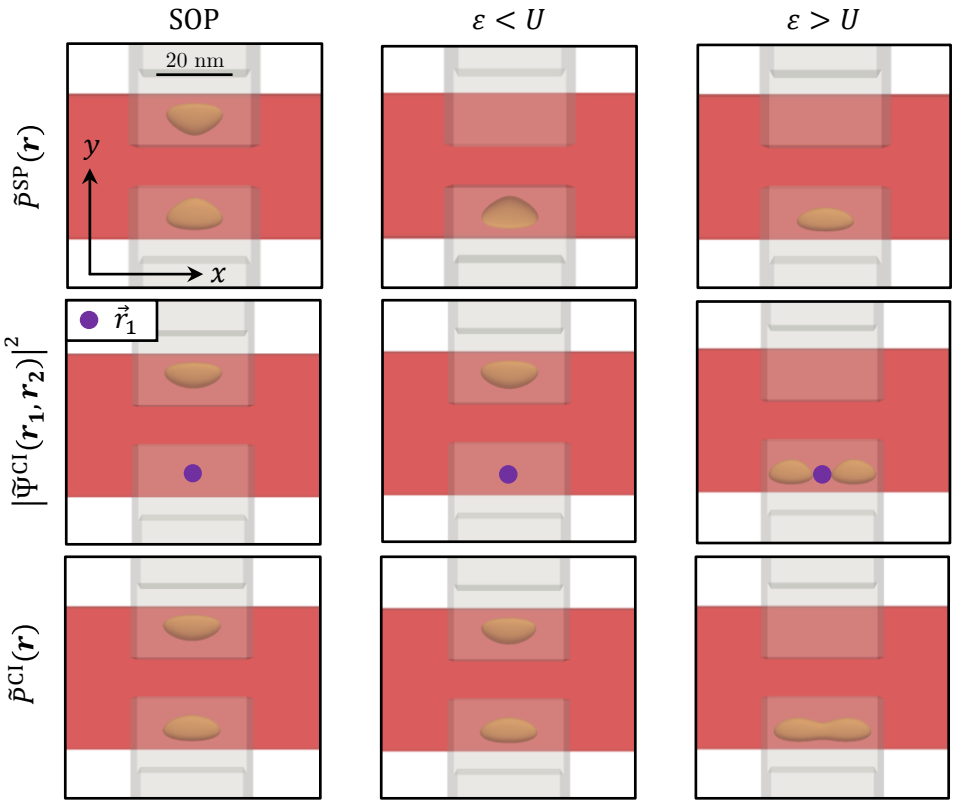

Figure 3.2: Example of the many-particle states in a face-to-face Si MOS device. The Si nanowire is shown in red, and the pair of face-to-face metallic gates in semi-transparent grey. The SP density, the CI squared wavefunction, and the CI density are plotted in orange for the ground state at the SOP, when the detuning ε is smaller than the charging energy U, and when it is larger. The purple dot in the squared wavefunction plots illustrates the position $\boldsymbol{r_1}$ of the first electron.

With the envelope functions φ obtained from a $\mathbf{k}\cdot\mathbf{p}$ calculation and the coefficients α_{ij} computed with CI, we can make use of equation 3.43 and 3.46 to reconstruct and visualize the full-CI wavefunction and density, respectively. The expressions hold for electrons and holes, and regardless of the $\mathbf{k}\cdot\mathbf{p}$ method used. For a single-band EMA calculation for electrons, $k = 1$, and for 4kp (6kp), $k = 4(6)$, respectively.

3.2.3 Textbook example

Let us now illustrate the physics of the CI density and squared wavefunction, and how can they help in the understanding and interpretation of the results for many-particle systems. For this purpose, we simulate a double QD system in a face-to-face Si MOS device, with charging energy U≈15 meV, and we plot $\tilde{P}^{SP}(\boldsymbol{r})$, $|\tilde{\Psi}^{CI}(\boldsymbol{r}_1, \boldsymbol{r}_2)|^2$, and $\tilde{P}^{CI}(\boldsymbol{r})$ at three different biases: at the SOP (detuning $\varepsilon = 0$), when $0 < \varepsilon < U$, and when $\varepsilon > U$, see Figure 3.2.

At the SOP, the two-particle system is in the (1,1) charge configuration, while the SP is right at the (0,1)-(1,0) anticrossing (we label the charge states so that the first index is for the

site under the gate on top, and the second is for the site under the gate at the bottom of the illustrations in Figure 3.2). Consistently, we see that $\tilde{P}^{\mathrm{SP}}(\boldsymbol{r})$ extends under the two gates, and so does $\tilde{P}^{\mathrm{CI}}(\boldsymbol{r})$. Moreover, the squared wavefunction is located under the gate on top when the first particle is located under the bottom gate. These three observations are in agreement with the expected charge configurations.

When $0 < \varepsilon < U$, the SP system is already in the (0,1) charge state, and the SP density indeed shows now a single QD located below the bottom gate. For the two-particle system, however, U is the energy price to bring two electrons together in the same QD. Since $\varepsilon < U$, the system still prefers to stay in the (1,1) charge state, as Coulomb repulsion dominates over ε. We indeed recover, in this situation, the $\tilde{P}^{\mathrm{CI}}(\boldsymbol{r})$ of a (1,1) charge configuration, and if we place the first particle under the bottom gate, the second particle clearly goes to the gate on top in the squared wavefunction.

Finally, if ε rules over U, the two-particle system is expected to be in the (0,2) charge configuration. The SP density shows in this case a reduction of the QD extension along $\boldsymbol{y}$, owing to the stronger confinement induced by the larger ε. Regarding the CI squared wavefunction and density, we do indeed recover now a (0,2) charge state. Interestingly, we can even see how the squared wavefunction adapts so as to avoid the position of the first particle when both are within the same QD, and how the shape of $\tilde{P}^{\mathrm{CI}}(\boldsymbol{r})$ changes with respect to $\tilde{P}^{\mathrm{SP}}(\boldsymbol{r})$. The partial splitting of $\tilde{P}^{\mathrm{CI}}(\boldsymbol{r})$ into two strongly-coupled parts hints to a "molecularization" effect of the QD due to correlation effects, which motivated the work in Chapter 7.

3.3 Chapter 3 in a nutshell

In this chapter we have described the contributions to the TB_Sim computational framework that were developed during this thesis. First, the modelling of electron spin qubits in presence of MMs has been achieved thanks to the derivation of the expressions for the vector potential generated by slabs of magnetic material. These expressions allow to include the inhomogeneous magnetic environment in the SP calculation, and the results capture the induced artificial SOC. Finally, we have implemented the reconstruction of the many-particle wavefunctions from the results of the CI calculations and the SP states. These contributions, together with the algorithm to extract tunnel couplings in defective devices discussed in Appendix B, enabled the realization of the different studies encompassed in this thesis, and are integrated in TB_Sim for future uses.

Chapter 4

Variability of single-qubit properties

Contents

It is patent in different experimental realizations of spin qubits that there is a significant variability [23, 66, 91]. Some of it surely comes from differences in the device layout and operating points, yet even in the still scarce multi-qubit experiments, neighboring qubits show sizable spread in their properties. Holes, due to their intrinsic spin-orbit coupling, may *a priori* be more sensitive to changes in their electrical environment, which may indeed be a source of variability. As an illustration, in the recently reported four-qubits quantum processor in a Ge/SiGe heterostructure [23], the four hole spin qubits show Larmor frequencies of 2.304, 3.529, 3.520, 3.882 GHz; and Rabi frequencies of 24, 15, 18, 16 MHz. For electrons, spins are not intrinsically coupled to electric fields. However, if a source of extrinsic SOC (such as

micro-magnets) is introduced to perform EDSR, the coupling is allowed, opening the door to variability. For devices based on Si/SiGe heterostructures, different driving powers have been required to homogenize the qubits Rabi frequencies [66, 92]. Moreover, in Ref. [92] relaxation and decoherence times range in between 18-29 ms and 1.70-1.89 μs, respectively. In a recent six-qubit array experiment, power corrections to ensure $f_R = 5$ MHz showed a variability of roughly 13% [16]. Regarding Si MOS technology, the data is even more scarce. $f_R \approx 0.5$ and 1.5 MHz have been reported for electrons in a two-qubit experiment [91]. For holes, significant variations of the g-factors are observed in the existing experiments [15, 56, 57, 93, 94]. It is clear, therefore, that there is some variability in the present quantum processors based on spin.

Even though in the current experiments variability in the properties of the different (few) qubits is manageable, it may be a rock-in-the-shoe for scalability. In this Chapter, we focus on variability on Larmor and Rabi frequencies as key properties at the one-qubit level. Indeed, they determine the frequency of the RF signal needed to perform spin rotations, and the speed of these rotations. If a large-scale quantum processor has uncontrollable variability in the Larmor frequencies of the individual qubits, the resonance condition to drive EDSR may not be achieved, since it would be technically unmanageable to have individual RF lines for each qubit. Also the variability in the Rabi frequencies, together with variability on the relaxation and decoherence times, may have an impact on the figures of merit of the eventual quantum processor.

In the following, we focus on Si spin qubits in MOS devices. This is the platform used at CEA and fabricated at LETI. As exposed in section 1.4, Si MOS devices are prone to show large variability due to the defective nature of the Si/SiO_2 interfaces. They have been widely considered as scalable by analogy with the classical Metal-Oxide-Semiconductor Field-Effect Transistor (MOSFET) technology, yet it is still an open question whether this scalability is compromised by variability. To answer this question, we study a prototypical example of a Si MOS device for electrons and hole spin qubits and evaluate the impact of disorder.

4.1 Sources of variability

We have centered this study on the variability induced by the imperfections of the Si/SiO_2 interfaces. These are mainly two: Surface Roughness (SR) and Charge Traps (CT). Even though their effect is moderate and manageable when MOSFETs are operated as transistors at room temperature, they may have a strong impact on the properties of spin qubits when these devices are cooled down to cryogenic temperatures and operate at very small carrier densities (few carriers per qubit).[1] We have neglected other sources of disorder, such as inhomogeneous nuclear environments bringing different hyperfine interactions in the QDs, since they are irrelevant in ^{28}Si. More related to fabrication, micro-magnet misalignment or imperfections may also play a role for electron devices. Such sources of variability are discussed in Appendix C.4.

4.1.1 Surface roughness

In the fabrication of a Si-MOS device, due to the irregularities in the BOX and the etching processes, the obtained nanowire may not a perfect rectangular parallelepiped, but it may have some fluctuations in the position of its interfaces. Such fluctuations may have an impact on Rabi

[1] SR is known to be more important for large carrier densities, as it is the limiting factor for classical transistors. CT may be more relevant for small carrier densities, which is the regime for QDs.

and Larmor frequencies in presence of SOC mechanisms, since they may reshape the confinement potential of the QDs.

The ensemble auto-correlation function ($E[f(x)f(x+\delta x)]$) of the height fluctuations of the interface (δh) can be approximated as a Gaussian function [95],

$$E[\delta h(\boldsymbol{R}_\parallel)\delta h(\boldsymbol{R}_\parallel + \boldsymbol{r}_\parallel)] = \Delta^2 e^{-r_\parallel^2/L_c^2}, \tag{4.1}$$

where $\boldsymbol{R}_\parallel$ and $\boldsymbol{r}_\parallel$ are in-plane positions of the interface. This expression allows to fit experimental observations and characterize the roughness through the correlation length L_c and the rms amplitude Δ, and to reconstruct random surface roughness profiles from these parameters. Δ, as a pre-factor in the Gaussian function, controls the average height of the surface roughness fluctuations, whereas L_c sizes the typical length of the fluctuations.

4.1.1.1 Numerical implementation

To evaluate the impact of surface roughness numerically, we need to introduce it explicitly in the simulations. We therefore generate a surface roughness profile along the lines of Ref. [96], and we include it in the SP calculation. The translation of the auto-correlation function in equation 4.1 into the actual fluctuations in the position of the Si/SiO_2 interface $\delta h(\boldsymbol{R}_\parallel)$ relies on the spatial auto-correlation function, which reads

$$\overline{\delta h(\boldsymbol{R}_\parallel)\delta h(\boldsymbol{R}_\parallel + \boldsymbol{r}_\parallel)} = \frac{1}{S}\int_S \delta h(\boldsymbol{R}_\parallel)\delta h(\boldsymbol{R}_\parallel + \boldsymbol{r}_\parallel) d\boldsymbol{R}_\parallel, \tag{4.2}$$

with S the total surface. In the regime where the correlation length of the fluctuations L_c is smaller than $\sqrt{S}$, the ensemble and spatial auto-correlation functions coincide, and

$$\overline{\delta h(\boldsymbol{R}_\parallel)\delta h(\boldsymbol{R}_\parallel + \boldsymbol{r}_\parallel)} = \Delta^2 e^{-r_\parallel^2/L_c^2}. \tag{4.3}$$

We can now take the Fourier transform $\mathcal{F}[\overline{\delta h(\boldsymbol{R}_\parallel)\delta h(\boldsymbol{R}_\parallel + \boldsymbol{r}_\parallel)}] = \mathcal{F}[\Delta^2 e^{-r_\parallel^2/L_c^2}]$, and expanding $\delta h(\boldsymbol{R}_\parallel) = \sum_q \delta h(\boldsymbol{q}) e^{i\boldsymbol{q}\boldsymbol{R}_\parallel}$, we end up with

$$|\delta h(\boldsymbol{q})|^2 = \pi L_c \Delta^2 e^{-\frac{L_c^2 \boldsymbol{q}^2}{4}}. \tag{4.4}$$

Consequently, $\delta h(\boldsymbol{q})$ is defined up to an arbitrary random phase $\phi(\boldsymbol{q})$ as

$$\delta h(\boldsymbol{q}) = \Delta\sqrt{\pi L_c} e^{-i\phi(\boldsymbol{q})\frac{L_c^2\boldsymbol{q}^2}{8}}. \tag{4.5}$$

Moreover, $\delta h(\boldsymbol{q}) = \delta h(-\boldsymbol{q})$ since $\delta h(\boldsymbol{r})$ is real, so that $\phi(\boldsymbol{q}) = \phi(-\boldsymbol{q})$. We can finally do a backward Fourier transform of $\delta h(\boldsymbol{q})$ to obtain $\delta h(\boldsymbol{R}_\parallel)$ as

$$\delta h(\boldsymbol{R}_\parallel) = \Delta\sqrt{\pi L_c}\sum_q e^{-i\phi(\boldsymbol{q})\frac{L_c^2\boldsymbol{q}^2}{8}} e^{i\boldsymbol{q}\boldsymbol{R}_\parallel}. \tag{4.6}$$

Numerically, we can make use of equation 4.6, with a sampling of the $\boldsymbol{q}$ space, to map the surface roughness δh to the spatial mesh where the device is built, and consequently generate random samples of surface roughness with correlation length L_c and rms amplitude Δ just by choosing a set of random $\phi(\boldsymbol{q})$.

4.1.1.2 Experimental state-of-the-art

The experimental characterization of the surface roughness in Si/SiO_2 interfaces has historically been addressed in the field of classical transistors. The analogies between devices and fabrication processes make them valuable estimates for MOS devices in quantum computing. Typically, $L_c = 1 - 2$ nm and $\Delta = 0.2 - 0.4$ nm [97–100]. We must take into account, however, that such parameters are typically extracted from high carrier density mobility measurements, which are sensitive to small L_c's. QDs operate at much lower densities hence probe larger correlation lengths [97], so we must make sure to scan larger L_c's to track its impact as well. Here, we choose a range $L_c = 2 - 30$ nm, and $\Delta = 0.2 - 0.4$ nm to cover all the plausible experimental situations.

4.1.2 Charge traps

Charge traps (also known as P_b defects) appear in the Si/SiO_2 interface as a consequence of the amorphous character of SiO_2. The defects in the interface between an amorphous and a crystalline material are formed due to the impossibility to complete all the bonds of the atoms at the interface. The rigidity of the crystalline structure and the disordered nature of the amorphous SiO_2 are the main causes. These dangling bonds, highly unstable radicals, will trap the first carriers entering the channel and become charged species. They are amphoteric: they can either release the electron radical (accept a hole) and form a positively charged defect or accept an electron and form a negatively charged defect. Their behavior will simply depend on the type of device: n-type devices form negatively charged P_b defects, whereas those on p-type devices are positively charged. Therefore, the interaction between charge traps and the QD is always repulsive. As for surface roughness, distortions on the QD shape due to the repulsive interaction with the CT may translate into variability in presence of SOC mechanisms.

4.1.2.1 Numerical implementation

Charge traps are included in the numerical simulations by randomly placing the number of point charges corresponding to the desired charge density at the Si/SiO_2 interface. Charges are set negative (positive) for electron (hole) devices. They are treated as point charges, not accounting for their finite volume, yet this is rather irrelevant given their repulsive interaction with the QD. Poisson's equation then accounts for these charge defects, and so does the resulting potential landscape input to the SP calculation.

4.1.2.2 Experimental state-of-the-art

As for the SR, the characterization of charge traps density in Silicon channels has been widely studied in MOSFET devices. Experimental charge trap density (n_i) estimations range from 10^{10} to 10^{11} cm^{-2} [101–103]. We explore the same range in the numerical simulations.

4.2 Simulation details

For the quantification of variability we have chosen to simulate a simple MOS device, similar to those previously studied in the group [42, 58]. The simulated device, see Figure 4.1a, is made

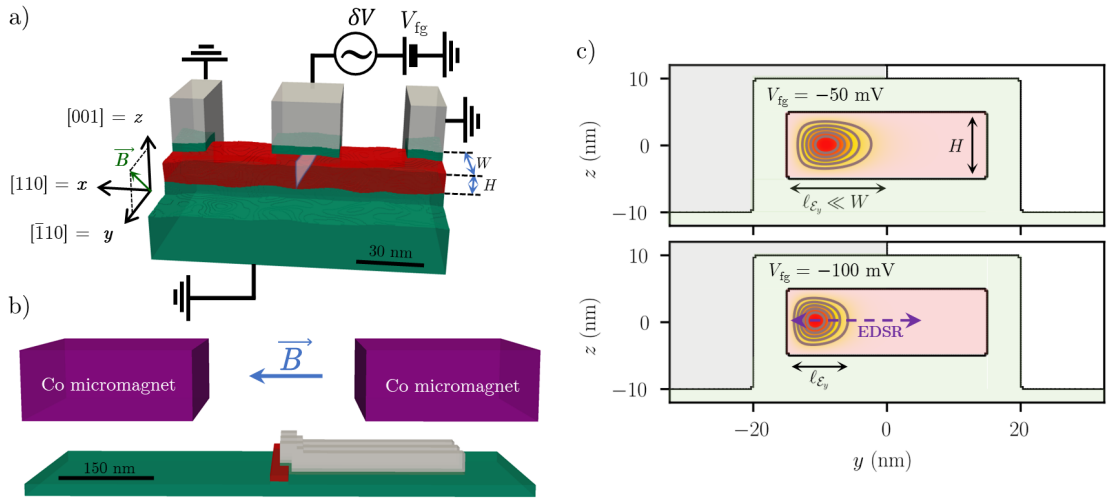

Figure 4.1: a) Example of a simulated device with surface roughness. The Si nanowire (in red), embedded by a 5 nm thick SiO_2 (in green), is supported by a 25 nm thick BOX (in green). On top, the front gate (in grey) is connected to a DC (V_{fg}) and AC (δV) voltage sources; and the lateral gates (also in grey) are grounded. Below the BOX, a ground plane is also added to simulate the Silicon substrate. The SiO_2 embedding the nanowire and the encapsulating Si_3N_4 have been removed for clarity. b) Schematic of the Co micro-magnets included in the simulations of electron devices. The extension of the micro-magnets has been cut for clarity. c) Ground state hole wavefunction for the pristine device at $V_{\text{fg}} = -50$ and -100 mV. The front gate mostly modulates the confinement of the QD along $\boldsymbol{y}$, and so does the AC signal.

of a 30 nm long single front gate covering half of a $H = 10$ nm thick, $W = 30$ nm wide Si nanowire, oriented along [110]. It lays on top of a 25 nm thick BOX. Two identical lateral gates are included 30 nm apart from the central front gate to mimic the neighboring sites in a 1D array, yet they are grounded throughout this study. The whole device is embedded in Si_3N_4.

For electrons, we introduce two Cobalt micro-magnets (with saturated magnetic polarizability $J_s = 1.84$ T) on top of the device to enable EDSR, see Figure 4.1b. The MMs are placed 100 nm above the Si nanowire, with a 200 nm gap between them. They are 0.3 μm thick, and semi-infinite in plane. The effect of the MM is accounted for in the simulations as exposed in section 3.1. We include two face-to-face micro-magnets to double the $\frac{\partial B_z}{\partial y}$ gradient, responsible for the Rabi oscillations. Most of the experimental micro-magnet designs include a third MM that brings a finite $\frac{\partial B_y}{\partial z}$, used to have distinct Larmor frequencies between neighboring qubits in a 1D array [104, 105]. We do not include it in our simulations since our unit cell comprises a single qubit. The magnetic field and gradients created by the simulated micro-magnets at the QD position for $V_{\text{fg}} = 50$ mV are

$$\langle \boldsymbol{B}_m \rangle = (0.00, 0.28, -0.01)\ \text{T}\,, \tag{4.7a}$$

$$G = \begin{pmatrix} 0.00 & 0.00 & 0.00 \\ 0.00 & 0.12 & 2.56 \\ 0.00 & 2.56 & -0.12 \end{pmatrix}\ \text{mT/nm}. \tag{4.7b}$$

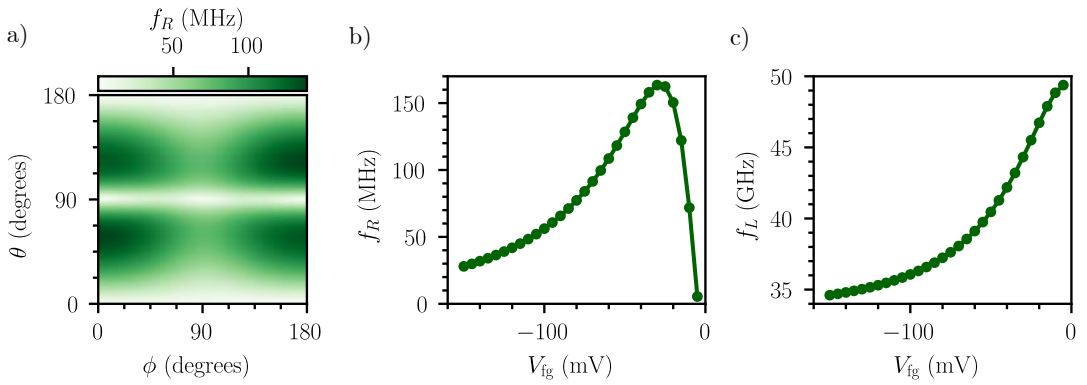

Figure 4.2: Physics of the simulated hole spin qubit in absence of disorder. a) Anisotropy of the Rabi Frequency with the orientation of the magnetic field $\boldsymbol{B} = B(\sin(\theta)\sin(\phi), \sin(\theta)\cos(\phi), \cos(\theta))$ for $B = 1$ T, $V_{\rm fg} = -50$ mV, and $V_{\rm ac} = 1$ mV. b) Rabi frequency dependence on $V_{\rm fg}$ for B T along $\boldsymbol{x} + \boldsymbol{y}$, and $V_{\rm ac} = 1$ mV. c) Larmor frequency dependence on $V_{\rm fg}$ for $B = 1$ T along $\boldsymbol{x} + \boldsymbol{y}$.

For both electrons and holes we drive the spin with an AC field (δV) applied to the front gate. For holes, this yields to a (mostly) g-TMR mechanism, whereas for electrons this translates into a motion of the quantum dot in the magnetic field gradient mainly along $\boldsymbol{y}$. We provide data on a (mostly) IZ-EDSR mode for holes in Appendix C.1.

The anisotropy of the Rabi frequency for hole qubits hosted in such devices has already been reported [58]. For the device under study, the data are shown in Figure 4.2a for $V_{\rm fg} = -50$ mV. The Rabi frequency shows a significant anisotropy with the B field orientation; f_R is maximal near $\boldsymbol{B} = \boldsymbol{x} + \boldsymbol{y}$, and $f_R = 0$ when $\boldsymbol{B}$ is along $\boldsymbol{z}$ or in the $(\boldsymbol{xy})$ plane. There is an anisotropy in the effective g factor as well: the three main g factors for the simulated device read $g_x = 1.24$, $g_y = 1.58$, and $g_z = 3.80$. We choose a magnetic field orientation $\boldsymbol{B} = \boldsymbol{x} + \boldsymbol{y}$ for the variability study of holes, and the dependence of Rabi and Larmor frequencies on $V_{\rm fg}$ for this orientation are reported in Figures 4.2b and 4.2c, respectively. While f_L decreases for increasing electrical confinement, f_R peaks at $V_{\rm fg} \approx -30$ mV. For the following study, we target $V_{\rm fg} = -50$, -75, and -100 mV, and the values for Larmor and Rabi frequencies at these biases, as well as the QD size along $\boldsymbol{y}$ ($\ell_y = \sqrt{\langle y^2 \rangle - \langle y \rangle^2}$) are provided in Table 4.1. More insights in the above-discussed trends can be found in Ref. [58].

For electrons the physics is simpler. The absence of intrinsic SOC leaves a perfectly isotropic g factor $g^* = g_0 = 2$. Moreover, the magnetic field orientation is fixed by the micro-magnets: it must be parallel to their polarization direction, in this case $\boldsymbol{y}$ (see Figure 4.1b), and large enough to fully polarize the magnets. Regarding the dependence on $V_{\rm fg}$, f_L shows a very weak residual variation due to the slight modulation of the position of the QD within the gradient of B field, whereas there is a significant decrease of f_R with increasing $V_{\rm fg}$, see Table 4.1. Details on the origin of this decrease are discussed in section 4.3.2. For electrons, we monitor $V_{\rm fg} = 25$, 50, and 75 mV. All the Rabi and Larmor frequencies provided in this Chapter are normalized for $B = 1$ T and $V_{\rm ac} = 1$ mV.

We collect the data at fixed gate voltage. We may, alternatively, collect data at fixed chemical potential μ in the dot (fixed ground state energy). This is closer to the experimental situation

Holes				Electrons			
$V_{\rm fg}$ (mV)	f_L^0 (GHz)	f_R^0 (MHz)	ℓ_y^0 (nm)	$V_{\rm fg}$ (mV)	f_L^0 (GHz)	f_R^0 (MHz)	ℓ_y^0 (nm)
-50	40.46	128.47	3.28	25	35.837	3.20	5.20
-75	37.62	84.00	2.71	50	35.845	2.22	4.69
-100	36.06	56.19	2.38	75	35.853	1.48	4.21

Table 4.1: Larmor frequency f_L^0 and Rabi frequency f_R^0 of the pristine hole and electron devices, computed at $B = 1$ T along $\boldsymbol{y} + \boldsymbol{z}$ for holes and along $\boldsymbol{y}$ for electrons, and $V_{\rm ac} = 1$ mV. The size of the QD along $\boldsymbol{y}$, $\ell_y^0 = \sqrt{\langle y^2\rangle - \langle y\rangle^2}$, is also given.

where the dots remain connected to reservoirs of particles while being operated. The computational procedure is, however, more complex and time-consuming, as the bias must be corrected for each disordered device in order to achieve the target chemical potential (similarly to the methodology discussed in Appendix B.1). Our attempts for interface roughness and charge traps showed similar variabilities using both strategies, so we worked at fixed gate voltages for the extensive numerical study.

The variability is estimated as follows. We perform independent simulations on sets of $N \geq 500$ random samples of disorder. Then the average ($\overline{f}$) Larmor or Rabi frequency, and its Standard Deviation (SD) $\sigma(f)$ are obtained as:

$$\overline{f} = \frac{1}{N}\sum_{i=1}^{N} f_i \tag{4.8a}$$

$$\sigma(f) = \left[\frac{1}{N-1}\sum_{i=1}^{N}\left(f_i - \overline{f}\right)^2\right]^{1/2}, \tag{4.8b}$$

where the f_i are the sampled frequencies. We characterize the variability by the Relative Standard Deviation (RSD):

$$\tilde{\sigma}(f) = \sigma(f)/\overline{f}. \tag{4.9}$$

For those distributions that are not normal, $\overline{f}$ and $\sigma(f)$ are not sufficient information to fully describe their shape. When this is the case, we provide the 25th and 75th percentiles (first and third quartiles), which can highlight the eventual tailed character of the distributions. These are the value of f such that 25% ($f(25\%)$) and 75% ($f(75\%)$) of the simulations fulfill $f < f(25\%)$ and $f < f(75\%)$, respectively. To evaluate the convergence of the statistics, we compute the 95% confidence intervals for $\overline{f}$ and $\tilde{\sigma}(f)$. All the statistics are estimated using a bootstrap (resampling) method [106] to ensure their robustness.

4.3 Variability due to Surface Roughness

4.3.1 Numerical simulations

4.3.1.1 Holes

In Figure 4.3a we report the dependence of the variability of f_R and f_L for holes as a function of the surface roughness parameters Δ and L_c. We observe a non-monotonous dependence on

L_c, that peaks at $L_c \approx 10$ nm. Qualitatively, we indeed expect the SR fluctuations at a length scale much smaller than the QD ($L_c \to 0$) to average out, whereas the surface looks flat in the scale of the QD when $L_c \to \infty$. Along the same lines, the variability could be expected maximal when the L_c is on the order of the size of the QD.

Regarding the rms amplitude, variability increases linearly with Δ in the 0.2-0.4 nm range. In the worst-case scenario, variability reaches 25% for f_R and 10% for f_L (at $L_c = 10$ nm and $\Delta = 0.4$ nm). Note that variability would further increase for larger Δ's.

From the different columns in Figure 4.3a we can see that variability has a very weak dependence on V_{fg}. When V_{fg} is made further negative, the QD is squeezed into the lateral facet, see Figure 4.1. Its in-plane size, therefore, decreases; so does its exposure to the disorder on the top and bottom interfaces. Consequently, the SD $\sigma(f_R)$ and $\sigma(f_L)$ are expected to decrease. As shown in Figure 4.2, however, f_R (and to a much lesser extent f_L) also decreases with V_{fg}, substantially smoothing the decrease of the RSD $\tilde{\sigma}(f_R)$. Moreover, when the QD gets squeezed against the lateral facet, it probes more its roughness, which weakens even further the decay of $\tilde{\sigma}$. Only 18% of the total variability in f_L comes from the lateral facets at $V_{\text{fg}} = -50$ mV, whereas it reaches 32% at $V_{\text{fg}} = -100$ mV. For f_R, it goes from 10% to 16%. The increasing role of the roughness at the lateral facets, together with the decrease of both $\overline{f_R}$ and $\overline{f_L}$ explain the weak dependence of variability on V_{fg}. Consequently, working with a strongly confined QD would not mitigate the impact of surface roughness in these devices.

Figure 4.3b shows the distribution of f_R and f_L for certain L_c and Δ values. Both f_R and f_L follow a normal distribution, with $\overline{f_R} = f_R^0$ and $\overline{f_L} = f_L^0$. Despite that both decrease with increasing confinement (see Figure 4.2), there is no correlation between the deviations of f_R and f_L of the individual simulations. The details behind this absence of correlation are discussed in section 4.3.2. To put in context the magnitude of the deviations, we include the V_{fg} dependence of f_R and f_L for the pristine device, for intervals of 10 mV, in Figure 4.3b. Most of the simulations lie outside a ± 10 mV window.

4.3.1.2 Electrons

The data for electrons are shown in Figure 4.4. For $\Delta = 0.4$ nm, variability in f_L reaches 0.05%, whereas variability in f_R peaks at roughly 6% close to $L_c = 10$ nm. The results for the Rabi frequency dependence on L_c and Δ follow the same trends discussed for holes. For the Larmor frequency, we recover a very small variability that saturates when $L_c \to \infty$. Indeed, with an isotropic $g_0 = 2$, we expect a very weak variability on f_L for electrons. Regarding the dependence of variability on V_{fg}, we do again observe a weak dependence for $\tilde{\sigma}(f_R)$ and no dependence for $\tilde{\sigma}(f_L)$.

In Figure 4.4b we show the scattering of the individual simulations. The scattering of the f_L in presence of surface roughness is very weak, in line with the small variability reported above. The Larmor and Rabi scatterings are again not correlated. As for holes, we provide in orange the dependence of the ideal device properties on V_{fg}. Note that while f_R suffers a sizable modulation, the changes in f_L with V_{fg} for the ideal device are extremely small. Indeed, the reduced $\tilde{\sigma}(f_L)$ comes with an associated negligible electric tunability of f_L.

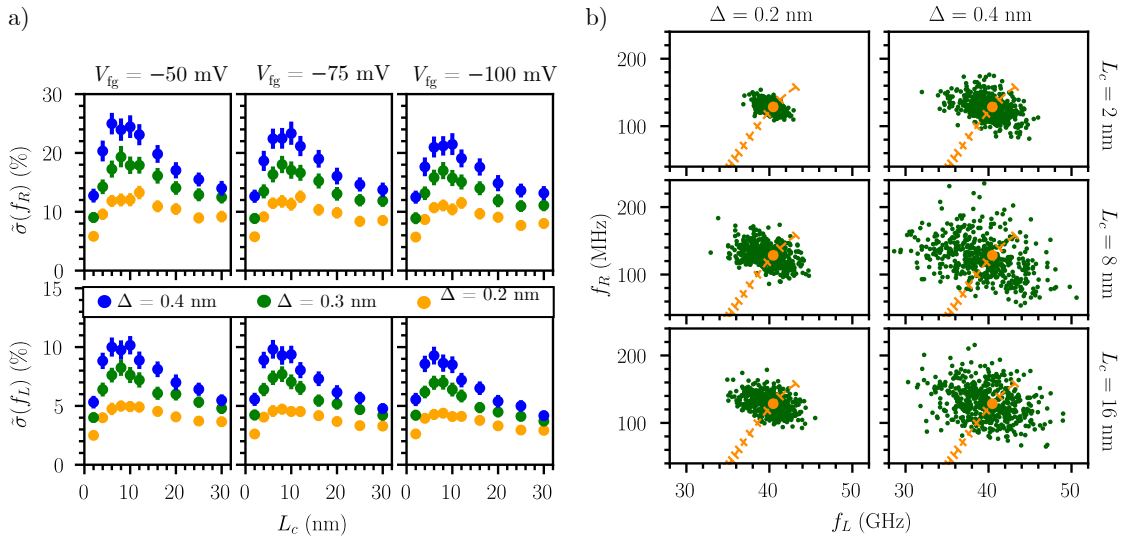

Figure 4.3: a) RSD $\tilde{\sigma}(f_R)$ of the Rabi frequency and RSD $\tilde{\sigma}(f_L)$ of the Larmor frequency of rough hole qubits as a function of L_c for different Δ and gate voltages V_{fg}. The error bars outline the 95% confidence interval. b) Distribution of the rough hole devices in the (f_L, f_R) plane for different Δ and L_c at $V_{\text{fg}} = -50$ mV. Each green point is a particular realization of the interface roughness disorder. The orange dashed line is the pristine device frequencies as a function of V_{fg} (crosses by steps of 10 mV, increasingly negative from top right to down left, with the orange point at $V_{\text{fg}} = -50$ mV).

4.3.2 Analytical insights in the numerical results

Now that we have quantified the variability arising due to the presence of surface roughness in the Si/SiO_2 interfaces, we disentangle the origin and mechanisms behind it. In the simulated device, electrons and holes are confined in the cross section of the channel by the vertical component $\mathcal{E}_z$ and the lateral component $\mathcal{E}_y$ of the electric field from the front gate. The strength of this electric field can, therefore, be characterized by the electric confinement lengths $\ell_{\mathcal{E}_z} = [\hbar^2/(2m^*_\perp e\mathcal{E}_z)]^{1/3}$ and $\ell_{\mathcal{E}_y} = [\hbar^2/(2m^*_\parallel e\mathcal{E}_y)]^{1/3}$, where $m^*_\perp$ is the vertical confinement mass along [001], and $m^*_\parallel$ the in-plane mass [60]. In the regimes explored in this work, $\ell_{\mathcal{E}_z} \gtrsim H$ while $\ell_{\mathcal{E}_y} \lesssim W$: the vertical confinement is dominated by the structure, while the in-plane confinement is dominated by the electric field (see Figure 4.1c).

When $H \ll \ell_{\mathcal{E}_z}$, the interface roughness on the main top and bottom facets, resulting on a modulation of H dependent on the position in the (x, y) plane, essentially modulates the structural confinement energy $E_\perp = \hbar^2\pi^2/(2m^*_\perp H^2)$. In a single band model, long wavelength thickness fluctuations of $\delta H(x, y)$ translate into a potential

$$W(x, y) \approx \delta H(x, y)\frac{\partial E_\perp}{\partial H} \approx -\delta H(x, y)\frac{\hbar^2\pi^2}{m^*_\perp H^3} \tag{4.10}$$

for the motion in the weakly confined ($\boldsymbol{xy}$) plane [107–109]. The appearance of $\delta H(x, y)$ is what gives rise to variability.

When the driving RF signal is applied to the front gate, it mainly shapes the dot size ℓ_y and

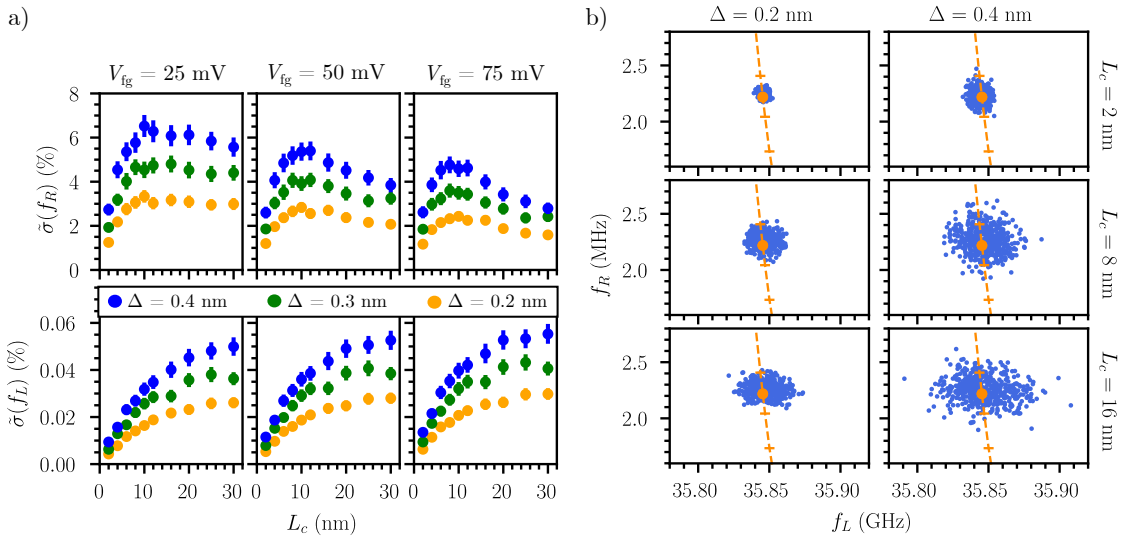

Figure 4.4: a) RSD $\tilde{\sigma}(f_R)$ of the Rabi frequency and RSD $\tilde{\sigma}(f_L)$ of the Larmor frequency of rough electron qubits as a function of L_c for different Δ and gate voltages V_{fg}. They are normalized with respect to the average Rabi frequency $\overline{f_R} \simeq f_R^0$ and average Larmor frequency $\overline{f_L} \simeq f_L^0$, given in Table 4.1. The error bars outline the 95% confidence interval. b) Distribution of the rough electron devices in the (f_L, f_R) plane for different Δ and L_c at $V_{\text{fg}} = 50$ mV. Each blue point is a particular realization of the interface roughness disorder. The orange dashed line is the pristine device frequencies as a function of V_{fg} (crosses by steps of 10 mV, increasing from top right to down left, with the orange point at $V_{\text{fg}} = 50$ mV).

position $\langle y \rangle$, as the electric dipole is small along the strong confinement axis $\boldsymbol{z}$. For electrons, as discussed in section 3.1, $f_R \propto \langle y \rangle'$. Modulations of the dot polarizability therefore translate into a variability in f_R. In the simplest models for the dot (hard-wall or harmonic confinement potential with homogeneous AC electric field along $\boldsymbol{y}$ [59, 60]), a dimensional analysis of the perturbation series for $\langle y \rangle'$ suggests that $\partial \langle y \rangle / \partial V_{\text{fg}} \propto \ell_y^4$: the stronger the confinement, the weaker the electrical response. Although the potentials of the individual realizations of disorder are rather complex, we can still expect correlations between the lateral size of the dot and the Rabi frequency. These data are reported in Figure 4.5, where we not only recover the correlations between f_R and ℓ_y, but also a good agreement with the predicted slope of 4 (dashed orange line).

If we consider the disorder potential W in equation 4.10 as a first-order perturbation to a pristine situation, assume a harmonic confinement in the $(\boldsymbol{yz})$ plane, and homogeneous electric field along $\boldsymbol{y}$, we can analytically compute $\tilde{\sigma}(f_R) = \tilde{\sigma}(\langle y \rangle')$. The details of the calculation can be found in Ref. [110]. The final expression for $\tilde{\sigma}(f_R)$ reads

$$\tilde{\sigma}(f_R) = \sqrt{6}\pi^2 \frac{m_{\parallel}^*}{m_{\perp}^*} \frac{\Delta L_c \ell_y^0}{H^3} \left(\frac{\ell_y^0}{\ell_x^0}\right)^{1/2} \left(\frac{4(\ell_x^0)^2}{4(\ell_x^0)^2 + L_c^2}\right)^{1/4} \left(\frac{4(\ell_y^0)^2}{4(\ell_y^0)^2 + L_c^2}\right)^{5/4}, \tag{4.11}$$

where ℓ_x^0 and ℓ_y^0 are the characteristic sizes of the pristine dot ($\ell_i = \sqrt{\langle i^2 \rangle - \langle i \rangle^2}$, with i in $[x, y, z]$).

The above expression allows us to analyze the dependence of variability on the surface roughness parameters. $\tilde{\sigma}(f_R)$ is expected to be linear with Δ, while the dependence on L_c is more complex. Variability is maximal when L_c is

$$L_c = \frac{1}{\sqrt{2}}\Big(\sqrt{(\ell_y^0)^4 + 26(\ell_x^0\ell_y^0)^2 + 9(\ell_x^0)^4} + (\ell_y^0)^2 - 3(\ell_x^0)^2\Big)^{1/2}, \tag{4.12a}$$

$$\simeq 2\sqrt{\frac{2}{3}}\ell_y^0 \text{ when } \ell_x^0 \gg \ell_y^0\,. \tag{4.12b}$$

Indeed, the model agrees with the qualitative analysis of the trends discussed in section 4.3.1: $\tilde{\sigma}(f_R)$ vanishes when the length-scale of the disorder is much larger or smaller than that of the QD, and peaks when they are comparable. Equation 4.11 also recovers the linear dependence on Δ reported in Figures 4.3 and 4.4.

Regarding the Larmor frequency of electrons, the absence of intrinsic SOC leaves an isotropic $g_0 = 2$. The residual fluctuations of the Larmor frequency actually result from fluctuations of the position of the QD in the inhomogeneous B field created by the MMs. In the present configuration, B is parallel to $\boldsymbol{y}$, so at first order only $\frac{\partial B_y}{\partial z}$ will give rise to fluctuations in f_L, as $\delta f_L \propto \frac{\partial B_y}{\partial z}\delta\langle z\rangle$. Therefore, variability arises due to modulations of the position of the QD along $\boldsymbol{z}$. Surface roughness tunes the position of the top and bottom interfaces on a length-scale L_c, and so tunes $\langle z\rangle$. In the limit $L_c \to 0$, $\sigma(\langle z\rangle) = 0$, yet note that when $L_c \to \infty$, the surface becomes flat but there is still a variation of H, since the fluctuations of the top and bottom interfaces are uncorrelated. In this limit, we can approximate $\langle z\rangle$ to

$$\langle z\rangle \approx \frac{1}{2}\left(z_b + z_t\right), \tag{4.13}$$

where z_b and z_t are the positions of the bottom and top interfaces. The variability on $\langle z\rangle$ directly depends on the amplitude of the SR fluctuations Δ, $\sigma((z_b + z_t)/2) = \Delta/\sqrt{2}$. Therefore, the variability in f_L obeys

$$\tilde{\sigma}(f_L) \to \frac{1}{B_y}\frac{\partial B_y}{\partial z}\frac{\Delta}{\sqrt{2}} \tag{4.14}$$

when $L_c \to \infty$, and $\tilde{\sigma}(f_L) = 0$ when $L_c \to 0$. We do indeed recover these trends in the data of Figure 4.4. Note that, as explained in section 3.1, $\frac{\partial B_y}{\partial z} = \frac{\partial B_z}{\partial y}$, which is the gradient bringing finite f_R's. Therefore, micro-magnet designs optimized to maximize Rabi frequencies also maximize $\tilde{\sigma}(f_L)$ in this device.

The situation is more complex for holes. The model of Ref. [60] suggests that the Rabi frequency is inversely proportional to the gap $\Delta_{\text{LH}} \propto 1/H^2$ between the heavy- and light-hole sub-bands, and proportional to ℓ_y^α, where α can range from 1 ($W \ll \ell_{\mathcal{E}_y}$) to 4 ($W \gg \ell_{\mathcal{E}_y}$). The difference in the exponent with respect to electrons essentially results from the fact that $f_R \propto \partial\langle k_y^2\rangle/\partial V_{\text{fg}}$ instead of $\propto \partial\langle y\rangle/\partial V_{\text{fg}}$, where $k_y = -i\partial/\partial y$ and the expectation value is computed for the ground state heavy-hole envelope function. We may, therefore, expect correlations between f_R and ℓ_y and/or ℓ_z. Figure 4.5 actually shows stronger correlations with ℓ_y ($\delta f_R/f_R^0 \approx 3\delta\ell_y/\ell_y^0$) than with ℓ_z in the numerical data. Therefore, the variability of the Rabi frequency for holes is dominated by fluctuations of the in-plane size of the dot (as for electrons), and not by modulations of the Heavy Hole (HH)-Light Hole (LH) splitting.

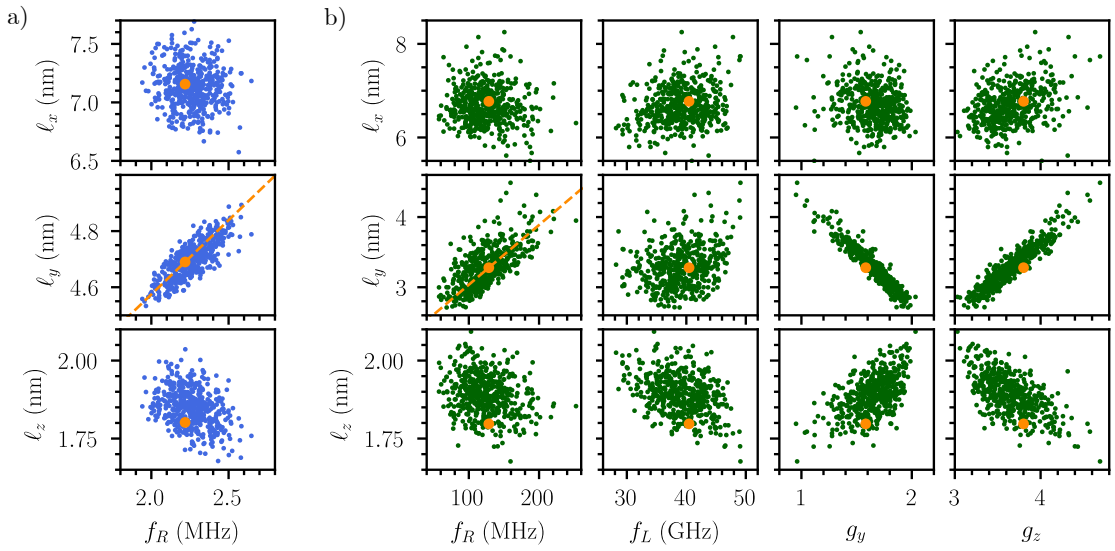

Figure 4.5: a) Correlations between the Rabi frequency f_R of the electron qubits and the extension ℓ_x, ℓ_y and ℓ_z of the dots along the $\boldsymbol{x}$, $\boldsymbol{y}$, and $\boldsymbol{z}$ axes respectively. Each point is a particular realization of interface roughness disorder with $\Delta = 0.4$ nm and $L_c = 10$ nm ($V_{\rm fg} = 50$ mV). The orange dot is the pristine device. The dashed orange line $\delta f_R/f_R^0 = 4\delta\ell_y/\ell_y^0$ is a guide to the eye. b) Same for hole qubits: correlations between the Rabi frequency f_R, the Larmor frequency f_L, the gyromagnetic factors g_y and g_z, and the extension of the dots ℓ_x, ℓ_y and ℓ_z ($V_{\rm fg} = -50$ mV). The dashed orange line $\delta f_R/f_R^0 = 3\delta\ell_y/\ell_y^0$ is a guide to the eye.

Regarding the Larmor frequency for holes, it can be reconstructed from the proper combination of the three principal gyromagnetic factors g_i, and each one is expected to have a different dependence on the strength of the disorder. The heavy-hole ground state gets mixed with a light-hole component by the electric field $\mathcal{E}_y$ due to the competition between vertical (structural) confinement along $\boldsymbol{z}$ and lateral (electric) confinement along $\boldsymbol{y}$ [58]. As a consequence, the gyromagnetic factor g_z should decrease while g_y should increase with decreasing ℓ_y and increasing ℓ_z [60]. We recover such trends in the correlations of Figure 4.5b. In fact, both g_y and g_z show stronger correlations with ℓ_y than with ℓ_z because the system is more polarizable along $\boldsymbol{y}$ than along $\boldsymbol{z}$. With the magnetic field $\boldsymbol{B} = \boldsymbol{x}+\boldsymbol{y}$, the Larmor frequency $f_L \simeq \mu_B B\sqrt{(g_y^2+g_z^2)/2}$ is, therefore, also expected to show dominant correlations with ℓ_y, even though the variations of g_y and g_z do partly cancel. We do not observe, however, such correlations. In the pristine device, $\boldsymbol{x}$, $\boldsymbol{y}$ and $\boldsymbol{z}$ are very good approximations to the principal axes of the g-matrix [58]. In disordered devices, the channel axis $\boldsymbol{x}$ remains, in general, a good principal axis; yet in the presence of interface roughness, the two other principal axes can make an angle of up to ≈ 10 degrees with $\boldsymbol{y}$ and $\boldsymbol{z}$. This rotation results from the coupling between the in-plane and out-of-plane motions induced by the interface roughness. Although small, it has sizable effects on the distribution of Larmor frequencies: f_L is not proportional to $\sqrt{(g_y^2+g_z^2)/2}$ since g_y and g_z are not the principal g factors anymore; and the expected correlation of f_L with ℓ_y is lost. This is also the cause for the absence of correlations between f_L and f_R in Figure 4.3b.

Lastly, the variability in Rabi frequencies is significantly larger in hole than in electron qubits

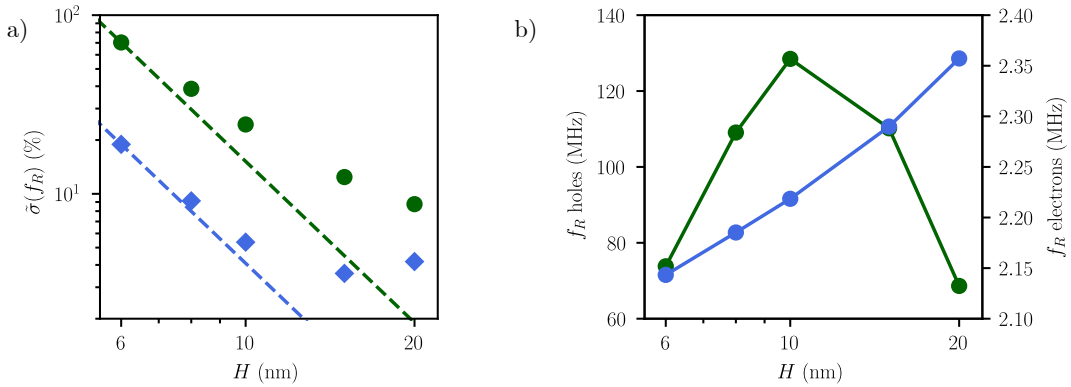

Figure 4.6: a) Dependence of the RSD $\tilde{\sigma}(f_R)$ of the Rabi frequency of electrons (in blue) and hole (in green) qubits on the channel thickness H (interface roughness disorder with $\Delta = 0.4$ nm and $L_c = 10$ nm; $V_{\text{fg}} = +50$ mV for electrons and $V_{\text{fg}} = -50$ mV for holes). The dashed lines are $\propto 1/H^3$ extrapolations from $H = 6$ nm. b) Dependence of the Rabi frequency of electrons (in blue) and hole (in green) qubits for the pristine device on the channel thickness H.

(see Figures 4.3, 4.4, and 4.6). We learn from equation 4.10 that this mostly results from the different electron and hole effective masses. The in-plane mass of electrons and holes are similar ($m^*_{\parallel} \simeq 0.2\, m_0$), but the confinement mass $m^*_{\perp}$ are different: $m^*_{\perp} = m^*_l = 0.916\, m_0$ for electrons and $m^*_{\perp} = m_0/(\gamma_1 - 2\gamma_2) = 0.277\, m_0$ for heavy holes. Holes hence suffer from the heavier confinement mass $m^*_{\perp}$ which makes them more sensitive to thickness fluctuations. Additionally, we also recover the $1/H^3$ dependence in the thin-film limit in Figure 4.6. Unfortunately, working with films thicker than 10 nm drastically reduces f_R for holes, see Figure 4.6b. $10 < H < 15$ nm seems a good tradeoff to achieve large f_R with nearly-minimal variability. Note that the latter tends to saturate for H >10 nm, probably due to the breakdown of the $H > \ell_{\mathcal{E}_y}$ condition. Indeed, for thicker films the structural confinement is weaker, and the electrical confinement becomes dominant.

4.4 Variability due to charge traps

4.4.1 Numerical simulations

4.4.1.1 Holes

The data on variability for holes due to charge defects are reported in Figure 4.7. The very large variability and the tailed (non-normal) distributions of the data for the individual simulations in presence of disorder forced us to increase the sample size, here ranging between 1.500 and 2.500 simulations for each n_i. Moreover, we provide the first and third quartiles to highlight the tailed character of the distributions (shaded areas in Figure 4.7). Also, the strong impact of the disorder brings few simulations with very large f_R. We considered strong outliers those simulations with $f_R > f_R(75\%) + 4\text{IQR}$, where the Inter-Quartile Range (IQR) is $f_R(75\%) - f_R(25\%)$, and discarded ∼5% of the simulations from the statistics following this criterion. For charge traps, we choose as a reference $f_R^{0\prime}$, $f_L^{0\prime}$ those of the pristine device including a homogeneous density of charges at the Si/SiO_2 interface to account for the average electrostatic effect of the defects.

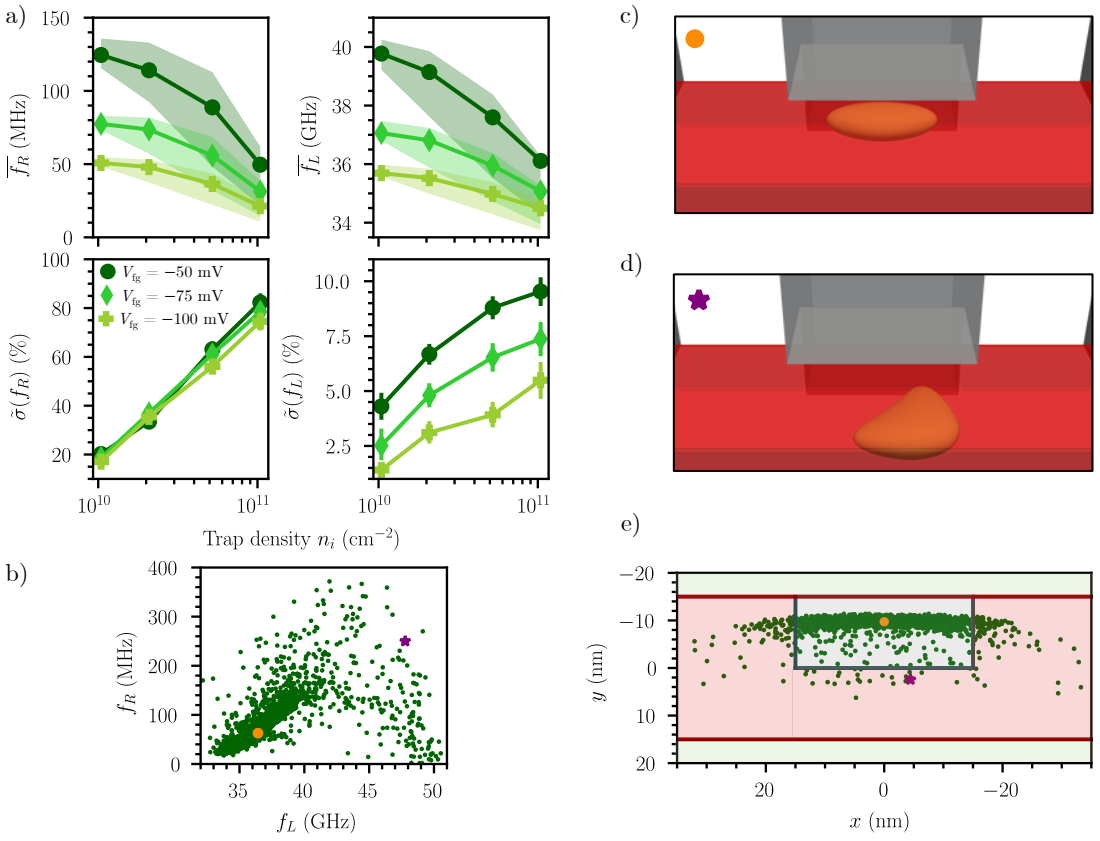

Figure 4.7: a) Average $\overline{f_R}$ and RSD $\tilde{\sigma}(f_R)$ of the Rabi frequency of hole qubits as a function of the density of charge traps n_i at the Si/SiO_2 interface, for different V_{fg}; average $\overline{f_L}$ and RSD $\tilde{\sigma}(f_L)$ of the Larmor frequency of the same hole qubits. The error bars are the 95% confidence intervals. The first and third quartiles of the distribution of devices are also displayed as a shaded area for each V_{fg}; 25% of the devices lie below, 25% above, and 50% within this shaded area. b) Distribution of the hole devices in the (f_L, f_R) plane at $n_i = 5 \times 10^{10}$ cm^{-2} and $V_{fg} = -50$ mV. Each green point is a particular realization of the charge disorder. c)-d) Iso-density surface of the squared ground state wavefunction of the pristine hole device c) and a disordered device d) at $n_i = 5 \times 10^{10}$ cm^{-2} and $V_{fg} = -50$ mV. e) Distribution of the average position of the ground state ($\langle x \rangle$, $\langle y \rangle$) for different realizations of the charge disorder at $n_i = 5 \times 10^{10}$ cm^{-2} and $V_{fg} = -50$ mV. The orange point and purple star are the devices of panels c) and d).

Therefore, the reference Larmor and Rabi frequencies plotted in Figure 4.7 slightly differ from those in Table 4.1.

Figure 4.7a shows a decrease of the average Rabi frequency $\overline{f_R}$ and the average Larmor frequency $\overline{f_L}$ with the charge trap density n_i. Note that no dependence of the averages on the severity of the disorder was observed for surface roughness. Also, for surface roughness $\overline{f_R} = f_R^0$ and $\overline{f_L} = f_L^0$, while for charge traps both $\overline{f_R}$ and $\overline{f_L}$ differ from the reference ones. The shaded areas highlighting the IQR show that most of the simulations lie below the average. Consequently, some of those that lie above suffer strong deviations. This can also be observed in Figure 4.7b, and illustrates the tailed character of the distributions. Charge traps will, therefore,

bring slower qubits (smaller f_R's) in most of the cases, while there may be few qubits showing strongly increased f_R. Those very large Rabis generally appear in very distorted QDs.

The scattering of the Rabi frequencies induced by charge traps is extremely large; it spans over one order of magnitude, see Figure 4.7b. Consequently, $\tilde{\sigma}(f_R)$ is also very large, reaching $\sim 60\%$ for $n_i = 5 \times 10^{10}$ cm^{-2} (which is equivalent to 5 charges in the whole Si/SiO$_2$ interface of the simulated device). Even at $n_i = 10^{10}$ cm^{-2}, where there is only a single charge trap in the device, variability is as large as 20%.

Regarding the Larmor frequencies, variability is slightly smaller than for surface roughness, and ranges between 4% and 10% for n_i between $10^{10} - 10^{11}$ cm^{-2} and $V_{\text{fg}} = -50$ mV. Details on the reasons behind this smaller variability are provided in Section 4.4.2. Contrarily to $\tilde{\sigma}(f_R)$, $\tilde{\sigma}(f_L)$ shows some dependence on V_{fg}. For SR, both the bias dependence of $\overline{f_L}$ and $\overline{f_R}$ and the increasing impact of the lateral facets for stronger confinements smoothed the V_{fg} dependence of $\tilde{\sigma}$. The latter does not occur for charge traps, yet the large modulations of $\overline{f_R}$ with V_{fg} (see top-left panel of Figure 4.7a) still blur the decrease of $\tilde{\sigma}(f_R)$. For $\overline{f_L}$, these modulations are weaker, and the bias dependence of $\tilde{\sigma}(f_L)$ prevails.

Charge traps do not only modulate the spin properties, but also the spatial properties of the QDs. We illustrate the strong impact that they can have on the shape of the QD in Figure 4.7d. Also its position can be strongly affected, especially along $\boldsymbol{x}$, which is the direction of weakest confinement. Strong modulations of the QD position may complicate not only the formation of the QDs and their manipulation, but also the management of exchange interactions between neighboring qubits. We discuss this matter in further detail in Chapter 5.

4.4.1.2 Electrons

The data for electrons are reported in Figure 4.8. The situation for the Rabi frequencies is very similar to holes. They are again very scattered, and variability reaches $\sim 50\%$ for $n_i = 5 \times 10^{10}$ cm^{-2}. The average f_R also shows a strong dependence on n_i, and the individual f_R's follow a tailed distribution, with most of the devices displaying slower Rabi oscillations. $\tilde{\sigma}(f_R)$ shows no dependence on V_{fg} for the same reasons as for holes.

For the Larmor frequency the modulations due to charge traps are again very weak. Also the dependence of $\overline{f_L}$ on n_i and V_{fg} is very small. The residual increase owes to the larger confinement resulting from either stronger gate voltages or larger charge trap densities. As a consequence, $\langle z \rangle$ increases in average, which yields to a larger B due to the inhomogeneous field, and a larger f_L.

As for holes, the variability in f_L remains similar to that of surface roughness, and charge traps arise as the main source of variability in f_R, with $\tilde{\sigma}(f_R)$ >20% even for n_i at the state-of-the-art of the Si/SiO$_2$ interface quality.

4.4.2 Analytical insights on numerical results

The mechanisms driving variability due to charge traps are the same as for surface roughness. Therefore, in Figure 4.9 we recover the expected correlation of f_R with ℓ_y for both electrons and holes, with roughly the same scaling factors as in Figure 4.5. For holes, we additionally recover the expected correlation of f_L with ℓ_y. In contrast with interface roughness, the charge traps directly modulate the lateral (rather than vertical) confinement, because the hole gets

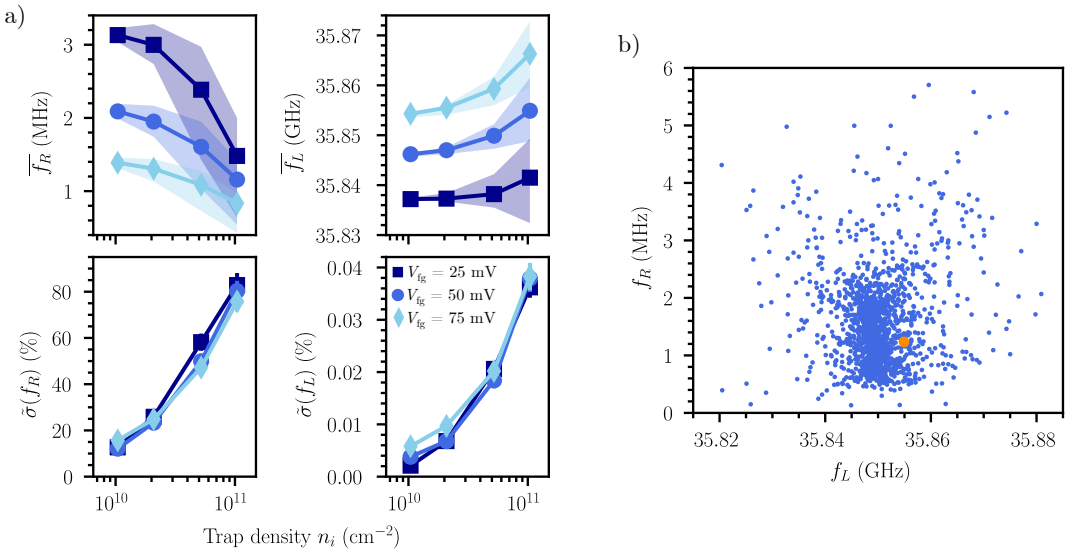

Figure 4.8: a) Average $\overline{f_R}$ and RSD $\tilde{\sigma}(f_R)$ of the Rabi frequency of electron qubits as a function of the density of charge traps n_i at the Si/SiO_2 interface, for different V_{fg}; average $\overline{f_L}$ and RSD $\tilde{\sigma}(f_L)$ of the Larmor frequency of the same electron qubits. The error bars are the 95% confidence intervals. The first and third quartiles of the distribution of devices are also displayed as a shaded area; 25% of the devices lie below, 25% above, and 50% within this shaded area. b) Distribution of the electron devices in the (f_L, f_R) plane at $n_i = 5 \times 10^{10}$ cm^{-2} and $V_{fg} = 50$ mV. Each blue point is a particular realization of the charge disorder. The orange point is the pristine device.

excluded from the whole thickness of the film in the vicinity of a defect ($\sigma(\ell_z) = 0.01$ Å at $n_i = 5 \times 10^{10}$ cm^{-2} and $V_{fg} = -50$ meV, while $\sigma(\ell_z) = 0.6$ Å on Figure 4.5). As a consequence, $\boldsymbol{y}$ and $\boldsymbol{z}$ remain good principal axes of the g tensor, so that f_L shows significant correlations with ℓ_y despite partial cancellations between the variations of g_y and g_z (see Figure 4.9b). The deviations of the Larmor and Rabi frequencies are, therefore, both primarily dependent on ℓ_y and are broadly correlated. The rotation of the magnetic axes is an extra source of variability that adds to the modulations of the main g factors, which explains why $\tilde{\sigma}(f_L)$ is slightly larger for surface roughness than for charge traps.

Electrons and holes show similar $\tilde{\sigma}(f_R)$, especially at the highest trap densities. The potential of the charge traps is, indeed, the same (up to a change of sign) for electrons and holes, in contrast with the effective potential for interface roughness, which depends on the confinement mass of the carriers (see equation 4.10). In fact, the charge traps have a stronger effect on the in-plane motion of holes (larger $\tilde{\sigma}(\ell_y)$) owing to the multi-bands character of the Hamiltonian. Yet the scaling of the Rabi frequency is softer for holes ($\delta f_R / f_R^{0\prime} \approx 3\delta\ell_y/\ell_y^{0\prime}$) than for electrons ($\delta f_R / f_R^{0\prime} \approx 4\delta\ell_y/\ell_y^{0\prime}$). Therefore, the net impact of charged traps is about the same for electrons and holes.

In the simplest models for charge traps, their scattering strength is expected to scale as $\sqrt{n_i}$ within first-order perturbation theory [110]. In Figure 4.10 we can see that $\tilde{\sigma}(f_R)$ actually increases faster than $\sqrt{n_i}$, but slower than n_i. This is presumably due to the fact that $\overline{f_R}$ also decreases with increasing n_i, and that $\sigma(f_R)$ is dominated by the P_b defects very near or in the

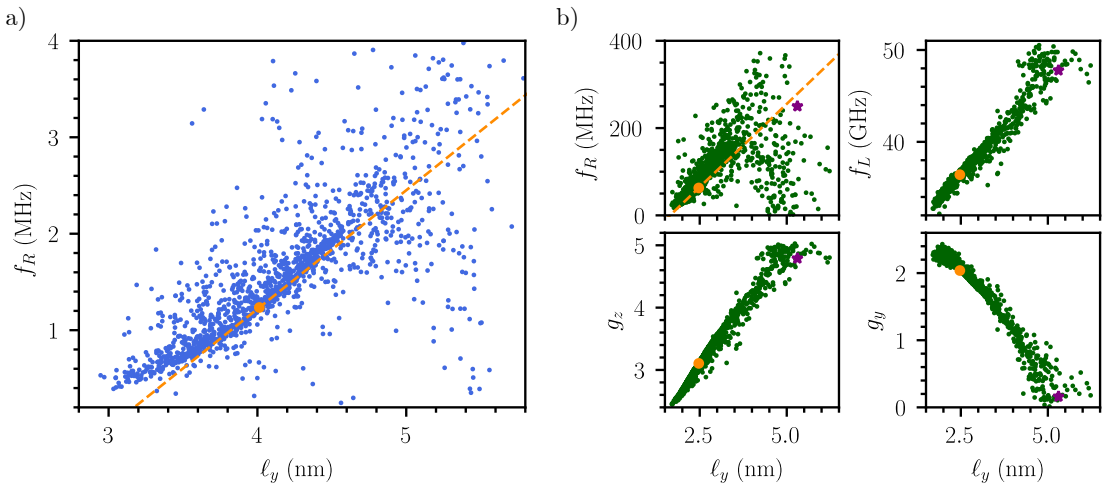

Figure 4.9: a) Correlations between the Rabi frequency f_R of the electron qubits and the extension ℓ_y of the dots along $\boldsymbol{y}$. Each point is a particular realization of charge disorder at $n_i = 5 \times 10^{10}$ cm^{-2} and $V_{\text{fg}} = 50$ mV. b) Correlations between the Rabi frequency f_R, the Larmor frequency f_L, the gyromagnetic factors g_y and g_z of the hole qubits and the extension ℓ_y of the dots along $\boldsymbol{y}$ at $n_i = 5 \times 10^{10}$ cm^{-2} and $V_{\text{fg}} = -50$ mV. The orange point is the pristine device, and the purple star the disordered device of Figure 4.7d. The dashed orange line $\delta f_R/f_R^{0\prime} = 4\delta\ell_y/\ell_y^{0\prime}$ for electrons and $\delta f_R/f_R^{0\prime} = 3\delta\ell_y/\ell_y^{0\prime}$ for holes is a guide to the eye.

dot, to which the response is non linear. Also, at small densities, the likelihood to have a defect within the dot directly scales as n_i. These two limits define an upper and lower bound for the numerical data, which are in all cases encompassed within this range.

4.5 Implications for a quantum processor

Up to now we have seen that variability in spin qubits hosted in a MOS platform may be large, especially for f_R and due to charge traps. We have also understood the mechanisms behind this variability. The remaining point to address is, therefore, what would be the impact of such variability on the performance of an eventual large-scale quantum processor.

At this point it is clear that the ideal situation of a quantum computer with the individual qubits showing identical f_R and f_L is too challenging for the current technologies. Even though the management of such quantum processor would be much easier, the large sensibility to disorder observed in the previous sections highlights a situation in which each qubit has its individual personality. It is clear, then, that a characterization of all qubits is indispensable as a previous step to the execution of any task. In the following, we discuss how having distinct qubits degrades the performance of a quantum processor, and analyze to what extent variability can be palliated.

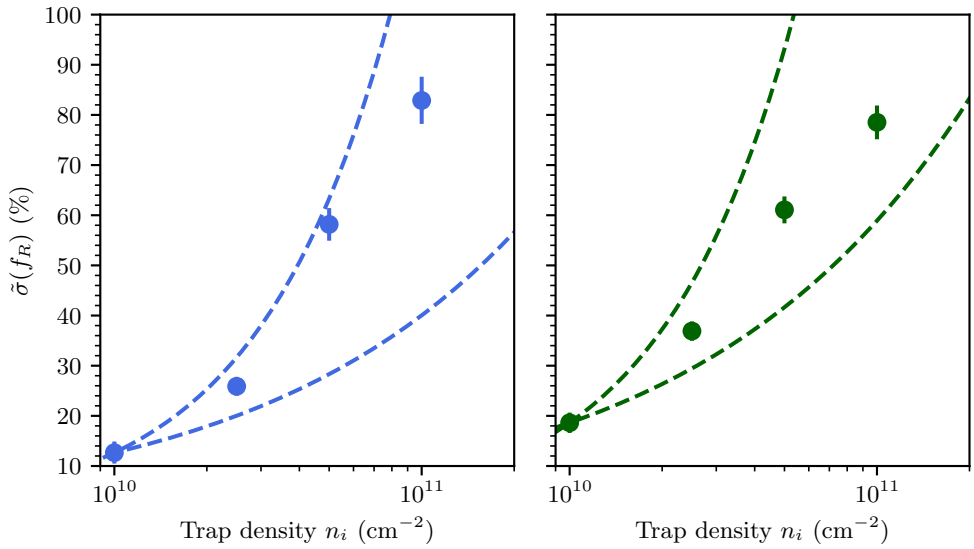

Figure 4.10: Scaling of $\tilde{\sigma}(f_R)$ with the density of charge traps n_i for electrons (in blue, left panel) and holes (in green, right panel). The upper dashed line represents a $\tilde{\sigma}(f_R) \propto n_i$ scaling, while the lower dashed line represents a $\tilde{\sigma}(f_R) \propto \sqrt{n_i}$ scaling.

4.5.1 Larmor frequency variability

To manipulate a qubit, we need to deliver a RF signal matching f_L. The linewidth of the resonance is very narrow (a few MHz), which implies that tiny deviations in the qubit frequency already fall out of the absorption spectrum, preventing the qubit from being manipulated. A variability in f_L, therefore, means that each qubit would need a different RF drive to be addressed. Having individual AC lines for each qubit is unfeasible, as a proper scalability requires the minimization of the electrical lines going down to the chip at cryogenic temperatures, both due to the lack of physical space and the associated heating problems. The RF sources are versatile and offer a wide range of frequencies. Working with a single source and adapting its frequency to the individual qubits is manageable for few-qubits experiments, yet it prevents manipulations in parallel, key for the operation of large scale quantum processors. Ideally, one would like to adapt the qubits to the RF source rather than the source to the individual qubits.

The solution that remains is, therefore, to try to correct for the deviations in f_L by tuning the device degrees of freedom to which it is sensitive to. The most straightforward way is to tune V_{fg}, and rely on the so-called Stark effect [111] to bring back the individual f_L's to the reference f_L^0. To evaluate whether this is possible, we computed the strength of the Stark effect $(\partial f_L/\partial V_{\text{fg}})$ for each individual simulation, and assuming linear response, we estimated the gate correction needed to shift f_L back to the reference f_L^0 (for SR) or $f_L^{0\prime}$ (for CT).[2] We plot such data in Figure 4.11 for electrons ($V_{\text{fg}} = 50$ mV) and holes ($V_{\text{fg}} = -50$ mV) for surface roughness at $L_c = 10$ nm, $\Delta = 0.4$ nm; and for charge traps at $n_i = 5 \times 10^{10}$ cm^{-2}.

For holes we observe that the gate corrections needed are very large, both for surface rough-

[2] As mentioned above, the reference device for charge traps includes a uniform charge distribution of density n_i. Consequently, it differs from the pristine device for surface roughness, so do their reference Larmor and Rabi frequencies.

ness and charge traps. The shaded areas in Figure 4.11 highlight the range within which 50% of the simulations are encompassed. This range is roughly 45 mV for surface roughness, and 40 mV for charge traps. Such gate corrections induce energy shifts larger than the charging energy U ∼10 meV of the qubits, and would require high isolation to avoid charge leakages from/to neighboring QDs. To achieve such isolations, a stiff control of the tunneling rates is essential. If we fix the RF signal at the Larmor frequency of reference, and allow for a window $\delta V_{\text{fg}} = \pm 20$ mV, only 46% and 54% of the qubits can be corrected for surface roughness and charge traps, respectively. The consequences of this are dramatic, since it means that the ∼10% variability induced by both sources of disorder would already make roughly 50% of the qubits useless simply because they cannot be addressed.

Electrons showed a very small $\tilde{\sigma}(f_L)$, being at worst 0.05%. It is large enough, however, to require corrections. With the absorption linewidth being on the order of magnitude of f_R, for electrons on the 1-3 MHz range, very few devices could be addressed, see x-label of Figures 4.11c and 4.11d. It is important to note, also, that for the same reason electrons have a weak $\tilde{\sigma}(f_L)$, they also have an extremely weak Stark effect. While the Stark effect for holes relies on the electrical modulation of g^*, for electrons $g_0 = 2$. The small remaining Stark effect relies, then, simply on the modulation of $\langle z \rangle$ in the gradient of magnetic field. The gate corrections for electrons aim to move the QD to the same position as the reference, whereas for holes only the same g^* is sought; and the tunability of g^* for holes is much larger than that of $\langle x \rangle$ for electrons. As a consequence, the gate corrections needed to bring the individual f_L back to f_L^0 are for electrons of the same order as those reported for holes. With a correction window of ±20 mV, only 37% and 69% of the qubits can be re-tuned for surface roughness ($L_c = 10$ nm, $\Delta = 0.4$ nm) and charge traps ($n_i = 5 \times 10^{10}$ cm^{-2}), respectively.

At this point it is important to draw attention to the fact that electron spin qubits are subject to additional sources of variability not accounted for in this work. First, Spin Valley Coupling (SVC) is neglected in the present EMA. Interface roughness is known to be responsible for a significant variability of the valley splitting and spin-valley mixing, as discussed for example in Refs. [42, 112]. This is not expected to have a strong impact on the Rabi frequencies (the dipole matrix elements between valley states being small along the main direction ($\boldsymbol{y}$) of the EDSR motion), unless the valley and Zeeman splittings are close enough to allow for intrinsic SVC-driven Rabi oscillations [42, 63]. However, SVC may slightly lower the g-factor of electrons (by up to a few hundreds) [64, 113–115]. Fluctuations of the g-factor $\delta g = 0.005$ would give rise to variations of the Larmor frequency $\delta f_L = 70$ MHz at a net field $B = 1$ T. Such fluctuations are on the scale or even larger than those reported in Figure 4.11. Achieving robust and controllable valley splitting is actually a key to the realization of well-defined electron two-level systems for spin manipulation and readout. Also, the electron spin qubits may be sensitive to local inhomogeneities (roughness, variations of the magnetic polarization...) and global misalignment (misplacement/misorientation) of the micro-magnets [105, 116]. These disorders, which are specific of extrinsic spin-orbit coupling, are addressed in Appendix C.4. As a consequence, the variability reported in this work for the f_L of electrons must be considered as a lower bound of the actual variability. Even in this case, the consequences are already critical.

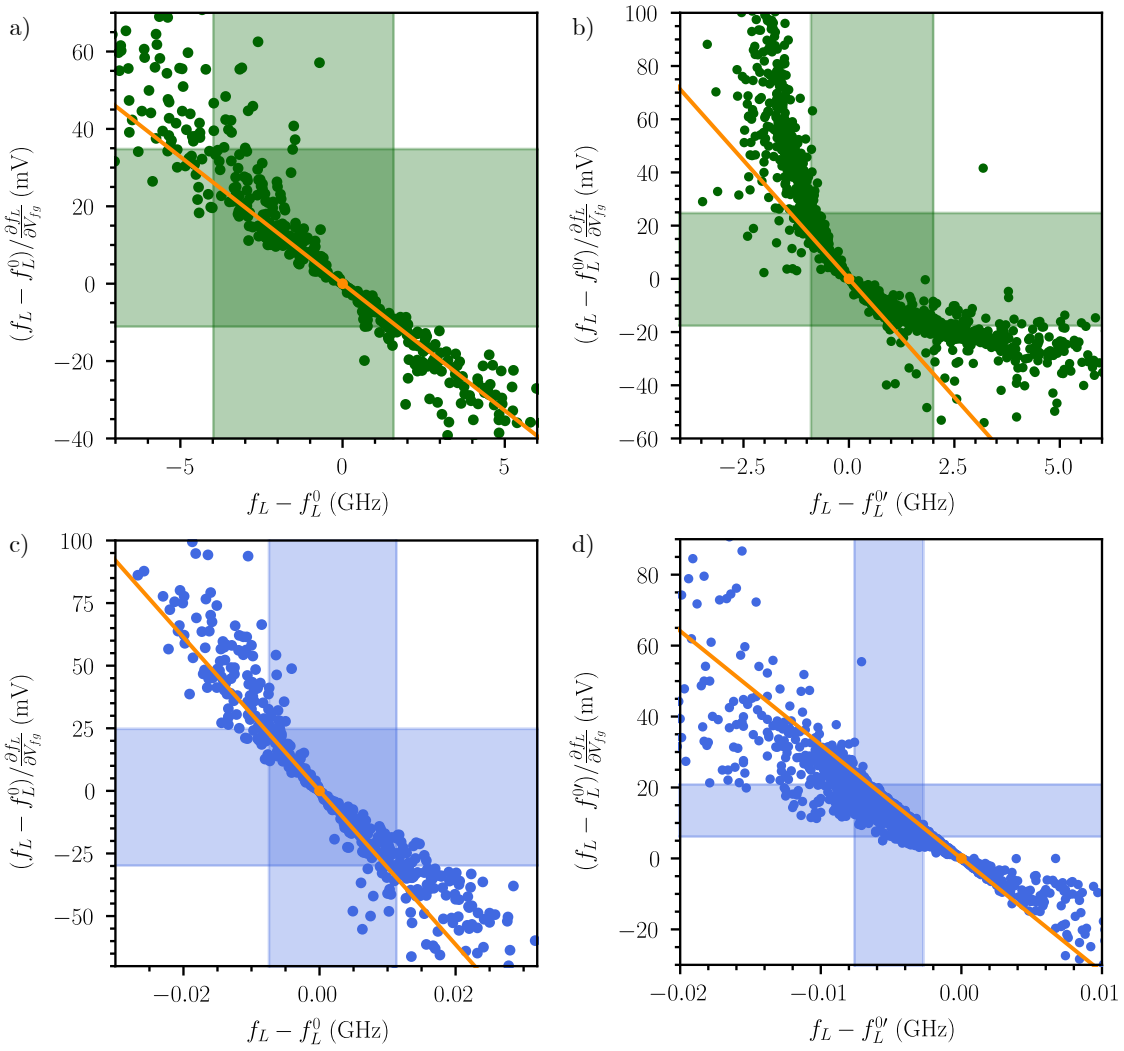

Figure 4.11: Correction of the Larmor frequency variability with V_{fg}. a) Gate voltage corrections with respect to $V_{\text{fg}} = -50$ meV required to tune the Larmor frequency f_L of disordered hole devices back to the Larmor frequency of the pristine device in presence of surface roughness ($L_c = 10$ nm, $\Delta = 0.4$ nm). The orange line is the slope $\partial f_L/\partial V_{\text{fg}}$ of the pristine device. b) Same as a) but for a charge traps, with $n_i = 5 \times 10^{10}$ cm^{-2}. c) Gate voltage corrections with respect to $V_{\text{fg}} = 50$ meV required to tune the Larmor frequency f_L of disordered electron devices back to the Larmor frequency of the pristine device in presence of surface roughness ($L_c = 10$ nm, $\Delta = 0.4$ nm). The orange line is the slope $\partial f_L/\partial V_{\text{fg}}$ of the pristine device. d) Same as c) but for a charge traps, with $n_i = 5 \times 10^{10}$ cm^{-2}.

4.5.2 Rabi frequency variability

The variability in Rabi frequencies is *a priori* not as critical as that of Larmor frequencies for the operation of the quantum processor. It will nonetheless impact its performance. Indeed, if an ensemble of qubits has different f_R's, the time to perform a given operation will vary for each of them. The fastest qubits, therefore, will typically have to wait for the slowest to finish, which

may cause the loss of quantum information through decoherence mechanisms. The correction of $\tilde{\sigma}(f_R)$ may be attempted by tuning the power for each individual qubit ($f_R \propto V_{\mathrm{ac}}$), yet this would further complicate the management of the RF signals on the chip.

In an ensemble of qubits, disorder will also give rise to variability in T_1 and T_2^*. We expect as a general trend that the devices with the largest Rabi frequencies also show the shortest relaxation times T_1. As a rule-of-a-thumb, the relaxation rate $\Gamma_1 = 1/T_1 \propto \sum f_L^n |\langle\uparrow| \mathcal{M}_1 |\downarrow\rangle|^2$ in the Fermi-Golden rule/Bloch-Redfield approximation, where $\mathcal{M}_1$ is some spin-electric coupling and the exponent n depends on the relaxation mechanism ($n = 1$ for Johnson-Nyquist noise, $n = 3$ to 5 for phonons [41, 117–119]). Indeed, $1/T_1$ can be expected to scale with f_R as both are proportional to a transverse matrix element. The pure dephasing rate is, likewise, $\Gamma_2^* = 1/T_2^* \propto \sum |M_2|^m$, where $M_2 \equiv \langle\Uparrow| \mathcal{M}_2 |\Uparrow\rangle - \langle\Downarrow| \mathcal{M}_2 |\Downarrow\rangle$ for some coupling operator $\mathcal{M}_2$, with $m = 2$ for regular noise (Bloch-Redfield approximation) and $m = 1$ for quasi-static $1/f$ noise [117]. Although the relations between the longitudinal matrix elements involved in Γ_2^* and the transverse matrix elements involved in f_R and Γ_1 is far from obvious, we can still expect that devices with stronger spin-electric coupling show, on average, larger f_R, Γ_1, and Γ_2^*, unless some sweet spot has been found.

Assuming that we do not correct for the variability in f_R, we can quantify its impact on the quality of a quantum processor by computing its quality factors. The quality factors of an individual qubit are defined as $Q_1 = 2f_R \times T_1$ and $Q_2^* = 2f_R \times T_2^*$ (number of π rotations that can be achieved within T_1 or T_2^*). The relevant figures-of-merit of the whole quantum processor are, however, $\hat{Q}_1 = 2\min(f_R) \times \min(T_1)$, $\hat{Q}_2^* = 2\min(f_R) \times \min(T_2^*)$. They are limited by the slowest and by the shortest-lived qubits, which are in principle different. This highlights how detrimental the variability can be for the operation of an ensemble of qubits. In order to estimate $\hat{Q}_1$ and $\hat{Q}_2^*$, we need to compute the relaxation and decoherence times of all the individual qubits.

The relaxation time (T_1) is typically limited by the electron-phonon interaction for QD-based spin qubits. It can be numerically estimated as shown in Ref. [42] for electrons, and in Ref. [41] for holes. Regarding dephasing, in the case of zero or limited hyperfine interaction (valid for Si spin qubits), it is typically dominated by $1/f$ charge noise. Such noise can be modeled as an effective fluctuation $\delta V_{\mathrm{fg}}(t)$ of the gate voltage with rms amplitude $\delta V_{\mathrm{fg,rms}}$. In this case [120],

$$\Gamma_2^* = \frac{1}{\sqrt{2}\hbar} e |\langle\Uparrow| D |\Uparrow\rangle - \langle\Downarrow| D |\Downarrow\rangle| \delta V_{\mathrm{fg,rms}} \,. \tag{4.15}$$

We used these models to extract T_1 and T_2^* from the simulations of holes for surface roughness at $L_c = 10$ nm, $\Delta = 0.4$ nm; which induces a variability of $\tilde{\sigma}(f_R) \approx 25\%$. We do not extend the discussion to electrons since the absence of valleys in the $\mathbf{k}\cdot\mathbf{p}$ simulations makes the obtained T_1 and T_2^* unrealistically large. The distribution of Rabi frequencies f_R and relaxation rates Γ_1 is plotted in Figure 4.12a, and the data for Γ_2^* are plotted in Figure 4.12c. They are computed at $B = 1$ T along $\boldsymbol{y} + \boldsymbol{z}$ (Γ_1 scales as B^5 [41] and Γ_2^* as B). As hinted above, the larger the Rabi frequency, the larger Γ_1 (and, to a much lesser extent, Γ_2^*) tends to be. There is, nonetheless, a significant spread of the single qubit quality factors Q_1 and Q_2^*, as shown in Figures 4.12b and 4.12d.

If we now compute the quality factors of a 500-qubits quantum processor operating the 90% best performing ones in presence of surface roughness ($\Delta = 0.4$ nm, $L_c = 10$ nm), we obtain

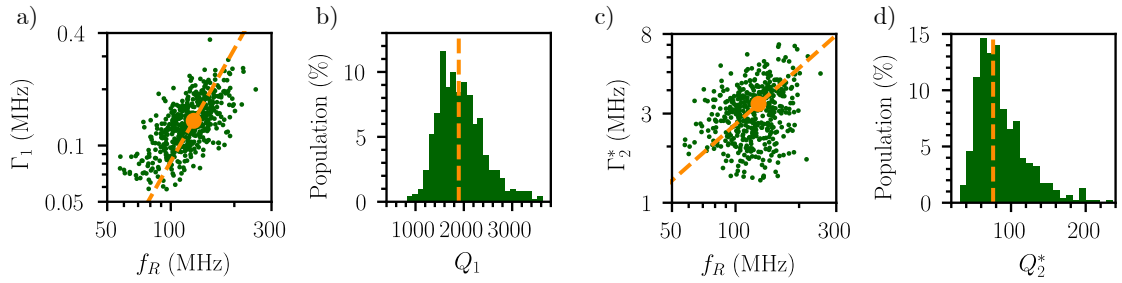

Figure 4.12: a) Distribution of the rough hole devices in the (f_R, Γ_1) plane ($\Delta = 0.4$ nm, $L_c = 10$ nm, $V_{\text{fg}} = -50$ mV and $B = 1$ T). Each green point is a particular realization of the interface roughness disorder. The orange point is the pristine device. The dashed orange line, $\Gamma_1 \propto (f_R/f_R^0)^2$, is provided as a guide to the eye. b) Histogram of the quality factors $Q_1 = f_R \times T_1$ for the same set of devices. The orange dashed line is the quality factor of the pristine device. c) Distribution of the rough hole devices in the (f_R, Γ_2^*) plane (same conditions as before). The dashed orange line, $\Gamma_2^* \propto f_R/f_R^0$, is provided as a guide to the eye. d) Histogram of the quality factors $Q_2^* = f_R \times T_2^*$ for the same set of devices.

$\hat{Q}_1 = 444$ and $\hat{Q}_2^* = 16.7$. These values are smaller by a factor of ≈ 4 than the quality factors of the pristine device ($Q_1^0 = 1895$ and $Q_2^{*0} = 76.0$), which implies that the number of operations that can be realized in the processor would be four times smaller due to surface roughness. It is important to highlight that these results are an illustration for surface roughness, where $\tilde{\sigma}(f_R) = 25\%$. Charge traps in standard-quality Si/SiO_2 interfaces ($n_i = 5 \times 10^{10}$ cm^{-2}) induce variabilities of 60%, which would degrade even more the figures shown here.

As discussed previously, $\tilde{\sigma}(f_R)$ can be corrected by adjusting the power of the AC drive for each individual qubit. This would smooth the degradation of the quality factors, which would read $\hat{Q}_1 = 2f_R^0 \times \min(T_1)$ and $\hat{Q}_2^* = 2f_R^0 \times \min(T_2^*)$, but the variability in the relaxation and decoherence times would still deteriorate the figures of merit. If we consider T_1 and T_2^* independent of the power applied, the quality factors of the processor at power-corrected f_Rs read $\hat{Q}_1 = 991$ and $\hat{Q}_2^* = 37.2$. They are still a factor of 2 smaller with respect to the pristine device.

4.6 Mitigation of disorder

The qubits may be made more resilient to variability through material and/or device engineering. In particular, the previous sections highlight how critical is the quality of materials and interfaces for the control and reproducibility of spin qubits. Improving the quality of the Si/SiO_2 interface would certainly reduce variability; yet a RSD $\tilde{\sigma}(f_R) < 10\%$ calls for very clean interfaces with charged defect densities $n_i < 10^{10}$ cm^{-2} that are beyond the state-of-the-art.

The interface roughness variability can be partly alleviated by a proper optimization of the film thickness H and confinement strength in order to reach the best balance between single qubit performances and sensitivity to disorder. Charge traps, however, are insensitive to both parameters.

Probably the best solution is to tackle directly the origin of the problem: the poor quality of the Si/SiO_2 interface and its proximity to the qubits. In this sense, it is appealing to switch

from a crystalline/amorphous interface such as Si/SiO_2 to an epitaxial interface such as Si/SiGe (electron qubits) or Ge/SiGe (hole qubits). Epitaxial interfaces show, in principle, low roughness and very small density of traps; and devices based on Si/SiGe and Ge/SiGe heterostructures have the poor-quality crystalline/amorphous interfaces deported far above the active layer. We further discuss the effect of moving the charges away from the qubits in Appendix C.2. Additionally, surrounding the qubits by materials with higher dielectric constant (SiGe vs. SiO_2), and by a dense set of gates will reduce the impact of charged defects on variability (and possibly of charge noise on qubit lifetimes). Working in the many electrons/holes regime may also enhance screening, but it usually makes the dots larger and more responsive to disorder. The optimal number of particles in the dots (as far as variability is concerned) remains, therefore, an open question [121].

Finally, the model of section 4.3.2 shows that the variability increases with the in-plane mass $m_\parallel^*$ (at given dot sizes ℓ_x^0 and ℓ_y^0). Heavier particles indeed localize more efficiently in the disorder. It is, therefore, *a priori* advantageous to switch from Silicon to lighter mass materials such as Germanium for holes (for interface roughness, the variability is $\propto m_\parallel^*/m_\perp^*$ when $H \ll \ell_{\mathcal{E}_z}$ so Ge is advantageous over Si even in this regime). However, the dots are usually made larger in light mass materials (the dot sizes ℓ_x^0 and ℓ_y^0 scale as $(m_\parallel^*)^{-1/4}$ in a given parabolic potential for example, and as $(m_\parallel^*)^{-1/2}$ at given confinement energy), hence can be more polarizable and sensitive to disorder, so variability may not necessarily improve when decreasing the mass at given confinement energy, especially in the presence of long-wavelength disorders such as charge traps.

4.7 Chapter 4 in a nutshell

The quantification and analysis of variability of spin qubits in Si MOS devices showed how critical it can be when such platforms are to be scaled up. For holes, variability in f_R and f_L results from the modulation of the QD size ℓ_y and its coupling with the spin properties through SOC. The absence of SOC leaves electrons with a very small residual variability in f_L due to modulations of the position of the QD in the gradient of magnetic field, whereas the variability in f_R can still be traced back to modulations of ℓ_y.

The Larmor frequencies of electrons are more robust to disorder than the Larmor frequencies of holes yet both cases require very strong gate corrections to mitigate such variability, to the point that nearly 50% of the qubits may not be addressable with a single AC frequency for realistic surface roughness and charge trap densities. The Rabi frequencies show much larger variability than the Larmor frequencies for both kinds of carriers, and together with the scattering of dephasing and relaxation times, may largely reduce the number of operations that can be realized on an eventual quantum processor.

Holes are more sensitive to interface roughness than electrons because the confinement mass of the heavy-holes is smaller than the confinement mass of the electrons in the Z-valleys (hence the effects of fluctuations of the film thickness are larger). The main source of variability is, however, charge traps at the Si/SiO_2 interface, which can spread both electron and hole Rabi frequencies over one order of magnitude. The dots can be significantly distorted and displaced by charge disorder, which does not only scatter one-qubit properties, but may also complicate the management of exchange interactions between the dots.

Low variability $\tilde{\sigma}(f_R) < 10\%$ calls for smooth and clean interfaces with charge traps densities $n_i < 10^{10}$ cm^{-2}. This is presumably more easily achieved with epitaxial heterostructures such as Si/SiGe or Ge/SiGe, where the residual (surface) charge traps can be deported tens of nanometers away from the active layer. Variability in Ge heterostructures is studied in-depth in Chapter 6.

Chapter 5

Management of two-qubit interactions

Contents

For the experimental realization of two-qubit operations, control on the tunnel coupling between QDs is required. One must be able to turn on the interaction between the pair of qubits involved in the operation, while isolating them from all of their neighbors. As discussed in section 1.4, in the latest generation of LETI devices at the beginning of this thesis there were no gates for this purpose. Even though the detuning between QDs may be an alternative way of controlling the tunnel coupling (and therefore performing two-qubit operations), relying on it for the management of quantum processors with a large number of qubits may, in view of the expected strong variability in single-qubit properties, be completely unfeasible. Therefore, it is essential to introduce new elements of control in the devices to enable a proper tunability of the tunnel coupling. The major advance included in the design of the next generation of LETI devices is indeed the introduction of such gates, hereafter named exchange gates (or J-gates). In the following, we explore the physics of the new J-gates to understand their functioning, we optimize the device design to deliver the best efficiency, and analyze the impact of variability for electrons and holes in the two-qubit properties. We also propose in Appendix D.1 a design for an alternative control of the tunnel couplings by a small modification of the current front gates stack.

5.1 J-gates in Si MOS devices

Figure 5.1 illustrates the design of the J-gates envisioned by the LETI fabrication team. These gates are introduced at the top of the device after etching the encapsulating SiO_2 down to the Contact Etch Stop Layer (CESL) (encapsulating Si_3N_4). The 50-100 nm deep etched trenches

are then filled with Ti/TiN/W, and behave as metallic gates. The envisioned pattern for the J-gates is to extend them perpendicular to the channel, matching the spacings between front gates. They are intended, therefore, to control mainly the coupling between parallel QDs. The main question marks on the performance of the designed J-gates were on their efficiency, given the large distance (≈ 100 nm) between the gates and the Si nanowire in the initial designs.

5.1.1 Simulation details

We simulate a pristine 1D device composed by pairs of split face-to-face front gates. Such device would operate with a 1D array of qubits on one side of the nanowire, and a 1D array of readout dots on the opposite side. The nanowire is $H = 10$ nm thick, and the total width along $\boldsymbol{y}$ is W. The front gates always overlap the channel by 20 nm, so the spacing between face-to-face gates is $L_\perp = W - 2 \times 20$ nm. The spacing between adjacent gates is $L_\parallel$. The BOX is 145 nm thick, and the gate oxide thickness is 5 nm. The front gate thickness is H_{fg} and the CESL thickness is H_{CESL}. On top of it the exchange gates are $L_\parallel$ wide, and match the lateral spacing between front gates. We model a simulation box containing two pairs of face-to-face gates, see Figure 5.1, and apply periodic boundary conditions along the nanowire axis to simulate an infinitely large 1D array. We perform EMA calculations for electrons, yet conclusions hold as well for holes. We simulate the four QD tuned by applying the same $V_{\text{fg}} = 50$ mV to all front gates, and map the results to the model below to extract the tunnel couplings.

If the four QDs are tuned, a model Hamiltonian of the system can be easily built in the basis of the ground state wavefunction of the individual dots $\{\varphi_1, \varphi_2, \varphi_3, \varphi_4\}$ by looking at the connection between neighbors (see Figure 5.1b). It reads

$$H = \begin{pmatrix} E_0 & 2\tau_\parallel & 2\tau_d & \tau_\perp \\ 2\tau_\parallel & E_0 & \tau_\perp & 2\tau_d \\ 2\tau_d & \tau_\perp & E_0 & 2\tau_\parallel \\ \tau_\perp & 2\tau_d & 2\tau_\parallel & E_0 \end{pmatrix}, \tag{5.1}$$

where E_0 is the energy of each of the four-fold degenerated QDs; and $\tau_\parallel$, $\tau_\perp$ and τ_d are the tunnel coupling between parallel, perpendicular, and diagonal dots, respectively. The diagonalization of the Hamiltonian in equation 5.1 leads to the bonding and anti-bonding combinations of the individual dots (ψ_1, ψ_2, ψ_3, ψ_4) and their distinct energies (E_1, E_2, E_3, E_4),

$$\begin{aligned} E_1 &= E_0 + 2\tau_\parallel + 2\tau_d + \tau_\perp, \quad \psi_1 = (\varphi_1 + \varphi_2 + \varphi_3 + \varphi_4)/2; \\ E_2 &= E_0 - 2\tau_\parallel - 2\tau_d + \tau_\perp, \quad \psi_2 = (\varphi_1 - \varphi_2 - \varphi_3 + \varphi_4)/2; \\ E_3 &= E_0 + 2\tau_\parallel - 2\tau_d - \tau_\perp, \quad \psi_3 = (\varphi_1 + \varphi_2 - \varphi_3 - \varphi_4)/2; \\ E_4 &= E_0 - 2\tau_\parallel + 2\tau_d - \tau_\perp, \quad \psi_4 = (\varphi_1 - \varphi_2 + \varphi_3 - \varphi_4)/2; \\ &\quad . \end{aligned} \tag{5.2}$$

The result of a $\mathbf{k}\cdot\mathbf{p}$ simulation with all front gates at the same V_{fg} provides the four lowest-lying states $\widetilde{\psi}_i$ and their energies $\widetilde{E}_i$, yet we need to relate them to those in equation 5.2.[1] To

[1] Depending on the particular values of $\tau_\parallel$, $\tau_\perp$ and τ_d, the eigenenergies and eigenstates shown in equation 5.2 may not be in order of increasing energy. Determining the state parity is then crucial to map the single-particle results to the model.

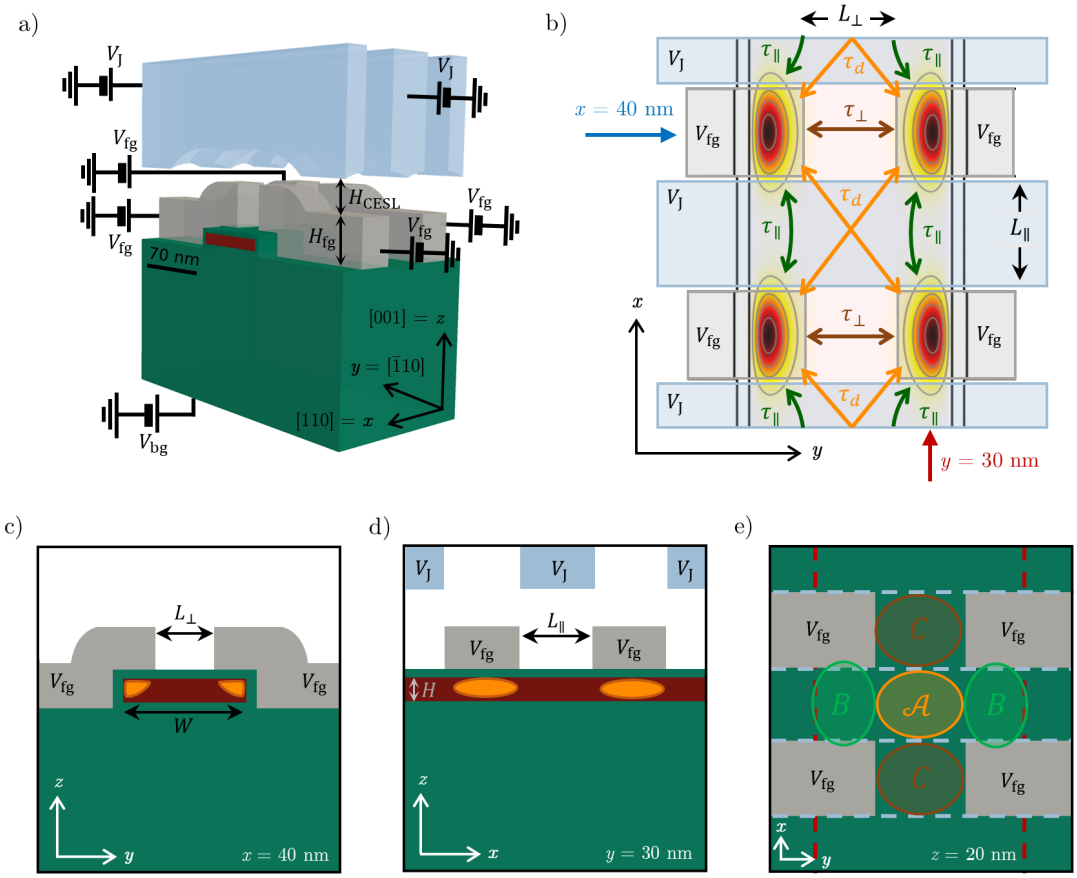

Figure 5.1: a) Simulated device for the study of the J-gates, with $H = 10$ nm, $W = 70$ nm, $L_\parallel = 40$ nm, and $L_\perp = 30$ nm. Silicon is represented in red, SiO_2 and BOX in green, the metallic front gates in grey, and the J-gates in blue. b) Cross section of the device in a) with the ground state wavefunction for $V_{fg} = 50$ mV. Colored arrows represent the connectivity of each QD with its nearest neighbors. Blue and red dashed lines highlight the plane of the cross sections illustrated in c) and d), respectively. c) Cross section of the device in a) in the $(\boldsymbol{zy})$ plane at $x = 40$ nm (the origin of coordinates is fixed at the center of the Si nanowire). The quantum dots are sketched in orange. d) Cross section of the device in a) in the $(\boldsymbol{zx})$ plane at $y = 30$ nm. e) Cross section of the device in a) in the $(\boldsymbol{xy})$ plane at $x = 20$ nm. Dashed red and blue lines outline the limits of the Si nanowire below and of the J-gates above, respectively. The highlighted areas $\mathcal{A}$, $\mathcal{B}$, $\mathcal{C}$ show the relevant areas for the control of τ_d, $\tau_\parallel$, $\tau_\perp$.

do so, we evaluate the sign of the $\mathbf{k}\cdot\mathbf{p}$ eigenstates $\widetilde{\psi}_i$ at the four QD sites. As an example, if $\widetilde{\psi}_1$ is positive in all sites, then $\widetilde{\psi}_1 \equiv \psi_1$ and $\widetilde{E}_1 \equiv E_1$. Once we have correctly assigned all $\mathbf{k}\cdot\mathbf{p}$ states and therefore know E_1, E_2, E_3, E_4, we can solve the system of equations in equation 5.2 to extract $\tau_\parallel$, $\tau_\perp$ and τ_d.

To explore the efficiency of each gate of the device on the control of the tunnel couplings we can make use of the existing analytical solutions for this problem to fit the numerical data. There are several analytical expressions for the dependence of the tunnel coupling on the tunnel barrier height for model barriers. One of these is the Wentzel–Kramers–Brillouin (WKB) approximation,

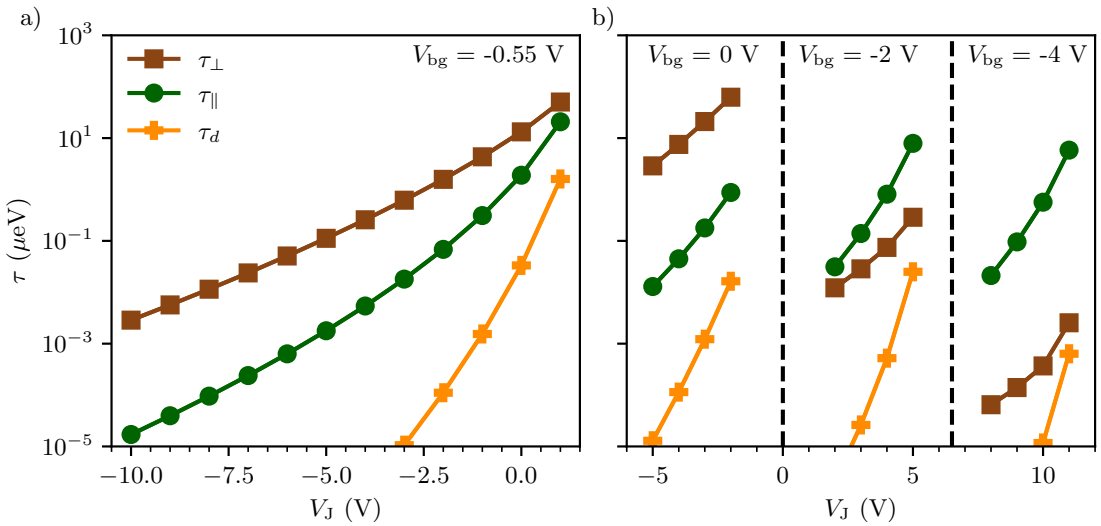

Figure 5.2: Proof of principle of the tunnel control using the J-gates. The simulated device has a 70 nm wide nanowire, with $L_\parallel = 40$ nm and $L_\perp = 30$ nm. $H_{fg} = 50$ nm and $H_{CESL} = 35$ nm. a) J-gate scan of the three tunnel couplings at $V_{bg} = -0.55$ V. b) Same as a) for different back gate voltages. Readout ($V_{bg} = 0$ V) and manipulation ($V_{bg} = -4$ V) regimes are reachable by playing with both exchange and back gates.

which predicts $\tau \propto \exp(\sqrt{E_a})$, where E_a is the barrier height, proportional here to V_J [122]. Consequently, $\log^2\tau$ should depend linearly on V_J. This allows to build a simple model that we can use to fit the numerical data and extract the tunnel barrier lever-arms ($\alpha_{k,i}$) for each gate and tunnel coupling,

$$\log^2\tau_i = \sum_k \alpha_{k,i} V_k + C, \tag{5.3}$$

where k stands for the different gates, and i refers to $\parallel$, $\perp$ or d. The tunnel lever-arms $\alpha_{k,i}$ are a direct indicator of the efficiency of the gate on the control of each tunnel coupling. In the latter discussions we refer to efficiency as the absolute value of $\alpha_{k,i}$, and selectivity to the ratio $\alpha_{k,i}/\alpha_{k,j}$ between tunnel couplings.

5.1.2 Proof of principle

Figure 5.2a shows the effect of the J-gates on the three tunnel couplings. The simulated device is made of a 70 nm wide Si nanowire, and has a parallel inter-gate distance $L_\parallel = 40$ nm, and a face-to-face inter-gate distance of $L_\perp = 30$ nm. For such configuration, we observe a very weak control of the tunnel couplings, and roughly 10 V in the J-gates are required to switch them on and off. In addition, the selectivity of the exchange gates is very poor, as the three tunnel couplings react very similarly to V_J. Given the geometry of the J-gates, which cover the spacings between parallel front gates, one would expect a tight control of $\tau_\parallel$ and τ_d, and a rather weak control of $\tau_\perp$. Results evidence, however, very similar tunabilities.

The mode of operation of the device, with a 1D array of qubits in front of a second array of readout dots, would require a strong parallel coupling $\tau_\parallel$ between qubits while keeping the

interaction with the readout dots $\tau_\perp$ closed for manipulation; whereas the opposite situation would be necessary for readout. From Figure 5.2a it is clear that both $\tau_\parallel \gg \tau_\perp$ and $\tau_\parallel \ll \tau_\perp$ are not reachable by tuning only V_J. Therefore, a second degree of freedom is essential to achieve both regimes. As exposed in Section 1.4, LETI devices include a back gate: the Si substrate. Unfortunately, this substrate does not behave as a metal at cryogenic temperatures, and its potential can only be set at the beginning, but cannot be tuned during the experiments.[2] In the simulation box, the back gate is treated as an equipotential plate at the bottom of the device (see Figure 5.1a), and we show in Figure 5.2b that a fully-tunable back gate, together with the J-gates, would allow us to reach the two regimes of interest: $\tau_\parallel \gg \tau_\perp$ with $V_\mathrm{J} = -1$ V and $V_\mathrm{bg} = 0$ V, and $\tau_\parallel \ll \tau_\perp$ with $V_\mathrm{J} = 10$ V and $V_\mathrm{bg} = -4$ V. In view of these findings, efforts have been made in the addition of metallic back gates in the LETI devices as an extra postprocessing step. The current status is discussed in section 5.1.6.

Now that we have a device that can reach a readout and a manipulation regime, we can analyze why the J-gates are so inefficient. Very large potential shifts are needed, and their effect is very similar for the three tunnel couplings. The answer to both points is related, and comes from the large distance between the exchange gates and the nanowire. Indeed, imprinting the J-gate pitch of 30-40 nm in the potential energy of the channel from a distance of nearly 100 nm is hardly feasible. The J-gates potential is in fact largely smoothed in the active layer, which explains the weak selectivity of V_J in Figure 5.2, and why there is a finite control of $\tau_\perp$ even though the J-gates do not overlap the $\mathcal{C}$ area. This has some consequences on the J-gate design, as eventual misalignments between front and J- gates become little relevant. Moreover, the potential of the J-gates is strongly screened by the front gates, which further reduces their efficiency.

5.1.3 Selectivity optimization

Even with the highly non-local potential generated by the J-gates, we can still observe a (weak) selectivity on the different tunnel couplings. We can relate this selectivity to the ratio of the distance between parallel and face-to-face gates, $L_\parallel/L_\perp$. The J-gates potential needs to cross the front gates spacing to reach the Si nanowire. This area undergoes a strong screening, significantly smoothing their effect. The screening produced by two metal plates is strongly dependent on the distance between them, so a $L_\parallel/L_\perp$ ratio close to 1 would bring similar screenings for the $\mathcal{B}$ and $\mathcal{C}$ areas (see Figure 5.1e), thus similar control over $\tau_\parallel$ and $\tau_\perp$. To illustrate this statement, and relying on equation 5.3, we have sampled the three τ_i for different biases and fitted the data to the dependence of the three tunnel couplings on V_J and V_fg,

$$\log^2\tau_i = \alpha_{\mathrm{J},i} V_\mathrm{J} + \alpha_{\mathrm{bg},i} V_\mathrm{bg} + C, \tag{5.4}$$

where C is a constant, and extracted α_J and α_bg. These are plotted in Figure 5.3a for different $L_\parallel/L_\perp$ ratios. We observe that, even though the J-gates are 50 nm closer to the QDs than the back gate, α_bg are systematically larger than α_J. This illustrates the strong impact of the

[2] At cryogenic temperatures, the Si does not rapidly adapt to the changes of potential applied, and it reaches equilibrium very slowly when the applied potential is varied. To speed up this process, the device is sometimes irradiated with photons so as to promote the electron dynamics within the semiconductor. This is not possible during an experiment, since it would also impact the qubits and destroy the information. Therefore, the back gate in current devices is hardly tunable during the experiments.

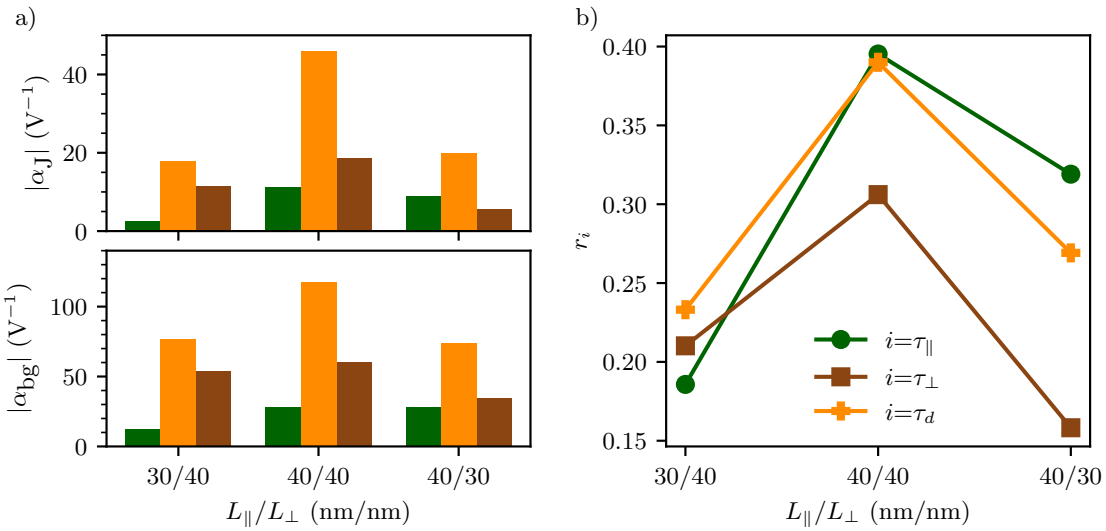

Figure 5.3: Efficiency and selectivity of the tunnel control. a) J-gate and back gate efficiencies on the control of $\tau_\parallel$, $\tau_\perp$ and τ_d for different $L_\parallel/L_\perp$ ratios. b) Selectivity (r_i ratio between back gate and J-gate tunnel responses) on the control of each tunnel coupling.

screening due to the front gates. The tunnel coupling with the largest tunability by both back and J- gates is τ_d. This is indeed in line with the screening argument, as the $\mathcal{A}$ area of the device is the one that suffers the weakest screening. Regarding selectivity, we observe that the $L_\parallel/L_\perp$ ratio clearly impacts α_J. In particular, enlarging $L_\parallel$ leads to an increase of $\alpha_{J,\parallel}$, while decreasing $L_\perp$ decreases $\alpha_{J,\perp}$. Consequently, for $L_\parallel/L_\perp = 30/40$ we have $\alpha_{J,\parallel} < \alpha_{J,\perp}$, while for $L_\parallel/L_\perp = 40/30$ we reach the opposite situation. The design of the device layout becomes then critical to engineer the proper selectivity of the exchange gates.

Let us now define r_i as the ratio between $\alpha_{J,i}$ and $\alpha_{bg,i}$,

$$r_i = \frac{\alpha_{J,i}}{\alpha_{bg,i}}. \tag{5.5}$$

This parameter is relevant because it determines whether we are able or not to reach readout and manipulation regions. Ideally, we would like to have one gate controlling exclusively $\tau_\perp$, and another gate controlling exclusively $\tau_\parallel$. In terms of r_i, this translates into $r_\parallel \to \infty$ and $r_\perp \to 0$, or *vice versa*. When this is not the case, any gate correction tunes both tunnel couplings, and the more similar $r_\perp$ and $r_\parallel$, the larger the bias shifts needed to switch from manipulation to readout. Moreover, r_d also plays a key role. For both manipulation and readout we need to keep τ_d small. To fulfill this condition we must have r_d in between the values of $r_\parallel$ and $r_\perp$. As an example, let us consider the case $r_\parallel > r_d > r_\perp$. In the limit of $V_J \gg 0$ and $V_{BG} \ll 0$, $\tau_\parallel \gg 0$, $\tau_\perp \to 0$, and $\tau_d \to 0$ (manipulation). In the opposite limit, when $V_J \ll 0$ and $V_{BG} \gg 0$, $\tau_\parallel \to 0$, $\tau_\perp \gg 0$, and $\tau_d \to 0$ (readout). In the case where r_d is the largest (or smallest), τ_d will dominate over $\tau_\parallel$ (or $\tau_\perp$) in the manipulation (or readout) regime, making it inaccessible. So we need two gates as selective as possible on controlling $\tau_\parallel$ and $\tau_\perp$, and as little selective as possible on controlling τ_d, which translates into having r_d in between the values of $r_\parallel$ and $r_\perp$, these being as different as possible.

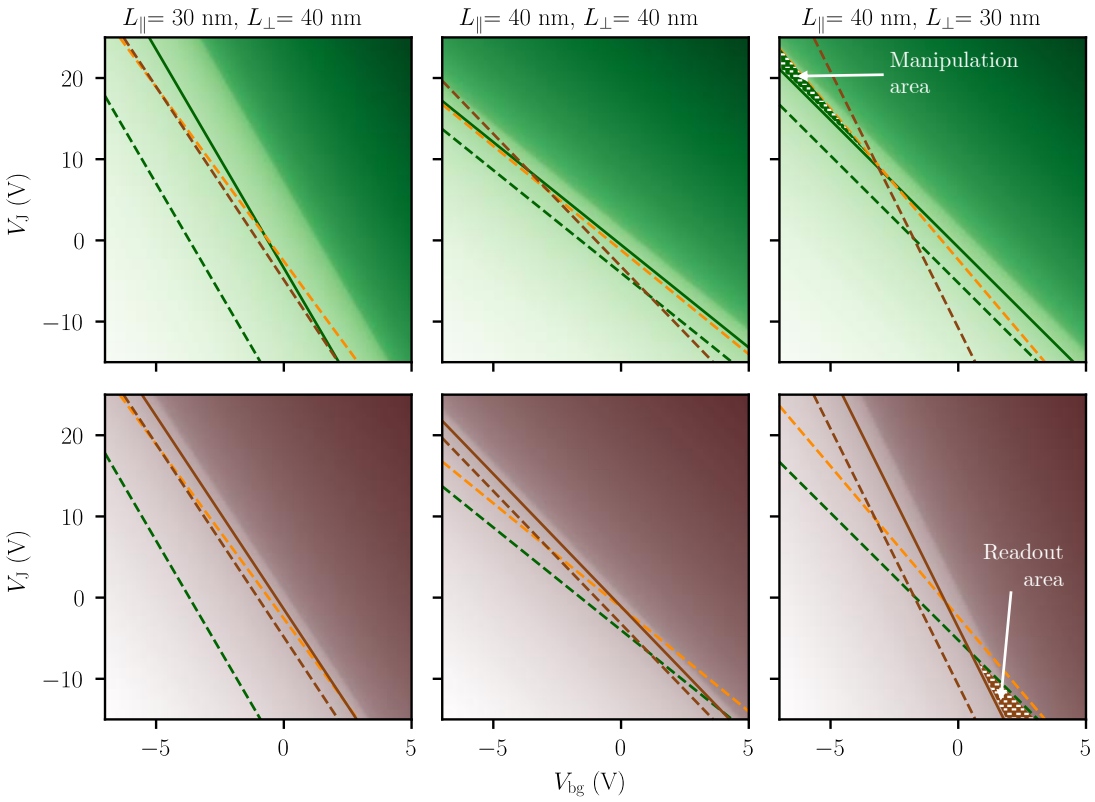

Figure 5.4: Maps of $\tau_\parallel$ (first row) and $\tau_\perp$ (second row) as a function of V_J and V_{BG} for different interdot spacings. Color maps illustrate the strength of the coupling (the lighter the color the weaker the coupling), whereas the plotted lines outline isolines of interest: dashed lines show $\tau = 10^{-2}$ μeV, and solid lines $\tau = 10^{1}$ μeV. Green, brown and orange stand for $\tau_\parallel$, $\tau_\perp$ and τ_d, respectively.

We can now do this analysis on the values of r_i obtained for the three $L_\parallel/L_\perp$ ratios studied here, see Figure 5.3b. It is clear that the ratio providing the largest differences between r_i's is $L_\parallel = 40$ nm, $L_\perp = 30$ nm. Note that the $\boldsymbol{z}$ axis of the device is not a C4 symmetry axis, and therefore $r_\parallel = r_\perp$ does not have to occur necessarily at $L_\parallel/L_\perp = 1$. In fact, this occurs close to $L_\parallel/L_\perp = 30/40$, placing the $L_\parallel = 40$ nm, $L_\perp = 30$ nm layout as the best suited for achieving both readout and manipulation regimes.

The simple model in equation 5.4 also allows us to explore very easily the two-parameter space spanned by V_J and V_{bg}. In Figure 5.4 we plot the maps for $\tau_\parallel$ (first row) and $\tau_\perp$ (second row) obtained from the fitting of equation 5.5. We show the maps for the same $L_\parallel/L_\perp$ ratios discussed above. The dashed lines outline $\tau = 10^{-2}$ μeV, solid lines outline $\tau = 10^{1}$ μeV, and we assume a difference of three orders of magnitude in τ sufficient to open/close the barrier. Tunnel couplings increase from the bottom-left to the upper-right corner. We can identify manipulation region as the area where $\tau_\parallel > 10^{1}$ μeV and $\tau_\perp, \tau_d < 10^{-2}$ μeV, which on the first rows of Figure 5.4 corresponds to the area at the right of the solid green line, and at the left of the brown and orange dashed lines. In line with the previous discussion in terms of α's and r_i's, we can only identify such an area in the range of voltages explored here for the $L_\parallel = 40$ nm,

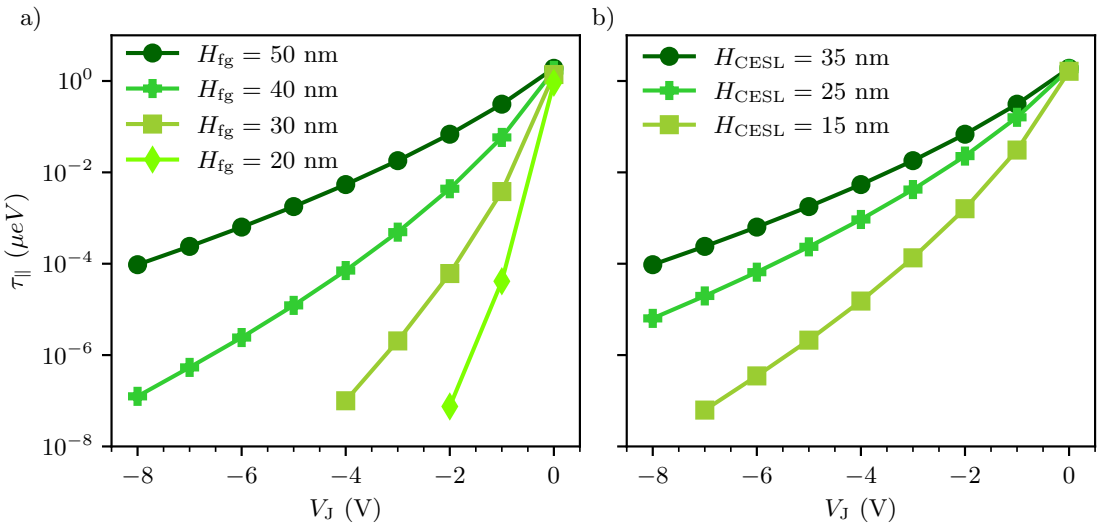

Figure 5.5: a) Dependence of the parallel coupling tunability by the J-gates on the thickness of the front gates. b) Same for the thickness of the CESL layer.

$L_\perp = 30$ nm layout. Similarly, we can locate readout areas by searching where $\tau_\perp > 10^1$ μeV and $\tau_\parallel, \tau_d < 10^{-2}$ μeV, which is on the right of the solid brown line, and on the left of the dashed orange and green lines. Again, in the range of parameters explored here only the $L_\parallel = 40$ nm, $L_\perp = 30$ nm layout shows a reachable readout regime.

Note that the slopes of the iso-lines highlighted in Figure 5.4 are proportional to $1/r_i$. Consequently, the condition of r_d being in between $r_\parallel$ and $r_\perp$ becomes also evident when analyzing the 2D maps. An example of this is $L_\parallel = 30$ nm, $L_\perp = 40$ nm in Figure 5.4, where readout is not reachable because $\tau_\parallel$ can only be closed while keeping $\tau_\perp = 10^1$ μeV at the top left corner of the 2D map, and $\tau_d = 10^{-2}$ μeV, in a larger scale, would cross the $\tau_\perp = 10^1$ iso-line in the bottom right area. Therefore, the three conditions are not reachable at the same time.

In view of these results, we advised to design gate layouts with different $L_\parallel$ and $L_\perp$ to ensure the proper control of the tunnel rates. In particular, one should prioritize $L_\parallel > L_\perp$, since $r_\parallel$ and $r_\perp$ become equal at $L_\parallel < L_\perp$. There are alternatives to deal with τ_d if it cannot be totally suppressed by means of J- and back gate corrections, such as detuning the readout dots from the qubits when manipulating, and detuning the neighbor qubits when performing readout. We would lose, however, the possibility to do readout in parallel for all the qubits in the array. In any case, it is indispensable to have independent control on $\tau_\parallel$ and $\tau_\perp$, so the conclusions stated above remain crucial.

5.1.4 Efficiency optimization

The screening produced by the front gates, responsible for the J-gates selectivity, also explains why the absolute values of $\alpha_{J,i}$ are so small, thus why so large bias corrections are needed to tune the couplings. Larger inter-gate distances would help to increase the J-gates efficiency, yet such approach is limited since the qubits would also be moved apart. Similarly, the screening is strongly dependent on the front gates thickness (H_{fg}). In Figure 5.5a we plot how the dependence of $\tau_\parallel$ on V_J is impacted by H_{fg}. We can qualitatively observe how $\alpha_{J,\parallel}$ drastically increases when

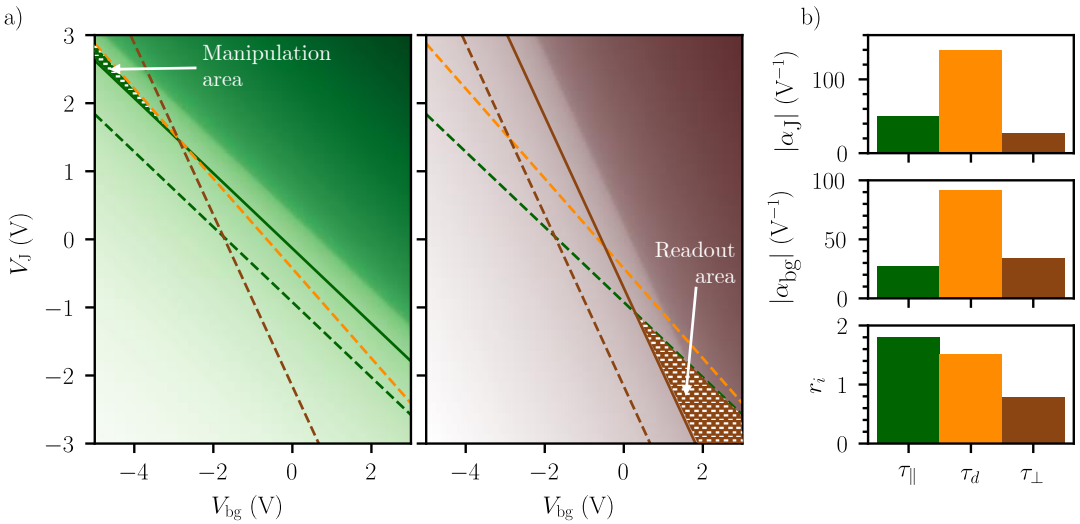

Figure 5.6: Properties of a device with optimized geometry. a) Tunnel maps for $\tau_\parallel$ (left panel) and $\tau_\perp$ (right panel). Color code as in Figure 5.4. b) Efficiency and selectivity on the control of $\tau_\parallel$ (green), $\tau_\perp$ (brown), and τ_d (orange) with the back gate and the J-gates.

the thickness of the front gates, and therefore the screening, is reduced. We also evaluated the impact of the CESL thickness (H_{CESL}), see Figure 5.5b, which is significantly weaker. Indeed, the increase of efficiency due to a reduction of H_{CESL} comes merely from the reduction of the distance between the Si nanowire and the J-gates, while the reduction of H_{fg} implies as well a reduction of the volume suffering from screening. The message conveyed to the fabrication team was, consequently, that efforts must be concentrated on reducing H_{fg} to the fullest extent to enhance the efficiency of the J-gates.

5.1.5 Figures of merit of an optimal layout

Taking into account all the conclusions stated previously, we illustrate here the figures of merit of a device with optimal dimensions for the tunnel control, yet feasible with the present fabrication process. We stick to a 70 nm wide nanowire with $L_\parallel = 40$ nm, $L_\perp = 30$ nm. We reduce H_{fg} to 30 nm, still achievable experimentally; and even though it is not the most important parameter, we reduce H_{CESL} to 25 nm, since this can be realized without much inconvenient. The results for this geometry are shown in Figure 5.6.

In Figure 5.6a we can see that significantly smaller shifts of V_J are required to turn from manipulation to readout than those observed in Figure 5.4. More precisely, biases of 3 V should be sufficient. This owes to the increase of α_J, see Figure 5.6b. Since the back gate efficiency remains essentially the same, r_i are increased. This geometry delivers tight enough control on the tunnel couplings so as to perform two-qubit operations in such a 1D array of spin qubits.

5.1.6 Experimental results

All the findings discussed in the previous sections guided the fabrication of the new LETI devices towards a more optimal gate layout. Here we discuss and illustrate the actions that were taken

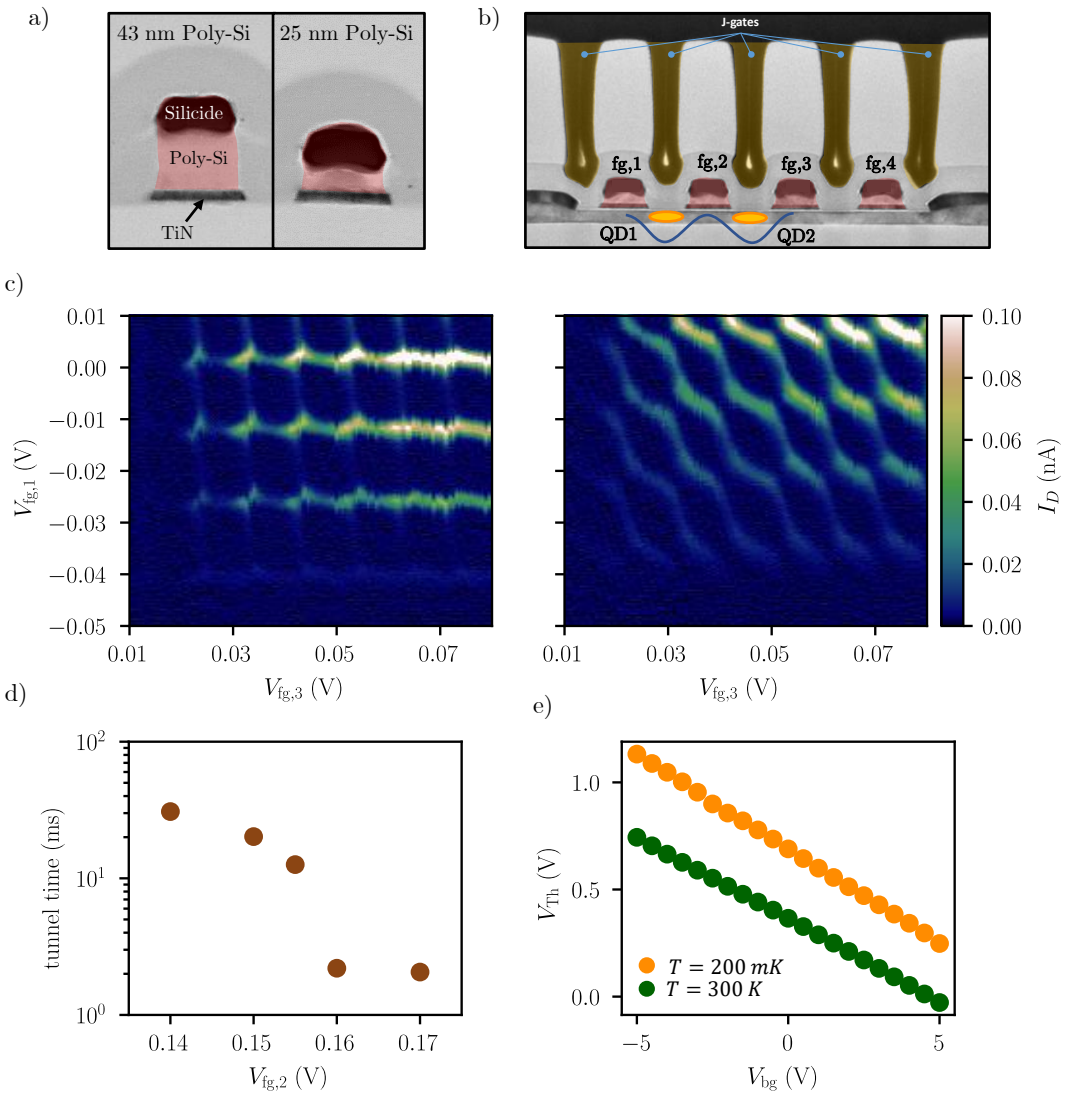

Figure 5.7: a) False-colored TEM image of a cross section of front gates with different thickness. b) False-colored TEM image of a cross section of a device with J-gates. c) Charge stability diagrams of the double QD shown in b) for $V_{fg,2} = 50$ mV (left) and 90 mV (right). d) Tunnel time dependence on $V_{fg,2}$, extracted from the time-average of the tunnel events at the charge anticrossing. e) Threshold voltage V_{Th} dependence on the back gate voltage V_{bg} at 200 mK and 300 K for a device with a tunable metallic back gate.

by the fabrication team as a result of the numerical simulations. To enhance the efficiency of the J-gates, the polysilicon layer of the front gates has been thinned down. Figure 5.7a shows an example of a Transmission Electron Microscopy (TEM) image of the cross section of two front gates with different thicknesses, with a 18 nm reduction of the polysilicon thickness in this case. A device including J-gates is shown in Figure 5.7b. In the preliminary experiments performed so far, the double QD system is operated in a slightly different way than what we have simulated. The two QDs are formed below the J-gates, and only the front gates are tuned

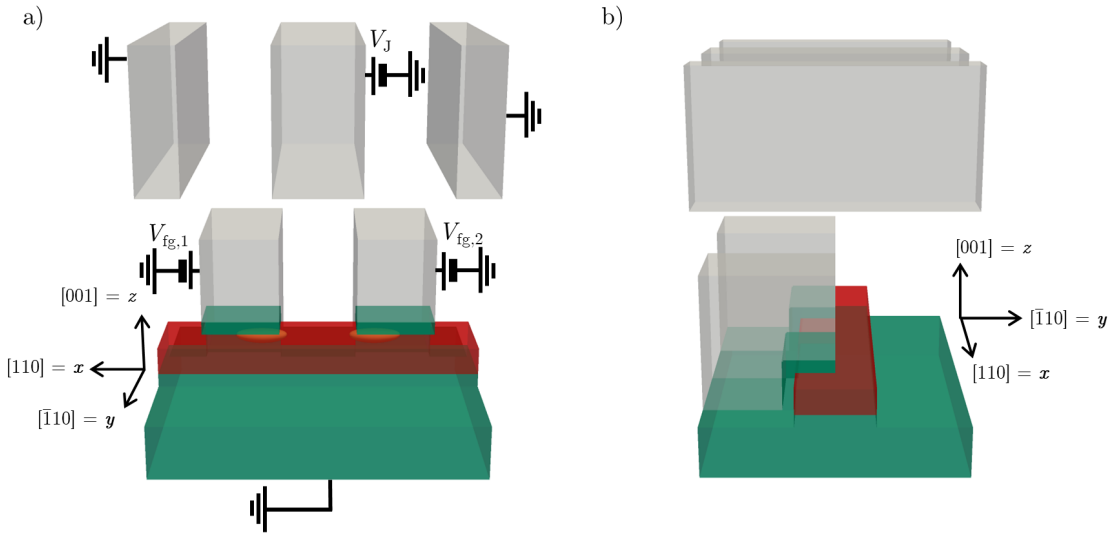

Figure 5.8: Two-qubit device used for the quantification of the two-qubit variability of electron and hole spin qubits. a) 3D representation of the simulated device. A pair of front gates define the double QD system, and the tunnel coupling can be controlled with a J-gate lying above. Silicon is represented in red, SiO_2 and BOX in green, and the metallic front and J-gates in grey. An example of a ground state electron wavefunction of the double QD system is shown in orange. The encapsulating SiO_2 and Si_3N_4 have been removed for clarity. b) Different orientation of the device in a).

during the experiment to control the charge occupancy (with $V_{fg,1}$ and $V_{fg,3}$) and the tunnel coupling (with $V_{fg,2}$). Such a configuration overcomes the large V_J shifts needed to open/close τ that simulations predicted by tuning only V_{fg} during the experiments, since the lever-arm of the front gates is significantly larger. A potential drawback is, however, a stronger charge noise due to charge traps in the Si_3N_4 spacer between the J-gates and the Si channel. The QD is more sensitive to them than when it is located below the front gate that screens their action.

The charge stability diagrams of the double QD system for different $V_{fg,2}$ are shown in Figure 5.7c. They illustrate the ability to control the charge occupancy of the two QDs by playing with the two side front gates. Moreover, we can also see that the charge-transition lines are essentially vertical at $V_{fg,2} = 50$ mV, and they are considerably tilted at $V_{fg,2} = 90$ mV. This is a clear signature of an increase of the tunnel coupling. We can even estimate the tunneling time if we sit at a charge anticrossing and we track the time trace of the tunneling events. This is shown for different $V_{fg,2}$ in Figure 5.7d, which indeed confirms that such configuration allows a tunnel-coupling tunability of more than one order of magnitude for gate voltage shifts of 30 mV.

Finally, an important requirement for the manipulation of 1D devices with a face-to-face gate architecture was to include an effective, tunable back gate. Efforts have been made in this direction experimentally, and the deposition of a metallic back gate as a postprocessing step after drilling a hole at the bottom of the Silicon substrate is being implemented and tested. Preliminary results are shown in Figure 5.7e, where a device with a metallic back gate is used as a transistor, and its threshold voltage (V_{Th}) is extracted for different V_{bg}. The observed tunability of V_{Th} with V_{bg} indicates that the fabrication process works, that the back gate is

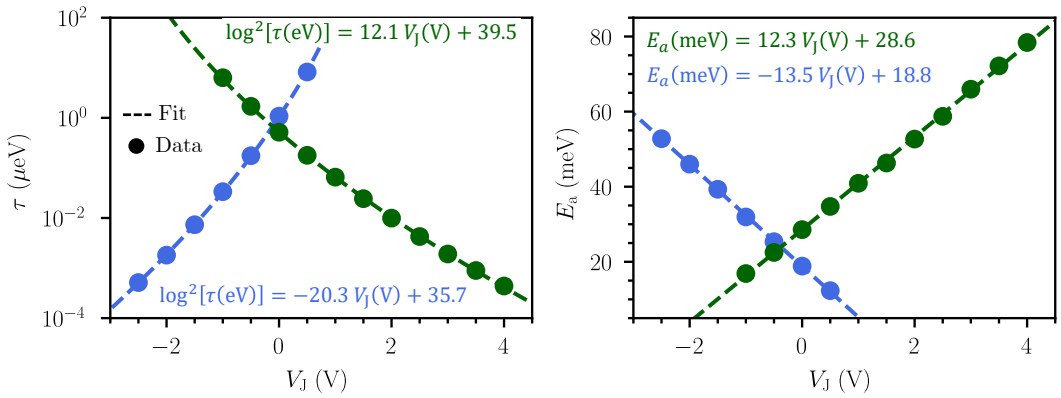

Figure 5.9: Fits of the ideal-device dependence of t and E_a on V_J used for the extraction of ΔV_J and ΔE_a for the defective devices. a) Fit of $\log^2(t)$ vs. V_J for electrons (in blue) and holes (in green). Inset expressions give the fitting parameters. a) Fit of E_a vs. V_J for electrons (in blue) and holes (in green). Inset expressions give the fitting parameters.

correctly connected, that there is no charge leakage, and that it has an electrostatic control over the channel. The testing of these back gates for QDs remains to be tackled, yet the results so far are promising, and effective back gates may be present in LETI devices in the near future.

5.2 Variability in two-qubit properties

Scalable and industrially-compatible Si MOS devices with a proper control of the tunnel coupling between qubits seem to start becoming a reality, yet this raises the question of what will be the impact of disorder on two-qubit gates. As discussed in Chapter 4, a poor quality of the Si channel interface may have a strong impact on one-qubit properties. In particular, as shown in Figure 4.7e, the presence of charge traps may strongly displace the QDs. While manageable for single qubits, a variability in the QD position can be critical for a two-qubit system, since it will translate in large variations of τ. In this section we address the quantification of variability for two-qubit operations due to charge traps at the Si/SiO_2 interface of a Si MOS device, including J-gates as a control for τ, for both electron and hole spin qubits.

5.2.1 Device and methodology

For the simulation of the two-qubit system, we use a device with the same geometry shown in Figure 5.1a, yet we do not include the front gates forming the 1D array of readout dots for simplicity. An illustration of this geometry can be found in Figure 5.8. We form the double QD system with a pair of front gates $V_{fg,1}$, $V_{fg,2}$, and control $\tau_{||}$ with the J-gates. As $\tau_{||}$ is the only tunnel coupling in this system, we refer to it simply as τ hereafter. The Si nanowire is $H = 10$ nm thick and $W = 30$ nm wide, with a gate overlap of 15 nm. The BOX is 25 nm thick, and the J-gates are placed 65 nm above the Si channel. The front gates are $H_{fg} = 30$ nm thick, and $H_{CESL} = 25$ nm. We impose a charge trap density $n_i = 5 \times 10^{10}$ cm^{-1}, we stay in the single-particle case, and extract the variability of the SP tunneling τ on sets of 500 random

	$\overline{\Delta V}_{\text{fg}}$	$\overline{\Delta E}$	$\overline{\Delta V}_{\text{J}}$	$\overline{\Delta E}_a$	$\sigma(\Delta V_{\text{fg}})$	$\sigma(\Delta E)$	$\sigma(\Delta V_{\text{J}})$	$\sigma(\Delta E_a)$
Electrons	-4.59	3.29	362.46	-4.91	11.35	8.15	886.45	12.01
Holes	4.38	-3.29	-400.50	-4.95	12.73	9.54	1363.40	16.81

Table 5.1: Averages and standard deviations of ΔV_{fg} and ΔV_{J} (in mV), ΔE and ΔE_a (in meV) for electrons and holes.

realizations of disorder. We select the pristine device at $V_{\text{fg},1} = V_{\text{fg},2} = 50$ mV (-50 mV) for holes (electrons),[3] we ensure that $\tau < 10^{-3}$ μeV with the lateral J-gates, and set the central J-gate so as to have $\tau_0 = 10$ μeV. The system is therefore at the (0,1)-(1,0) anticrossing, with reference ground state energy E_0 and tunnel coupling τ_0.

Disorder will detune the system away from the anticrossing, and shift its energy and tunnel coupling. To quantify its impact, we extract the gate corrections (ΔV_i) needed to retune the system to the reference situation, and compute their average, $\overline{\Delta V}_i$, and standard deviation, $\sigma(\Delta V_i)$.[4] We provide here a qualitative description of the methodology, yet an extended discussion is given in Appendix B.1. We apply three types of gate corrections aiming to fulfill three conditions: to be at the center of the (1,0)-(0-1) anticrossing, and to achieve the same ground state energy (E) and tunnel coupling (τ) as that of a reference device (E_0, τ_0). To seek the anticrossing, we apply gate corrections of the type $\Delta V_{\text{fg},1} = -\Delta V_{\text{fg},2}$. This effectively acts on the detuning between QDs, eventually reaching the tuned condition. To reach $E = E_0$, we apply the same bias correction at both front gates $\Delta V_{\text{fg},1} = \Delta V_{\text{fg},2}$, which mainly shifts the energy of the two-qubit system. Finally, to reach $\tau = \tau_0$, we pulse the central J-gate by ΔV_{J}. Due to disorder, each individual correction does not leave the other conditions invariant,[5] and we need to apply them iteratively until convergence is reached.

Unfortunately, the extrapolations to reach $\tau = \tau_0$ did not work due to the strength of the variability (see Appendix B.2 for more details), and we used this algorithm only to find the anticrossing with energy $E = E_0$. We then keep track of the scattering of τ, and we translate it into an approximate ΔV_{J} using the linear fits of $\log^2(\tau)$ vs. V_{J} for the pristine device, see Figure 5.9b. Moreover, if the statistics are converged, $\overline{\Delta V}_{\text{fg},1} = \overline{\Delta V}_{\text{fg},2}$ and $\sigma(\Delta V_{\text{fg},1}) = \sigma(\Delta V_{\text{fg},2})$, so we define ΔV_{fg} as a superset that includes $[\Delta V_{\text{fg},1}, \Delta V_{\text{fg},2}]$ and we only keep track of ΔV_{fg} and ΔV_{J}.

Additionally, the gate voltage corrections are not the best property to use when comparing the strength of disorder between different device layouts, as they depend on the gate lever-arms. Consequently, we may want to transform them into the actual shifts in ground state energy E induced to the individual QD (for ΔV_{fg}), and into the shift in barrier of potential E_a between qubits (for ΔV_{J}). We achieve the former by using the lever-arm of the pristine device $\alpha^0_{\text{fg},1} = \alpha^0_{\text{fg},2} = \alpha^0_{\text{fg}}$ to compute $\Delta E = \alpha^0_{\text{fg}} \Delta V_{\text{fg}}$, with $\alpha^0_{\text{fg}} = 0.72$ for electrons and 0.75 for holes; and we extract E_a from the linear fit of its dependence on V_{J} for the pristine device as well (see Figure 5.9b). With this model, we assume that only the front gate above the QD controls its energy, and only the J-gate controls the tunnel coupling. Although a more accurate model

[3] The reference pristine device includes a uniform charge trap density of 5×10^{10} cm^{-1}.

[4] As for the single-qubit properties, we make use of the bootstrap method to ensure the robustness of the statistics.

[5] Disorder breaks the device symmetry, the lever-arms of the front gates are not equal anymore, and modulations of the J-gate also modify the detuning. Consequently, the system is shifted from the (1,0)-(0,1) anticrossing when τ and E are corrected.

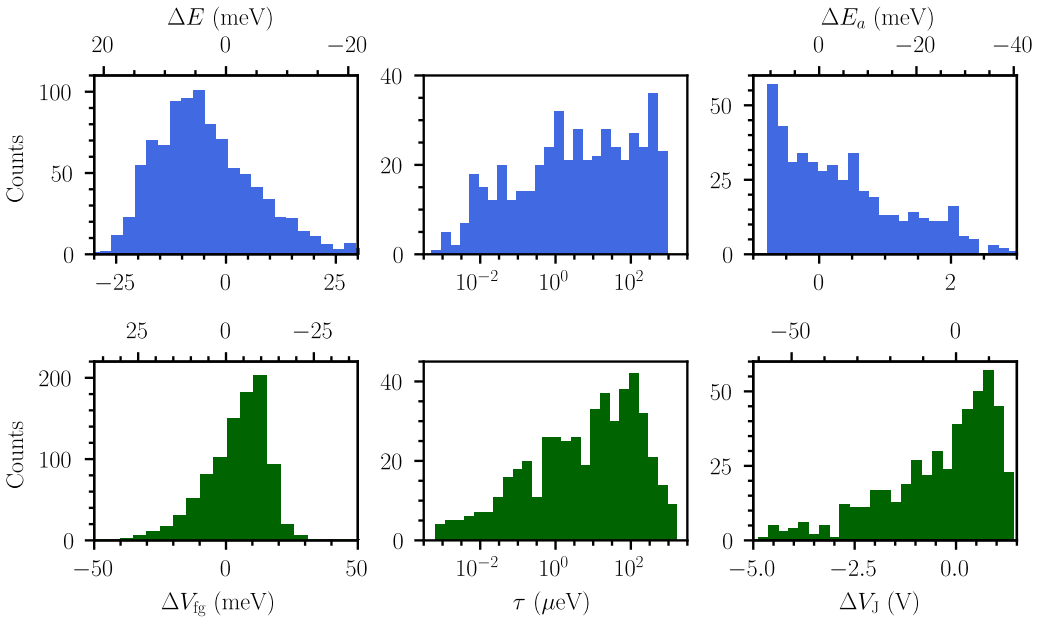

Figure 5.10: Distribution of the front gate corrections ΔV_{fg}, τ, and J-gate corrections ΔV_{J} for electrons (in blue) and holes (in green). Top x-axes show the equivalent energy shift ΔE computed using the ideal device lever-arm $\alpha_{\text{fg}}^{0,e} = 0.72$ for electrons and $\alpha_{\text{fg}}^{0,h} = 0.75$ for holes, and barrier height shift ΔE_a extracted using the fits given in Figure 5.9.

would be $\Delta E = \alpha_{\text{fg},1}^0 \Delta V_{\text{fg},1} + \alpha_{\text{fg},2}^0 \Delta V_{\text{fg},2} + \alpha_{\text{J}}^0 \Delta V_{\text{J}}$, the small lever-arms of the neighboring front gate and J-gate leaves the considered term as the most relevant one.

In summary, we collect statistics on the gate corrections ΔV_{fg} and ΔV_{J}, and on the scattering of the qubits ground state energy ΔE and energy barrier ΔE_a, due to charge traps for electron and hole two-qubit systems. We then compute their averages and standard deviations, and discuss to what extent charge traps can compromise two-qubit operations in Si MOS devices.

5.2.2 Results and discussion

The distribution of ΔV_{fg}, τ, and ΔV_{J} for electrons and holes are shown in Figure 5.10, where the upper axis of the figures illustrates the corresponding ΔE and ΔE_a; and Table 5.1 shows the statistical properties of these distributions. Results are similar for electrons and holes, showing no advantage on using one over the other. The minor differences likely result, as for the single-qubit properties, from the slightly different effective masses. The scattering of ΔV_{fg} spans an interval of roughly 60-70 mV, which translates to an interval of ΔE of 40-50 meV.[6] Note that the charging energy of these devices is typically around 10 meV for the second electron. In terms of gate corrections, $\sigma(\Delta V_{\text{fg}}) \approx 12$ mV, which highlights that very heterogeneous V_{fg} would be needed for each qubit to reach a 1D array with uniform chemical potential. The distribution of τ spans over four orders of magnitude, which suggests that, if it is not characterized and corrected for each pair of qubits, two-qubit operations relying on exchange are completely unfeasible. $\overline{\Delta E}_a$

[6] With the current model, we assume a fixed lever-arm. In reality, there may be a variability in α_{fg} as well. The interval of ΔE computed here is in fact an "effective" interval, as it includes the effect of $\sigma(\alpha_{\text{fg}})$.

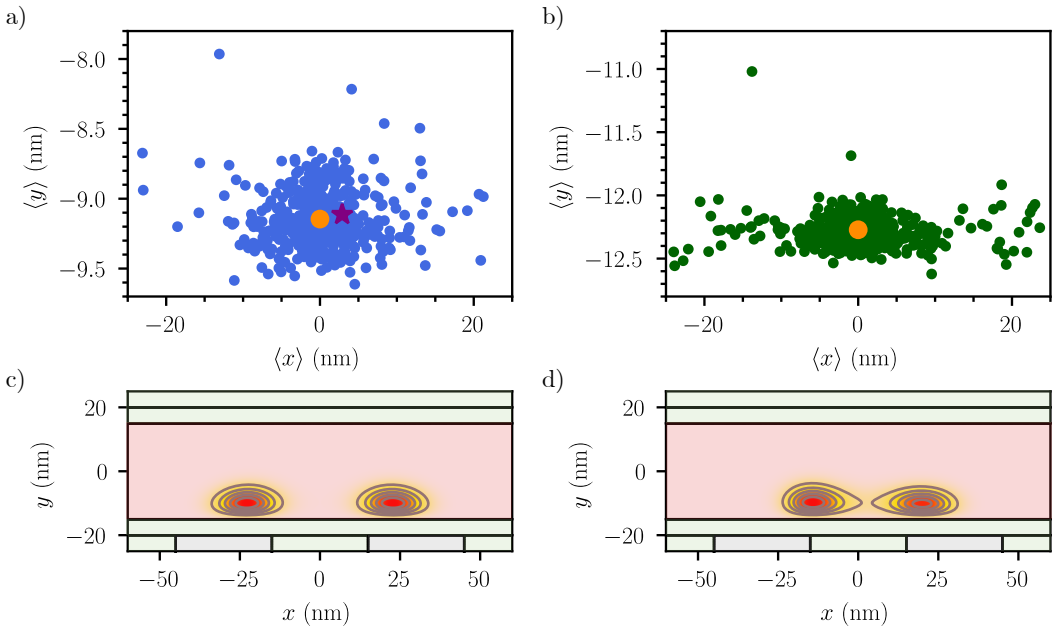

Figure 5.11: Variability in the double QD position. a) Average position in the $(\boldsymbol{xy})$ plane of the double QD system for electrons. Orange point denotes the ideal device, whereas purple star shows the device whose ground state wavefunction is plotted in d). b) Average position in the $(\boldsymbol{xy})$ plane of the double QD system for holes. Orange point denotes the ideal device. c) Cross-section of the ground state wavefunction for the electrons' pristine device. d) Cross-section of the ground state wavefunction for a particular realization of disorder in an electron device.

is negative for both electrons and holes, showing that charge traps tend in average to reduce the tunnel coupling between QDs. Moreover, the corrections of V_{J} that would be needed to re-tune τ to the reference τ_0 are again very large, with $\sigma(\Delta V_{\mathrm{J}})$ above 0.8 V. It is clear, then, that for two-qubit systems in Si MOS devices the energy scales of the fluctuations due to disorder are larger than the energy scales of the qubits themselves, which may strongly compromise the management of two-qubit operations.

As we already anticipated in Chapter 4, the main problem compromising the two-qubit properties is the variability in the QD position. Figure 5.11a and 5.11b show the average position of the double QD system for the individual realizations of disorder for electrons and holes, respectively. The scattering is large, especially along $\boldsymbol{x}$. Note that, in the simulated device, the front gates span from $x = +(-)15$ nm to $x = +(-)35$ nm, so those cases where $|\langle x\rangle| > 7.5$ nm are likely to involve QDs with large misalignments with respect to the gates above. Large displacements of the position of the two-qubit system cause strong modulations of τ, which increases when the two qubits get closer, and decreases when they are split apart. Indeed, we recover a clear correlation between the QD distance, $r(\mathrm{QD}_1, \mathrm{QD}_2)$, and τ in Figure 5.12a, showing that this is clearly key in compromising the two-qubit operations. Figure 5.11c and 5.11d show a cross section of the system ground state wavefunction for the pristine and a defective device, which exemplify the discussed modulation of $\langle x\rangle$ due to disorder.

We may now wonder what is the requirement that dominates the gate corrections: reaching $E = E_0$ or tuning the two-qubit system to the (1,0)-(0,1) anticrossing. To analyze this, we

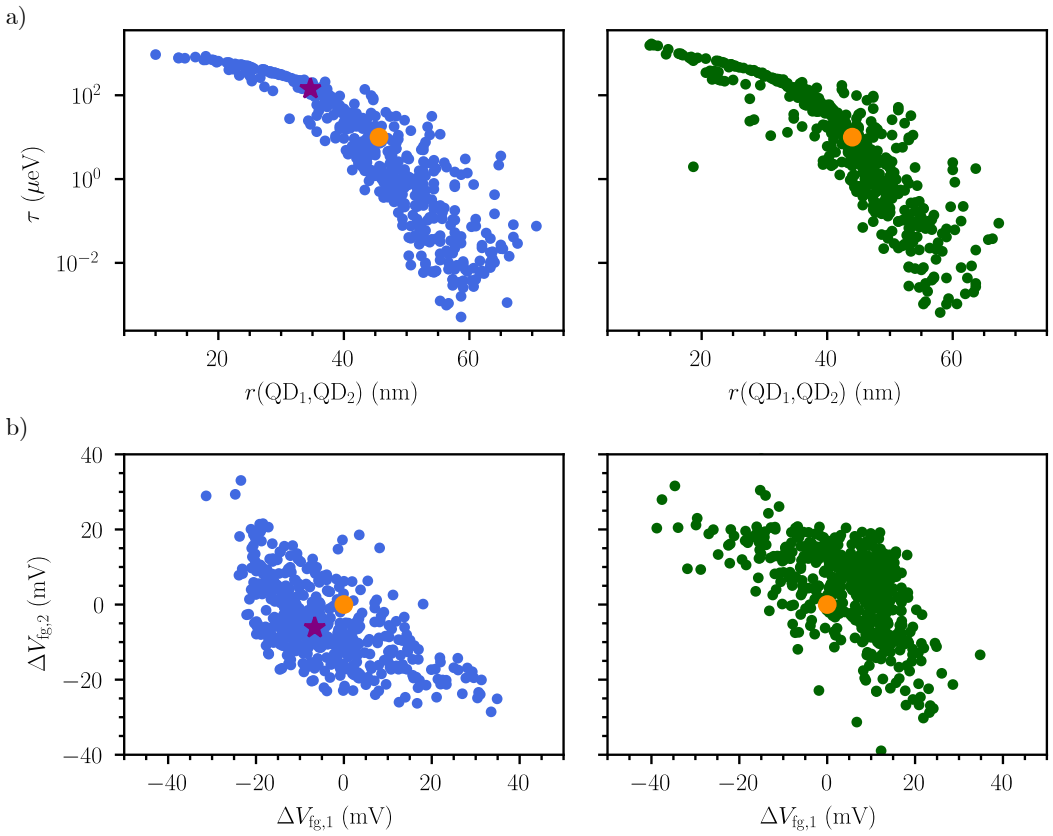

Figure 5.12: Origin of the two-qubit variability. a) Correlation between τ and the distance between the two peaks in the ground state wavefunction of the double QD system for electrons (in blue) and holes (in green). The orange dot denotes the pristine device, whereas the purple star denotes the disordered device from Figure 5.11d. b) Correlation between the gate corrections applied to each front gate for electrons (in blue) and holes (in green).

plot the correlations between $\Delta V_{fg,1}$ and $\Delta V_{fg,2}$ in Figure 5.12b. Note that E is corrected with $\Delta V_{fg,1} = \Delta V_{fg,2}$, while the system is re-tuned to the anticrossing with corrections of $\Delta V_{fg,1} = -\Delta V_{fg,2}$. The anti-correlations shown in Figure 5.12b denote that the dominant corrections are to tune the double QD, which rule over those shifting E.

5.3 Chapter 5 in a nutshell

To achieve a two-qubit operation for spin qubits in industrially-compatible Si MOS devices we need gates dedicated to control the tunnel coupling. These gates are, for the devices fabricated at LETI, a second layer on top of the front gates, and lay several tens of nm above the Si channel. The optimization of the gate layout *via* numerical simulations showed that, if a 1D array of qubits is meant to be operated in parallel, an extra control knob is needed, since the independent tunability of both $\tau_\perp$ and $\tau_\parallel$ cannot be reached only with the J-gates. We proposed a fully-tunable metallic back gate as second tuning parameter. Moreover, the selectivity of the

J-gates is actually determined by the ratio of the space between face-to-face and parallel gates, $L_{\parallel}/L_{\perp}$, being $L_{\parallel} \gg L_{\perp}$ the optimal situation. Their efficiency is strongly compromised by the screening of the first level of gates, so efficient J-gates call for thin and largely-spaced front gates. The ensemble of these findings has been taken into account in the fabrication of the new generation of LETI devices, which should ensure enough tunability of the system to reach readout and two-qubit manipulation regimes with bias shifts of a few Volts in the back and the J-gates. Preliminary experimental results confirm the achievement of the electrostatic control over τ with such devices.

Ideally, the designed Si MOS platform should be suited to host and control large 1D arrays of spin qubits. In practice, however, disorder plays a critical role. We have already seen for the single-qubit properties variability that charge traps can strongly affect the spatial properties of the QDs. Their impact on the two-qubit properties is also critical: we may have to correct for shifts on the qubits' chemical potential of the order of their charging energy, and deal with a scattering of τ spanning over four orders of magnitude. The variability in τ can be traced back to modulations of the QD-QD distance. In Chapter 4 we have also seen that variability for single-qubit properties appears due to modulations of the QD size ℓ_y. Consequently, good scalability requires very similar and reproducible QDs. This may be difficult to reach in Si MOS devices, limited by possibly defective Si/SiO_2 interfaces. Although two-qubit properties variability may still be manageable in few-qubits experiments, the associated difficulties may start to appear as the spin qubits quantum processors continue to grow.

Chapter 6

The Germanium route

Contents

The variability figures we have seen so far presage a critical role of disorder on the viability of spin qubit platforms. Maybe not in the nearest future, yet at some point disorder will become the limiting factor on the growth of the number of qubits in the quantum processors. In fact, Si MOS platforms may be already hitting this wall in the one- and two-qubit devices. Better-suited devices are those with a lower level of disorder, or those where the defective interfaces are far away from the qubits. This is the case of epitaxial heterostructures like Si/SiGe or Ge/SiGe. In such heterostructures, the active layer makes interfaces with materials that have the same crystalline structure, and the proper growth conditions ensure no charge traps and surface roughness as low as some eventual atomic steps. The disorder is in fact shifted a few tens of nanometers above, where there is an interface with an oxide material. The meteoric progress made experimentally in the last years with this kind of devices presages a much better situation in terms of variability. This caught the interest of the experimental groups at CEA, who are already making progress towards the demonstration of Ge/SiGe spin qubits.

The experimental efforts have been mainly focused on the increase of the number of qubits [16, 21–23]. For electrons in Si/SiGe with micro-magnets as source of SOC, the physics is well understood. For holes in Ge/SiGe, the understanding and exploitation of their richer physics is still at an earlier stage. Theoretical work, mainly driven by Loss group, already spotted a variety of opportunities arising from this richness [89, 123], yet things as paramount as the Rabi frequency anisotropy are still not well established.

In this Chapter, we focus on holes in Ge/SiGe heterostructures. We discuss first the f_R anisotropy and estimate the variability one can expect in this kind of devices. We then propose an alternative gate layout that should further improve the variability figures and be an optimal spin qubit platform based on epitaxial heterostructures.

6.1 Physics of Ge/SiGe qubits

6.1.1 A Ge spin qubit device

Spin qubit devices fabrication in Ge/SiGe heterostructures start from a Si substrate as for Si MOS devices. Then, SiGe is grown on top, and due to the non-negligible lattice mismatch between Si and Ge (5.431 Å and 5.658 Å, respectively), the first atomic layers of SiGe experience large biaxial strain (in the 1% range).[1] The magnitude of the strain depends on the proportion x of Si in the Si_xGe_{1-x} layer, with x typically between 0.2-0.3 [22, 23, 124]. Such large strain triggers the formation of dislocation defects as the thickness of the SiGe layer increases, which relax the lattice. Consequently, the SiGe layer is grown thick enough so the structure is eventually free (or almost free) of strain, with a thickness (H_B in Figure 6.1) of a few μm [125]. This leaves a crystalline, defectless support at the top of the SiGe.

With a fully (or almost fully) relaxed SiGe layer, the Ge well grown on top suffers again a biaxial strain. Its thickness is typically $H_L = 15 - 20$ nm [124], and it is again limited by the appearance of dislocations due to strain. Their presence would be severely harmful for the qubits, which are hosted in the Ge layer in this kind of devices (see Figure 6.1). On top of the Ge well, another layer of SiGe is epitaxially grown with a thickness H_T around 50 nm. Since all layers are lattice-matched, the top SiGe layer experiences the same level of strain as the buffer layer underneath.

Such material stack leaves the active Ge layer free of defects. Epitaxial interfaces are known to be free of charge traps, and to present surface roughness with typical rms amplitudes as low as an atomic step and very large correlation lengths. In fact, the defects are shifted up to the top SiGe interface. These devices typically include a few-nm thin Si cap (which oxidizes to SiO_2) on top of the SiGe followed by Al_2O_3, which yields to positive charge trap densities possibly above 10^{11} cm^{-2} at the SiGe/oxide interface [126]. In the modelled device, we do not include the Si cap for simplicity. The cleanness of devices based on epitaxial interfaces is patent in the measured mobilities. They are typically a few orders of magnitude higher than those measured in SOI-based devices [127], which cannot be explained only in terms of the smaller effective masses of Ge.

The metallic gates lay above the top SiGe interface. In the results discussed hereafter we emulate the gate layouts fabricated at TU Delft [22, 23, 125, 128]. In particular, we model the device from Ref. [22] (see Figure 6.1). In the simulations, however, we form a single qubit under the circular plunger gate P_1, which is surrounded by rectangular lateral gates B_1, B_2, B_3, B_4. The unit cell also includes the second plunger gate P_2, which in our simulations does not host any qubit, yet it is included to mimic the electrical environment of the experiments. We copy the system parameters from the experiment: $D_P = 100$ nm, $T_B = 40$ nm, $L_B = 100$ nm, $A = 160$ nm, $H_B = 150$ nm, $H_L = 16$ nm, $H_T = 50$ nm, $H_P = 20$ nm, $H_B = 40$ nm, $S_B = 10$ nm.

[1] The lattice parameter of SiGe is in between that of Si and Ge.

Moreover, the top gates are separated from the SiGe/Al_2O_3 interface by 5 nm of oxide. Regarding the strains, a residual biaxial strain of $\varepsilon_{\parallel}(\text{SiGe}) = 0.26\%$, $\varepsilon_{\perp}(\text{SiGe}) = -0.186\%$ is reported in SiGe at the bottom SiGe/Ge interface in the experimental devices [124]. Consequently, the strain in the Ge layer is $\varepsilon_{\parallel}(\text{Ge}) = -0.63\%$, $\varepsilon_{\perp}(\text{Ge}) = 0.441\%$. [2] It is important to recall that Ge, due to its substantially lighter in-plane effective masses, can host QDs of much larger size with respect to Si. This allows to work with considerably larger devices and ease the fabrication processes (note that the gate diameter for the device in Figure 6.1a is 100 nm, whereas typical gate lengths in Si MOS devices are around the 40 nm).

6.1.2 Anisotropies in Ge spin qubits

Ge qubits, due to the large κ and HH-LH splitting induced by strain, have very asymmetric principal g-factors. Several experiments have measured g_z in the range of 9-14, and $g_{\parallel}$ in the 0.1-0.2 range depending on the strain [22, 23, 125, 128, 129]. Indeed, we expect g_z,g_x,g_y = $(-6\kappa, 0, 0)$ in absence of HH-LH mixing, and corrections increasing the in-plane component and decreasing the out-of-plane one when it becomes important [60]. Regarding the Rabi frequency, experiments up-to-now place the magnetic field in-plane to minimize the hyperfine interaction with the nuclear spins [22, 23, 125, 128], yet no systematic information on its dependence on B orientation has been obtained experimentally. From the theory side, a few works in the bibliography discuss the different mechanisms giving rise to Rabi oscillations in Ge qubits. A standard g-TMR contribution may appear due to the modulation of the main g factors. Such term vanishes when $\boldsymbol{B} \parallel \boldsymbol{x}, \boldsymbol{y}, \boldsymbol{z}$. For perfectly isotropic dots and symmetric potentials, it additionally vanishes everywhere in the $(\boldsymbol{xy})$ plane. Moreover, two IZ-EDSR mechanisms have been described in the literature. For circular QDs, a mechanism giving rise to finite f_R appears when the dot is laterally displaced in presence of a vertical electric field [130], the so-called "cubic Rashba SOC". It is maximal when $\boldsymbol{B} \parallel \boldsymbol{z}$, and zero when $\boldsymbol{B}$ is in the $(\boldsymbol{xy})$ plane. Moreover, in Ref. [89] finite f_R are reported when $\boldsymbol{B}$ is in the $(\boldsymbol{xy})$ plane for strongly squeezed QDs, a mechanism known as "1D direct Rashba SOC". The origin behind the experimental Rabi oscillations still remains an open question. The AC drives are typically applied to lateral gates (*e.g.*, to drive the qubit under P_1 in Figure 6.1a, the RF signal is applied to P_2), which should induce an in-plane motion of the QD, thus an IZ-EDSR mechanism. With $\boldsymbol{B}$ in plane and QDs that should be fairly circular (due to the circular shape of the plunger gates), neither 1D Rashba nor cubic Rashba should give rise to finite f_R's. Moreover, unexplained differences between qubits have been observed when driving with different gates [131], which presages a rather complex interplay between g-TMR and IZ-EDSR mechanisms.

With the purpose of clarifying the experimental situation, we model with 6kp simulations a realistic reproduction of the experimental device in Ref. [22] in order to account for its complex electrostatics. We compute the Rabi frequencies for the two-qubit device of Figure 6.1b when driving with different gates so as to explore all the experimental possibilities. We form the QD under gate P_1 by applying $V_{P_1} = -50$ mV, and we detune P_2 by 2 mV. All the other gates are set to 200 mV to mimic the isolation of the qubit under P_1 from its neighbors. We apply the RF drive first with P_1, which should mainly modulate the size of the QD, and give rise to finite f_R due to a standard g-TMR mechanism. Such drive has only been employed

[2] Biaxial strain is ruled by the elastic constants of the material C_{12} and C_{11}, and follows $\varepsilon_{\perp} = -2C_{12}/C_{11}\varepsilon_{\parallel}$. For Ge, $C_{12} = 44$ GPa and $C_{11} = 126$ GPa, and for $Si_{0.2}Ge_{0.8}$ $C_{12} = 48$ GPa and $C_{11} = 134$ GPa.

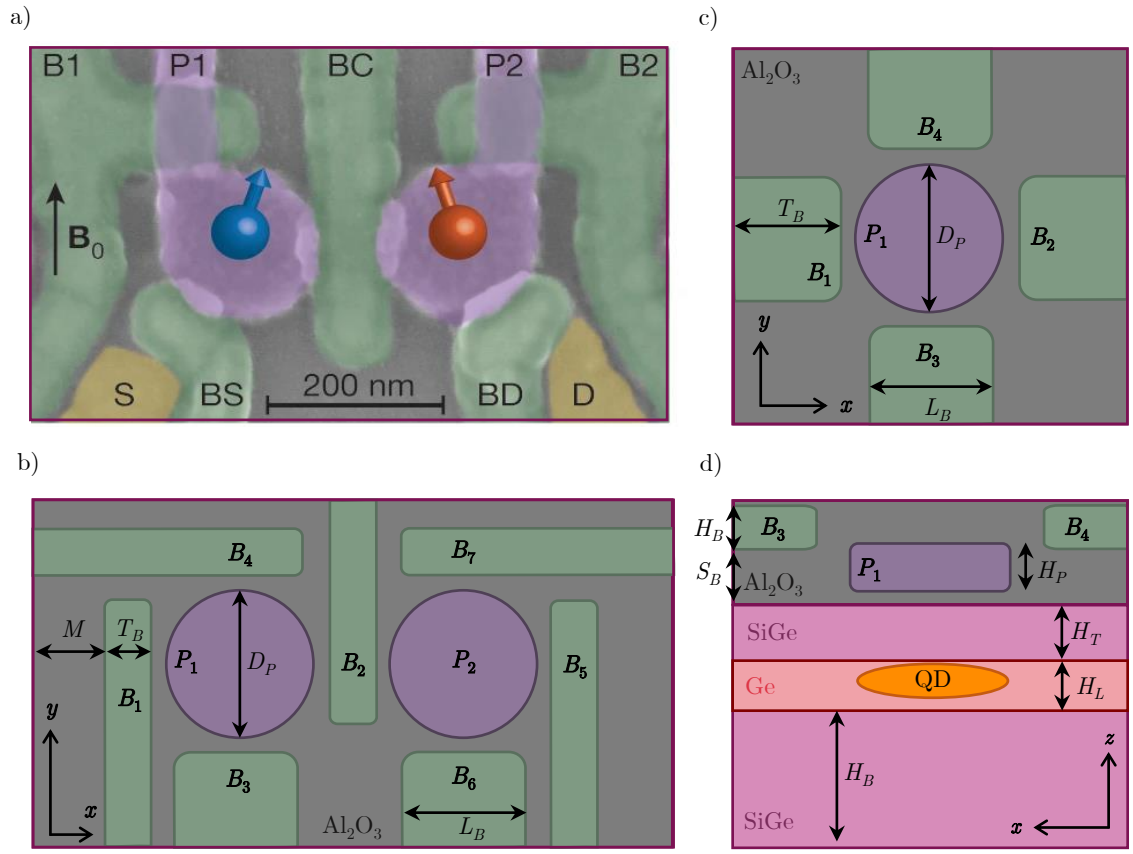

Figure 6.1: Schematic representation of the modelled devices. a) False-colored scanning electron micrograph picture of the two-qubit device of Ref. [22]. b) Top view of the gate layout of the simulated double QD device. The gate layout is formed by two plunger gate P_1 and P_2 (in purple) with diameter D_P, surrounded by rectangular lateral gates B_1, B_2, B_4, B_5 and B_7 (in green) of width T_B; and B_3, B_6 (in green) of width L_B. c) Top view of the gate layout of the simulated single QD device. A plunger gate P_1 (in purple) with diameter D_P is surrounded by lateral gates B_1, B_2, B_3, B_4 (in green) with width L_B. d) Cross-section in the $(\boldsymbol{xz})$ plane of the device in c). A strained Ge layer of thickness H_L (in pink) lays in between two SiGe layers of thickness H_B and H_T (in purple). On top of it, two levels of metallic gates are embedded in Al_2O_3 (in grey). The simulated devices include a back gate below the lower SiGe layer.

experimentally in some of the qubits from Ref. [131]. We also consider driving on B_1 and B_2 with opposite modulation, which should induce an in-plane motion of the QD. This drive gathers the ingredients needed for the exploitation of cubic Rashba (and 1D Rashba if the QDs are anisotropic). Finally, we drive with P_2, which mimics what is done experimentally in most of the cases [22, 23, 128]. In Figure 6.2 we plot the f_R anisotropy for the three mentioned cases. We show it at constant $B = 1$ T and at constant f_L. The simulated g factors for this device are $g_z = 12.814$, $g_x = 0.073$, $g_y = 0.112$,[3] so $B = 1$ T out-of-plane would yield to unmanageable

[3]Due to the asymmetries of the potential, the QD is slightly anisotropic, with $\ell_x = 12.85$ nm, $\ell_y = 12.10$ nm.

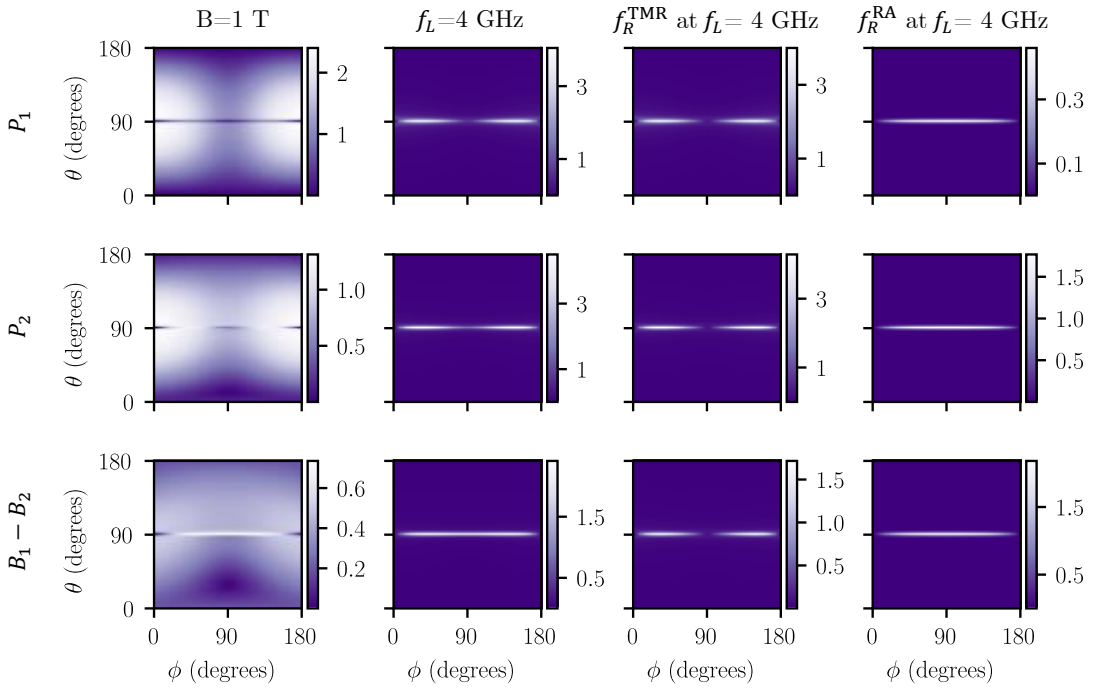

Figure 6.2: Rabi frequency anisotropy with the orientation of the magnetic field for the two-cell device shown in Figure 6.1. The RF voltage driving the spin is applied to P_1 (first row), P_2 (second row), and to B_1 and B_2 with a π phase shift (third row). The maps are computed at constant $B = 1$ T (first column), and constant $f_L = 4$ GHz (second column). The third and fourth column show the anisotropy of f_R contributions coming from the modulation of the principal g-factors (TMR) and from the rotation of the magnetic and spin axes of the g-matrix, respectively. f_R is in MHz and normalized for a $V_{\mathrm{ac}} = 1$ mV.

$f_L \approx 180$ GHz (experiments have technical constraints and are typically limited to $f_L <$ 15-20 GHz). Therefore, the maps at constant f_L give a better overview of the f_R anisotropy that can be explored experimentally. These are shown in the second column of Figure 6.3. We also split f_R into two contributions: f_R^{TMR} gathers the modulation of the principal g-factors, and accounts for the standard g-TMR mechanism. In f_R^{RA}, we include the rotation of the magnetic and spin axes of the $\hat{g}$ matrix induced by the drive. Such contribution includes the Rashba-type terms giving rise to IZ-EDSR, yet it may also include non-conventional g-TMR mechanisms appearing due to the rotation of the magnetic axes of $\hat{g}$. Consequently, f_R^{RA} is not a pure Iso-Zeeman (IZ) term. More details about this decomposition are given in Appendix A.1.

The anisotropy map at constant B when the RF drive is applied to P_1 does indeed resemble that of g-TMR [58–60], with f_R vanishing when $\boldsymbol{B}$ is parallel to $\boldsymbol{x}$, $\boldsymbol{y}$, or $\boldsymbol{z}$, and being maximal near $\theta = 45\,^\circ$, $\phi = 0\,^\circ$. However, the large anisotropy of g^* completely reshapes the map when it is plotted at constant f_L, and the maximum appears then in-plane. Since $f_R \propto B$ and $f_L \propto g^* B$, plotting the map at constant f_L reduces f_R in the areas where g^* is large, and enhances it where g^* is small. Indeed, we observe this renormalization in the maps at fixed f_L of Figure 6.2. In fact, due to the large g^* anisotropy, f_R is largest in-plane at constant f_L regardless of the driving mechanism. The splitting into conventional g-TMR and rotations of the $\hat{g}$ matrix axes (f_R^{RA})

shows that, as expected, f_R's driven with P_1 are dominated by the former contribution. The fact that f_R only vanishes at $\boldsymbol{B} \parallel \boldsymbol{x}$ or $\boldsymbol{y}$ and not everywhere at the $(\boldsymbol{xy})$ plane is a signature of an anisotropic potential. The finite in-plane f_R when driving with P_1 is in line with the observations in Ref. [131].

Interestingly, when the system is driven with opposite modulation on B_1 and B_2, the map shows an unexpected shape. As discussed above, for a cubic Rashba mechanism, f_R is expected to be maximal for $\boldsymbol{B} \parallel \boldsymbol{x}$, and zero when B is in-plane [60, 130]. In the simulated map, however, it is in-plane where the maximal f_R is obtained (both at constant B and constant f_L). Such trend cannot come from a 1D Rashba mechanism either, as the simulated QD remains very isotropic. The splitting into the individual contributions show that part of the in-plane f_R comes from a standard g-TMR mechanism, analogous to what we observed for the P_1 drive. The complexity (and asymmetry) of the real electrostatics indeed yields to a deformation of the QD when it is displaced, which brings a standard g-TMR contribution. Still, the f_R^{RA} term shows unexpected finite in-plane f_R, as large as the TMR term.[4] We discuss the origins of this novel feature in section 6.1.2.1.

When the drive is applied to P_2, the anisotropy is dominated by g-TMR, and it gives very similar features to the drive with P_1. Yet, the same unexpected anisotropy in f_R^{RA} observed when driving with P_2 appears for the $B_1 - B_2$ drive. It even dominates over the pure IZ mechanisms, as we barely see any trace of the cubic Rashba term from Ref. [130].[5] Such results are again consistent with the experimental observations showing finite in-plane f_R when driving with lateral gates [22, 23, 128], which can be attributed to the appearance of strong standard g-TMR contributions.

Regarding the magnitude of the different drives, we see that f_R arising from the drive with P_1 seems more efficient than that of $B_1 - B_2$. Yet, a large part of this difference can be attributed to the different gate lever-arms. f_R is normalized to $V_{\mathrm{ac}} = 1$ mV, yet the effective drive seen by the qubit is renormalized by the smaller lever-arm of B_1, B_2 with respect to P_1 ($\alpha_{B_1} = \alpha_{B_2} = 0.07$, $\alpha_{P_1} = 0.26$). Consequently, the lateral driving is very likely to be the most efficient mechanism if the results are normalized for the same effective drive. Also the comparison of the absolute f_R's with the Si MOS qubits simulated in Chapter 4 must be addressed carefully. Even though results show significantly slower Rabi oscillations for holes in Ge than in Si, a fair comparison must take into account that in Si MOS devices $\alpha_{\mathrm{fg}} \approx 0.7$.

6.1.2.1 Finite in-plane Rabi frequencies for isotropic quantum dots

The complex electrostatics in the experiments appears to be crucial to explain the finite in-plane f_R of the experimental results. They appear to result from a combination of a conventional g-TMR term, plus an unexpected mechanism bringing a rotation of the $\hat{g}$ matrix axes in f_R^{RA} when driving with B_1 or $B_1 - B_2$. In fact, the rotation responsible for this term appears in the magnetic axes of $\hat{g}$ and it does not leave the Zeeman splitting invariant, thus it is also a (non-conventional) g-TMR mechanism.[6] The origin of such term, not explained by the current analytical models, is also found on the complexity of the electrostatics generated by the gate layout. In particular, it finds its origin on the coupling between the in-plane and out-of-plane motion of the QD. To

[4] Note that $f_R = |f_R^{\mathrm{TMR}} + f_R^{\mathrm{RA}}| \neq |f_R^{\mathrm{TMR}}| + |f_R^{\mathrm{RA}}|$, and what is plotted in Figure 6.2 is $|f_R^{\mathrm{TMR}}|$ and $|f_R^{\mathrm{RA}}|$.

[5] We indeed expect g-TMR to be more efficient than IZ-EDSR for a HH [60].

[6] More details on how to split f_R into the different contributions can be found in Appendix A.1.

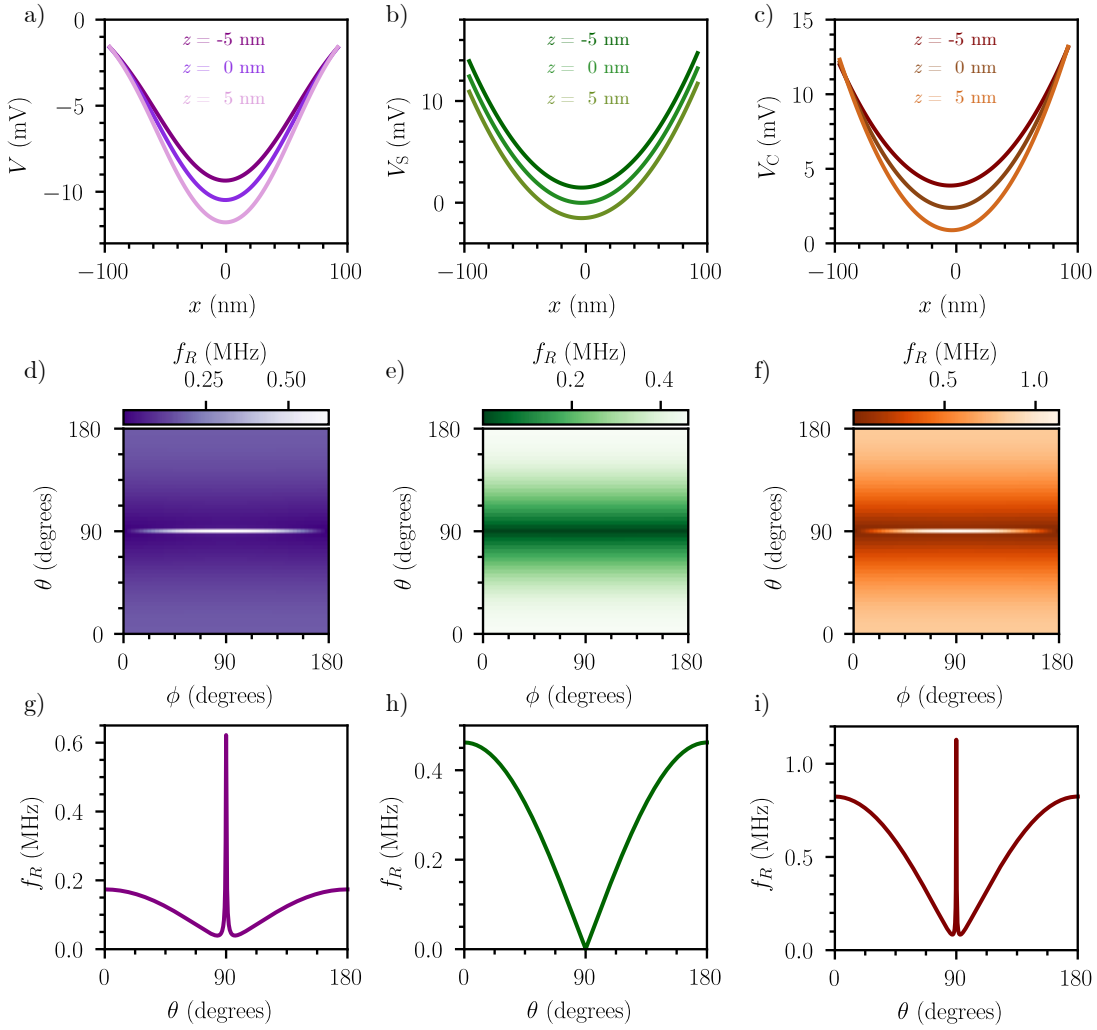

Figure 6.3: Comparison of the results for the realistic and model potentials. a) Potential along $\boldsymbol{x}$ at $x = 5$, 0, and -5 nm resulting from solving Poisson's equation on a single unit cell device as shown in Figure 6.1c with $V_{P_1} = -50$ mV, $V_{B_i} = 10$ mV with $i \in [1, 2, 3, 4]$, and $V_{\text{bg}} = 0$ V. b) Potential along $\boldsymbol{x}$ at $x = 5$, 0, and -5 nm for the model potential in equation 6.1, with $E_z = -0.3$ mV/nm, $z_0 = 0$ nm, $L_y = L_z = 18$ nm. c) Potential along $\boldsymbol{x}$ at $x = 5$, 0, and -5 nm for the model potential in equation 6.2, with $E_z = -0.3$ mV/nm, $z_0 = 8$ nm, $L_y = L_z = 18$ nm, $L_z = -40$ nm. d) Rabi frequency anisotropy with B orientation at constant $B = 1$ T for the realistic potential in a). An opposite modulation of gates B_1 and B_2 with 1 mV amplitude is applied to drive the spin. e) Rabi frequency anisotropy with B orientation at constant $B = 1$ T for the model potential V_{S}. An in-plane oscillatory electric field E_{ac} of amplitude 10 nV/nm is applied to drive the spin. f) Rabi frequency anisotropy with B orientation at constant $B = 1$ T for the model potential V_{C}. An in-plane oscillatory electric field E_{ac} of amplitude 10 nV/nm is applied to drive the spin. g) Cut along $\phi = 90$ degrees of the map in d). h) Same for the map in e). i) Same for the map in f).

illustrate this effect, we simulate now a single-cell device (see Figure 6.1c). In such device, the potential is perfectly symmetric, and f_R^{TMR} is zero when $\boldsymbol{B}$ is in the $(\boldsymbol{xy})$ plane. We perform a $B_1 - B_2$ drive, and we compare the results obtained from solving Poisson's equation with simulations including two model potentials. First, we consider a textbook potential: a parabolic in-plane confinement potential centered at $x = y = 0$, and a constant vertical electric field (E_z),

$$V_{\mathrm{S}}(x, y, z) = E_z(z - z_0) + 2\left(\frac{y^2}{L_y^2} + \frac{x^2}{L_x^2}\right) + xE_{\mathrm{ac}} \tag{6.1}$$

where z_0 is an arbitrary position that sets the reference of potential, L_y and L_z are the confinement lengths of the in-plane confinement potential, and E_{ac} is the in-plane AC drive. In addition, we consider a potential with a term coupling x and y, z,

$$V_{\mathrm{C}} = E_z(z - z_0) + 2\left(\frac{y^2}{L_y^2} + \frac{x^2}{L_x^2}\right)\left(1 - \frac{z - z_0}{L_z}\right) + xE_{\mathrm{ac}} \tag{6.2}$$

where L_z controls the strength of the coupling.

In Figure 6.3, we compare the potential landscape generated by the realistic simulation and the two model potentials and compute the f_R anisotropy maps for each case. For V_{S} we set $E_z = -0.3$ mV/nm, $z_0 = 0$ nm, $L_y = L_z = L_{\parallel} = 18$ nm, and $E_{\mathrm{ac}} = 0.01$ mV/nm; whereas for V_{C} we input $z_0 = 8$ nm, and additionally set $L_z = -40$ nm.[7] This yields to QDs with similar sizes in the realistic and model potentials ($\ell_x = \ell_y = 17.3$, 17.6, 18.6 nm for the realistic potential at $V_{P_1} = -50$ mV, and for the potential without and with coupling, respectively). In Figure 6.1a we do indeed see that in the realistic potential there is a coupling between in-plane and out-of-plane motions due to the non-separability of the potential. Physically, this can be interpreted as a vertical electric field (E_z) that depends on the in-plane position, and brings $V(x, y, z_1) - V(x, y, z_2) \neq V(x', y', z_1) - V(x', y', z_2)$. This feature of the realistic potential is not recovered by V_{S} (see Figure 6.1b). When a coupling term is added, however, the output potential V_{C} does reproduce it (see Figure 6.1c).

The f_R anisotropy map for the textbook potential in equation 6.1 recovers the expected anisotropy for cubic Rashba discussed above: It vanishes in plane, and it is maximal when $\boldsymbol{B} \parallel \boldsymbol{z}$. Remarkably, the model potential with the simple coupling of equation 6.2 is able to reproduce the in-plane maximum of f_R. Although the cubic Rashba contribution is also present, the in-plane feature dominates even at constant magnetic field. The origin of the novel feature is then found on the coupling between in-plane and out-of-plane motions.[8] This also raises an important message: the complexity of the real electrostatics can reshape completely the f_R map, and bring new features that are not accounted, even qualitatively, in the simple potentials typically assumed to model spin qubits [59, 60, 89, 123]. This feature in particular is of vital importance, since it allows the manipulation of spins in perfectly isotropic QDs with $\boldsymbol{B}$ along the direction where the hyperfine interaction and g^* are the smallest. The latter allows to apply larger B and reach larger f_R.[9] In the context of spin-photon coupling, superconducting

[7] z_0, while it is a simple potential shift for V_{S}, plays an important role for V_{C}: The $(\boldsymbol{xy})$ plane is an equipotential plane at $z = L_z - z_0$.

[8] The total potential $V(x, y, z)$ cannot be expressed in the form $V(x, y, z) = V(z) + V(x, y)$.

[9] As we learnt in section 2.5.1.2, the Rabi frequency is proportional to B for hole spin qubits relying on intrinsic SOC to perform EDSR.

resonators see their superconductivity compromised with out-of-plane magnetic fields, so working with B in plane is highly beneficial [132].

We may now try to analyze the behavior of the novel mechanism with respect to the potential parameters, and compare the model potential V_{C} and the realistic potential more in-depth. We track the f_R at $\boldsymbol{B} \parallel \boldsymbol{x}$ and the Full Width Half Maximum (FWHM), which we define as the width of the f_R peak along θ where $f_R = \max(f_R)/2$. Therefore, the FWHM quantifies how narrow is the appearing feature. We analyze the impact of strain, $L_\parallel$ and L_z for the model potential; and strain, V_{P_1} and V_{bg} for the realistic one. Results are shown in Figure 6.4. We observe a strong impact of strain on f_R and FWHM for both realistic and model potentials with coincident trends. The HH-LH splitting (Δ_{HL}) is proportional to the level of strain and to the vertical confinement (through the dependence on ℓ_z),

$$\Delta_{\mathrm{HL}} = \frac{A}{\ell_z^2} + B\varepsilon_\parallel, \tag{6.3}$$

where A and B are two constants, and their expressions can be found in Ref. [60]. It also controls the intensity of SOC effects, as it determines the mixing between HHs and LHs. Reducing the strain, therefore, increases f_R due to the larger SOC. Regarding the impact of the model potential parameters, we observe an increase of f_R with $L_\parallel$. It controls the in-plane confinement, and consequently the QD size. Indeed, a larger dot is more polarizable, and its response to the AC drive is stronger, thus f_R is larger. L_z tunes the strength of the coupling between in-plane and out-of-plane motions. When $|L_z| \to \infty$, the coupling vanishes, and we fall back to V_{S}. We indeed observe this behavior in the computed data, where the in-plane f_R clearly decreases when L_z increases.

For the realistic potential, the results are shown in Figure 6.5b, and the situation is more complex. V_{P_1} is the available knob to control $\ell_\parallel$ and it should behave rather equivalently to $L_\parallel$ in V_{C}, yet when we increase $|V_{P_1}|$ to reduce $\ell_\parallel$ we also reduce ℓ_z and thus increase Δ_{HL} (if it is not dominated by the strain part). Still, we recover a trend that is consistent with the model potential: The stronger the $|V_{P_1}|$, the smaller the QD, the weaker it responds to the AC field, thus the smaller the f_R is. Similarly, $|V_{\mathrm{bg}}|$ should mainly act as L_z in V_{C}, since it decreases ℓ_z due to the increase of the vertical confinement, and it hinders the vertical motion of the QD. Without vertical motion, the potential becomes again separable, and the features due to the non-separability vanish. Additionally, $|V_{\mathrm{bg}}|$ also impacts $\ell_\parallel$ and Δ_{HL} (through ℓ_z). Nonetheless, we do observe in Figure 6.5b that f_R is maximal when $V_{\mathrm{bg}} \to 0$, which is when we expect the largest ℓ_z and therefore the largest out-of-plane motion.

Regarding the FWHM, we observe that it is extremely small, and it shows a clear correlation with g_x/g_z, see Figure 6.5. The origin of such correlation and of the strongly narrow nature of the in-plane feature can be understood with a very simple model. When we have an interplay between two mechanisms giving rise to Rabi oscillations that are maximal at perpendicular B field orientations, as it is the case for the novel mechanism and the cubic Rashba, we can describe the physics of the system with the following effective Hamiltonian,[10]

$$H_{\mathrm{eff}} = H_0 + (\beta\sigma_1 + \gamma\sigma_3)V_{\mathrm{ac}}(t), \tag{6.4}$$

[10]This minimal Hamiltonian can also be formally obtained from a Schrieffer-Wolff transformation including the AC drive, the S term, and the Zeeman Hamiltonian $\hat{H}_z$ [133].

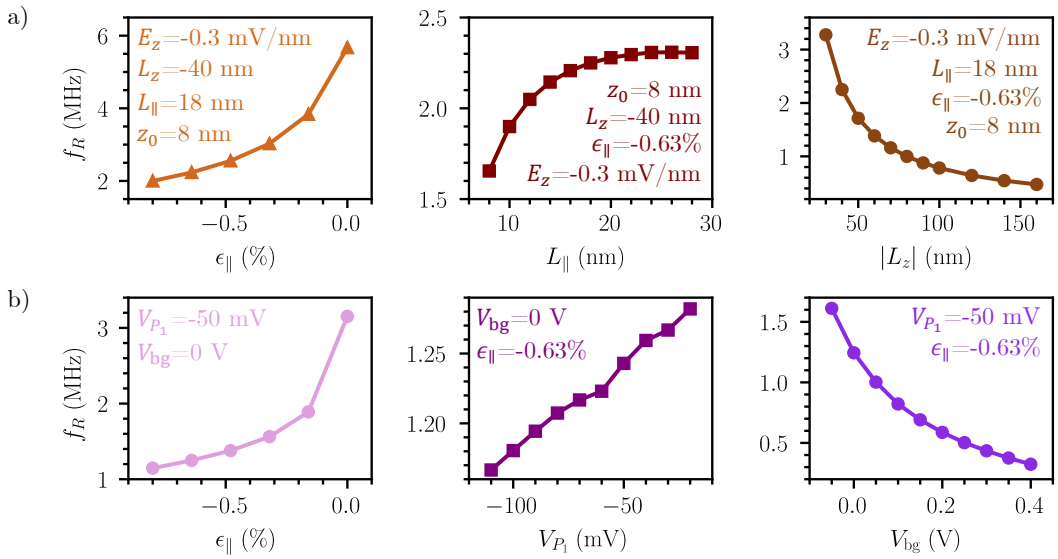

Figure 6.4: a) Dependence of the f_R for $B = 2$ T $\parallel \boldsymbol{x}$ on strain, L_x, $|L_z|$ for the model potential V_C. b) Dependence of the f_R for $B = 2$ T $\parallel \boldsymbol{x}$ on strain, V_{P_1}, and V_{bg} for the single-unit cell in Figure 6.1c with the realistic potential resulting from the resolution of Poisson's equation.

where $H_0 = \mu_B \boldsymbol{\sigma}(\hat{g} \cdot \boldsymbol{B})$ is the Hamiltonian in absence of RF drive (with $\boldsymbol{\sigma}$ the vector of Pauli matrices), $V_{ac}(t)$ is the time-dependent electrical drive, and the two $\beta\sigma_1$ and $\gamma\sigma_3$ terms are the cubic Rashba and the "non-separability" mechanisms, with relative strengths given by the two constants β and γ. In such model, since H_0 is proportional to $\boldsymbol{\sigma}$, the mechanism giving rise to Rabi oscillations depend on the orientation of the magnetic field.[11] For the two mechanisms of interest here, if the Larmor vector $\boldsymbol{f_L} = \hat{g} \cdot \boldsymbol{B} = (g_x B_x, g_y B_y, g_z, B_z)$ is parallel to $\boldsymbol{z}$, the cubic Rashba mechanism brings Rabi frequencies and the novel mechanism induces dephasing. If $\boldsymbol{f_L} \parallel \boldsymbol{x}$, the situation is the opposite: the novel mechanism is responsible for the Rabi oscillations and cubic Rashba is a source of dephasing. Consequently, the orientation of $\boldsymbol{f_L}$ determines whether the non-separability mechanism is bringing dephasing or Rabi oscillations. If we define θ_L as the angle of $\boldsymbol{f_L}$ with respect to $\boldsymbol{z}$ ($\tan(\theta_L) = g_x B_x / g_z B_z$), and keep in mind the definition of θ (see Figure 4.2), we find that

$$\tan(\theta_L) = \tan(\theta)\frac{g_x}{g_z}. \tag{6.5}$$

When $\theta_L \to 90$, the novel term brings Rabi oscillations, whereas when $\theta_L \to 0$ it is responsible for dephasing. Note that in the previous equation the relation between θ_L and the rotation of the magnetic field θ is scaled by the ratio g_z/g_x. If $g_z \gg g_x$, small rotations of the magnetic field along θ rapidly project $\boldsymbol{f_L}$ onto the $\boldsymbol{z}$ axis. As an illustration, with Ge g factors $g_z \approx 13$ and

[11] The mechanism responsible for the Rabi oscillations is that bringing off-diagonal elements to H_{eff} (as shown in equation 2.25, f_R is proportional to a $\langle\uparrow|D|\downarrow\rangle$ matrix element). For $\boldsymbol{B} = (B_x, 0, 0)$, $H_0 = \mu_B g_x B_x \sigma_1$, the mechanism adding off-diagonal matrix elements is that proportional to σ_3. Moreover, the mechanism that is proportional to σ_1 brings modulations of the Zeeman splitting, thus dephasing. Alternatively, when $\boldsymbol{B} = (0, 0, B_z)$, $H_0 = \mu_B g_z B_z \sigma_3$, the mechanism responsible for f_R is that proportional to σ_1, and the responsible for dephasing is that proportional to σ_3.

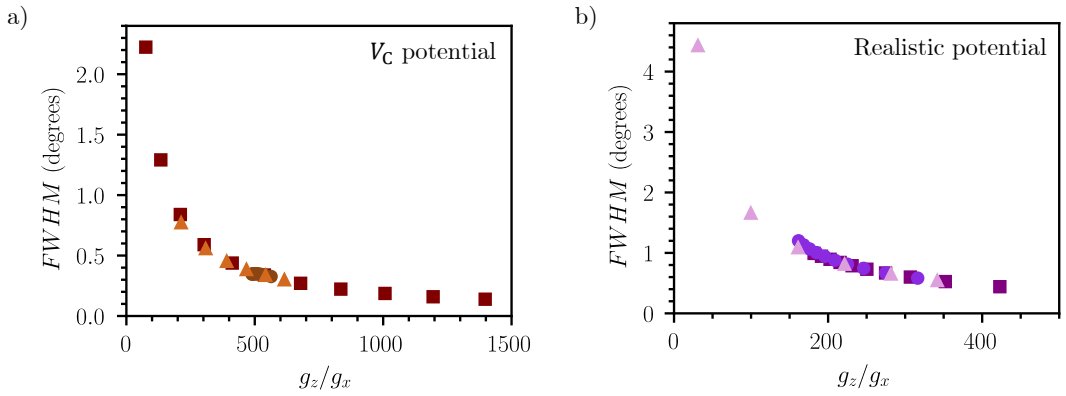

Figure 6.5: a) Correlation between FWHM and g_z/g_x for all the simulations in Figure 6.4a for the V_C potential. b) Same as a) for all the simulations in Figure 6.4b for the realistic potential computed with Poisson's equation. Color and marker codes as in Figure 6.4.

$g_x \approx 0.1$, a slight rotation of the magnetic field $\delta\theta = 1$ degree brings a rotation of the Larmor vector $\delta\theta_L = 89.992$ degrees. This explains both why the in-plane feature is so narrow, and why we observe a clear correlation between the FWHM and g_z/g_x in Figure 6.5.

The discussed model also highlights another important message. The two mechanisms are always present, yet the novel feature seems to be dominant over cubic Rashba for realistic parameters. If the magnetic field is placed out of plane so as to benefit from cubic Rashba to drive Rabi oscillations, the non-separability of the QD motion brings a source of dephasing. Moreover, it cannot be easily turned off, as its origin is linked to the complexity of the electrostatics. Therefore, in absence of other mechanisms dominating dephasing, in-plane magnetic fields may bring a better resilience against it.

In summary, we have confirmed that the unexpected finite in-plane f_R for circular QDs is a non-conventional g-TMR mechanism due to the rotation of the magnetic axes of $\hat{g}$, and its origin is found in the inhomogeneity of E_z. f_R decreases with the confinement of the QDs, which are less polarizable by the AC drive. This suggests working with large QDs to maximize f_R. However, a weak in-plane confinement reduces g_x, which also reduces FWHM. The in-plane feature is extremely narrow, and a small B_z component rapidly makes f_R vanish. If the f_R peak becomes narrower than the experimental precision on the orientation of B the novel feature may remain inaccessible. Reducing the strain is also an interesting possibility, since both f_R and FWHM are inversely proportional to Δ_{HL}.

6.2 Variability

One of the arguments in favor of Ge/SiGe heterostructures is the absence of charge traps in the epitaxial interface, and a surface roughness reduced to very few atomic steps. Such a clean interface should greatly improve the variability figures with respect to what we have seen for Si MOS devices in the previous Chapters. The main source of variability is here on the top SiGe/Al_2O_3 interface, which can indeed host a significant density of charge traps (typically 10^{11} cm^{-2} or above) [134]. We evaluate the variability induced by these charge traps on the single-qubit properties of hole spin qubits, and we scan n_i from $5{\cdot}10^{10}$ to $5 \cdot 10^{11}$ cm^{-2}, which should

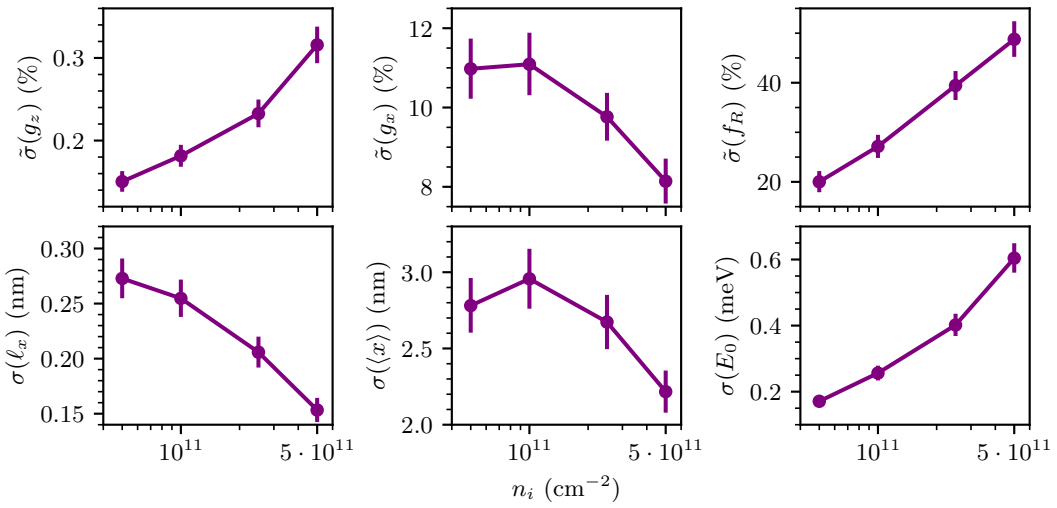

Figure 6.6: Single-qubit properties variability for hole spin qubits for the Ge/SiGe device in Figure 6.1c as a function of the charge trap density at the SiO_2/Al_2O_3 interface. The SiGe layers in the simulated device are unstrained, and the strain in Ge is $\varepsilon_{\parallel} = -0.8\%$, $\varepsilon_{\perp} = 0.56\%$. Relative standard deviation for the gyromagnetic g-factors g_x, g_z and for f_R (for a drive applied to gates B_1, B_2 with opposite modulation, and $B \parallel \boldsymbol{x}$); absolute standard deviation for the QD size and position ℓ_x, $\langle x \rangle$, and the ground state energy E_0. Vertical lines denote the 95% confidence interval.

cover from the best to a rather standard scenario. We track the RSD of the main g factors and f_R (for a drive with opposite modulation in gates B_1 and B_2, and B along $\boldsymbol{x}$),[12] and the SD of ℓ_x, $\langle x \rangle$, and the ground state energy (E_0). We model the single-qubit device in Figure 6.1c, here considering for simplicity that the SiGe is fully relaxed, and that the Ge layer experiences a biaxial strain of $\varepsilon_{\perp} = 0.56$ %, $\varepsilon_{\parallel} = -0.80$ %. Results are shown in Figure 6.6, and we do not show data for g_y, ℓ_y and $\langle y \rangle$ because with the pristine dot being circular, the statistical properties are the same for x and y.

While the RSD of g_z is remarkably small, the variability of g_x can reach 11%. This value is directly $\tilde{\sigma}(f_L)$ if $B \parallel \boldsymbol{x}$, and is even larger than the variability of f_L reported in Chapter 4 for Si MOS devices. The causes for this are the small value of g_x, and the fact that it is much more sensible to variability. We learnt from Ref. [60] that $g_z = -6\kappa + \gamma$, where γ is a correction term due to the HH-LH mixing. γ is sensible to variability, yet the 6κ term is not. For Ge, $\kappa = 3.41$, and the latter is the main contribution to g_z. Modulations of γ due to disorder translate then into small modulations of g_z, and therefore the RSD is expected small. Indeed, the numerical results showing $\tilde{\sigma}(g_z) < 0.4\%$ confirm these predictions. For the in-plane g-factor, however, $g_x \propto 1/(\ell_x^2 + \ell_y^2)$ [60], so it is fully sensitive to disorder through modulations of the dot size ℓ_x, ℓ_y. This explains why $\tilde{\sigma}(g_z) < \tilde{\sigma}(g_x)$, and also why we observe consistent trends in the dependence of variability on n_i for g_x, ℓ_x, and $\langle x \rangle$. Surprisingly, variability decreases at large n_i for these three variables. The origin of this trend is two-fold. On the one hand, the charge traps have in average a confining effect, which translates into smaller dots (in average) when n_i

[12] Note that in the fully symmetric device considered here, driving with P_1 is inefficient as the standard g-TMR is zero in the ($\boldsymbol{xy}$) plane.

increases, thus less sensitive to disorder. Moreover, when the number of charges increases, their individual effect decreases due to the same $\tilde{\sigma}(f_R) \propto \sqrt{n_i}$ dependence discussed in Chapter 4.[13]

Although the variability in ℓ_x and $\langle x \rangle$ are not much lower than those for holes in Si MOS devices ($\sigma(\ell_x) = 0.90$ nm, $\sigma(\ell_y) = 0.75$ nm, $\sigma(\langle x \rangle) = 9.00$ nm, $\sigma(\langle y \rangle) = 2.19$ nm for Si MOS with $n_i = 5 \cdot 10^{10}$ cm^{-2}), the impact on the ground state energy is significantly smaller. For Ge/SiGe devices $\sigma(E_0)$ hardly reaches 1 meV, whereas it was 5.75 mV for the holes in Si MOS devices for $n_i = 5 \cdot 10^{10}$ cm^{-2}. With the QDs being substantially larger in Ge ($\ell_x^\circ = 17.25$ nm for the pristine device), their position and size seems to be more sensitive to disorder, yet with little impact on E_0. However, f_R in Ge still shows a significant variability, reaching 50 % for $n_i = 5 \cdot 10^{11}$ cm^{-2}. If the Ge qubits are operated with B in plane, the variability in f_L is expected to be similar than in Si MOS. Having the defects a few tens of nm away from the QDs indeed improves variability, and the small $\sigma(E_0)$ in Ge should guarantee a better operability of QD arrays and their charge occupation, yet the individual qubits still show sizable differences in their spin properties, and we are still far from homogeneous arrays.

6.3 Tip gates as improved device layout

We have seen that even if the qubits are hosted in an active material surrounded by clean epitaxial interfaces, the charge defects present at the interface with the dielectric still have a strong impact. We may split the impact of charge traps at the top interface of a Ge/SiGe device in two: on the one hand, there are the charges laying below the metallic gates. These are the charges that are the closest to the QDs, but they are screened by the metallic gate which is located a few nm above. On the other hand, there are the charges laying elsewhere, that even though they are further away from the QD, they are not much screened. We may now think on ways to mitigate the disorder for these two types of charges. Regarding the charges located below the gates, there is not much to be done besides reducing the thickness of Al_2O_3 between the SiGe and the metallic gates. It must be thick enough to prevent charge leaking from the gates to the SiGe, but it could still be decreased to 2-3 nm. The impact of the charge traps laying in the spacers can be very efficiently reduced by device engineering. We have already seen in section 5.1 the impact of screening on the efficiency of the J-gates, whose effect is strongly suppressed by the front gates. We can use this phenomenon in our favor to design a new gate layout that should eliminate the effect of these charges.

The tip gates are gates that can range from circular to square shape and that penetrate into the SiGe layer, see Figure 6.7b. They are envisioned to be fabricated in Ge/SiGe heterostructure devices where the top SiGe layer is grown thicker.[14] Before the deposition of the oxide, holes are to be etched in the SiGe, and then filled first with a dielectric, and finally with a metal. In this way, the gate layout emulates that of the current standard layouts (hereafter named planar devices), yet the top interface in the inter-gate spacing has been shifted up by H_I. The large-scale architecture of such gates is envisioned as a 2D array of tip gates as shown in Figure 6.7a, acting alternatively as plunger gates (P_1 and P_2) or tunnel gates (J and all B). The unit cell from Figure 6.7a can be replicated in the ($\boldsymbol{xy}$) plane to form large-scale arrays.

[13] Since variability scales as $\sqrt{n_i}$ [110], the variability induced by the 1st charge is stronger than the variability induced by the n-th charge.

[14] All the discussion hereafter focuses on Ge/SiGe heterostructures, yet the results should extend to any device based on epitaxial heterostructures.

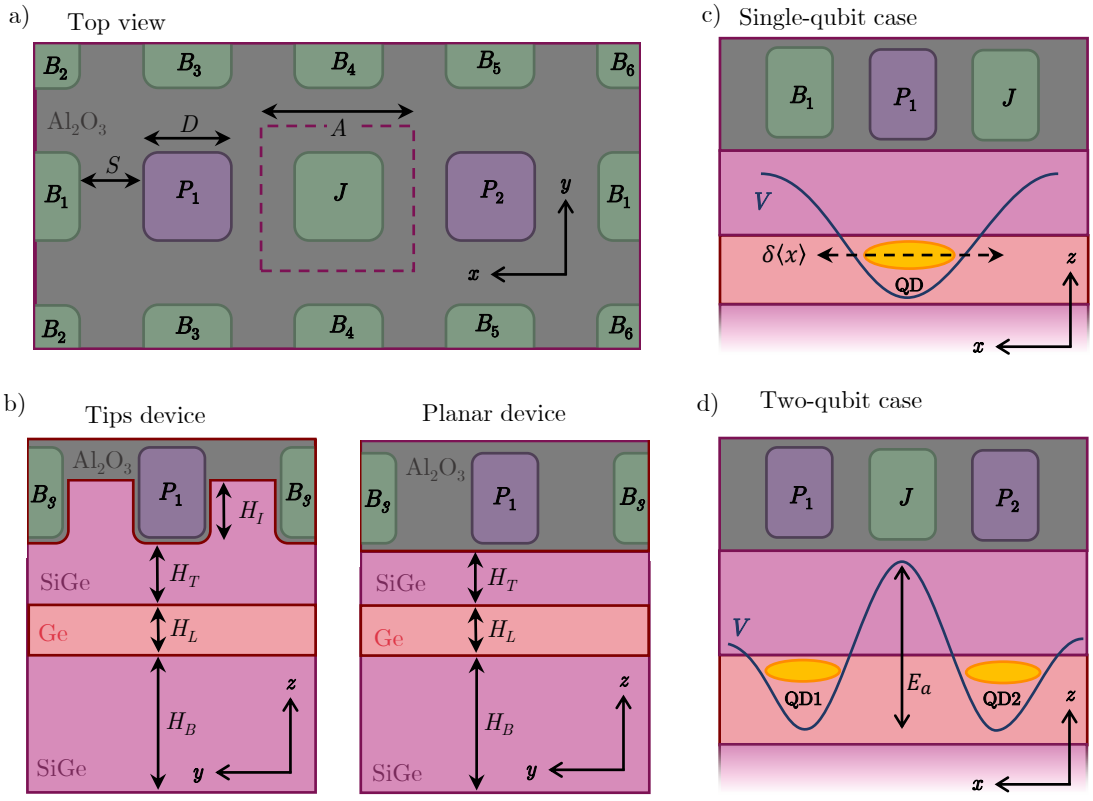

Figure 6.7: The Germanium tips device. a) Schematic representation of a top-view of the simulated device. Color code as in Figure 6.1. Dashed purple line denotes the building block of the 2D array. b) Comparison between the gate layout based on penetrating gates, the tips device, and the standard planar device. c) Mode of operation of the device in a) for a single qubit simulation. d) Mode of operation of the device in a) for a two-qubit experiment.

The expected improvement in variability is inspired in the observations for the J-gates in Si MOS devices. The tip gates layout does not only shift the charges in the spacers even further, but it also strongly screens their potential, which should barely reach the Ge layer. This should eliminate the impact these charges and improve variability. Unfortunately, the area of SiGe/Al_2O_3 interface increases, so does the absolute number of charges with respect to the planar device, which may compromise the improvement in some regimes. At the limit where the gates overlap completely all the interface ($D \to A$), planar and tip devices should converge to the same figures of variability (or slightly worse for the tips device due to the larger number of charges). Yet, tips devices should outperform their planar counterparts when the spacing between gates (S) increases.

In the following, we analyze the properties of a gate layout based on tip gates. We optimize the device parameters to maximize both f_R and the control of the tunnel coupling. To do so, we perform 4kp simulations on the unit cell device shown in Figure 6.7a. The device is made of a first SiGe layer of thickness $T_B = 100$ nm laying above an effective back gate (grounded unless otherwise stated). We assume the SiGe to be fully relaxed, and therefore the Ge layer of

thickness H_L grown on top suffers a biaxial strain of $\varepsilon_\perp = 0.56$ %, $\varepsilon_\parallel = -0.80$ %. The top SiGe layer is 100 nm thick, yet the tip gates penetrate by H_I. The thickness of the Al_2O_3 between the SiGe and the penetrating part of the tip gates is 5 nm. We work with circular gates of diameter D for the device optimization.

6.3.1 Device optimization

The device in Figure 6.7a can be operated as a single-qubit and two-qubit device. When operated as a single-qubit device, the QD is formed under gate P_1, and all the other gates are set so as to close the tunnel coupling with the surrounding replicas.[15] To drive Rabi oscillations, we rely on the non-separability of the potential to drive Rabi oscillations, and place $\boldsymbol{B} \parallel \boldsymbol{x}$ to benefit from the maximum in f_R due to the non-separability mechanism. The RF signal is applied with opposite modulation on B_1 and J gate. Alternatively, the same device can be operated in a two-qubit mode, see Figure 6.7d. In this case, P_1 and P_2 form the double QD system, and J controls the energy barrier between qubits. Again, all the lateral B_i gates are set so as to close the tunnel coupling with the neighboring replicas of the device.

6.3.1.1 Rabi frequencies

In this section we discuss the optimal device parameters to reach maximal f_R. We work in the single-qubit mode, and apply $V_{B_i} = V_J = V_{P_2} = 0.1$ V and $V_{P_1} = -50$ mV. Rabi frequencies are shown for $B = 1$ T, and $V_{\mathrm{ac}} = 1$ mV. Figure 6.8a shows the dependence of f_R on the thickness of the Ge layer. It follows a non-monotonous trend, which reassembles that of Figure 4.6b, yet for Ge f_R peaks at $H_L = 25$ nm. Optimal Ge layers thickness are in between 20 and 30 nm. Also the dependence of f_R on H_T is peaked (see Figure 6.8b), likely due to the interplay between two different aspects. When H_T increases, the gates are shifted farther away and their lever-arm decreases. Consequently, the RF drive is less effective, and f_R decreases, as we see for $H_T > 25$ nm. For small H_T, however, the inhomogeneity of the vertical electric field is reduced. Since the finite f_R with $\boldsymbol{B} \parallel \boldsymbol{x}$ results from the x, y dependence of E_z, when H_T is reduced the anisotropy of f_R approaches that of Figure 6.3e, and it vanishes in plane. The interplay between the two trends yields to an optimal H_T where f_R is maximal, which is found to be between 20 and 30 nm.

The dependence of f_R on S and D is shown in Figure 6.8c, and it appears to be maximal for small D and S. Indeed, we can approximate the in-plane electric field created by the drive as $E_{\mathrm{ac}} = V_{\mathrm{ac}}/(2S+D)$. Consequently, a minimization of the distance between lateral gates ensures the strongest in-plane electric drive. Moreover, several screening effects play a (secondary) role. Small D reduces the screening by the plunger gates of the drive applied to the lateral gates, and consequently f_R. Reducing D also makes the QDs smaller; yet this effect is rather weak ($\ell_x = 7.6$ and 11.8 nm for $D = 30$ and 80 nm, respectively). Additionally, a smaller D also reduces the size of the lateral gates, which should yield to a less efficient drive. An optimal gate layout may be composed of plunger gates with small D to minimize the screening of the RF drive, and lateral gates with large D to maximize the effective drive amplitude, with small S.

[15] The simulations are made with PBC along $\boldsymbol{x}$ and $\boldsymbol{y}$.

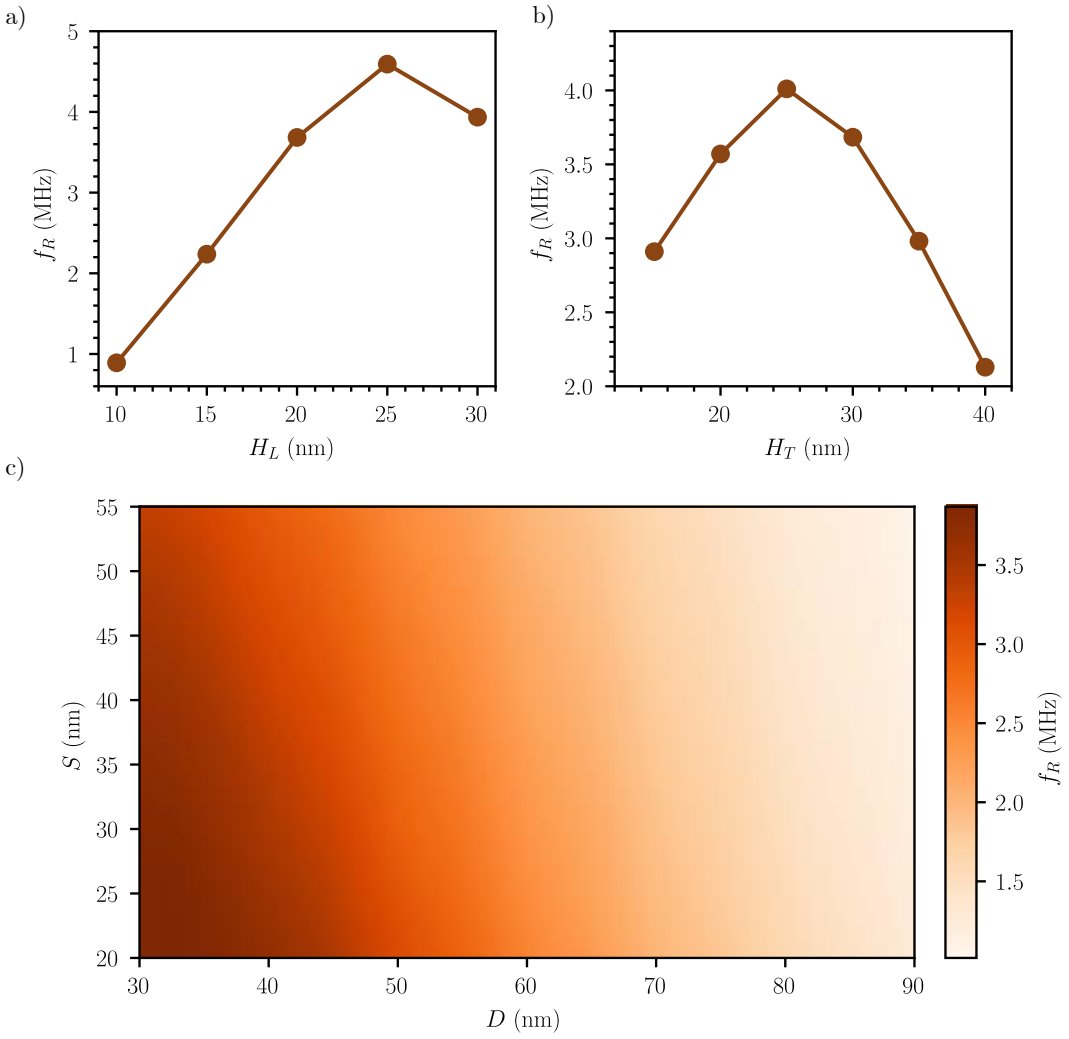

Figure 6.8: Optimization of the gate layout to maximize f_R (for a $B_1 - B_2$ drive of amplitude $V_{\text{ac}} = 1$ mV, and $\boldsymbol{B} \parallel x = 1$ T). a) Dependence of f_R on the thickness of the Ge layer (H_L) for a device with $D = 40$ nm, $S = 20$ nm, $H_T = 20$ nm. b) Dependence of f_R on the thickness of the top SiGe layer below the penetrating gates (H_T) for a device with $D = 40$ nm, $S = 20$ nm, $H_L = 20$ nm. c) Dependence of f_R on the diameter of the gates (D) and the spacing left between gates (S) for a device with $H_L = 20$ nm, $H_T = 20$ nm. All the simulations are carried out with a device made of a 3x2 repetition of the primitive cell shown in dashed purple line in Figure 6.7a, with a gate layout made of circular gates, $V_{P_1} = -50$ mV, and all other B_i gates set to 0.1 V.

6.3.1.2 Tunnel control

The optimization of the tunnel control is examined in the two-qubit mode shown in Figure 6.7d, and we set $V_{B_i} = 0.1$ V, and $V_{P_1} = V_{P_2} = -50$ mV. We tune D and A as device parameters, and analyze their impact on the maximal reachable tunnel coupling (τ_{max}) and on the efficiency

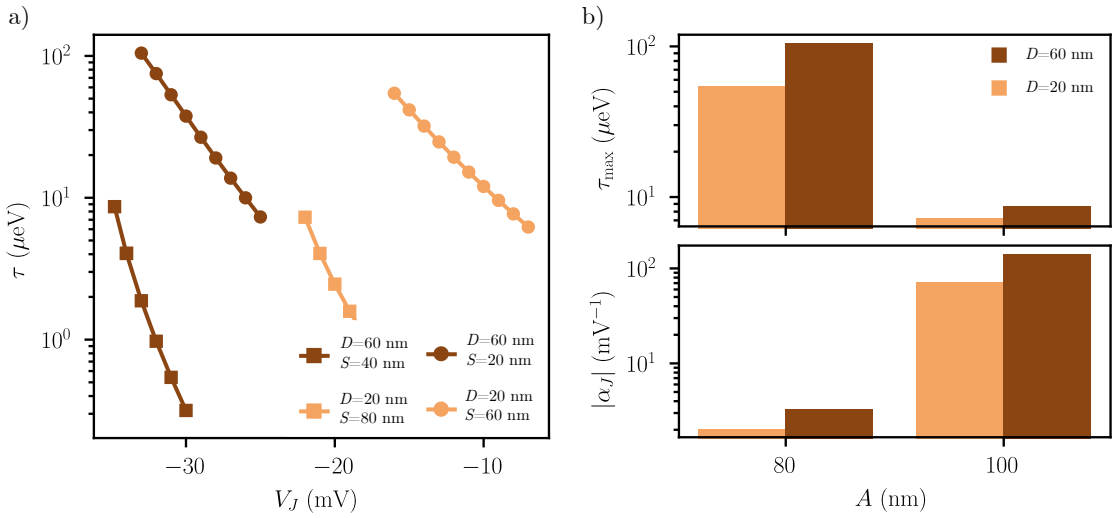

Figure 6.9: a) Tunnel coupling dependence on V_J for different gate dimensions in a device like the one shown in Figure 6.7a, with a gate layout made of circular gates, $V_{P_1} = V_{P_2} = -50$ mV, and all other B_i gates set to 0.1 V. b) Maximum reachable t ($t_{\max}$) and exchange gate efficiency (α_J) for different gate dimensions. All the simulations are made for devices with $H_L = 10$ nm and $H_T = 20$ nm, at $B = 0$ T.

of the tunnel control $\alpha_J = \partial \log^2(\tau)/\partial V_J$.

Figure 6.9a shows the dependence of τ on V_J for different device dimensions. Whereas the lower point for each case is arbitrary (τ can be closed completely), there is a limit on the maximal τ we can reach. Indeed, since we apply an attractive V_J to decrease the barrier height E_a, it eventually creates a potential well that forms a third QD. This $\tau_{\max}$, given in Figure 6.9b, strongly depends on the device and gate dimensions. In particular, we find that $\tau_{\max}$ is the largest for small A and large D; yet A shows the strongest impact. Figure 6.9 illustrates why. The J gate has a maximal electrostatic control of the area underneath, and a weaker control of its surroundings. When A is large and D is small, the area with tight control is reduced, and when a V_J is applied to reduce E_a, only the peak of the potential barrier is properly controlled, see Figure 6.9b. Consequently, the center of the barrier decreases faster than the sides, giving rise, for large attracting V_J, to a potential well with two side barriers that cannot be electrostatically tuned. The potential well under the J gate triggers the formation of a third QD, see Figure 6.10a, and kills the two-qubit system. This effect can be greatly palliated if the spacing between plunger gates is reduced (small S) and the gate coverage is large (large D), see Figure 6.9b. In this case, the electrostatic control of the area between QDs is more homogeneous, and the appearance of a third QD is delayed. As a consequence, the coupling between the two QDs is much larger when this happens (see Figure 6.10a), and so $\tau_{\max}$ is enhanced. Reaching large tunnel couplings therefore calls for a small gate pitch with large gate coverage.

The efficiency of the tunnel control (α_J) also shows an important dependence on A, with tighter tunnel control for the gate layouts with larger A. This is in good agreement with the WKB approximation discussed in section 5.1, which predicts the tunnel control to be proportional to the distance between the two minima in the potential energy profile [122]. The minor dependence

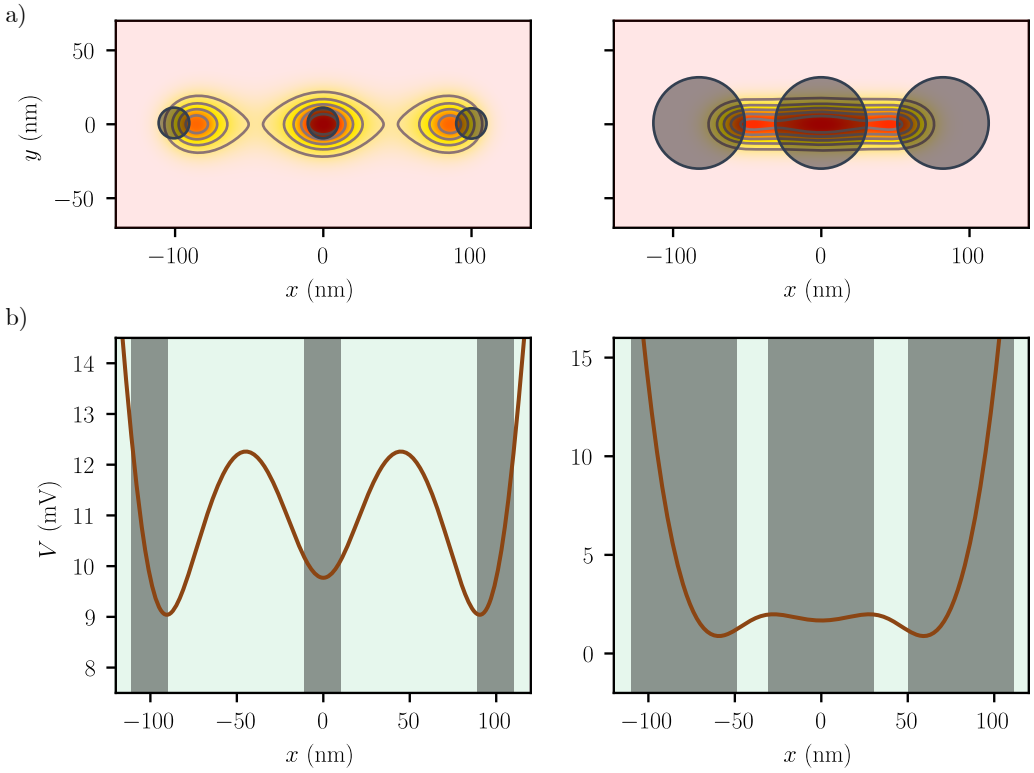

Figure 6.10: Illustration of why $\tau_{\max}$ depends on the gate dimensions. a) Cross section of the ground state wavefunction in the $(\boldsymbol{xy})$ plane at $z = 0$ nm (center of the Ge layer) for the device of Figure 6.7a, with a gate layout made of circular gates, $V_{P_1} = V_{P_2} = -50$ mV, all other B_i gates set to 0.1 V, and V_J set so as to have $\tau > \tau_{\max}$. The grey circles highlight the position and dimensions of the gates above. For the left plot, $D = 20$ nm and $A = 100$ nm, whereas for the right plot $D = 60$ nm and $A = 80$ nm. b) Potential along $\boldsymbol{x}$ for $y = 0$ nm, $z = 0$ nm for the gate layout in a) (left plot) and b) (right plot). The grey shaded areas highlight the extension of the gates above.

on the gate diameter owes to the strengthening of the electrostatic control, yet α_J is again ruled mostly by A.

Overall, there is a compromise to be made on the layout dimensions to optimize the tunnel coupling parameters. Large $\tau_{\max}$ are achieved with small A, whereas large α_J require the opposite. Being restricted to $\tau < 10$ μeV by the device geometry is a strong handicap for two-qubit operations and readout, so A should be kept at 80 nm, which is also favorable for f_R. Regarding the gate diameter, large D increases both $t_{\max}$ and α_J, yet large f_R calls for small D if the gate pitch is homogeneous. Again, a non-homogeneous gate pitch with large J gates and small P, ideal for f_R, would be also beneficial for τ.

6.3.2 Improvement in variability

So far, we have seen that a gate layout based on tip gates penetrating the SiGe layer can be functional, and provides sufficiently large f_R's and tight enough control of τ to perform one-

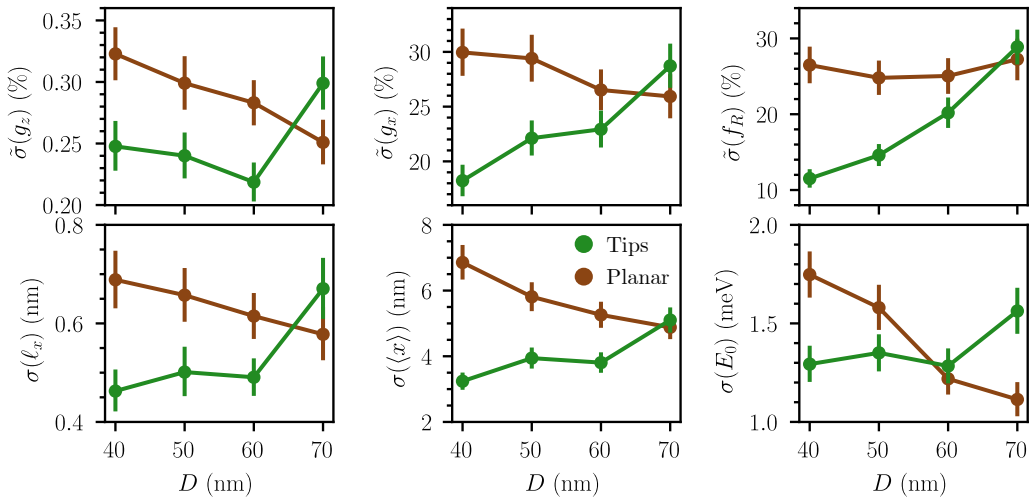

Figure 6.11: One-qubit properties variability comparison between a tip and planar gate layout for a charge trap density $n_i = 10^{11}$ cm^{-2}: RSD of the gyromagnetic g factors g_z and g_y, of f_R (for a drive with opposite modulation of gates B_1, J, and $\boldsymbol{B} \parallel \boldsymbol{x}$); and SD of ℓ_x, $\langle x \rangle$, and the ground state energy E_0 as a function of the gate diameter D for the device in Figure 6.7a with $A = 80$ nm, operating in the single-qubit regime as shown in Figure 6.7c. $V_{\text{bg}} = 0.1$ V, $V_{B_i} = V_{P_2} = V_J = 0$ mV, and V_{P_1} is set so as to ensure that the tunnel coupling due to PBC with the neighboring cells is smaller than 25 neV: $V_{P_1} = -72, -63, -57, -53$ mV for $D = 20$, 25, 30, 35 nm for the tips device, and $V_{P_1} = -72, -65, -59, -57$ mV for the planar device. Vertical lines denote the 95% confidence interval.

and two-qubit operations. The main claim of such a layout was to improve the figures-of-merit of variability due to charge traps. In the following, we discuss the improvement of variability brought by the tip gates. To do so, we compare the tips and planar devices in Figure 6.7b, for a unit cell as in Figure 6.7a. We set $H_B = 128$ nm, $H_L = 16$ nm, $A = 80$ nm and $H_T = 32$ nm, and discuss the improvement of variability for one- and two- qubit properties as a function of D for datasets of 500 randomly generated defective devices. We stick here to squared gates with rounded corners as illustrated in Figure 6.7a, since we want to discuss the impact of gate coverage and they allow to reach larger coverage than circular gates.

6.3.2.1 One-qubit properties

Figure 6.11 shows the dependence of the variability of one-qubit properties on the gate diameter for the planar and tips devices. The overall trend for all the tracked properties follows what was expected: the tips device outperforms the planar device at small gate coverages, and it is slightly worse when $D \to A$ due to the larger SiGe/Al_2O_3 area. Remarkably, the variability in g_x and f_R reduces by a factor of approximately 1/2 at $D = 40$. Also $\tilde{\sigma}(g_z)$ and $\sigma(E_0)$ show a slight improvement, yet they are already small for the planar device.

Note that the comparison with the simulations in Figure 6.6 must be done carefully, since H_T is different ($H_T = 32$ nm for the tips device and $H_T = 50$ nm for the device in Figure 6.6). Here, the defective interface is closer to the Ge layer, thus the variability is larger. A fair

comparison between devices should be made with the same H_T, where the device simulated in Figure 6.6 should present a similar variability to that of the planar device simulated here. The differences between the two planar devices also highlights the gain in variability when shifting the defective interface farther from the active layer. For variability, the larger H_T the better, yet at the expense of losing electrostatic control.

In Appendix E.1 we dig deeper into the details of this improvement in variability. We confirm that indeed the tips device gets rid of the effect of the charges laying in the spacing between gates, and that the variability is limited by the impact of the charges surrounding the penetrating part of the gates. Thanks to this, at the single-qubit level the tips device can considerably reduce the variability on the relevant properties (g_x, f_R) with respect to planar devices.

6.3.2.2 Two-qubit properties

Let us now analyze what are the figures of merit of variability for the two-qubit properties in the planar and tips device. We use the same methodology as in section 5.2, yet here we have been able to correct the variability in τ by explicit V_J pulses, and we have collected V_P as the superset of $[V_{P_1}, V_{P_2}]$ and V_J for each disordered device. Then, we transform the voltage shifts into energy shifts as we did for the Si MOS devices: $\Delta E = \alpha_P^0 \Delta V_P$ (where α_P^0 is the lever-arm of the P_i gates in the pristine device), and ΔE_a is obtained from the linear fit of E_a vs. V_J for the pristine device.

The general trend observed for the ensemble of two-qubit properties is consistent with that of the single-qubit properties, see Figure 6.12. Again, tips devices present better variabilities than planar devices at small D, and slightly worse when $D \to A$. For $D = 40$ nm, both $\sigma(\Delta V_P)$ and $\sigma(\Delta V_J)$ are reduced by a factor of roughly $1/2$, going from gate corrections of $\sim$12 mV to $\sim$6 mV. Consistently, the same is observed for $\sigma(\Delta E)$ and $\sigma(\Delta E_a)$, which are reduced from 2.25 to 1.33 mV and from 1.85 to 0.99 mV, respectively.

Disorder has a remarkably weaker impact on the two-qubit properties variability in Ge/SiGe devices than in Si MOS devices in section 5.2. This is patent in the distribution of both ΔE and ΔE_a, see Figures 6.12c and 6.12f. Unlike in Si MOS where the distributions were significantly tailed (see Figure 5.10), here they follow a normal distribution centered at zero, and the only remarkable difference between tips and planar devices is the SD. Since the Si MOS and Ge/SiGe devices have different lever-arm parameters, the meaningful quantitative comparison involves ΔE and ΔE_a rather than the gate corrections. For holes in Si MOS devices, we have reported $\sigma(\Delta E) = 8.15$ mV and $\sigma(\Delta E_a) = 12.01$ mV, see Table 5.1, which are even substantially larger than those of the planar device in Figures 6.12b and 6.12e. Interestingly, even if the variability in single-qubit properties is comparable, devices based on Ge/SiGe heterostructures (even the planar devices) seem significantly more robust for the realization of two-qubit operations. In a sense, this is in line with the current status of experimental progress, where quantum processors based on epitaxial heterostructures reached 6 qubits [16] whereas those based on Si MOS only reached two [65].

6.4 Chapter 6 in a nutshell

In this chapter we have explored the physics of hole spin qubits hosted in Ge/SiGe-based devices. Such devices embed the active strained Ge layer in SiGe forming epitaxial interfaces, which are

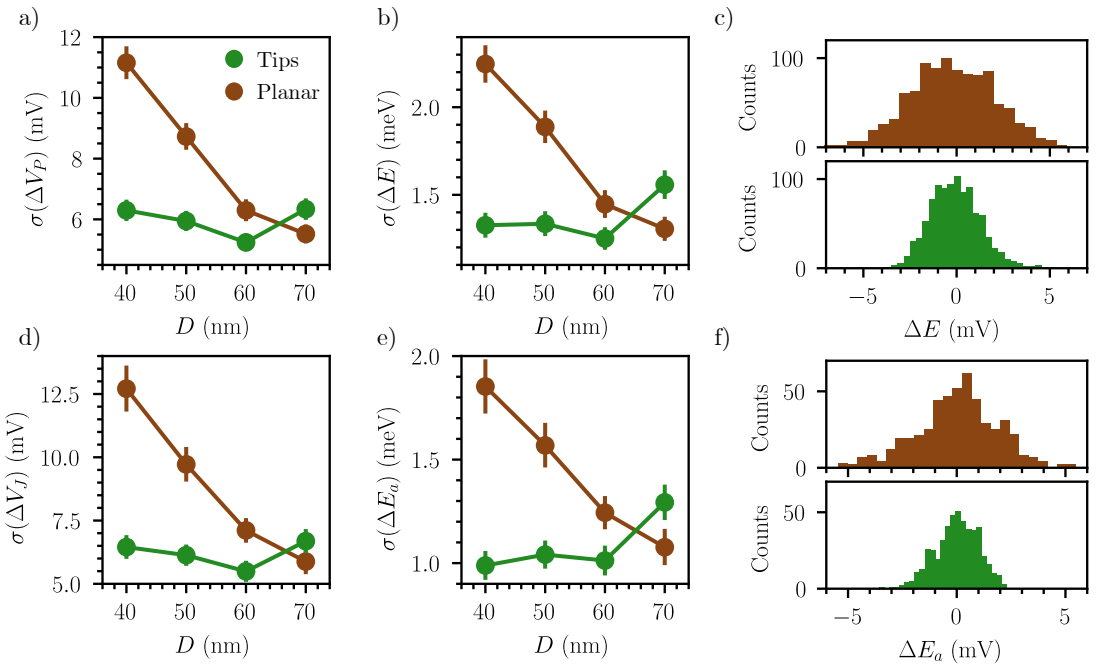

Figure 6.12: Two-qubit properties variability comparison between a tip and planar gate layout for a defective SiGe/Al_2O_3 interface with $n_i = 10^{11}$ cm^{-2}. a) SD of ΔV_P dependence on the gate diameter D for the device in Figure 6.7a with $A = 80$ nm, operating in the two-qubit regime as shown in Figure 6.7d. The initial biases are set as in Figure 6.11, yet here V_J is initially set to have $\tau = 15$ μeV ($V_J = -37.5$, -33.8, -30.7, and -29.5 mV for $D = 40$, 50, 60, 70 nm for the tips device, and $V_J = -38.4$, -35.2, -32.2, and -31.1 mV for the planar device). b) Same as a) for ΔE. c) Histogram of ΔE for $D = 40$ nm for the tips (top panel) and planar (bottom panel) gate layouts. d) SD of ΔV_J dependence on the gate diameter D. e) Same as d) for ΔE_a. f) Histogram of ΔE_a for $D = 40$ nm for the tips (top panel) and planar (bottom panel) gate layouts. Vertical lines in a),b),d),e) denote the 95% confidence interval.

free of defects. Experiments are making remarkable progress with such platforms to scale up the number of qubits in the quantum processors, yet some fundamental aspects as the anisotropy of f_R with the orientation of B are still not characterized experimentally. We have reported this f_R anisotropy for a realistic potential in the typical gate layout of Ge/SiGe devices, and unveiled an unexpected mechanism involving the coupling of the in-plane and out-of-plane motions of the QD that brings the maximal f_R when B is placed in plane for circular QDs. With $g_x \approx 0.1$ and $g_z \approx 13$, an in-plane magnetic field allows the application of large B while having reasonable f_L, which boosts f_R due to the $f_R \propto B$ dependence. The appearance of the maximal f_R where it was expected to be zero by the simplest models highlights the importance to account for the complex electrostatics of the experimental devices in the modelling of their properties.

The plea behind Ge/SiGe devices lays on their expected better variability figures with respect to Si MOS platforms. We have analyzed the impact of variability due to the defective top SiGe/Al_2O_3 interface, located a few tens of nm above the Ge layer. While remarkably better for two-qubit properties, where the induced shifts on the qubits' energy and on the energy barriers

remain below 2.5 mV, variability in single-qubit properties is still large. In particular, the very small in-plane g-factors are highly sensitive to variability, which reaches 11% for standard charge trap densities in the Ge/Al_2O_3 interface. Also f_R shows large scatterings, with variabilities hitting 40%, not much below the values obtained in Si MOS devices.

Based on the strong screening effects observed during the design of the J-gates in Si MOS devices in Chapter 5, we have proposed a new gate layout that can reduce by roughly a half the variability on f_R, g_x, and the energy shifts of E_0 and E_a. The novel gate layout consists of a 2D array of rounded-square-shaped gates (the "tip" gates) that penetrate into a thicker SiGe down to a few tens of nm from the Ge layer. In this way, the charges lying in the space between front gates are shifted a few tens of nm farther from the Ge film. Moreover, the lateral facets of the tip gates screen the potential fluctuations that they may still induce. Consequently, their contribution to variability is totally eliminated, and the remaining variability is caused by the charges surrounding the gate insertions. We have demonstrated that such a gate layout provides large enough f_R and tight enough control of τ for practical use in a quantum processor.

Chapter 7

Correlation effects in multi-particle quantum dots

Contents

Up to now we have tackled the simulation of qubit systems from the single-particle perspective. Assuming single-electron (or single-hole) qubits ease the computational treatment of the problem, yet the qubits may be multiply-charged in some experiments. Moreover, the repulsive character of the electron-electron (or hole-hole) interactions may bring important many-body effects into the physics of spin qubits, raising significant differences with respect to the estimations at the single-particle level. In fact, some of the physics involved in spin qubits are many-body by nature, as exchange interactions or PSB readout. We can address the many-particle problems numerically in realistic device geometries thanks to the Configuration Interaction method (see section 2.4), yet the very large computational cost of such simulations limits the analysis to two- or three-particle systems at most. The CI calculations are integrated in the computational workflow of TB_Sim, and the tools to analyze two-particle wavefunctions developed in section 3.2 allowed to corroborate the findings discussed hereafter.

7.1 Molecularization effects

In the estimation of the tunnel couplings made in the previous Chapters, we evaluate the (1,0) $\rightarrow$ (0,1) anticrossing as a first approximation to the physics at the (1,1) $\rightarrow$ (2,0) anticrossing, which is in fact the relevant transition for PSB readout or exchange coupling of a two-qubit system. We now compute the energy diagram of the (1,1) $\rightarrow$ (2,0) transition for a hole Si MOS device like the one in Figure 5.9a using full CI and we compare it to the solution in the single-particle case, see Figure 7.1.

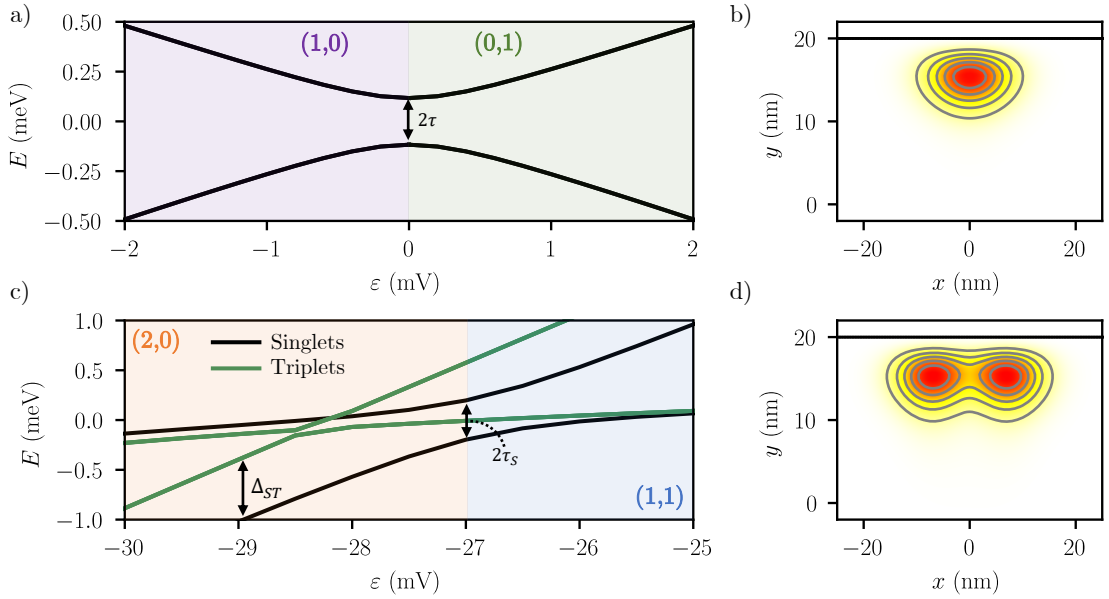

Figure 7.1: Comparison between the (1,0)-(0,1) and the (1,1)-(0,2) anticrossings for a hole Si MOS device as in Figure 5.9a. a) **k·p**-calculated energy diagram of the single-particle case at the (1,0)-(0,1) anticrossing. b) Cross section of the ground state wavefunction at $z = 0$ nm and $\varepsilon = -40$ mV. c) CI-calculated energy diagram of the two-particle case at the (1,1)-(0,2) anticrossing. d) Cross section of the ground state CI hole density at $z = 0$ nm and $\varepsilon = -40$ mV.

In the single-particle picture we miss the impact of the triplet states. In the two-particle case, we have $T(1,1)$ and $T(0,2)$ states. A triplet anticrossing with gap equal to $2\tau_T$ occurs at ε lower than that of the singlet anticrossing. In the (2,0) region, the singlet and triplet states are split by Δ_{ST}, which defines the position of the two anticrossings. The $T(2,0)$ states are discarded in the simplest models like the one discussed in section 2.5.2, assuming that they are far above in energy. In this Chapter, we will see that the presence of low-lying $T(2,0)$ states due to a small Δ_{ST} may have important implications when reading out, and it also may impact the management of exchange interactions between qubits. Additionally, accounting for Coulomb interactions can completely reshape the CI density of the two-particle state, see Figure 7.1d, which does not resemble at all that of the single-particle case.

The impact of Coulomb interactions in many-electron system wavefunctions is in fact something known for a long time. In electron gases, the formation of Wigner crystals was predicted by Eugene Wigner back in 1934, and it consists in the spatial localization of electrons due to correlation effects even if the potential energy landscape is completely flat [135, 136]. Similarly, in the context of quantum dots the spatial separation of electrons observed in Figure 7.1d is known as Wigner molecularization in the literature [137–143]. In a doubly occupied QD, the spatial splitting leaves the $(2,0)$ states with a (1,1)-like character, and consequently reduces the singlet-triplet splitting (Δ_{ST}) [144, 145]. Such predictions match with experiments reporting singlet-triplet gaps smaller than the orbital splittings in materials without valleys [146, 147], and unexpectedly dense energy spectrum in Silicon [148, 149] (even though valley states are rather robust against Coulomb interactions [150]).

Theoretical studies on the topic focused up to now on 2D QDs [151–154]. However, the QDs in MOS devices fabricated at LETI have a very anisotropic shape. Given the weaker confinement along the channel axis, they show a quasi-1D shape along this direction. For Ge/SiGe platforms, the QDs are generally more 2D-like, yet recent proposals suggest strengthening their 1D character to enhance f_R [89]. In terms of Wigner molecularization, we can naively guess that, in presence of repulsive electron-electron interactions, the only option for electrons to avoid each other in a quasi-1D QD is to split, while they shall avoid each other more easily in QDs with a circular shape. In this sense, one would intuitively expect the anisotropy of the QD to play a role on the proneness to Wigner molecularization, being strongest in largely anisotropic QDs. Consequently, we analyze hereafter the impact of anisotropy on the molecularization process, and on the renormalization of Δ_{ST}. We first discuss the insights with a semi-analytical model, and then we corroborate the observations with numerical simulations on realistic geometries for Si MOS and Ge/SiGe devices. Finally, we discuss the impact of the singlet-triplet renormalization on readout and exchange.

7.2 Toy-model insights

We consider a quantum dot strongly confined along the vertical ($\boldsymbol{z}$) direction, and with an anisotropic harmonic 2D confinement potential in the ($\boldsymbol{xy}$) plane. We stay on the single-band approximation, which is a good first approximation almost pure heavy-holes, and for electrons if we discard the possible valley states. In this approximation, the two-particle problem is known as the Hooke's atom [155, 156]. The Hamiltonian of the anisotropic 2D Hooke's atom with material-dependent parameters is

$$H = \sum_{i=1}^{2} \frac{\mathbf{p}_i^2}{2m} + \frac{1}{2} m \left(\omega_x^2 x_i^2 + \omega_y^2 y_i^2\right) + \frac{e^2}{4\pi\varepsilon|\mathbf{r}_1 - \mathbf{r}_2|}\,, \tag{7.1}$$

where $\varepsilon = \varepsilon_r \varepsilon_0$ is the dielectric permittivity and m is the in-plane effective mass. The confinement along $\boldsymbol{x}$ and $\boldsymbol{y}$ is characterized by the energies $\hbar\omega_x$ and $\hbar\omega_y$, or alternatively by the length scales $\ell_x = \sqrt{\hbar/(m\omega_x)}$ and $\ell_y = \sqrt{\hbar/(m\omega_y)}$. Given that the solutions for $\omega_x < \omega_y$ and $\omega_x > \omega_y$ are simply related by a permutation of the $\boldsymbol{x}$ and $\boldsymbol{y}$ axes, we assume $\omega_x \leq \omega_y$ ($\ell_x \geq \ell_y$) without loss of generality. In the absence of Coulomb interactions, equation 7.1 is the Hamiltonian of a 2D harmonic oscillator. The singlet is then the doubly occupied s-like ground state, and the triplet is obtained by promoting one electron to the first excited state. Therefore, the singlet-triplet splitting is $\Delta_{ST}^{(0)} = \hbar\omega_x$. In the presence of coulomb interactions, the Hamiltonian is separable in the center of mass and relative coordinates $\mathbf{R} = (\mathbf{r}_1 + \mathbf{r}_2)/2$ and $\mathbf{r} = \mathbf{r}_1 - \mathbf{r}_2$. Namely, $H = H_{\mathbf{R}} + H_{\mathbf{r}}$, where

$$H_{\mathbf{R}} = \frac{\mathbf{P}^2}{4m} + m\left(\omega_x^2 X^2 + \omega_y^2 Y^2\right)\,, \tag{7.2a}$$

$$H_{\mathbf{r}} = \frac{\mathbf{p}^2}{m} + \frac{m}{4}\left(\omega_x^2 x^2 + \omega_y^2 y^2\right) + \frac{e^2}{4\pi\varepsilon|\mathbf{r}|}\,, \tag{7.2b}$$

with $\mathbf{P}$ and $\mathbf{p}$ the conjugate momenta to $\mathbf{R}$ and $\mathbf{r}$, respectively. The motion of the center of mass remains described by the Hamiltonian $H_{\mathbf{R}}$ of a non-interacting 2D harmonic oscillator, but with

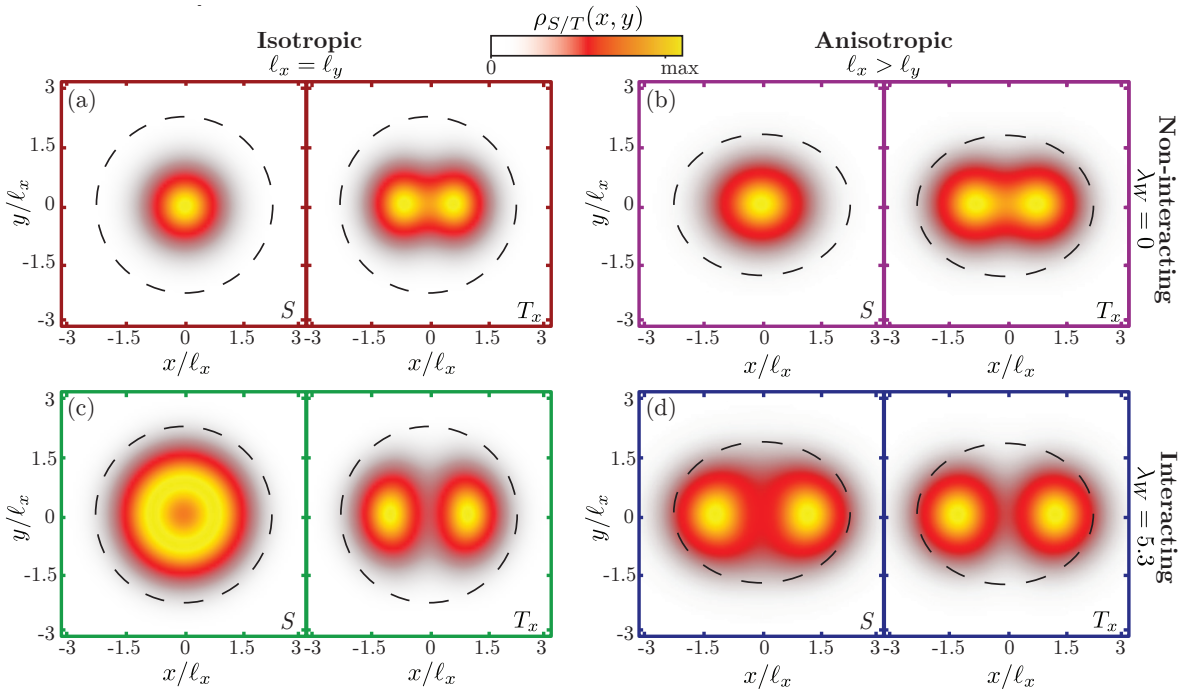

Figure 7.2: Pairs of singlet S and triplet T_x ground state densities for isotropic $\ell_x = \ell_y$ (left) and anisotropic $\ell_y = 0.8\ell_x$ (right) dots, and for non-interacting ($\lambda_W = 0$, top) and interacting ($\lambda_W = 5.3$, bottom) particles. The black dashed ellipses with major axis $4.5\ell_x$ and minor axis $4.5\ell_y$ delineate the shape of the dots.

a doubled mass, which has no effect on the eigenenergies but shrinks the wavefunctions. The relative motion is also described by the Hamiltonian of a 2D harmonic oscillator with a halved mass, plus the extra Coulomb potential.

The relevant energy scales of this problem are the orbital energy $E_{\text{orb}} = \hbar\omega_x$ and the Coulomb repulsion between two electrons separated by ℓ_x, $E_{\text{ee}} = e^2/(4\pi\varepsilon\ell_x)$. We introduce the reduced coordinates $(x', y') = (x/\ell_x, y/\ell_x)$ to write down an unitless Hamiltonian $H'_{\mathbf{r}} = H_{\mathbf{r}}/E_{\text{orb}}$:

$$H'_{\mathbf{r}} = -\partial^2_{x'} - \partial^2_{y'} + \frac{1}{4}\left(x'^2 + \alpha^2\, y'^2\right) + \frac{\lambda_W}{|\mathbf{r}'|}\,, \tag{7.3}$$

where the Wigner ratio λ_W is

$$\lambda_W = E_{\text{ee}}/E_{\text{orb}} \propto \ell_x\,, \tag{7.4}$$

and the anisotropy α reads

$$\alpha = \omega_y/\omega_x = \ell_x^2/\ell_y^2\,. \tag{7.5}$$

The limit $\lambda_W \to 0$ corresponds to effectively turned-off Coulomb interactions either due to $\varepsilon \to \infty$ (complete screening of Coulomb interactions) or a small dot $\ell_x \to 0$ (where the kinetic energy prevails over Coulomb interactions), while large λ_W is associated to a low ε and/or a large dot. Regarding α, perfectly isotropic dots correspond to $\alpha = 1$, whereas $\alpha \to \infty$ when we tend to 1D QDs.

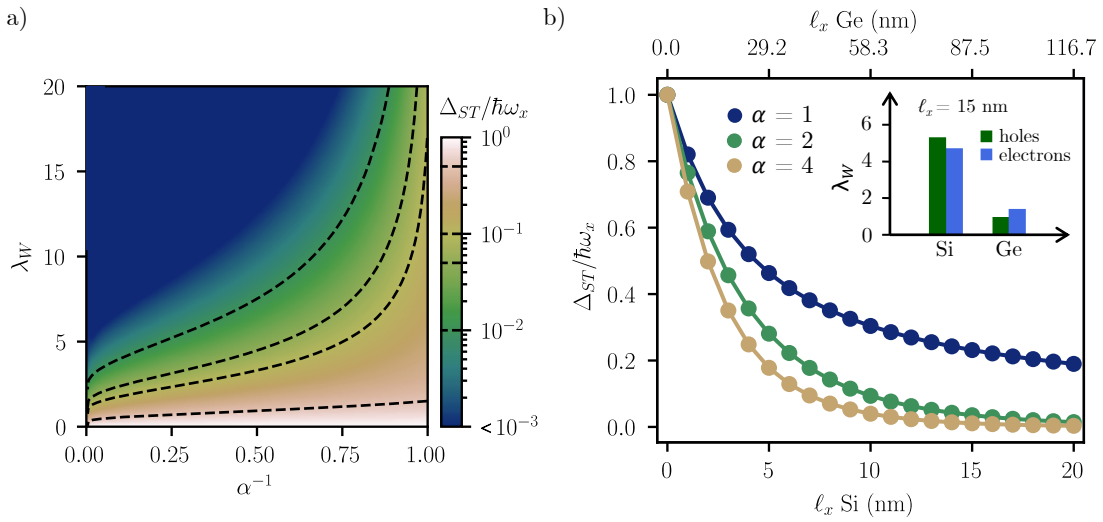

Figure 7.3: Singlet-triplet splitting Δ_{ST} renormalization. a) Effect of Wigner ratio and anisotropy on Δ_{ST}. b) Vertical cuts from a) at $\alpha = 1$, 2, and 4. The x axis has been translated from λ_W to dot size ℓ_x for holes in Si and Ge using the relation given in the inset.

In order to study the effect of interactions and anisotropy we solve equation 7.3 numerically to quantify the singlet-triplet splitting. Let us start discussing the impact of Coulomb interaction on the shape of the singlet and triplet states within the proposed model. For this purpose, we plot the two-particle densities, defined as $\rho_{S/T}(x_1, y_1) = 2\int d^2\mathbf{r}_2\, |\psi_0(\mathbf{R})\varphi_{0/1}(\mathbf{r})|^2$, where $\psi_0(\mathbf{R})$ is the Gaussian ground state wavefunction of the center of mass Hamiltonian in equation 7.2a, and $\varphi_{0/1}(\mathbf{r})$ is the ground/first-excited wavefunction of equation 7.2b.[1] Figure 7.2 shows the two-particle densities of the singlet and triplet states for an isotropic and an anisotropic case, and in presence and absence of interaction. In absence of interaction, we recover the shapes of the single-particle states. Indeed, the anisotropic case in Figure 7.2b resemble that obtained in Figure 7.1b. When the interaction is turned on, the QDs swell. In the isotropic case, the shape of the densities is still similar to those at $\lambda_W = 0$, yet the density maximum is not anymore at the center of the QD for the singlet state. The electron-electron repulsion drives a correlated "dance" between electrons, and the most efficient way to avoid each other is by being in a circular orbit around the origin. For the anisotropic case, however, the shape of the singlet state differs even qualitatively from the case without interaction. We indeed recover the formation of a Wigner molecule as spotted in Figure 7.1d. In this situation, the particles cannot cross each other without coming exceedingly close, and they must split to minimize the Coulomb interactions.

The modulation of the density shapes comes with a decrease of the singlet-triplet splitting, which is always smaller than $\Delta_{ST}^{(0)}$. We show the dependence of Δ_{ST} on the interaction strength λ_W and on the inverse of the anisotropy α^{-1} in Figure 7.3. We do indeed see a strong decay of

[1] $\varphi_0(\mathbf{r})$ corresponds to the singlet state because it is symmetric with respect to an exchange of particles $[\varphi_0(\mathbf{r}) = \varphi_0(-\mathbf{r})]$. Therefore, for the total wavefunction to be anti-symmetric, the spin part must be anti-symmetric. Consistently, the first excited state wavefunction $\varphi_1(\mathbf{r})$ corresponds to the triplet state as it is anti-symmetric $[\varphi_1(\mathbf{r}) = -\varphi_1(-\mathbf{r})]$, so that the spin part must be symmetric.

	γ_1	γ_2	$m_\parallel^{(h)}/m_0$	$m_\parallel^{(e)}/m_0$	ε_r	$\lambda_W^{(h)}/\ell_x$ (nm^{-1})	$\lambda_W^{(e)}/\ell_x$ (nm^{-1})
Si	4.29	0.34	0.21	0.19	11.7	0.35	0.31
Ge	13.38	4.24	0.06	0.08*	16.2	0.06	0.09

Table 7.1: Physical parameters of Silicon and Germanium and scaling factor λ_W/ℓ_x between the major dot radius ℓ_x and the Wigner ratio λ_W. $m_\parallel^{(e)}$ is the in-plane electron mass, $m_\parallel^{(h)} = m_0/(\gamma_1+\gamma_2)$ is the in-plane heavy-hole mass (with γ_1 and γ_2 the Luttinger parameters), and ε_r is the static dielectric constant. All dots are assumed to be strongly confined along $z = [001]$ except (*) for electrons in Germanium ($z = [111]$).

the singlet-triplet splitting when the interaction is turned on. For a given λ_W, the suppression is strongly enhanced by the anisotropy. In particular, $\Delta_{ST} \to 0$ in the pure 1D limit $\ell_y \gg \ell_x$. In Figure 7.3b we highlight such trends, and we see how for a given α we have an exponential decay of Δ_{ST} with increasing λ_W, and how $\alpha > 1$ further strengthens the decrease.

The inset of Figure 7.3b shows the value of λ_W in electron and hole QD with size $\ell_x = 15$ nm in Si and Ge. This allows to extract the expected Δ_{ST} renormalization we could expect on a QD with arbitrary size as $\lambda_W \propto \ell_x$. The different size of the bars already hints a strong dependence on the material. At a given QD size, Silicon is expected to suffer much stronger renormalizations than Germanium, and the differences between electrons and holes are secondary with respect to those between materials. Moreover, QDs in Germanium devices tend to be made isotropic, whereas for Si, and in particular in Si MOS LETI devices, the QDs are strongly anisotropic due to the gate layout.

The dependence on the material comes from the scaling factor in the proportionality between λ_W and ℓ_x shown in equation 7.4. In fact, $\lambda_W = me^2/(\pi\hbar^2\varepsilon)\cdot\ell_x$. We provide the relevant material parameters, together with the λ_W/ℓ_x scaling factor in Table 7.1. Indeed, the very similar effective masses between electrons and holes are responsible for their weak differences in the inset of Figure 7.3b. Moreover, Si shows larger masses and smaller dielectric constant than Ge, both responsible for the smaller $\Delta_{ST}/\hbar\omega_x$ of the former. It is important to remind, however, that experimentally QDs in Ge devices are generally larger than those hosted in Si, which would counteract the discussed benefits. Still, the present calculations highlight that dots can be made up to six times larger in Ge than in Si before undergoing a comparable reduction of $\Delta_{ST}/\hbar\omega_x$. In this context, it becomes of interest to estimate the reduction of the singlet-triplet splitting in experimental device geometries for both materials and obtain estimations for realistic dot sizes and shapes.

7.3 Simulation of realistic devices

Now that we have established how the singlet and triplet states are renormalized by Coulomb interactions in an ideal harmonic potential, we investigate how Wigner molecularization affects realistic Si and Ge devices, similar to those used experimentally. For Silicon, we focus on the Si MOS devices studied in Chapter 4; whereas for Germanium we analyze the impact on the planar device studied in section 6.3.

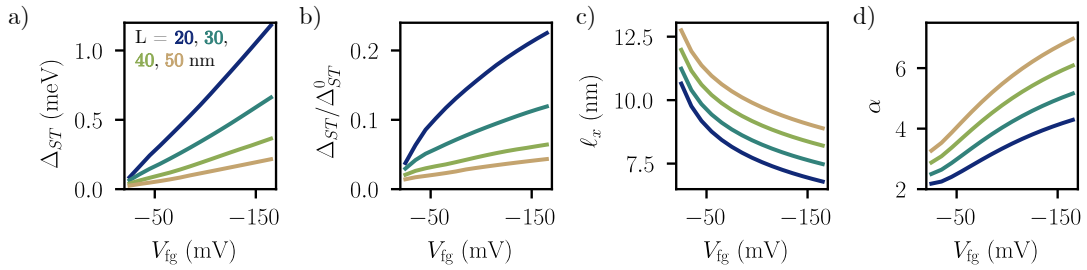

Figure 7.4: Simulations of the Si MOS device of Figure 4.1. a) Singlet-triplet splitting as a function of $V_{\rm fg}$ for different gate lengths L. b) Renormalization of Δ_{ST} in a) with respect to the single-particle picture. c) Dependence of the QD size ℓ_x on $V_{\rm fg}$ for different L. c) Dependence of the anisotropy α on $V_{\rm fg}$ for different L. $V_{\rm fg}$ controls both the QD size and its anisotropy.

7.3.1 Si MOS devices

As a Si MOS device we simulate the same single-gate device illustrated in Figure 4.1. We use two parameters to tune both λ_W and α: The front gate voltage ($V_{\rm fg}$) and the gate length (L). Longer gates increase ℓ_x thus λ_W, and enhance the anisotropy α. Similarly, a stronger $V_{\rm fg}$ reduces the size of the QD owing to a stronger confinement, and also modulates α. In the following, we explore $L = 20 - 50$ nm and $V_{\rm fg}$ ranging between -25 and -175 mV.

The results are shown in Figure 7.4. Figures 7.4c and 7.4d show the dependence of ℓ_x and α on $V_{\rm fg}$ and L, and we do indeed recover the expected results discussed above. A more negative $V_{\rm fg}$ increases the anisotropy and decreases the dot size, whereas a larger L increases both ℓ_x and α. Very anisotropic QDs with $\alpha > 6$ can be achieved with such gate layouts. The absolute singlet-triplet splitting Δ_{ST} is plotted as a function of $V_{\rm fg}$ in Figure 7.4a, and it can be lower than $100\,\mu$eV for weak $V_{\rm fg}$. The renormalization of the singlet-triplet gap by Coulomb interactions can be appreciated in Figure 7.4b, where Δ_{ST} is strongly reduced with respect to the orbital splitting $\Delta^{(0)}_{ST}$ in the non-interacting dot. For the gate lengths and biases considered here, $\Delta_{ST}/\Delta^{(0)}_{ST}$ hardly reaches 0.2. These trends are qualitatively consistent with the discussion in section 7.2: the bare singlet-triplet splitting $\Delta^{(0)}_{ST}$ is heavily suppressed by interactions. As expected, $\Delta_{ST}/\Delta^{(0)}_{ST}$ decreases with increasing gate length. It also decreases with decreasing $|V_{\rm fg}|$ (namely, with softening confinement), which shows that the impact of $|V_{\rm fg}|$ is dominated by the decrease of ℓ_x rather than by the increase of α. Altogether, the calculated suppression of $\Delta_{ST}/\Delta^{(0)}_{ST}$ can be considered strong in such Si MOS devices.

7.3.2 Ge/SiGe heterostructures

As previously mentioned, anisotropic QDs have been proposed as a way to achieve fast qubit operations in Germanium [89]. However, the previous results envision critical consequences due to electron-electron interactions if one tries to exploit such possibility. Here we evaluate the impact of anisotropy in the Wigner molecularization of Ge QDs in the single-qubit device of Figure 6.1c. Results are shown in Figure 7.5.

In contrast with Si MOS, where $V_{\rm fg}$ controls both the dot size ℓ_x and the anisotropy α, in Ge heterostructures there are two knobs tuning rather independently these two parameters.

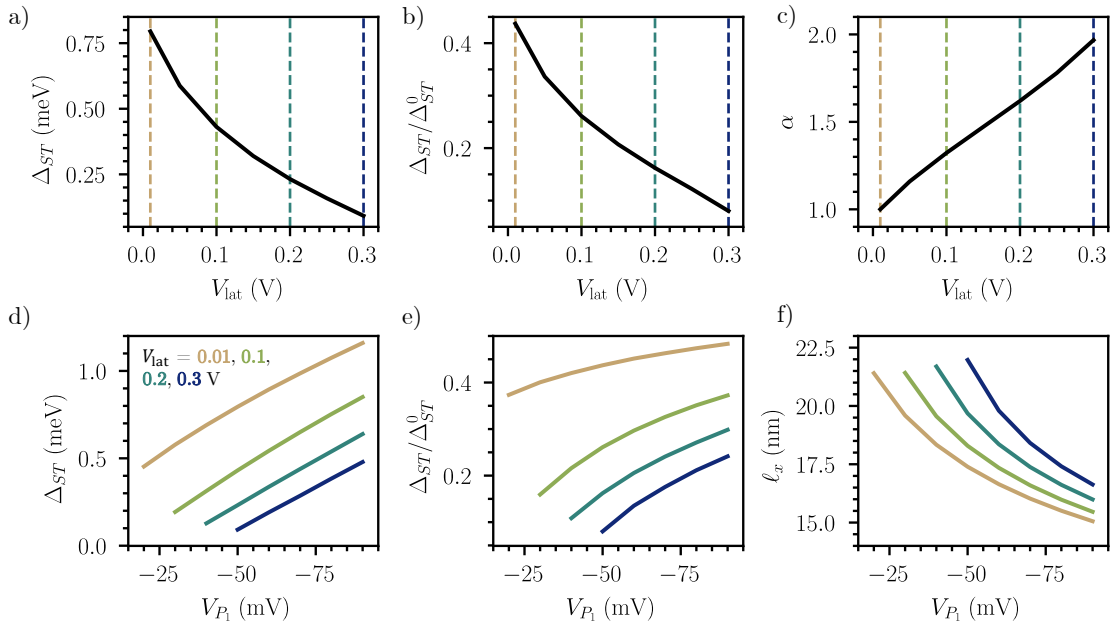

Figure 7.5: Simulations for the planar Ge device of Figure 6.1c. a) Singlet-triplet splitting dependence on the voltage applied to a pair of lateral gates $V_{\rm lat}$. The other pair is fixed at $V = 10$ mV, and $V_{\rm fg} = -50$ mV. b) Renormalization of the singlet triplet splitting in a). c) Dependence of the QD anisotropy on $V_{\rm lat}$. d) Singlet-triplet splitting dependence on $V_{\rm fg}$ for $V_{\rm lat} = 0.01$ (isotropic case), 0.1, 0.2, and 0.3 V. e) Renormalization of the singlet-triplet splittings in d). f) Dependence of the QD size on $V_{\rm fg}$ for the $V_{\rm lat}$ in d).

V_{P_1} controls mostly ℓ_x, whereas the ratio between the voltage applied to the lateral B gates determines α. Here, we fix $V_{B_1} = V_{B_2} = 10$ mV, and we tune $V_{B_3} = V_{B_4} = V_{\rm lat}$ to induce an anisotropy in the QD shape. Figure 7.5c shows how much α can be tuned electrostatically. Note that the anisotropy that can be reached is sensibly weaker than in the Si MOS devices, mainly due to the large distance between the QD and the gates.

The size of the QDs ℓ_x is controlled by V_{P_1}. In Figure 7.5f we can see for different anisotropies that indeed the QDs are substantially larger for Ge than for Si in the simulated realistic devices. Even though the figures of merit for Ge remain slightly better than for Si, even in the perfect isotropic case $\Delta_{ST}/\Delta^{(0)}_{ST}$ always remains below 0.5. Making the Ge QDs smaller indeed contributes to palliate the renormalization Δ_{ST}. The simulations show that, even though Germanium QDs are expected be less affected by molecularization effects than their Silicon counterparts, they are not so far in practice, and if the dots are made anisotropic, the situation rapidly degrades to similar values. For Germanium, the key remains the same: dots must be as isotropic and as small as possible to prevent strong renormalizations of the singlet-triplet gap.

7.4 Implications for spin qubits

All the discussion up to now focused on a doubly occupied QD, which in fact is not a spin qubit. Such system, however, becomes relevant in two situations for a quantum processor: when reading

out a spin qubit relying on PSB, and when leveraging exchange interactions. In both cases, a double QD system is involved. The Hamiltonian for such system at $B = 0$ in the minimal basis set $\{S(1,1),\, T(1,1),\, S(0,2),\, T(0,2),\, S(2,0),\, T(2,0)\}$,[2] where $T(1,1), T(0,2), T(2,0)$ are one of the three degenerate triplet states,[3] reads

$$H = \begin{pmatrix} 0 & 0 & \tau_S & 0 & \tau_S & 0 \\ 0 & 0 & 0 & \tau_T & 0 & \tau_T \\ \tau_S & 0 & -\varepsilon' + U & 0 & 0 & 0 \\ 0 & \tau_T & 0 & -\varepsilon' + U + \Delta_{ST}^{(2)} & 0 & 0 \\ \tau_S & 0 & 0 & 0 & \varepsilon' + U & 0 \\ 0 & \tau_T & 0 & 0 & 0 & \varepsilon' + U + \Delta_{ST}^{(1)} \end{pmatrix}, \tag{7.6}$$

where U is the intra-dot charging energy (assumed identical in both dots), and $\Delta_{ST}^{(1,2)}$ is the singlet-triplet splitting in dots 1 and 2. The detuning ε' is measured with respect to the SOP (the center of the (1,1) region). The energy diagram from this Hamiltonian is plotted in Figure 7.6a for different Δ_{ST}. The presence of triplet anticrossings nearby has an impact on the (1,1) states (see Figure 7.6c as an example), thus on the two-qubit system. Hereafter we discuss the impact that the renormalization of the singlet-triplet splitting can have in the management of readout and exchange interactions.

7.4.1 Pauli spin blockade readout

As explained in section 1.3.3, readout mechanisms relying on PSB make use of an auxiliary QD to attempt a (1,1) $\rightarrow$ (2,0) transition. There, the readout mechanism was explained in terms of the single-particle picture. In the two-particle picture, the readout consists in shifting ε adiabatically from the $(1,1)$ to the $(2,0)$ charge configuration. If the initial state is $S(1,1)$, a charge transition will occur when going through the $S(1,1)/S(2,0)$ anticrossing, whereas if the initial state is a $T(1,1)$ the system will remain in the $(1,1)$ state until ε reaches the triplet anticrossing. The presence (absence) of charge transition indicates the singlet (triplet) character of the initial state. Consequently, the performance of this readout mechanism is limited by the presence of low-lying $T(0,2)$ states that bring a $T(1,1)/T(0,2)$ anticrossing close to the $S(1,1)/S(0,2)$ one, see Figure 7.6b. Spurious transition from $T(1,1)$ to $T(0,2)$ during readout can be confused with the monitored $S(1,1) \rightarrow S(0,2)$ transition and spoil the measurement.

To quantify the readout error induced by $T(0,2)$ we assume that only tunneling between singlet and between triplet states with the same spin projection is allowed, and we consider the situation where the Zeeman splitting remains much smaller than Δ_{ST}. Within this approximation, the effective Hamiltonian of the $\{S(1,1), S(0,2), T(1,1), T(0,2)\}$ states reads:

$$H = \begin{pmatrix} 0 & \tau_S & 0 & 0 \\ \tau_S & -\varepsilon' & 0 & 0 \\ 0 & 0 & 0 & \tau_T \\ 0 & 0 & \tau_T & -\varepsilon' + \Delta_{ST} \end{pmatrix}, \tag{7.7}$$

[2] The basis set includes now the $T(2,0)$, $T(0,2)$ states disregarded in the model of section 2.5.2.

[3] At $B = 0$, the three triplet states (T_0, T_+, T_-) behave identically, so we include only one.

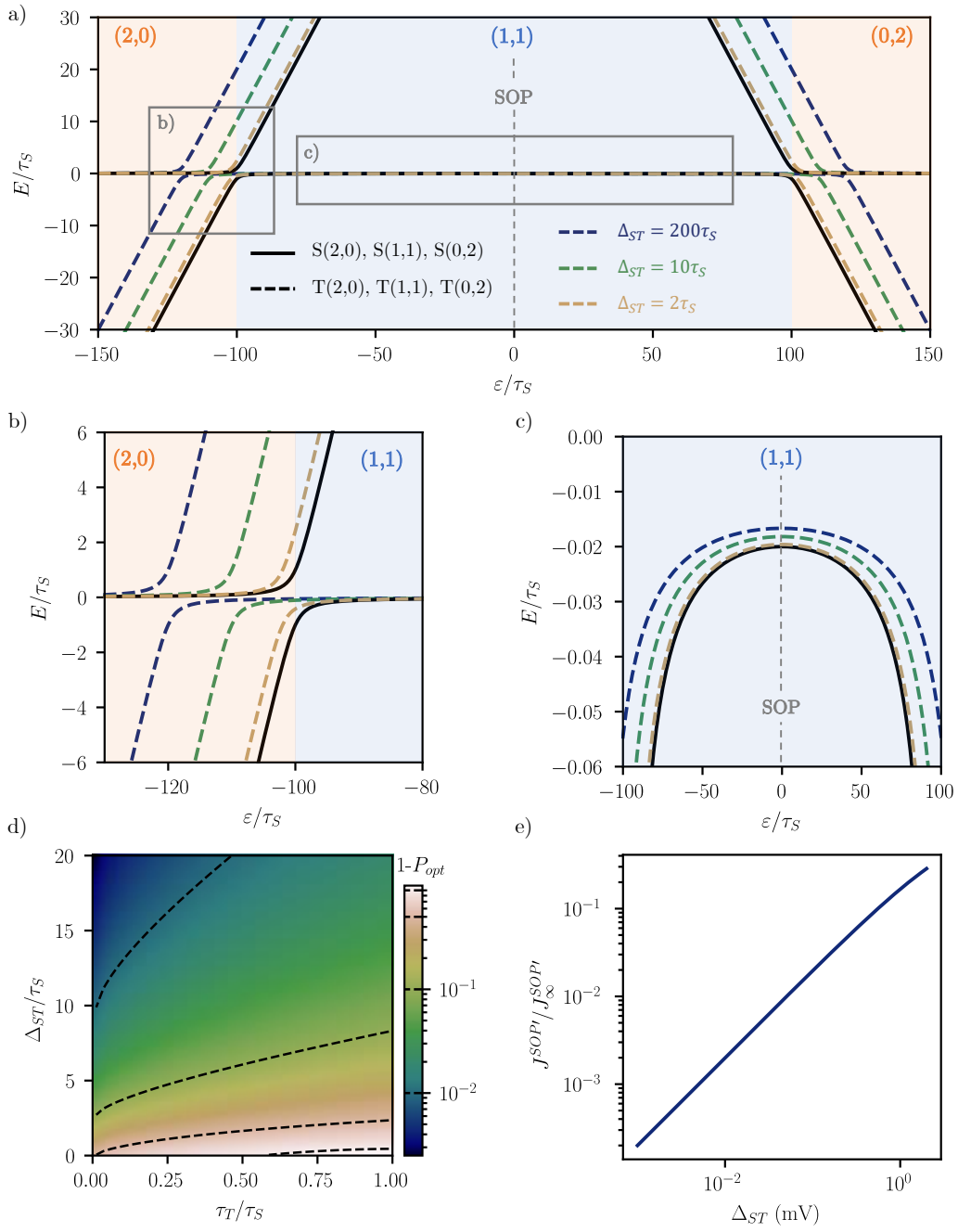

Figure 7.6: a) Energy diagram resulting from the diagonalization of equation 7.6 for different Δ_{ST}. We use $\tau_s = \tau_T$, and $U = 5$ meV. b) Zoom into the (2,0)-(1,1) anticrossing, relevant for Pauli spin blockade readout. c) Zoom into the SOP, relevant for exchange coupling. d) Probability of readout error $1 - P_{\text{opt}}$ at the optimal readout point as a function of the triplet tunnel coupling τ_T and the singlet-triplet splitting Δ_{ST}, both given in units of the singlet tunnel coupling τ_S. e) Tunability of $J^{SOP'}$ (in units of $J^{SOP'}_{\infty}$) as a function of Δ_{ST}.

where τ_S is the singlet-singlet tunneling, and τ_T the triplet-triplet tunneling. The energy diagram resulting from the diagonalization of the former Hamiltonian is shown in Figure 7.6b for different Δ_{ST}/τ_S. Realistic tunnel couplings are typically in the $\gtrsim 10$ μeV range. We do observe how the triplet anticrossing gets close to the singlet one when Δ_{ST} is reduced.

When performing PSB readout, ε' is swept from the $(1,1)$ to the $(0,2)$ charge configuration, and we assume that it can be swept adiabatically. Optimizing readout amounts to maximize the probability P_S of a $S(1,1) \rightarrow S(0,2)$ transition while minimizing the probability P_T of a $T(1,1) \rightarrow T(0,2)$ transition. From the eigenvectors of equation 7.7 we get

$$P_S = \frac{1}{2} + \frac{\varepsilon}{2\sqrt{\varepsilon^2 + 4\tau_S}}\,, \tag{7.8a}$$

$$P_T = \frac{1}{2} + \frac{\varepsilon - \Delta_{ST}}{2\sqrt{(\varepsilon - \Delta_{ST})^2 + 4\tau_T}}\,. \tag{7.8b}$$

We hence need to maximize the quantity $P = P_S - P_T$, which stands for the probability of having no error in the readout. Since the singlet and triplet anticrossings occur at different detuning, it is clear that there is an optimal value (ε_{opt}) that maximizes $P = P_S - P_T$. The optimal no-error probability P_{opt} depends on Δ_{ST}, τ_S, and τ_T. In Figure 7.6d we show the dependence of 1-P_{opt} (the probability to have an error) on Δ_{ST} and τ_T/τ_S. As an example, assuming $\tau_T = \tau_S = \tau$, achieving $1 - P_{\text{opt}} = 10^{-2}$ calls for $\Delta_{ST} > 28\tau$. With a readout tunnel couplings $\tau \gtrsim 10$ μeV, Δ_{ST} must, therefore, be at least $\simeq 300$ μeV, a value that may not be so easy to achieve in an anisotropic quantum dot in view of the numerical results discussed above.

In practice, τ_S and τ_T can be tuned electrically by a tunnel gate that controls the inter-dot space. However, the ratio τ_T/τ_S is likely difficult to adjust, as the tunnel gate will in general act in a similar way on τ_S and τ_T. The ratio Δ_{ST}/τ_S is *a priori* much easier to control: either the quantum dot gate is biased to reshape the confinement and increase Δ_{ST}, or the tunnel gate tuned to decrease τ_S. However, reducing τ_S too much will ultimately break adiabaticity along the $(1,1) \rightarrow (2,0)$ transition, thereby compromising the visibility of the singlet state. So, the main requisite to ensure a minimal error in the readout is to have the largest Δ_{ST} possible, which may be compromised by the Wigner molecularization effects.

7.4.2 Exchange coupling

From the energy diagram in Figure 7.6c it is clear that the reduction of Δ_{ST} will have an impact on J. As explained in Chapter 5, protocols to achieve exchange interaction can rely on detuning the two qubits close to the (1,1)-(2,0) anticrossing, or on tuning the tunnel coupling with J-gates. In both cases, there is a renormalization of J due to the many-body effects: at a given detuning point, it becomes smaller due to the triplet state having a similar bending as the singlet when Δ_{ST} decreases. When relying on detuning, it can be understood from Figure 7.6b that this bending also leaves a reduced effective exchange. In the limit where $\Delta_{ST} \rightarrow 0$, $J \rightarrow 0$.

It is of much more interest, however, to rely on J-gates to tune J, and stay at the SOP ($\varepsilon' = 0$). There, $\partial J/\partial\varepsilon = 0$, and J is consequently insensitive to detuning noise. At the SOP, the exchange coupling can be extracted as the splitting between the dressed $S(1,1)$ and $T(1,1)$

states from equation 7.6 and reads:

$$J^{\mathrm{SOP}} = J_{\infty}^{\mathrm{SOP}} - \frac{1}{2}\left(\frac{2\tau_T^2}{U+\Delta_{ST}^{(1)}} + \frac{2\tau_T^2}{U+\Delta_{ST}^{(2)}}\right), \tag{7.9}$$

where we have introduced $J_{\infty}^{\mathrm{SOP}} = 2\tau_S^2/U$, the usual exchange coupling at the SOP when $\Delta_{ST} \to \infty$. This quantifies the renormalization of J^{SOP} induced by the nearby triplet states, patent in the energy diagram of Figure 7.6c.

The renormalization of J^{SOP} itself is not too critical, since the J-gates are in fact dedicated to tune it. One could correct this renormalization by applying the corresponding pulses to the J-gates and end up with the desired exchange coupling. J^{SOP} indeed increases linearly with V_J. Unfortunately, the tunability of J is also strongly suppressed when Δ_{ST} decreases. If we assume symmetric dots, $\tau_S = \tau_T = \tau$, $\partial\tau_S/\partial V_J = \partial\tau_T/\partial V_J$, and $\Delta_{ST}^{(1)} = \Delta_{ST}^{(2)} = \Delta_{ST}$, we can easily evaluate $\partial J^{SOP}/\partial\tau$:

$$J^{SOP\prime} = \frac{\partial J^{SOP}}{\partial\tau} = \frac{\partial J_{\infty}^{SOP}}{\partial\tau} - \frac{4\tau}{\sqrt{2}}\frac{1}{U+\Delta_{ST}}, \tag{7.10}$$

where

$$J_{\infty}^{SOP\prime} = \frac{\partial J_{\infty}^{SOP}}{\partial\tau} = \frac{4\tau}{\sqrt{2}U}. \tag{7.11}$$

We can finally divide equations 7.10 and 7.11 to obtain:

$$J^{SOP\prime}/J_{\infty}^{SOP\prime} = 1 - \frac{U}{U+\Delta_{ST}}, \tag{7.12}$$

which indeed describes a strong decrease of the exchange tunability when Δ_{ST} becomes comparable or smaller than U. Note that typically $U = 5-10$ meV, whereas the values reported above for Δ_{ST} are systematically smaller.

We illustrate the magnitude of the renormalization of the J tunability in Figure 7.6e, assuming $U = 5$ meV. Indeed, the renormalization is strong, with $J^{SOP\prime}$ being more than one order of magnitude smaller than $J_{\infty}^{SOP\prime}$ for $\Delta_{ST} < 500$ μeV. It is very unlikely that we can reach $U \simeq \Delta_{ST}$ in presence of electron-electron interaction for any platform regardless of the anisotropy of the QDs, and therefore we should expect a strong decrease of $J^{SOP\prime}$. This effect certainly complicates the management of exchange interactions, yet the tunability of τ can reach experimentally almost 10 orders of magnitude [157]. With a tunability of J over 3-4 orders of magnitude being sufficient to manage two qubit operations, the renormalization discussed here may still be compensated by larger pulse amplitudes in practice.

7.5 Chapter 7 in a nutshell

In this Chapter, we have seen how much the electron-electron interactions can change the physics of a many-particle system with respect to the single-particle picture. The spatial separation of the two electrons in a doubly occupied QD brings a decrease of the singlet-triplet splitting Δ_{ST}, which may have critical implications for spin qubits. In particular, it may complicate the readout based on Pauli spin blockade due to the appearance of undesired T(1,1) $\to$ T(2,0) transitions;

and it may hinder the management of exchange interactions, since a renormalization of the exchange coupling J is accompanied by a strong decrease of its tunability *via* J-gate pulses. Overall, this highlights the strong impact of correlation on the properties of a qubit, and the importance of including them in the simulations if one wants to capture the correct physics of the system.

In practice, the above-mentioned problems are drastically enhanced with the anisotropy of the QD, so relying on highly symmetrical 2D QDs partly mitigates these effects. Small dots also prevent correlation to become dominant over kinetic energy and split the two particles, limiting the Δ_{ST} drop. In terms of materials, for QDs with the same size, Si is more strongly affected by molecularization effects than Ge, which suggests that Ge 2D QDs with $\ell_x < 20$ nm are the best choice to overcome such complications.

Here we have considered two-particle systems, where the qubits themselves are still considered as singly occupied QDs. There are still plenty of unknowns in the effect of many-body physics into the qubit properties. In view of these results, the simulation of a triply occupied QD becomes very relevant. The exploration of hole g-factors, Rabi frequencies, or even the variability as a function of the QD filling remains to be addressed.

Chapter 8

Conclusions

Quantum processors are complex systems that gather together several fields of research. From the software side, they require the deepest understanding on quantum mechanics to explain and exploit their potential advantages, and from the hardware side contributions from physics and materials science are key to make the quantum chips larger and more robust. Not to forget the massive engineering challenge that embedding together the classical electronics, the quantum chip and the cryogenics supposes. In this thesis we have focused on the hardware-side of the quantum computing problem, and identified several rocks-in-the-shoe that a very promising platform, the QD-based spin qubits, may have to face to become the powerful machines that quantum computers are entitled to be. On this journey, modeling in general, and numerical modelling in particular has a lot to say, and it has been proven to be a crucial tool describe and understand experimental observations, as well as to guide the development and improvement of spin qubit platforms.

We have learnt that Si MOS devices, even if they can benefit from the industrially compatible fabrication processes used in classical electronics, may see their scalability compromised by the defective character of their Si/SiO_2 interface. The amorphous nature of SiO_2 yields to rough interfaces and dangling Si bonds that become charge traps. Spins, *a priori* insensitive to electric fields, are sensitive to variations on the orbital part of the qubit in presence of SOC mechanisms. Disorder modulating the QD shape induces a variability on the spin properties. We have quantified this variability for the single- and two- qubit properties of electron and hole spin qubits in Si MOS devices. For the single-qubit properties, we have found that variability in the Rabi frequencies, dominated by charge traps, can reach 60% both for electrons and holes at a charge trap density $n_i = 5 \times 10^{10}$ cm^{-2}; and that it arises due to the induced fluctuations of the QD size. Larmor frequencies show similar variabilities due to surface roughness and charge traps, reaching 10% for holes and 0.05% for electrons. Still, such variability may prevent to address nearly 50% of the qubits with a single RF line by relying on the Stark effect for both types of carriers. Two-qubit properties also suffer strong modulations due to disorder, with variabilities in the qubits' energy and tunnel barrier of the order of 10 meV, which is comparable to qubits charging energy. The mitigation of variability to manageable values in a large-scale quantum processor would require $n_i << 10^{10}$ cm^{-2}, which is well-beyond the current state-of-the-art.

Spin qubits based on Germanium have impressively progressed in the last years, and are believed to be more resilient to variability due the epitaxial character of the Ge/SiGe interfaces. In such devices, the defects are shifted to the top $SiGe/Al_2O_3$ interface, which can host defects at a density of $n_i = 10^{11}$ cm^{-2} or higher. Along with the raising interest in Ge at CEA, we have modeled these qubit devices to explore their physics. The simulation of their complex electrostatics has unveiled a mechanism bringing finite Rabi frequencies for an in-plane magnetic field and RF drive, which appears due to the inhomogeneity of the vertical electric field. This feature, very narrow in plane, is enhanced for large dots and small HH-LH splitting; and its

width is entirely dominated by the g_z/g_x ratio. We have also evaluated the variability induced by charge traps in these devices, and while two-qubit properties appear to be more resilient (with variabilities of roughly 2 meV for the qubits energy and tunnel barrier), we still obtain RSDs for f_R and $g_{\|}$that are not much better than those of Si MOS devices.

As mentioned above, numerical modelling is an excellent tool to drive and optimize device designs. In this sense, we have aided in the design of the new J-gates included in the Si MOS devices fabricated at CEA LETI. We have highlighted that the non-locality of the potential they generate is a consequence of their large distance from the Si film, and we have found that their selectivity and efficiency is controlled by the different spacings between the front gates below. These discoveries have shaped the final design, which has recently been proven functional experimentally. Additionally, we have designed a novel gate layout for Ge/SiGe devices based on a 2D array of rounded-square-shaped gates that penetrate into the SiGe. Such architecture reduces significantly the variability of standard gate layouts for Ge/SiGe hole spin qubits, especially for small gate coverages.

Simulations are often limited to single-particle states. Many-body interactions may also impact the QD properties and condition the operation of spin qubits. We have discussed a many-body effect, the so-called Wigner molecularization, that splits the two particles apart in doubly occupied QDs. A drastic reduction of the singlet-triplet splitting comes along with this spatial separation, which can compromise readout techniques based on PSB and the manipulation of exchange interactions. We emphasized that this effect is enhanced with the anisotropy of the QD and with its size, suggesting that small, highly symmetric QDs are optimal to prevent Wigner molecularization. These results may explain recurrent experimental difficulties in performing PSB readout, and highlight the importance of including many-body interactions in the simulation of spin qubits.

Overall, we have identified and understood several key aspects that may play an important role not only in the near future, but also on the present QD-based spin qubits. Yet there is still a long path ahead for the modeling on the way towards robust quantum architectures. In the following we review open directions.

8.1 Future perspectives

The field of semiconductor spin qubits evolves fast, and part of what makes it so exciting is that it is hard to predict what the future holds. Even the most optimistic would have had troubles to believe back in 2018 that epitaxial heterostructures would show such a meteoric progress, and would overcome all existing spin qubit platforms in such a short time. Still, we can define a few lines of research that appear as crucial in the near future.

From the simulation perspective, in view of the strong impact of many-body effects in the singlet-triplet splitting, it becomes extremely relevant to study how correlations reshape the effective g-factors and Rabi frequencies of hole spin qubits. The simulation of a many-particle qubit would include at least three particles, and its modeling with CI becomes computationally expensive. Moreover, it still remains as an open question whether variability improves or degrades with the QD filling. To address it, specific methodological development is required.

Another crucial aspect for simulations is to improve the description of valley physics for electron spin qubits. In this thesis, we have overlooked the valley states when simulating elec-

trons, assuming that the valley splitting was large enough to be disregarded. Tight Binding simulations include the valley states and can describe valley effects, yet the current models for the passivation of Si films are not accurate enough to reproduce experimental evidences. The improvement of passivation models is key to understand and describe the behavior of valley states.

It will also be crucial to follow and assist the experimental progress in the near future. With the CEA starting experimental activities in Ge/SiGe spin qubits, it will be a great opportunity to experimentally demonstrate the novel mechanism for f_R unveiled in this thesis. Moreover, when devices relying on tip gates geometry arrive, the experimental characterization of their performance with respect to planar geometries will certainly be addressed. Regarding Si MOS devices, work will be focused on the exploitation of the J-gates to demonstrate two-qubit operations for hole spin qubits. In parallel, micro-magnets should be included in electron devices to enable electrical manipulation. Finally, great progress has been made in the last months at CEA on the coherent coupling of hole spin qubits with photons. Holes are an exciting platform for such experiments due to their intrinsic SOC, and great advances are to be expected in this field in the near future.

Appendices

Appendix A

Chapter 2

A.1 Disentangling the origin of the Rabi oscillations

In the following, we propose a splitting of the Rabi frequencies that enables to discuss the origin of the Rabi oscillations in terms of the g-TMR and IZ-EDSR (Rashba-type) contributions exposed in section 2.5.1.2. If we introduce Single Value Decomposition (SVD) of the g-matrix,

$$\hat{g}\left(V_0\right) = u\left(V_0\right)\hat{g}_d\left(V_0\right)v^{\dagger}\left(V_0\right) \tag{A.1}$$

where the matrices $u\left(V_0\right)$ and $v^{\dagger}\left(V_0\right)$ are the rotations of the spin and magnetic axes of $\hat{g}\left(V_0\right)$ that bring it into a diagonal form $\hat{g}_d$. We can now calculate $\hat{g}'\left(V_0\right)$, which reads

$$\hat{g}'\left(V_0\right) = u'\left(V_0\right)\hat{g}_d\left(V_0\right)v^{\dagger}\left(V_0\right) + u\left(V_0\right)\hat{g}'_d\left(V_0\right)v^{\dagger}\left(V_0\right) + u\left(V_0\right)\hat{g}_d\left(V_0\right)v^{\dagger\prime}\left(V_0\right) \tag{A.2}$$

where $\hat{g}'_d\left(V_0\right)$ is the diagonal matrix of derivatives of the main g-factors, and $v_d^{\dagger\prime}\left(V_0\right)$, $u'_d\left(V_0\right)$ are the derivatives of the magnetic and spin axes, respectively. Each of the terms in the sum above contributes to f_R, which can be computed individually as in equation 2.25,

$$\boldsymbol{f_R}[M] = \frac{\mu_B V_{\mathrm{ac}}}{2h|\hat{g}\left(V_0\right)\boldsymbol{B}|}\left[\hat{g}\left(V_0\right)\boldsymbol{B}\right] \times \left[M\left(V_0\right)\boldsymbol{B}\right], \tag{A.3}$$

where M is one of the three terms in the sum of equation A.2.

The $\hat{g}'_d\left(V_0\right)$ term, being a modulation of the principal g-factors, corresponds to a g-TMR mechanism. We can compute its contribution as

$$f_R^{\mathrm{TMR}} = |\boldsymbol{f_R}[u\left(V_0\right)\hat{g}'_d\left(V_0\right)v^{\dagger}\left(V_0\right)]|. \tag{A.4}$$

Moreover, we group the terms implying a rotation of the axes of $\hat{g}$ in what we label as f_R^{RA},

$$f_R^{\mathrm{RA}} = |\boldsymbol{f_R}[u'\left(V_0\right)\hat{g}_d\left(V_0\right)v^{\dagger}\left(V_0\right) + u\left(V_0\right)\hat{g}_d\left(V_0\right)v^{\dagger\prime}\left(V_0\right)]|. \tag{A.5}$$

The term with $u'_d\left(V_0\right)$, being a rotation of the spin quantization axes, does not modulate g^*, and can therefore be considered an IZ-EDSR mechanism. In fact, it gathers the Rabi oscillations arising from Rashba-type SOC [60, 89]. The term including $v_d^{\dagger\prime}\left(V_0\right)$ is the rotation of the magnetic axes, and it may (and may not) leave the Zeeman splitting invariant. Consequently, the f_R^{RA} term is not entirely IZ. This splitting differs from former proposals in the literature (see Ref. [63]), in which the segregation of f_R^{RA} into pure g-TMR and a pure IZ-EDSR may yield to strong cancellations between the individual contributions. The insights of these cancellations are discussed in detail in Ref. [58].

A.2 List of input parameters for the single-particle calculations

In this Appendix, we list the parameters used in this thesis to perform the **k·p** calculations. As explained in sections 2.1.1 and 2.1.2, both **k·p** and TB methods are semi-empirical, in the sense that they require a set of input parameters to perform the calculations. In the following, we give the main parameters we have used to perform **k·p**, and those used for TB can be found in Ref. [158].

	κ	γ_1	γ_2	γ_3	Δ_{SO} (eV)
Si	-0.42	4.285	0.339	1.446	0.044
Ge	3.41	13.38	4.24	5.69	0.290
$Si_{0.2}Ge_{0.8}$	2.64	11.56	3.46	4.84	0.241

Table A.1: List of input parameters required to perform a 6kp calculation for holes in Silicon, Germanium, and $Si_{0.2}Ge_{0.8}$.

	m_t	m_l
Si	0.916 m_0	0.191 m_0

Table A.2: List of input parameters required to perform an EMA calculation for electrons in Silicon.

Appendix B

Chapter 3

B.1 Tunnel coupling estimations in defective devices

In presence of disorder, the extraction of the tunnel coupling, even in the SP picture, is not straightforward. For a double QD, disorder may shift the anticrossing position to finite detuning, and it may as well change τ and shift the energy of the system (E). The mapping into the models discussed in section 2.5.2 requires the energy spectrum of the double QD system at the bias where the system is tuned. This bias, evident for pristine devices due to symmetries (typically the double QDs are tuned when the same gate voltage is applied to all gates forming the QDs.), is certainly not obvious in presence of disorder. In the following, we describe an automated process to numerically extract the gate corrections required to re-tune the defective device to $\varepsilon = 0$. Once the system is tuned, we can make use of the models in section 2.5.2 to estimate τ. However, we may also attempt to restore the QDs energy (E) and τ with gate pulses so as to reach the same energy and tunnel coupling as in absence of disorder. In this way, we can fully evaluate the impact of disorder on the two-qubit properties by analyzing how large are the corrections required to restore the pristine situation.

Let us think on a device with a double QD defined by two front gates ($V_{\mathrm{fg},1}$, $V_{\mathrm{fg},2}$), and with a gate dedicated to modulating the tunnel coupling (V_{J}). If the device has a ($\boldsymbol{yz}$) symmetry plane, in absence of disorder the lever-arm (α) of the two front gates is the same, and V_{J} tunes τ but not ε. We can take as reference the pristine device at the (1,0)-(0,1) anticrossing (ε=0, $V_{\mathrm{fg},1}$=$V_{\mathrm{fg},2}$) with a given energy at the center of the anticrossing E_0 and tunnel coupling τ_0. Disorder breaks the device symmetry, as it may displace and reshape the QDs; a defective device at the same bias as the reference one will not be at the center of the anticrossing, and will have a possibly different energy E and tunnel coupling τ. We may retune the device to the (1,0)-(0,1) anticrossing, to the same energy, and eventually to the same tunnel coupling as the reference device. Let us see how we can do it from a single SP calculation.

The impact of bias shifts in the SP Hamiltonian is included, at first order, in the $D_i = \partial H^{\mathrm{SP}}/\partial V_{\mathrm{i}}$ matrices, which can be computed for a SP calculation as the solution of Poisson's equation for a 1 V pulse in gate i and all other gates grounded. Therefore, we can make use of them to estimate H^{SP} to nearby biases, and search for the set of gate pulses needed to fulfill $E = E_0$, $\tau = \tau_0$, and $\partial E/\partial \varepsilon = 0$ (center of the anticrossing). To do so, we express H^{SP} and the D_i matrices in a subset of SP states, which must be large enough to catch the effect of the gate pulses in the Hamiltonian accurately.

To pulse the system to the (1,0)-(0,1) anticrossing we first evaluate the average position of the double QD system. If the device is not at the anticrossing, the system is in a single-dot regime, and the average position along $\boldsymbol{x}$ is shifted below front gate 1 (or front gate 2). We then seek for the attractive gate pulse $\Delta V_{\mathrm{fg},2}$ (or $\Delta V_{\mathrm{fg},1}$) that tunes the system back to the anticrossing by sequentially diagonalizing $H_n^{\mathrm{SP}} = H_{n-1}^{\mathrm{SP}} + \Delta V_{\mathrm{fg},2} D_{\mathrm{fg},2}$ (or $H_n^{\mathrm{SP}} = H_{n-1}^{\mathrm{SP}} + \Delta V_{\mathrm{fg},1} D_{\mathrm{fg},1}$) and

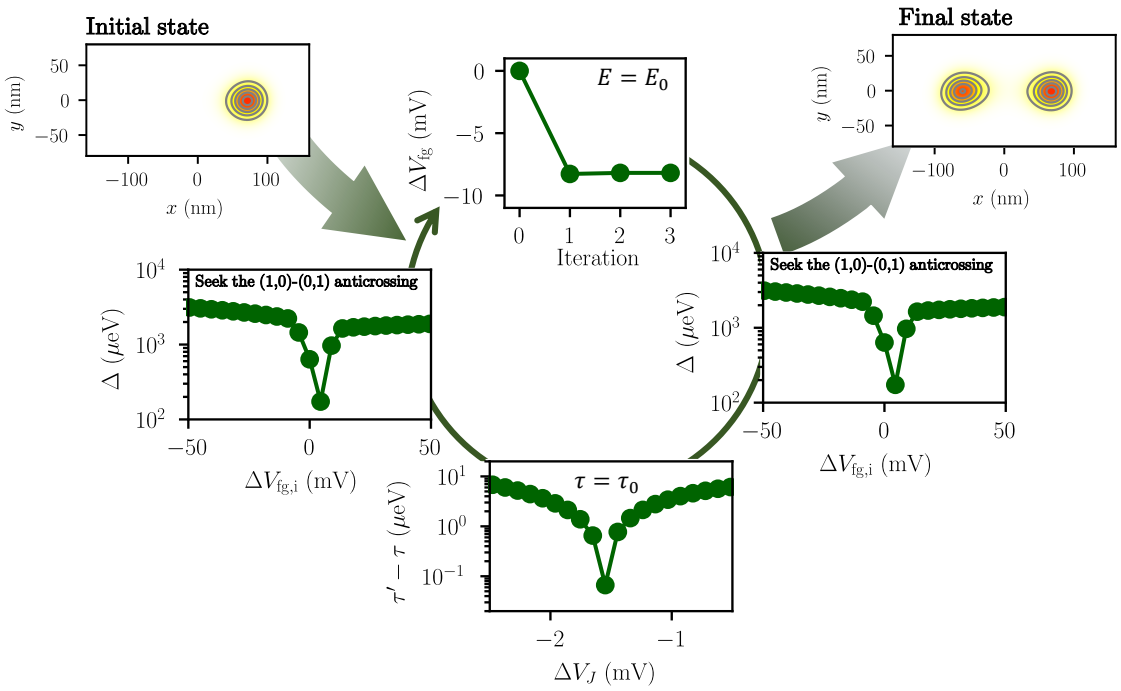

Figure B.1: Illustration of the search algorithm to extract the gate corrections needed to retune a defective double QD device into the (1,0)-(0,1) anticrossing (by minimizing the energy gap Δ between the two lowest-in-energy charge states) at a reference energy E_0 and tunnel coupling τ_0. The initial state with energy E and τ enters a loop that sequentially corrects the energy and the tunnel coupling, retuning the system to the (1,0)-(0,1) anticrossing after each correcting pulse. The inner panels show an example of the dichotomy (for finding the minimum of Δ and $\tau - \tau_0$) and Newton-Raphson (for finding $E = E_0$) steps for the first iteration $n = 1$; and a top-view of the hole probability P^{SP} for the initial and final states of the full process.

doing a dichotomy search to locate $\partial E/\partial\varepsilon = 0$.

The condition $E = E_0$ is achieved by a modulation of the QD confinement, and to do so the same ΔV_{fg} is applied to both front gates. The appropriate pulse is sought with a 1D Newton-Raphson method by computing $H_n^{\mathrm{SP}} = H_{n-1}^{\mathrm{SP}} + \Delta V_{\mathrm{fg}} D_{\mathrm{fg},1} + \Delta V_{\mathrm{fg}} D_{\mathrm{fg},2}$. $\tau = \tau_0$ can be achieved by adjusting V_{J}, with $H_n^{\mathrm{SP}} = H_{n-1}^{\mathrm{SP}} + \Delta V_{\mathrm{J}} D_{\mathrm{J}}$ and relying once more on a dichotomy search algorithm (technical difficulties linked to the implementation of V_J pulses are detailed in section B.2).

In presence of disorder, bias shifts of the type $\Delta V_{\mathrm{fg}} D_{\mathrm{fg},1} + \Delta V_{\mathrm{fg}} D_{\mathrm{fg},2}$ and $V_{\mathrm{J}} D_{\mathrm{J}}$ do not keep $\partial E/\partial\varepsilon = 0$, and they may shift the system away from the anticrossing. Consequently, an iterative process is required to fulfill $E = E_0$, $\tau = \tau_0$, and $\partial E/\partial\varepsilon = 0$ simultaneously. The proposed algorithm works as illustrated in Figure B.1. Bias pulses to reach $E = E_0$ and $\tau = \tau_0$ are sequentially applied, with intercalated pulses after each τ and E correction to tune the system back to the anticrossing. The algorithm eventually converges to a bias point that fulfills all three $E = E_0$, $\tau = \tau_0$, and $\partial E/\partial\varepsilon = 0$ conditions.

Figure B.2 illustrates an example of the convergence pattern for a defective double hole QD device in a Ge/SiGe heterostructure device, with reference energy E_0=8.75 meV and tunnel

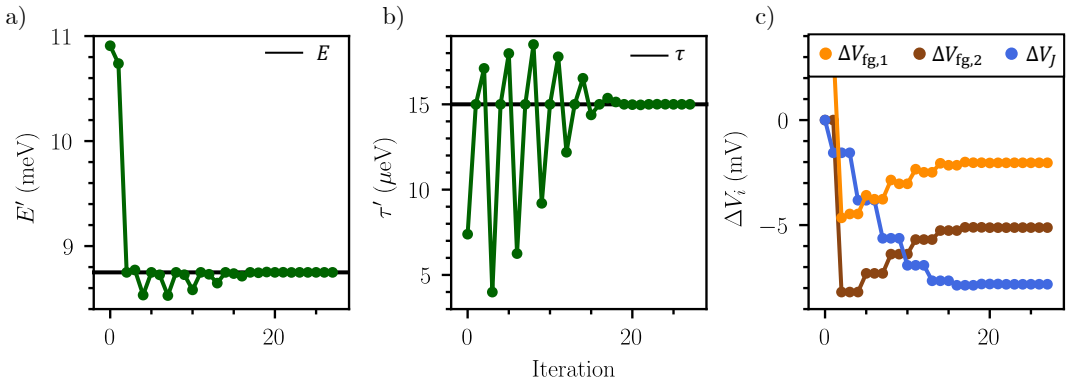

Figure B.2: Example of the convergence pattern of a disordered device using the algorithm shown in Figure B.1. a) Convergence of the anticrossing energy. Horizontal black line denotes the target energy E_0. b) Convergence of the tunnel coupling. Horizontal black line denotes the target τ_0. c) Evolution of the gate corrections during the algorithm steps.

τ_0=15 μeV. We can clearly see that several iterations are needed, since the gate corrections needed to achieve one of the three conditions break the other two. These gate corrections eventually converge, and the algorithm finishes when, after tuning the system to the (1,0)-(0,1) anticrossing, $E - E_0$ and $\tau - \tau_0$ are below a given threshold. As a result, we have all the gate corrections needed to re-tune a defective double QD system to a reference situation, and therefore an estimation of how strong the impact of disorder in the double QD system is.

B.2 Origin of the errors in the J gate pulses

When using the algorithm described above, we have systematically encountered problems when applying J-gate pulses. Although the algorithm was robust and accurate for the pulses on the front gates with a manageable basis set size, it did not capture the response of τ with V_J accurately, especially when the pulse was set to reduce the tunnel coupling. In the following, we describe the problem and discuss a possible origin, even though a proper understanding still requires a more in-depth study.

To illustrate the problem, we focus on the Si MOS device simulated in section 5.2 for electrons, and in absence of disorder. We show in Figure B.3a the true dependence of τ on V_J (in black), which increases for less negative gate voltages. In colored dashed lines we also show the result of the estimations of $\tau(V_J)$ from different initial biases, which are the points with matching color. We indeed observe that the methodology systematically fails when they intend to reduce τ, yet they remain rather accurate when they increase it. Surprisingly, even a dip is observed for the two estimations from the $V_J = 0$ V and -1.5 V initial biases. Such dips imply a crossing of the energy levels (as $\tau = |\Delta E/2|$ when the two QDs are tuned) and are numerical artifacts, as the explicit calculation of τ does not show this behavior. Moreover, as discussed in sections 1.3.2 and 2.5.2, a decrease of τ closes the anticrossing gap and consequently brings the two states closer in energy, but it cannot induce a level crossing.

We believe that the origin of this problem is on the finite character of the basis set in which we express H^{SP} and D_i to compute the effect of the gate pulses. In the minimal basis set of

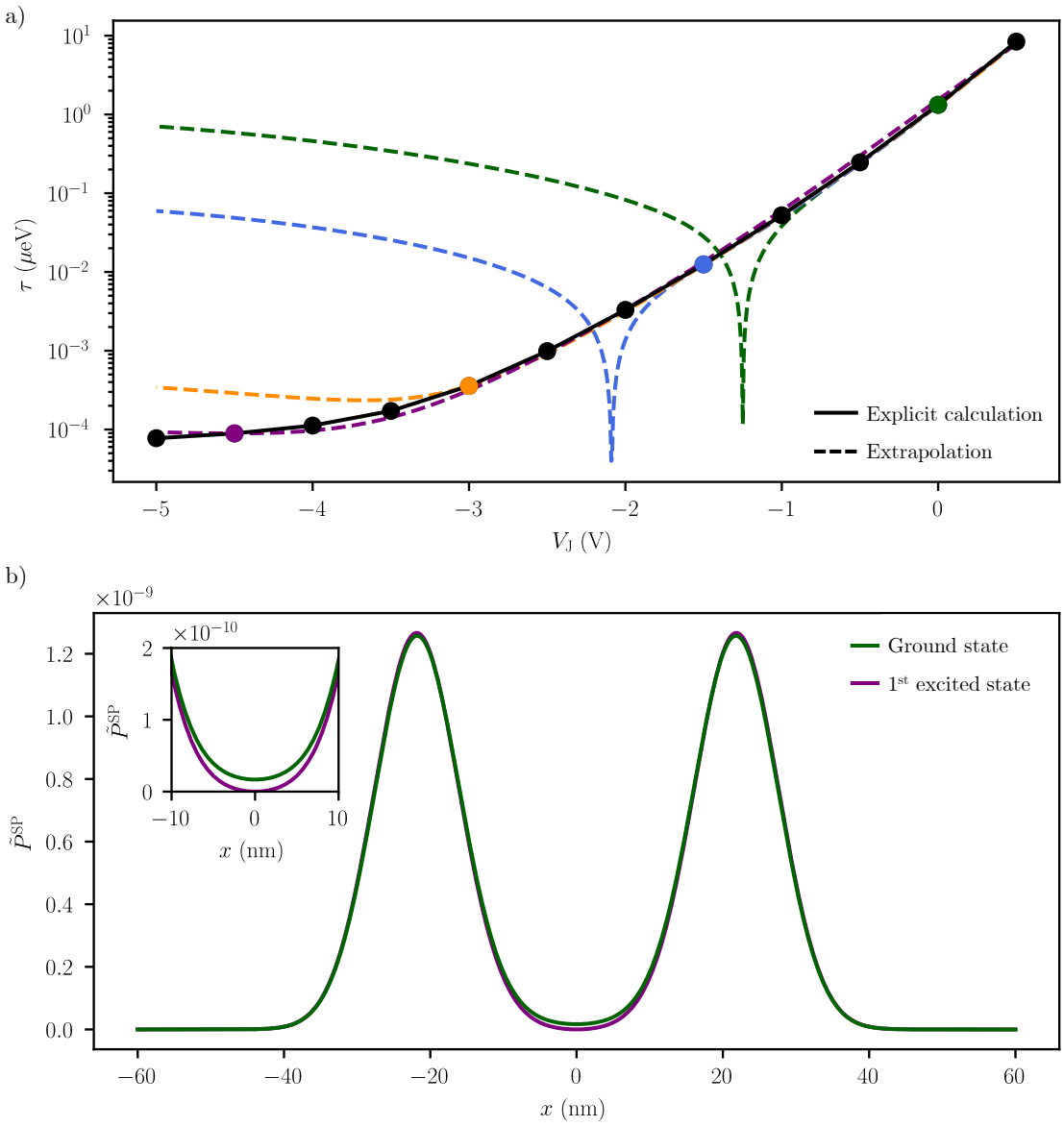

Figure B.3: a) Tunnel coupling dependence on V_J for the pristine Si MOS device simulated in section 5.2 for electrons. The black and colored points denote the explicit calculations of τ at different bias points, whereas the dashed lines correspond to the corrections of τ from an initial bias (the dot matching the color code). Black solid line connecting the dots highlights the exact trend of τ. b) Ground (bonding) state and first excited (antibonding) state electron probabilities at $V_J = -1$ V, $y = 0$ nm, and $z = 0$ nm. Inset Figure zooms into the region near $x = 0$ nm, where the two states show their main differences.

the bonding (Ψ_0) and antibonding (Ψ_1) states of $\hat{H}_0$, if the gate pulse (ΔV) does not break any symmetry (valid for the pristine device) the system Hamiltonian $\hat{H} = \hat{H}_0 + \Delta V$ remains diagonal. Consequently, in this minimal basis the wavefunctions do not adapt to the gate pulse. The variation of τ ($\Delta\tau$) with a change in the potential ΔV reads

$$2\Delta\tau = \langle\Psi_1|\Delta V|\Psi_1\rangle - \langle\Psi_0|\Delta V|\Psi_0\rangle\,, \tag{B.1}$$

which is also consistent with first order perturbation theory. Figure B.3b shows the electron probability along z for these two states for a SP calculation. Overall, they look very similar, showing two peaks at the position of the two tuned QDs. Yet, in the area of the tunnel barrier (around $x = 0$ nm) we can observe significant differences, see the inset in Figure B.3b. Indeed, the antibonding state wavefunction changes sign at $x = 0$ nm, and although its modulus squared remains positive everywhere, it goes to zero as a footprint of the antibonding character. This does not happen for the bonding state, which shows a small but finite probability all along z. With a larger electron probability at the area controlled by the J-gate, a J-gate pulse brings $\langle Psi_0|\Delta V|\Psi_0\rangle$ larger than $\langle Psi_1|\Delta V|\Psi_1\rangle$, thus a reduction of τ. This is in fact what happens in reality at first, as it is what causes the reduction of τ, yet such effect disappears when $\tau \to 0$ (when $\tau \to 0$, the two states should be degenerated and behave identically with V_J). In reality, the wavefunctions adapt when the barrier is tuned, and although the basis set used in practice is larger than the minimal basis set discussed above, we believe that it still fails to capture accurately the change in the wavefunction induced by the J-gate pulse. If the orbital effects are not correctly captured, equation B.1 already shows that the linear-response estimations when $\tau \to 0$ predict an "artificial" energy crossing, which is an artifact due to the limitations of the basis set. We indeed recover the fingerprints of level crossings in the estimations of Figure B.3a.

The impact of such inaccuracies on the functioning of the algorithm described in the previous section are very strong, as each time τ needs to be reduced there is the risk that its evaluation dramatically fails. Moreover, small τ may not even be reachable by the algorithm in some cases, see for example dashed orange line in Figure B.3b. Such errors inevitably spoil the convergence of the iterative process, and they may lead to gate pulses that are completely wrong. Therefore, as a rule-of-a-thumb, we can only pulse the J-gates safely to increase τ, but not to decrease it. When the impact of disorder is moderate, as for the Ge/SiGe devices with a tip and planar gate layout studied in Chapter 6, this problem can be overcome by setting an initial V_J smaller than that yielding to the target τ. When the disorder is very strong, as in the Si MOS devices of Chapter 5, the convergence of the iterative process becomes extremely complex if the condition $\tau = \tau_0$ is imposed, and we used the alternative methods exposed in section 5.2 to extract the variability in the energy barrier induced by disorder.

Appendix C

Chapter 4

C.1 Variability for the IZ-EDSR mode

The variability results for the Rabi frequency in Si MOS devices has been addressed in the main text for a drive applied to the front gate (labeled hereafter as g-TMR drive), which yielded to finite Rabi frequencies due to a g-TMR mechanism. It remains an open question, however, whether the reported high variability is a particular feature of g-TMR. Here we evaluate the impact of variability when relying on 1D Rashba SOC to achieve Rabi oscillations, thus on a IZ-EDSR mode for hole spin qubits. This requires the in-plane displacement of the QD in presence of a vertical electric field. The former is achieved with a drive with opposite modulation in the two lateral gates (referred hereafter as in-plane drive), whereas the latter is provided by the attracting potential of the front gate.

The anisotropy of the Rabi frequency for the pristine device is given in Figure C.1. To achieve an oscillatory electric field along $\boldsymbol{x}$, we drive the two lateral gates of the device in Figure 4.1 with $+\delta V$ and $-\delta V$. For such a drive, the maximum Rabi frequency is reached at a B field orientation close to $\boldsymbol{y}-\boldsymbol{x}$, so the magnetic field is fixed in this direction hereafter. The dependence of f_R on V_{fg} also differs from the g-TMR one. In fact, f_R is expected to increase with the increase of the vertical electric field [60]. The effect of the front gate is however two-

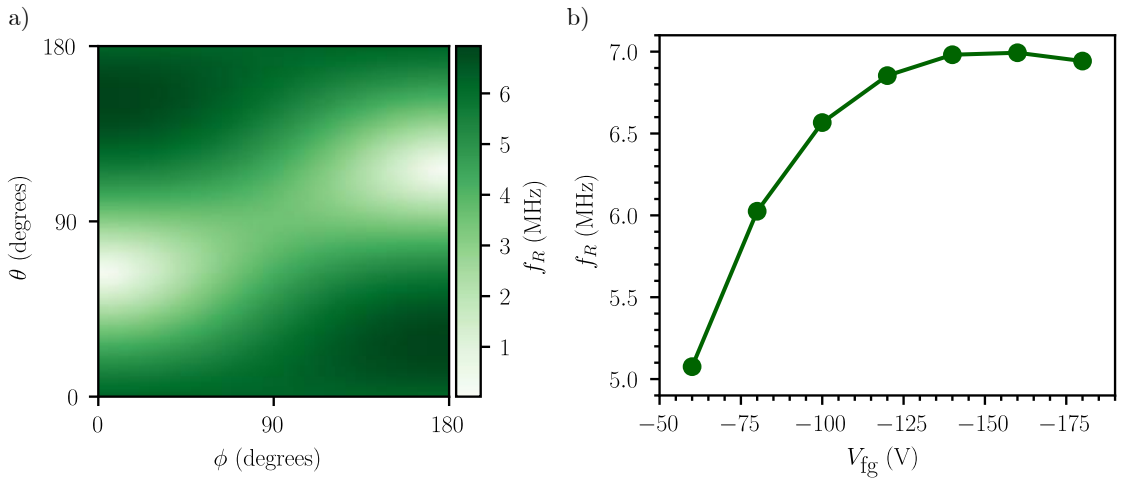

Figure C.1: a) Anisotropy of f_R with the magnetic field orientation for the pristine device in Figure 4.1, yet with the RF drive applied as $+\delta V$ and $-\delta V$ in the two lateral gates. The data is computed at $V_{\text{fg}} = -100$ mV and $V_{\text{lat}} = -75$ mV. b) Dependence of the f_R in a) on V_{fg} for $\boldsymbol{B} \parallel \boldsymbol{x}-\boldsymbol{y}$ ($\theta = 135$, $\phi = 0$) and $V_{\text{lat}} - V_{\text{fg}} = 25$ mV. The data is normalized for $B = 1$ T and $V_{\text{ac}} = 1$ mV.

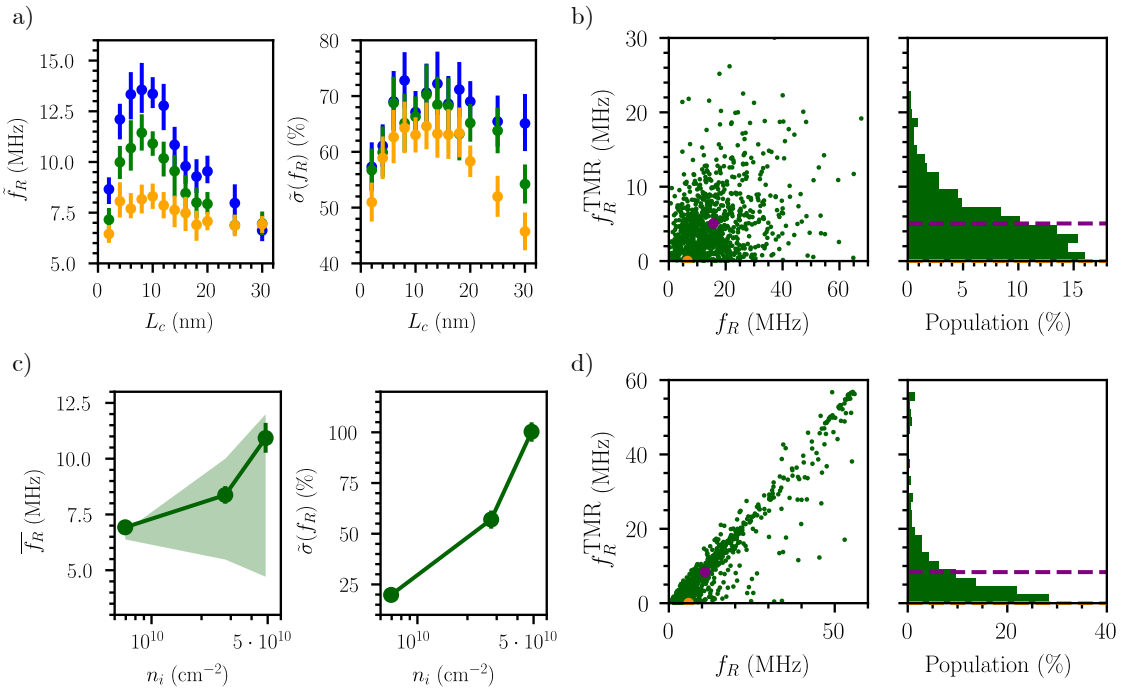

Figure C.2: Variability for an in-plane drive due to surface roughness and charge traps. a) Dependence of $\overline{f}_R$ and $\tilde{\sigma}(f_R)$ on the surface roughness parameters L_c and Δ for the device in Figure 4.1, with $V_{\mathrm{fg}} = -100$ mV and $V_{\mathrm{lat}} = -75$ mV. b) Correlation between the conventional g-TMR contribution to f_R (as defined in Appendix A.1) and the total f_R, and histogram of the former. The data corresponds to $L_c = 10$ nm and $\Delta = 0.4$ nm. Orange point and dashed line shows the pristine device, and the purple denote the average. Note that for the pristine device the g-TMR contribution is zero. c) Dependence of $\overline{f}_R$ and $\tilde{\sigma}(f_R)$ on the charge trap density n_i. Shaded areas show the first and third quartiles. d) Same as b) for charge traps, with $n_i = 5 \times 10^{10}$ cm^{-2}. In all cases, $V_{\mathrm{ac}} = 1$ mV and $B = 1$ T.

fold: the vertical component of the electric field indeed increases, therefore increasing f_R; but the consequent stronger confinement hinders the lateral motion of the QD. The saturation and even decrease of f_R at large V_{fg} in Figure C.1b is attributed to the latter contribution becoming dominant. For the variability analysis, we have chosen $V_{\mathrm{fg}} = -100$ mV.

The variability due to surface roughness for an in-plane drive of the QD is shown in Figure C.2a. There are certainly some differences with respect to the g-TMR results in Chapter 4. First, there is a strong dependence of the average Rabi frequency $\overline{f_R}$ on the strength of the surface roughness: $\overline{f_R}$ substantially increases following the same trend observed for $\tilde{\sigma}(f_R)$ in Figure 4.3. Given the dependence of $\overline{f_R}$ on the surface roughness parameters, $\tilde{\sigma}(f_R) = \sigma(f_R)/\overline{f_R}$ trends are partly blurred with respect to those obtained for the front-gate drive, especially the dependence on Δ.

The origin of this systematic increase of f_R is found on the appearance of a g-TMR contribution in presence of disorder. One can indeed intuitively expect some g-TMR to appear when the QD is displaced as a whole within the channel if the potential of this channel is irregular. Variations in the nanowire thickness, or even charge traps at the interface are prone to modify

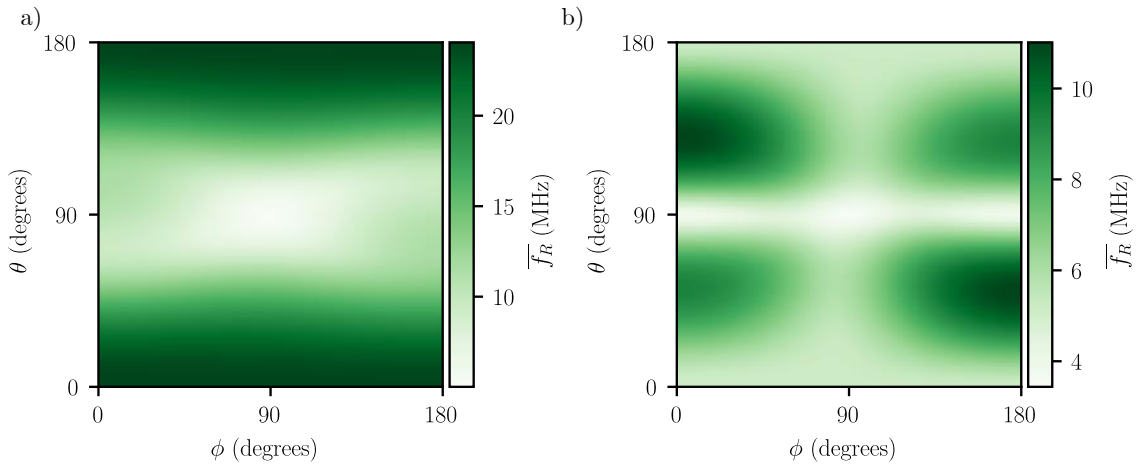

Figure C.3: Anisotropy of the average Rabi frequency ($\overline{f_R}$) with the magnetic field orientation for the simulations including a) surface roughness with $L_c = 10$ nm, $\Delta = 0.4$ nm; and b) charge traps with $n_i = 5 \times 10^{10}$ cm^{-2}. All the simulations are at $V_{\text{fg}} = -100$ mV, $V_{\text{lat}} = -75$ mV, $V_{\text{ac}} = 1$ mV and $B = 1$ T.

the QD shape while being displaced, yielding to a modulation of the principal g-factors. Moreover, note that $\boldsymbol{x}$ is the direction with a weakest confinement, so these effects have a stronger impact than for front-gate drive discussed in the main text, where the motion of the QD is along y. In Figure C.2 we define the conventional g-TMR contribution as exposed in Appendix A.1. We observe that it largely contributes to f_R in presence of disorder, being usually the dominant contribution to f_R. This new term, absent in the pristine device, is entirely dependent on the particularities of the roughness profile, so it is prone to present a very high variability. Consequently, the $\tilde{\sigma}(f_R)$ reported in Figure C.2 are much larger than the 25% previously observed for the front-gate drive, reaching up to a 70% of variability.

Results for charge traps show the same physics, yet the g-TMR contributions are even larger to the point that they become the dominant contribution to the total f_R, see Figure C.2c. This increases even more the 60% we give in the main text, and yields to a variability of 100% for $n_i = 5 \times 10^{10}$ cm^{-2}. Even at $n_i = \times 10^{10}$ cm^{-2} variability remains as large as 24%.

With the g-TMR component being dominant, even the anisotropy of the Rabi frequency for the individual defective devices may change considerably with respect to that of the pristine device, resembling that of a g-TMR driving. The interplay between two mechanisms with different anisotropies raises as well a variability in the shape of the f_R map, which becomes an extra contribution to $\sigma(f_R)$ when the orientation of B is fixed. To illustrate this, the dependence of $\hat{f}_R$ on the magnetic field orientation are plotted in C.3 for surface roughness and charge traps. The similarities of the map for charge traps with the g-TMR map of Figure 4.2 are clear, and even for surface roughness the map shows considerable variations from the pristine device characteristic shape shown in Figure C.1.

In light of the findings, the exploitation of the IZ-EDSR mode seems to demand extremely clean interfaces, and the Rashba-type mechanisms are unlikely to dominate the Rabi frequencies in disordered Si MOS devices. Moreover, an in-plane drive is discouraged in terms of variability, as the appearing g-TMR contributions on top of the IZ-EDSR mode yield to even larger

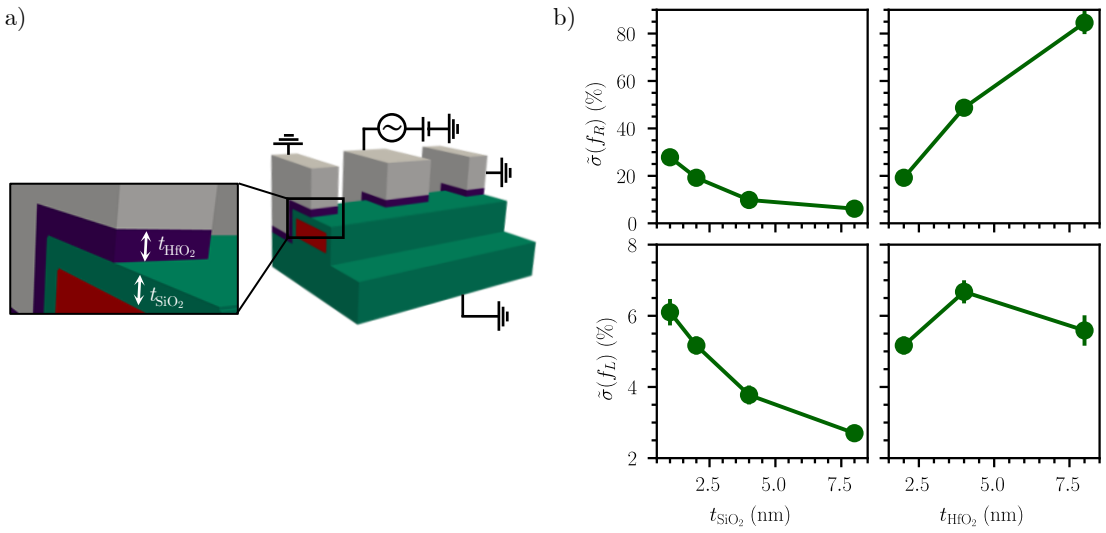

Figure C.4: a) Hole device with a SiO_2/HfO_2 gate stack. The thickness of the SiO_2 layer (green) is t_{SiO_2}, and the thickness of the HfO_2 layer (purple) is t_{HfO_2}. The HfO_2 layer extends only under the gates. b) RSD $\tilde{\sigma}(f_L)$ and $\tilde{\sigma}(f_R)$ of the Larmor and Rabi frequencies plotted as a function of t_{SiO_2} (at $t_{HfO_2} = 2$ nm), and as a function of t_{HfO_2} (at $t_{SiO_2} = 2$ nm). The density of trapped charges at the SiO_2/HfO_2 interface is $n_i = 5 \times 10^{11}$ cm^{-2}, and $V_{fg} = -50$ mV. The error bars are the 95% confidence intervals.

variabilities than when the QD is driven with the front gate.

C.2 Effect of distance between the QD and the defective interface

Throughout this thesis we discuss that the distance between the active layer and the defective interface is crucial for variability. This explains the smaller variability of epitaxial heterostructures, where defects are shifted a few tens of nanometers away from the QDs. But the direct comparison between Si MOS and Ge/SiGe devices is not totally fair, as the QDs have different sizes and shapes, and the different dielectric constants of the materials yield to different screenings. Here, as an illustration, we shift the defective interface away from the Si nanowire of a Si MOS device so as to estimate this impact in a consistent layout. We have considered SOI hole devices with a SiO_2/HfO_2 gate stack (see Figure C.4a). The channel is therefore now separated from the gate by a layer of SiO_2 with thickness t_{SiO_2}, and by a layer of HfO_2 with thickness t_{HfO_2} ($\kappa_{HfO_2} = 20$). This HfO_2 layer only extends below the gates and not under the spacers. We then introduce the charged defects at the SiO_2/HfO_2 instead of the Si/SiO_2 interface, with density $n_i = 5 \times 10^{11}$ cm^{-2} only chosen for illustrative purposes [159].[1] The RSDs $\tilde{\sigma}(f_L)$ and $\tilde{\sigma}(f_R)$ of the Larmor and Rabi frequencies are plotted as a function of t_{SiO_2} and t_{HfO_2} in Figure C.4b. The variability decreases when the SiO_2 is made thicker and the traps are moved away

[1] We emphasize that the SiO_2/HfO_2 interface is known to be a strong source of Coulomb scattering in classical CMOS devices [159], with apparent charge densities n_i reaching 10^{13} cm^{-2}. This test system is introduced to illustrate trends in a device similar to that of Chapter 4, and is not meant to give a realistic account of disorder at the SiO_2/HfO_2 interfaces, which shall preferably be avoided in qubit devices.

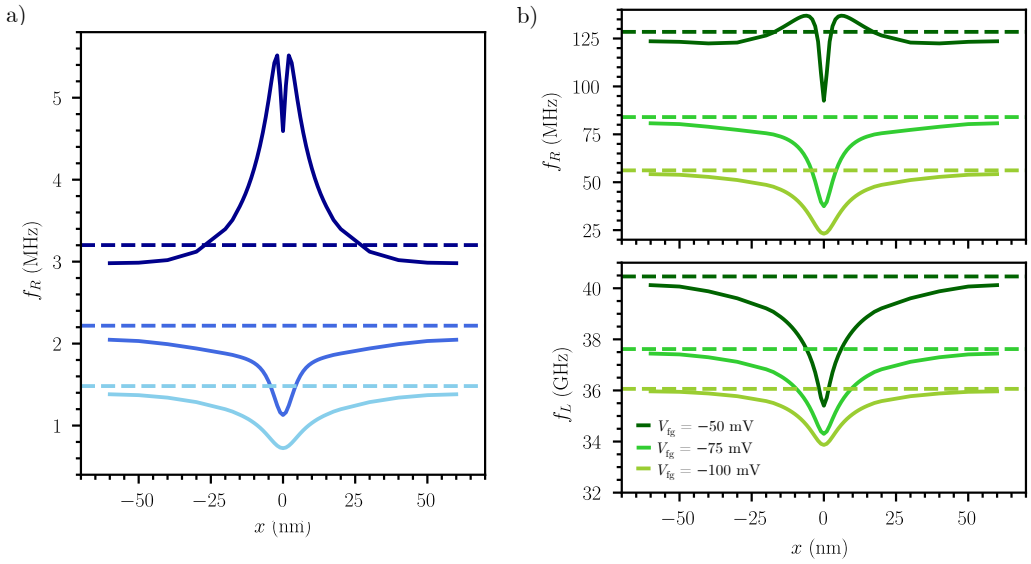

Figure C.5: a) Rabi frequency of electron qubits as a function of the position x of a single negative charge along the channel, for different gate voltages V_{fg}. The charge is located at the top Si/SiO_2 interface, at $y = 10$ nm. The horizontal lines are the Rabi frequencies of the pristine qubits. b) Rabi and Larmor frequency of hole qubits as a function of the position x of a single positive charge along the channel, for different V_{fg}. The charge is located at the top Si/SiO_2 interface, at $y = 0$ nm. The horizontal lines are the frequencies of the pristine qubits.

from the channel. Remarkably, the variability increases rapidly with the thickness of the HfO_2 layer because the screening of the charge traps by the metal gate is softened [159].

C.3 Effects of a single charge on electron and hole qubits

Here we discuss the impact of a single charge on the Rabi (with a front-gate drive) and Larmor frequencies of electron and hole qubits hosted in the Si MOS device of Figure 4.1. The Larmor and Rabi frequency of electron and hole qubits is plotted in Figure C.5 as a function of the position x of a single charge along the channel. This charge is positive for hole qubits, negative for electron qubits, and is located at the top facet. The deviations from the pristine qubit are sizable when the charge is within ≈ 25 nm from the qubit. Note the "overshoot" of the Rabi frequency at small bias when the charge goes through the gate and tends to split the dot in two strongly coupled pieces.

C.4 Effects of micro-magnet imperfections

In this Appendix, we briefly discuss the effects of disorder in the micro-magnets on the variability of electron spin qubits. The relevant parameters of the micro-magnets are displayed in Figure C.6a.

The qubits may be sensitive to local inhomogeneities of the magnets (roughness, variations of the magnetic polarization), and to "global" (but more systematic) deficiencies such as mis-

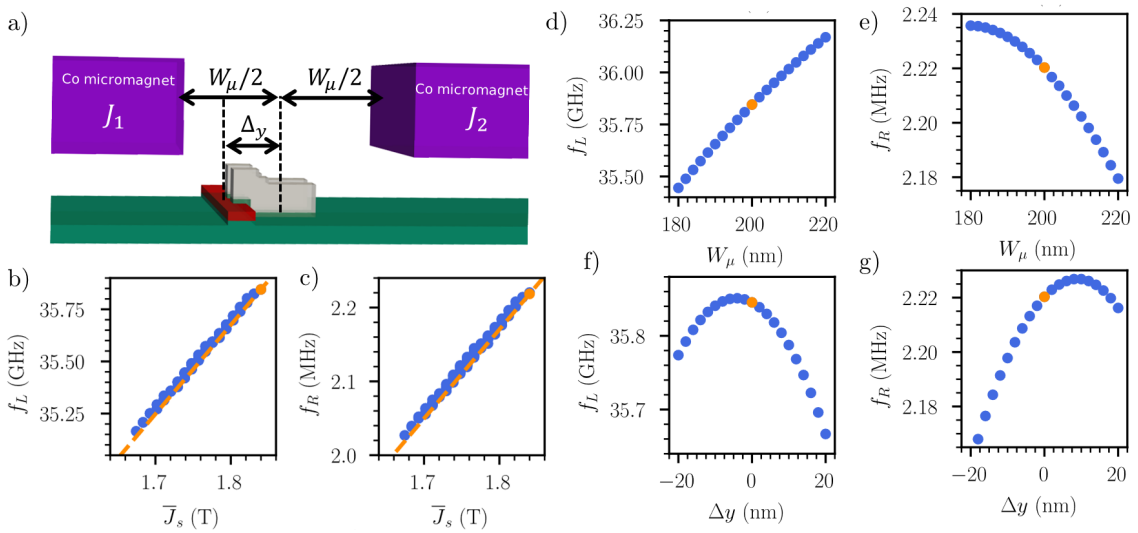

Figure C.6: a) Sketch of the device with the definition of the width W_μ and misalignment Δ_y of the trench between the micro-magnets. b) Larmor and c) Rabi frequency of the pristine electron qubit as a function of the average magnetic polarization $\overline{J}_s = (J_1 + J_2)/2$ of the two micro-magnets. The plots collect data for different $\Delta J = J_1 - J_2$ ranging from -0.17 to 0.17 T. The orange lines are simple linear models $f_R \propto \overline{J}_s$ and $f_L \propto \overline{J}_s + J_0$, where J_0 accounts for the static magnetic field. d) Larmor and e) Rabi frequency as a function of the width W_μ of the trench between the two magnets. f) Larmor and g) Rabi frequency as a function of the misalignment Δy between the channel and the trench. In all panels, $V_{\text{fg}} = 50$ mV and the orange point is the nominal device ($\overline{J}_s = 1.84$ T, $W_\mu = 200$ nm, and $\Delta y = 0$).

alignment (misplacement and misorientation) [105, 116]. The roughness of the magnets tends to be softened in the far field and is likely not a strong concern, unless particularly large or long-ranged. The variations of the magnetic polarization due to material inhomogeneity or incomplete saturation can be readily addressed when they take place over length scales much longer than the distance to the qubits (that is, in the hundreds of nm range). The magnetic polarization J_s can then be considered as locally homogeneous, but device dependent. The Larmor and Rabi frequencies of the pristine qubit are thus plotted in Figures C.6b,c as a function of the average magnetic polarization $\overline{J}_s = (J_1 + J_2)/2$ of the two magnets (they are almost independent on $\Delta J = J_1 - J_2$ in this range). The Rabi frequency being directly proportional to the gradient of the micro-magnets field, any relative variation of $\overline{J}_s$ results in a similar relative variation of f_R (dotted line shows $f_R \propto \overline{J}_s$ in Figure C.6c). The Larmor frequency f_L shows a weaker, yet significant linear dependence on $\overline{J}_s$ as the micro-magnets field is only $\simeq 20\%$ of the total magnetic field (dotted lined in Figure C.6b). As a matter of fact, a 1.3% variation of $\overline{J}_s$ results in a 100 MHz drift of the Larmor frequency, which is sizable with respect to the distributions shown in Figures 4.4 and 4.8. The homogeneity of the magnets can, therefore, be critical for the control of the Larmor frequencies.

We have also plotted in Figures C.6d and C.6e the Larmor and Rabi frequencies as a function of the width W_μ of the trench between the magnets (nominally $W_\mu = 200$ nm). f_L increases and f_R decreases when widening the trench because B_y increases (the qubit looks better aligned with the magnets) but $\partial B_z/\partial y$ decreases. Making a bevel trench is actually a solution to detune

the qubits on purpose in order to address them individually at different Larmor frequencies ($\partial f_L/\partial W_\mu \approx 18$ MHz/nm) [105]. Finally, the Larmor and Rabi frequencies are plotted in Figures C.6f and C.6g as a function of the misalignment Δy between the channel and the micro-magnets trench. The variations are small and mostly second-order in the $|\Delta y| < 20$ nm range because symmetric positions on both sides of the (xz) mirror plane of the magnets are roughly (but not strictly) equivalent (the major component B_y is the same but the minor component B_z changes sign). If the micro-magnets are misoriented by 2° with respect to the channel axis, neighboring qubits (that are 60 nm apart in the design of Figure 4.1b) are shifted by $\Delta y = \pm 2$ nm.

C.5 Validation of the variability results with TB simulations

All the variability data discussed during this thesis has been obtained with the **k**·**p** method. We may ask ourselves to what extent a continuum band model can capture the variability effects, and whether we are missing a part of them by using a method that gets rid of the atomistic structure. To validate the conclusions reached throughout this thesis, we perform a variability study with TB for the hole Si MOS device simulated in Chapter 4. We focus on the single-qubit properties and limit the study to the effect of surface roughness, which is clearly an atomistic source of disorder. We consider both front-gate and in-plane drives, so as to confirm that the appearance of spurious g-TMR terms with the latter described in Appendix C.1 are not an artifact of **k**·**p**.

In Figure C.7a we show the results for the g-TMR drive. We plot the data as a function of

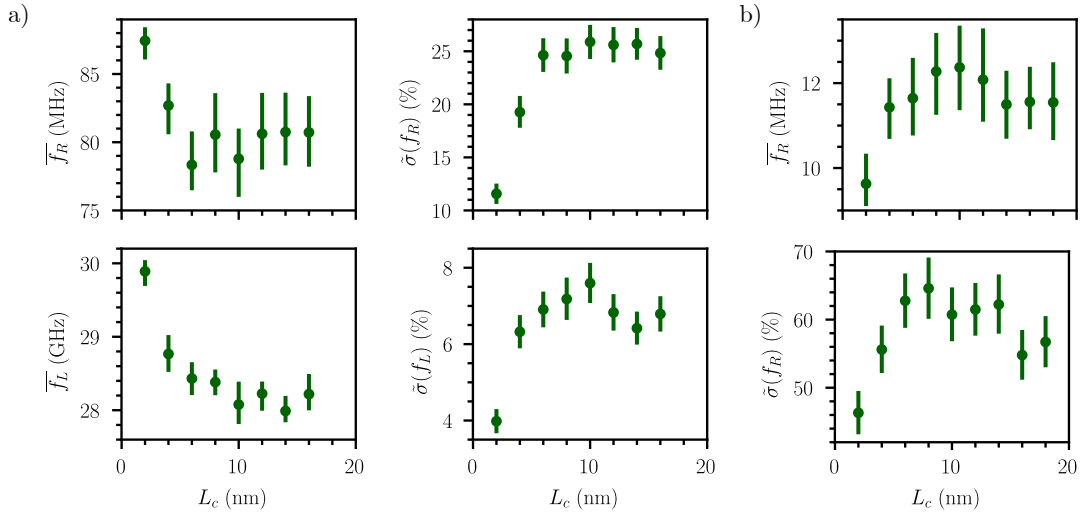

Figure C.7: Variability due to surface roughness for the front-gate and in-plane drives mechanisms with Tight Binding simulations. a) Dependence of the average f_R, average f_L, and RSD of f_R and f_L on L_c for the g-TMR driving mechanism. V_{fg} is set to -50 mV, and $\Delta = 0.4$ nm. b) Dependence of the average f_R and its RSD on L_c for the in-plane drive. V_{fg} is set to -50 mV, and $\Delta = 0.4$ nm. $B = 1$ T along $\boldsymbol{x} + \boldsymbol{y}$ for the front-gate drive and along $\boldsymbol{x} - \boldsymbol{y}$ for the in-plane drive, and $V_{\text{ac}} = 1$ mV.

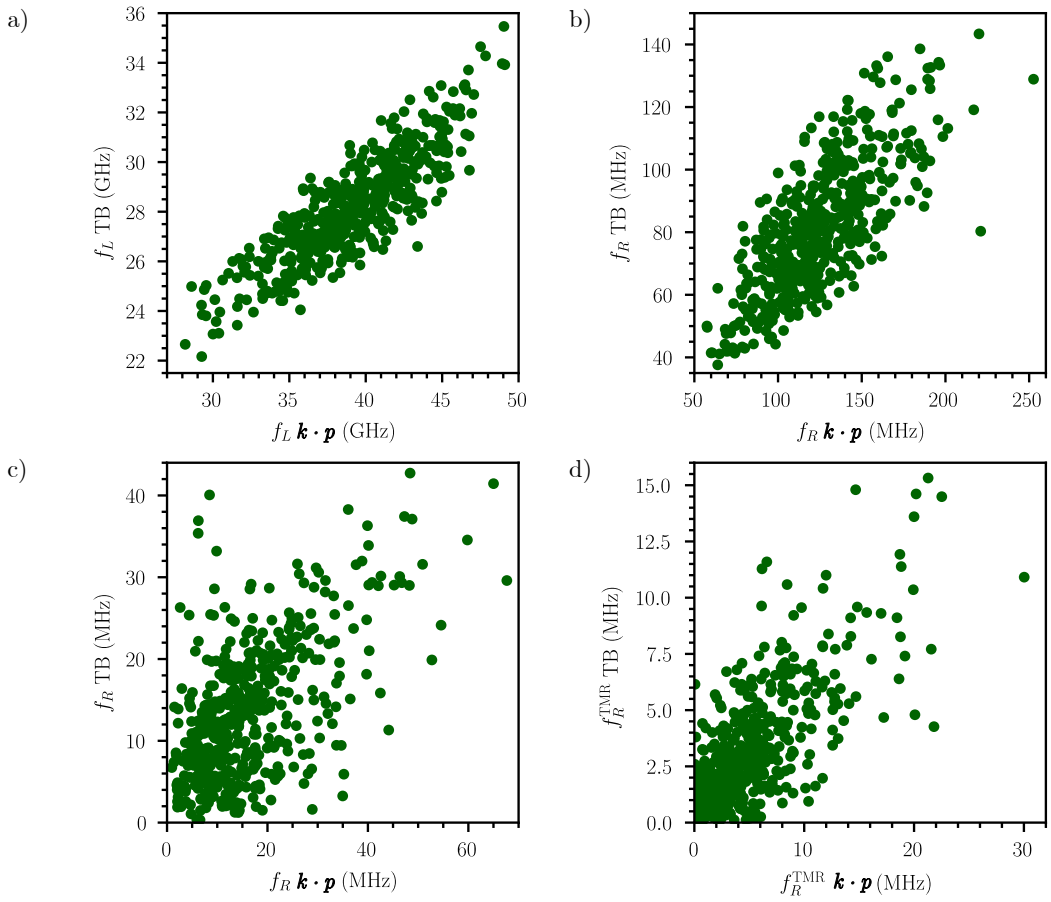

Figure C.8: a) Correlation of the TB and **k**·**p** Larmor frequencies for simulations with the same individual realizations of disorder. b) Same for the Rabi frequencies when driving with the front gate. c) Same as b) but driving with an in-plane AC drive (the AC drive is applied to the two lateral gates with opposite modulation). d) Correlation between the TB and **k**·**p** g-TMR contribution to the total f_R with an in-plane drive. In all cases, the introduced source of disorder is surface roughness with $L_c = 10$ nm and $\Delta = 0.4$ nm. We set $V_{\mathrm{fg}} = -50$ mV, $B = 1$ T along $\boldsymbol{x} + \boldsymbol{y}$ for the front-gate drive and along $\boldsymbol{x} - \boldsymbol{y}$ for the in-plane drive, and $V_{\mathrm{ac}} = 1$ mV.

L_c, for $\Delta = 0.4$ nm. Although we recover a weak modulation of $\overline{f_R}$ and $\overline{f_L}$ with L_c (not present in the **k**·**p** data), the RSD of both properties qualitatively shows the same trends observed in Figure 4.3. Also the magnitude of the variability itself is comparable. Moreover, the TB results for the in-plane drive also show a considerably larger variability in f_R, in agreement with **k**·**p**.

In Figure C.8 we go one step forward and compare the two methods for each individual realization of disorder. We compare f_L in Figure C.8a, and we recover a well-defined correlation. Nonetheless, the TB values are systematically smaller. The origin of this is still under study, yet we suspect that there are inaccuracies in the current treatment of magnetic fields with TB. We do the same comparison for the f_R due to a g-TMR drive in Figure C.8b, where the correlation remains very clear, yet again the TB f_R are smaller than the **k**·**p** ones. For the in-plane drive, the TB and **k**·**p** results also show a rough correlation for f_R (see Figure C.8c), and interestingly, TB also predicts the strong g-TMR contributions for the defective devices (see Figure C.8d).

We can therefore conclude that the estimations of variability made with **k**·**p** are in agreement with the predictions from the atomistic TB model.

C.6 Time-dependent resolution of the electron Rabi frequencies

In section 3.1 we have set up the methodology to compute Rabi oscillations for electrons in presence of MMs, and in section 2.5.1.2 we have discussed two different approaches to evaluate them for holes. There is still a third way to estimate the magnitude of f_R: by explicitly computing the dynamics of the system with the TDSE. The resolution of the dynamical problem is the most accurate solution, as it naturally captures all the effects of the drive, and it is not restricted to first order in perturbation.

In Figure C.9, we illustrate a time-dependent simulation of the electron Si MOS device studied in Chapter 4. We use a pristine device at $V_{\text{fg}} = 50$ mV, apply a driving pulse on the front gate of amplitude $V_{\text{ac}} = 1$ mV , and track the spin-up probability ($P(\uparrow)$) as a function of time. We additionally track the position of $\langle y \rangle$, whose variation in the inhomogeneous magnetic field created by the MMs is responsible for the finite f_R's.

We start the dynamics with $|\downarrow\rangle$ as initial state, and we do indeed recover spin rotations when the electrical drive is turned on. Moreover, the fitting of these oscillations gives an estimation of $f_R = 2.21$ MHz, which is essentially the same value we have listed in Table 4.1 for $V_{\text{fg}} = 50$ mV. The main difference between the direct evaluation used in Chapter 4 and the resolution of the TDSE is the linear response assumed for the electrical drive in the former. In view of the

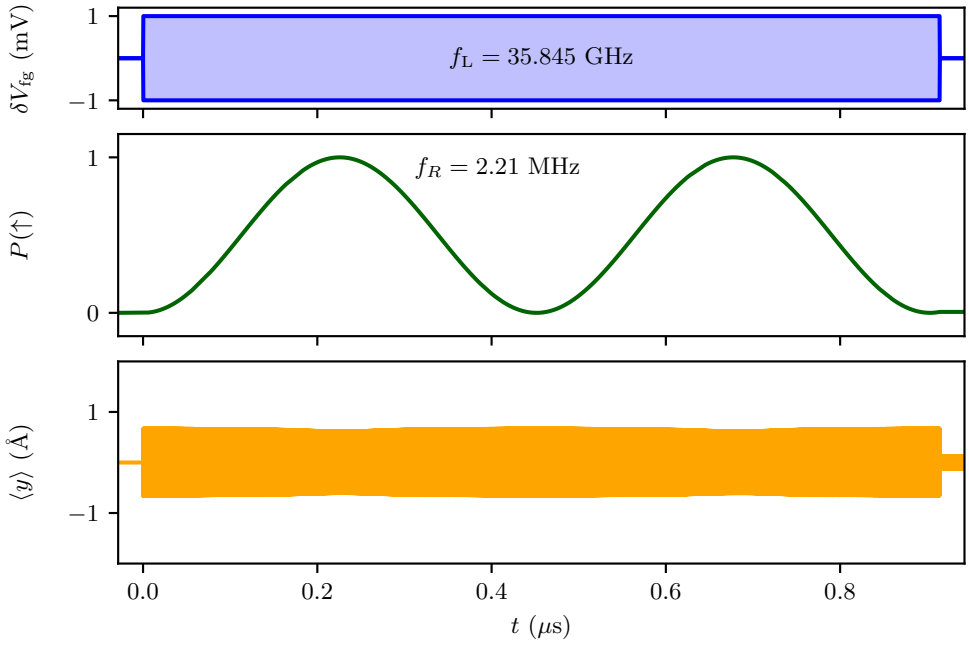

Figure C.9: Time-resolved Rabi oscillations for an electron spin qubit. The simulated device is that of Figure 4.1, and a RF drive of 1 mV is applied to the front gate. We show the dependence of the spin-up probability ($P(\uparrow)$) and the average position of the QD along $\langle y \rangle$ with time (t).

excellent agreement between the results of the two methods, we can conclude that considering the system response linear with δV is a safe approximation at the drive amplitudes assumed here.

The behavior of $\langle y \rangle$ with time also shows the expected trend. A fast oscillation of the QD position along $\boldsymbol{y}$ with amplitude of nearly 2 Å at frequency f_L is the origin of the orange area at the bottom subplot of Figure C.9. In addition, we can slightly see an envelope shaping the amplitude of the former oscillations at the timescale of f_R. In presence of a SOC mechanism, the spatial part of the $|\uparrow\rangle$ and $|\downarrow\rangle$ states are different, which provides different amplitudes for the $\langle y \rangle$ oscillations depending on the relative population of the two states. This imprints the pattern of the Rabi oscillations into the time dependence of $\langle y \rangle$. The remaining fluctuations when the drive is turned off owe to the precession of the final state in the Bloch sphere.

Appendix D

Chapter 5

D.1 Two-contact front gates as alternative layout

In this Appendix we present a proposal for an extra improvement of the current devices to add an extra control point of the tunnel couplings. As detailed in section 1.4, the gate stack of the front gates in the LETI devices is composed by a layer of TiN, in contact with a thick layer of polysilicon. With suck material stack, the experimental difficulties associated with the etching of thick TiN layers are overcome.[1] Nonetheless, when two metals with different work functions are put in contact, the equilibration of their chemical potentials yields to a net charge transfer between them, which impacts the resulting electrical potential generated by the gate stack. For a TiN/polysilicon interface, this difference of potential is computed to be -0.25 V, meaning that when the potential at the polysilicon is 0 V, the potential in the TiN is -0.25 V. In practice, this has strong implications on the functioning of the gates, since the polysilicon potential tends to control the area in between the QDs, and the TiN the area below it. Being the former 0.25 V more attractive (for electrons) than the latter, it can trigger the formation of the QDs under the spacers and prevent their formation under the TiN.

The present proposal pretends to benefit from the control of the polysilicon on the area between front gates to add an extra degree of control of the tunnel couplings between the QDs. The strategy is to isolate the TiN from the polysilicon with a dielectric (SiO_2), to have two independent contacts in the two materials, and bias them independently (see Figure D.1). In this way, TiN should effectively work as a front gate and control the formation of the QDs in

[1] When thick TiN is grown, the material becomes polycrystalline as different nucleation centers appear. This can potentially be a strong source of disorder.

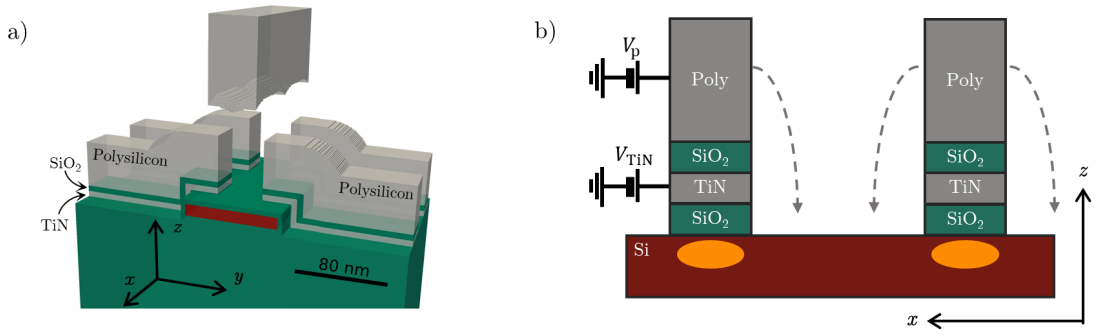

Figure D.1: a) Representation of the front gates in the two-contact gate stack. The full device includes a top J-gate parallel to the nanowire. Color code as in Figure 5.1. b) Sketch of the gate stack. The potential applied to TiN (V_{TiN}) is responsible for the formation of the QDs (in orange), and the polysilicon potential (V_p) controls the tunnel couplings.

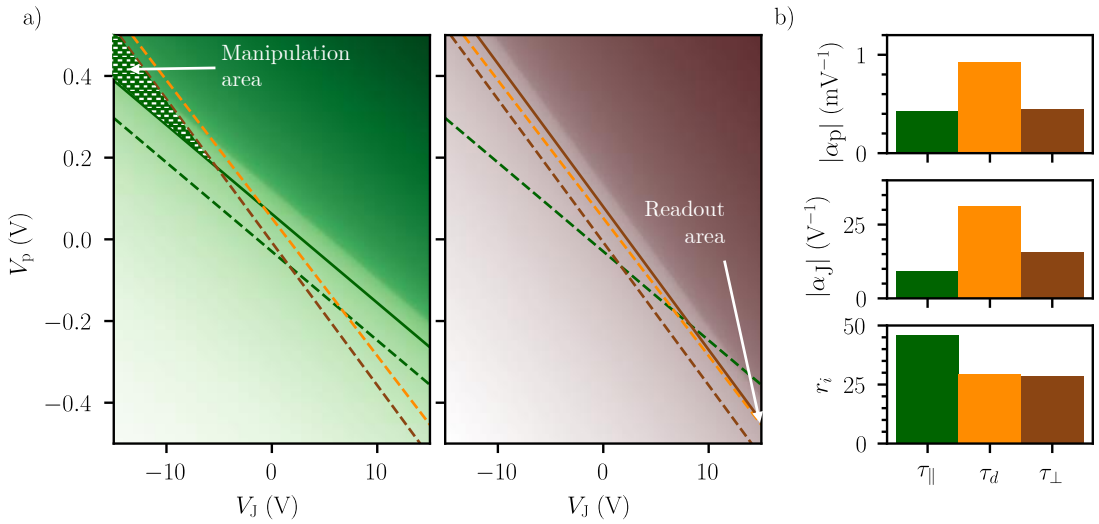

Figure D.2: Properties of a device with independent electric contacts to the TiN and polysilicon. a) Tunnel maps for the dependence of $t_\parallel$ (left panel) and $t_\perp$ (right panel) on the J-gates and polysilicon gates potentials. Color maps illustrate the strength of the coupling (the lighter the color the weaker the coupling), whereas the plotted lines denote isolines of interest: dashed lines show $\tau = 10^{-2}$, and solid lines denote $\tau = 10^{1}$ μeV. Green, brown and orange stand for $\tau_\parallel$, $\tau_\perp$ and τ_d, respectively. b) Efficiency and selectivity on the control of $t_\parallel$, $t_\perp$, and t_d with the J-gates and the polysilicon gates. Green, brown and orange stand for $\tau_\parallel$, $\tau_\perp$ and τ_d, respectively.

the proper position, while the polysilicon on top could work as an effective J-gate controlling the tunnel couplings. The problems related to the formation of spurious QDs in the spacers due to the different work functions of the metals in the gate stack would also be solved.

We now evaluate the efficiency of this proposal on controlling the tunnel couplings, and discuss the possibility of substituting the back gate by this novel implementation. To do so, we simulate the device showed in Figure D.1, including a single J-gate running parallel to the nanowire, which should *a priori* control $t_\perp$. The device dimensions mimic those used in section 5.1.2, here with an 80 nm wide nanowire ($L_\parallel$=40 nm and $L_\perp$=40 nm), and a 5 nm thick SiO_2 layer between the 5 nm and 40 nm thick TiN and polysilicon, respectively. The goal is to determine whether the new gate stack allows to control the tunnel couplings, and whether J-gates and polysilicon gates would be sufficient, and no metallic back gate would be needed to access manipulation and readout regimes.

Similarly to what we did in section 5.1, we used the model in equation 5.3 to extract the 2D maps of the three tunnel couplings, but this time with respect to V_p and V_J. Results are shown in Figure D.2. The first conclusion we may notice is that even though the J-gate runs now parallel to the nanowire, the α_J we obtain are very similar to those in Figure 5.3a for the same dimensions. Again, due to the distance between the J-gate and the nanowire, the potential it generates at the level of the QDs is nearly uniform. Second, the very large α_p denote that we can indeed control the tunnel couplings with the polysilicon gates. In fact, the control is much tighter, since they are only 15 nm away from the Si nanowire, and they do not face a screening as strong as the J-gates. Unfortunately, the $r_i = \alpha_p/\alpha_J$ computed for these two gates are very

close, in particular $r_\perp$ and r_d. Consequently, even though the latter remains in between $r_\parallel$ and $r_\perp$, very large potentials would be needed to reach readout, as illustrated in the 2D maps of Figure D.2a. In conclusion, a gate stack where the potential in TiN and polysilicon is tunable independently, which would solve the formation of spurious dots in the spacers between front gates, would also allow to control the tunnel couplings between QDs.

Appendix E

Chapter 6

E.1 Extended data on the variability of tips and planar devices

In this Appendix we dig deeper into the effect of tips devices and the improvement of variability they bring with respect to the standard planar gate layout. To do so, we split the total SiGe/Al_2O_3 interface into two distinct parts, see Figure E.1. We define the interface $\mathcal{G}$ as the area below and surrounding the gate insertions for the tips device, and below the metallic gates for the planar device. We also define the interface $\mathcal{T}$ as the area left between gates. As discussed in the main text, the tip gates aim to eradicate the impact of the charge traps in $\mathcal{T}$. Here we study to what extend this is achieved by placing the charge traps selectively at only one of the two areas.

Figure E.2a shows the splitting of the total variability into the contributions from $\mathcal{G}$ and $\mathcal{T}$ for the tips and planar device. The simulated devices have $A = 80$ nm and $D = 60$ nm. We observe that the variability reassembles that of Figure 6.11 when the charge trap density is included at the full interface. Interestingly, we observe that while the planar devices have a comparable contribution to variability from both $\mathcal{T}$ and $\mathcal{G}$ interfaces, the variability for the tips device comes exclusively from $\mathcal{G}$. As intended, the penetrating gates are able to eliminate the effect of the charge traps lying on the space between gates, and the remaining variability is limited to that of the charges in the SiGe/Al_2O_3 interface of the insertion.

The experimental realization of a gate layout based on penetrating gates requires the etching of holes in the SiGe, that are later filled first by a dielectric material, and then with a metal.

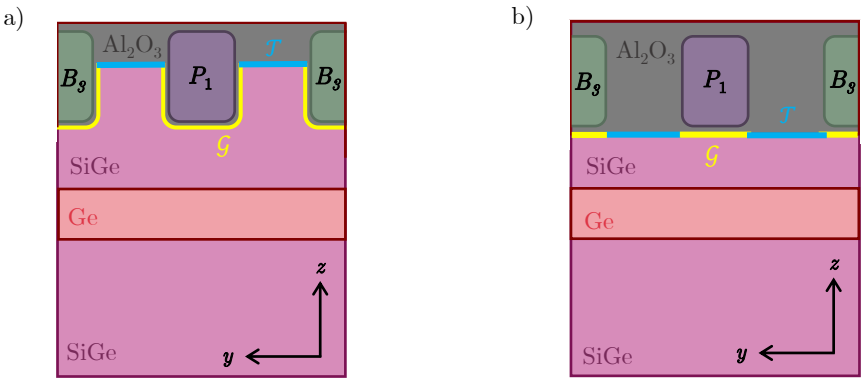

Figure E.1: Definition of the $\mathcal{G}$ and $\mathcal{T}$ areas of the devices in Figure 6.7 for a) the tips device and b) the planar device. We split the SiGe/Al_2O_3 interface in the area below the gates (and surrounding them for the tips device), and the area in the space left without any overlapping gate.

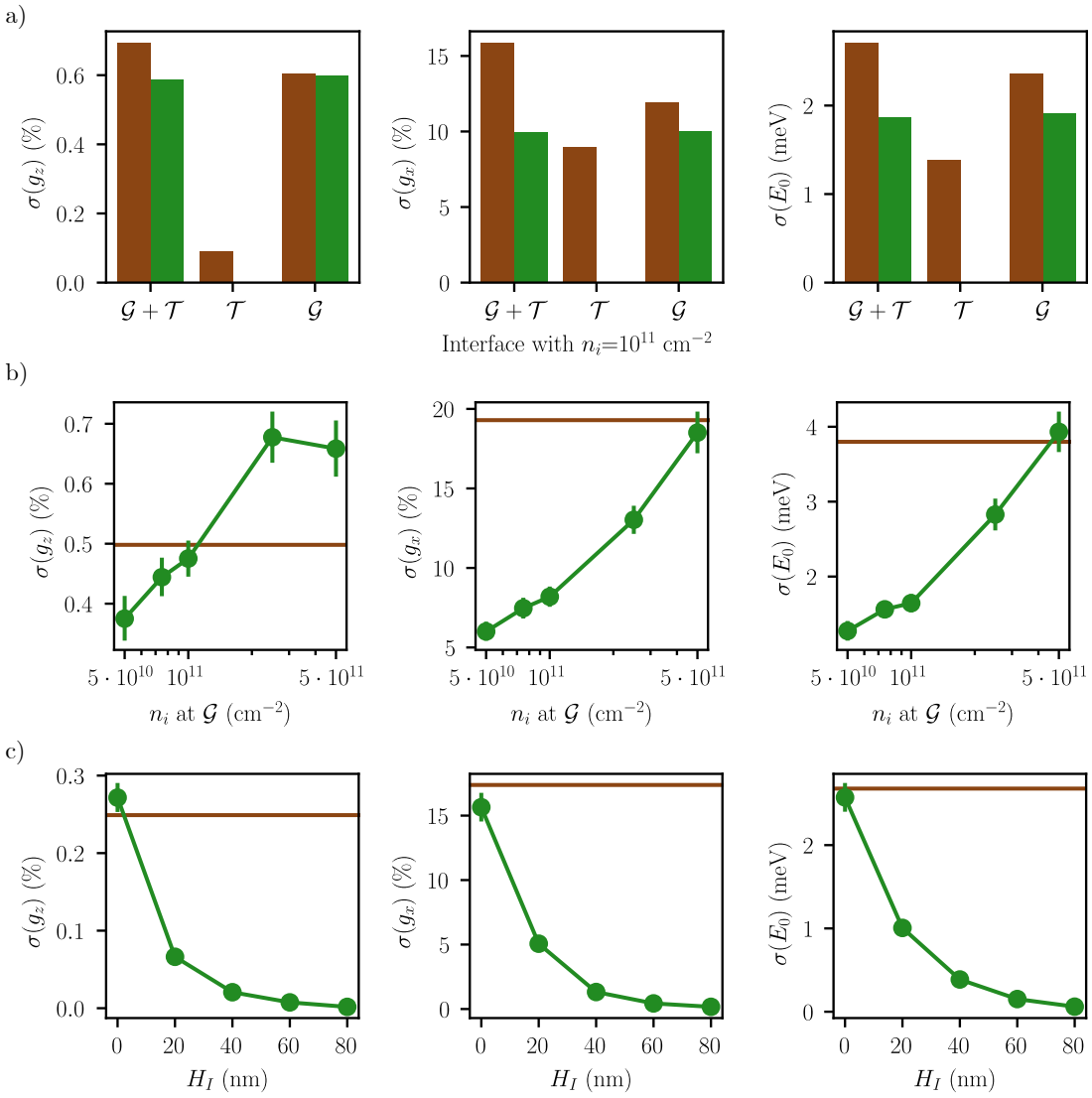

Figure E.2: Insights on the improvement in variability of a tips device. a) Variability in g_x, g_z, and E_0 of the tips (in green) and planar (in brown) devices ($A = 80$ nm, $D = 60$ nm, $H_I = 80$ nm) with a charge trap density $n_i = 10^{11}$ cm^{-2} at the full SiGe/Al_2O_3 interface ($\mathcal{G}$+$\mathcal{T}$), only at the interface of the space between gates ($\mathcal{T}$), and only at the interface of the gates ($\mathcal{G}$) (below, and on the sides for the tips device). b) Variability of the tips device ($A = 80$ nm, $D = 40$ nm, $H_I = 80$ nm) for g_x, g_z and E_0 as a function of the charge trap density at the SiGe/oxide interface of the gates' insertion (labelled as $\mathcal{G}$ area), including $n_i = 10^{11}$ cm^{-2} at $\mathcal{T}$. The horizontal brown line shows the variability of the equivalent planar device with $n_i = 10^{11}$ cm^{-2} at both $\mathcal{T}$ and $\mathcal{G}$. c) Improvement in variability of the tips device ($A = 80$ nm, $D = 40$ nm) for g_x, g_z and E_0 as a function of H_I for a charge trap density $n_i = 10^{11}$ cm^{-2} only at $\mathcal{T}$. The horizontal brown line shows the variability of the equivalent planar device, also with charges only at $\mathcal{T}$.

It is unclear what is the interface quality one may achieve in such processes, and the final SiGe/dielectric interface in the insertions may have a different n_i than the top SiGe/Al_2O_3 interface. In Figure E.2b we show the variability induced by a charge trap density $n_i = 10^{11}$ cm^{-2} at the $\mathcal{T}$ interface, and a range of n_i for the $\mathcal{G}$ interface. We observe that to reach the same variability as in a planar device with $n_i = 10^{11}$ cm^{-2} everywhere (brown horizontal line), the penetrating tips must have a charge trap density at the insertions of $n_i = 5 \times 10^{11}$ cm^{-2}. As long as the quality of the interface for the drilled holes host charge trap densities below this, the tip gate layout outperforms the planar counterpart.

Finally, we may wonder how deep the penetration must be in order to fully eliminate the effect of the charges at $\mathcal{T}$. To evaluate this, we place only charges at the top interface, and compute the variability of g_x, g_z and E_0 as a function of H_I, see Figure E.2c. We observe that variability starts to saturate around $H_I = 40$ nm, and we could consider it completely eliminated at $H_I \geq 80$ nm.

Bibliography

[1] P. Benioff, The computer as a physical system: A microscopic quantum mechanical Hamiltonian model of computers as represented by Turing machines, *Journal of Statistical Physics* **1980**, *22*, 563.

[2] R. P. Feynman, Simulating physics with computers, *International Journal of Theoretical Physics* **1982**, *21*, 467.

[3] K. Igeta, Y. Yamamoto in International Conference on Quantum Electronics, Quantum mechanical computers with single atom and photon fields, Optica Publishing Group, **1988**, TuI4.

[4] P. Shor in Proceedings 35th Annual Symposium on Foundations of Computer Science, Algorithms for quantum computation: discrete logarithms and factoring, **1994**, p. 124.

[5] L. K. Grover in Proceedings of the Twenty-Eighth Annual ACM Symposium on Theory of Computing, A fast quantum mechanical algorithm for database search, Association for Computing Machinery, Philadelphia, Pennsylvania, USA, **1996**, p. 212.

[6] D. P. DiVincenzo, Topics in Quantum Computers, arXiv:cond-mat/9612126, **1996**.

[7] D. P. DiVincenzo, The Physical Implementation of Quantum Computation, *Fortschritte der Physik* **2000**, *48*, 771.

[8] D. Loss, D. P. DiVincenzo, Quantum computation with quantum dots, *Physical Review A* **1998**, *57*, 120.

[9] B. E. Kane, A Silicon-based nuclear spin quantum computer, *Nature* **1998**, *393*, 133.

[10] P. J. J. O'Malley, R. Babbush, I. D. Kivlichan, J. Romero, J. R. McClean, R. Barends, J. Kelly, P. Roushan, A. Tranter, N. Ding, B. Campbell, Y. Chen, Z. Chen, B. Chiaro, A. Dunsworth, A. G. Fowler, E. Jeffrey, E. Lucero, A. Megrant, J. Y. Mutus, M. Neeley, C. Neill, C. Quintana, D. Sank, A. Vainsencher, J. Wenner, T. C. White, P. V. Coveney, P. J. Love, H. Neven, A. Aspuru-Guzik, J. M. Martinis, Scalable quantum simulation of molecular energies, *Physical Review X* **2016**, *6*, 031007.

[11] F. Arute, K. Arya, R. Babbush, D. Bacon, J. C. Bardin, R. Barends, R. Biswas, S. Boixo, F. G. S. L. Brandao, D. A. Buell, B. Burkett, Y. Chen, Z. Chen, B. Chiaro, R. Collins, W. Courtney, A. Dunsworth, E. Farhi, B. Foxen, A. Fowler, C. Gidney, M. Giustina, K. Graff, Roband Guerin, S. Habegger, M. P. Harrigan, M. J. Hartmann, A. Ho, M. Hoffmann, T. Huang, T. S. Humble, S. V. Isakov, E. Jeffrey, Z. Jiang, D. Kafri, K. Kechedzhi, J. Kelly, P. V. Klimov, S. Knysh, A. Korotkov, F. Kostritsa, D. Landhuis, M. Lindmark, E. Lucero, D. Lyakh, S. Mandrà, J. R. McClean, M. McEwen, A. Megrant, X. Mi, K. Michielsen, M. Mohseni, J. Mutus, O. Naaman, M. Neeley, C. Neill, M. Y. Niu, E. Ostby, A. Petukhov, J. C. Platt, C. Quintana, E. G. Rieffel, P. Roushan, N. C. Rubin, D. Sank, K. J. Satzinger, V. Smelyanskiy, K. J. Sung, M. D. Trevithick, A. Vainsencher, B. Villalonga, T. White, Z. J. Yao, P. Yeh, A. Zalcman, H. Neven, J. M. Martinis, Quantum supremacy using a programmable superconducting processor, *Nature* **2019**, *574*, 505.

[12] M. Gong, S. Wang, C. Zha, M.-C. Chen, H.-L. Huang, Y. Wu, Q. Zhu, Y. Zhao, S. Li, S. Guo, H. Qian, Y. Ye, F. Chen, C. Ying, J. Yu, D. Fan, D. Wu, H. Su, H. Deng, H. Rong, K. Zhang, S. Cao, J. Lin, Y. Xu, L. Sun, C. Guo, N. Li, F. Liang, V. M. Bastidas, K. Nemoto, W. J. Munro, Y.-H. Huo, C.-Y. Lu, C.-Z. Peng, X. Zhu, J.-W. Pan, Quantum walks on a programmable two-dimensional 62-qubit superconducting processor, *Science* **2021**, *372*, 948.

[13] J. J. Pla, K. Y. Tan, J. P. Dehollain, W. H. Lim, J. J. L. Morton, D. N. Jamieson, A. S. Dzurak, A. Morello, A single-atom electron spin qubit in Silicon, *Nature* **2012**, *489*, 541.

[14] M. Veldhorst, C. H. Yang, J. C. C. Hwang, W. Huang, J. P. Dehollain, J. T. Muhonen, S. Simmons, A. Laucht, F. E. Hudson, K. M. Itoh, A. Morello, A. S. Dzurak, A two-qubit logic gate in Silicon, *Nature* **2015**, *526*, 410.

[15] R. Maurand, X. Jehl, D. Kotekar-Patil, A. Corna, H. Bohuslavskyi, R. Laviéville, L. Hutin, S. Barraud, M. Vinet, M. Sanquer, S. De Franceschi, A CMOS Silicon spin qubit, *Nature Communications* **2016**, *7*, 13575.

[16] S. G. J. Philips, M. T. Mądzik, S. V. Amitonov, S. L. de Snoo, M. Russ, N. Kalhor, C. Volk, W. I. L. Lawrie, D. Brousse, L. Tryputen, B. P. Wuetz, A. Sammak, M. Veldhorst, G. Scappucci, L. M. K. Vandersypen, Universal control of a six-qubit quantum processor in Silicon, arXiv:2202.09252, **2022**.

[17] A. R. Mills, C. R. Guinn, M. J. Gullans, A. J. Sigillito, M. M. Feldman, E. Nielsen, J. R. Petta, Two-qubit Silicon quantum processor with operation fidelity exceeding 99%, *Science Advances* **2022**, *8*, eabn5130.

[18] P. Cerfontaine, T. Botzem, J. Ritzmann, S. S. Humpohl, A. Ludwig, D. Schuh, D. Bougeard, A. D. Wieck, H. Bluhm, Closed-loop control of a GaAs-based singlet-triplet spin qubit with 99.5% gate fidelity and low leakage, *Nature Communications* **2020**, *11*, 4144.

[19] F. Fedele, A. Chatterjee, S. Fallahi, G. C. Gardner, M. J. Manfra, F. Kuemmeth, Simultaneous operations in a two-dimensional array of singlet-triplet qubits, *PRX Quantum* **2021**, *2*, 040306.

[20] P.-A. Mortemousque, E. Chanrion, B. Jadot, H. Flentje, A. Ludwig, A. D. Wieck, M. Urdampilleta, C. Bäuerle, T. Meunier, Coherent control of individual electron spins in a two-dimensional quantum dot array, *Nature Nanotechnology* **2021**, *16*, 296.

[21] H. Watzinger, J. Kukučka, L. Vukušić, F. Gao, T. Wang, F. Schäffler, J.-J. Zhang, G. Katsaros, A Germanium hole spin qubit, *Nature Communications* **2018**, *9*, 3902.

[22] N. W. Hendrickx, D. P. Franke, A. Sammak, G. Scappucci, M. Veldhorst, Fast two-qubit logic with holes in Germanium, *Nature* **2020**, *577*, 487.

[23] N. W. Hendrickx, W. I. L. Lawrie, M. Russ, F. van Riggelen, S. L. de Snoo, R. N. Schouten, A. Sammak, G. Scappucci, M. Veldhorst, A four-qubit Germanium quantum processor, *Nature* **2021**, *591*, 580.

[24] N. A. Gershenfeld, I. L. Chuang, Bulk spin-resonance quantum computation, *Science* **1997**, *275*, 350.

[25] I. L. Chuang, N. Gershenfeld, M. Kubinec, Experimental implementation of fast quantum searching, *Physical Review Letters* **1998**, *80*, 3408.

[26] L. M. K. Vandersypen, M. Steffen, G. Breyta, C. S. Yannoni, M. H. Sherwood, I. L. Chuang, Experimental realization of Shor's quantum factoring algorithm using nuclear magnetic resonance, *Nature* **2001**, *414*, 883.

[27] Y. Nakamura, Y. A. Pashkin, J. S. Tsai, Coherent control of macroscopic quantum states in a single-Cooper-pair box, *Nature* **1999**, *398*, 786.

[28] F. Arute, K. Arya, R. Babbush, D. Bacon, J. C. Bardin, R. Barends, S. Boixo, M. Broughton, B. B. Buckley, D. A. Buell, B. Burkett, N. Bushnell, Y. Chen, Z. Chen, B. Chiaro, R. Collins, W. Courtney, S. Demura, A. Dunsworth, E. Farhi, A. Fowler, B. Foxen, C. Gidney, M. Giustina, R. Graff, S. Habegger, M. P. Harrigan, A. Ho, S. Hong, T. Huang, W. J. Huggins, L. Ioffe, S. V. Isakov, E. Jeffrey, Z. Jiang, C. Jones, D. Kafri, K. Kechedzhi, J. Kelly, S. Kim, P. V. Klimov, A. Korotkov, F. Kostritsa, D. Landhuis, P. Laptev, M. Lindmark, E. Lucero, O. Martin, J. M. Martinis, J. R. McClean, M. McEwen, A. Megrant, X. Mi, M. Mohseni, W. Mruczkiewicz, J. Mutus, O. Naaman, M. Neeley, C. Neill, H. Neven, M. Y. Niu, T. E. O'Brien, E. Ostby, A. Petukhov, H. Putterman, C. Quintana, P. Roushan, N. C. Rubin, D. Sank, K. J. Satzinger, V. Smelyanskiy, D. Strain, K. J. Sung, M. Szalay, T. Y. Takeshita, A. Vainsencher, T. White, N. Wiebe, Z. J. Yao, P. Yeh, A. Zalcman, Hartree-Fock on a superconducting qubit quantum computer, *Science* **2020**, *369*, 1084.

[29] B. Chiaro, C. Neill, A. Bohrdt, M. Filippone, F. Arute, K. Arya, R. Babbush, D. Bacon, J. Bardin, R. Barends, S. Boixo, D. Buell, B. Burkett, Y. Chen, Z. Chen, R. Collins, A. Dunsworth, E. Farhi, A. Fowler, B. Foxen, C. Gidney, M. Giustina, M. Harrigan, T. Huang, S. Isakov, E. Jeffrey, Z. Jiang, D. Kafri, K. Kechedzhi, J. Kelly, P. Klimov, A. Korotkov, F. Kostritsa, D. Landhuis, E. Lucero, J. McClean, X. Mi, A. Megrant, M. Mohseni, J. Mutus, M. McEwen, O. Naaman, M. Neeley, M. Niu, A. Petukhov, C. Quintana, N. Rubin, D. Sank, K. Satzinger, T. White, Z. Yao, P. Yeh, A. Zalcman, V. Smelyanskiy, H. Neven, S. Gopalakrishnan, D. Abanin, M. Knap, J. Martinis, P. Roushan, Direct measurement of nonlocal interactions in the many-body localized phase, *Physical Review Research* **2022**, *4*, 013148.

[30] T. Ayral, T. Louvet, Y. Zhou, C. Lambert, E. M. Stoudenmire, X. Waintal, A density-matrix renormalisation group algorithm for simulating quantum circuits with a finite fidelity, arXiv:2207.05612, **2022**.

[31] C. Wang, X. Li, H. Xu, Z. Li, J. Wang, Z. Yang, Z. Mi, X. Liang, T. Su, C. Yang, G. Wang, W. Wang, Y. Li, M. Chen, C. Li, K. Linghu, J. Han, Y. Zhang, Y. Feng, Y. Song, T. Ma, J. Zhang, R. Wang, P. Zhao, W. Liu, G. Xue, Y. Jin, H. Yu, Towards practical quantum computers: transmon qubit with a lifetime approaching 0.5 milliseconds, *npj Quantum Information* **2022**, *8*, 3.

[32] J. R. Petta, A. C. Johnson, J. M. Taylor, E. A. Laird, A. Yacoby, M. D. Lukin, C. M. Marcus, M. P. Hanson, A. C. Gossard, Coherent manipulation of coupled electron spins in semiconductor quantum dots, *Science* **2005**, *309*, 2180.

[33] F. H. L. Koppens, C. Buizert, K. J. Tielrooij, I. T. Vink, K. C. Nowack, T. Meunier, L. P. Kouwenhoven, L. M. K. Vandersypen, Driven coherent oscillations of a single electron spin in a quantum dot, *Nature* **2006**, *442*, 766.

[34] S. J. Devitt, W. J. Munro, K. Nemoto, Quantum error correction for beginners, *Reports on Progress in Physics* **2013**, *76*, 076001.

[35] L. Cywinski, W. M. Witzel, S. Das Sarma, Electron spin dephasing due to hyperfine interactions with a nuclear spin bath, *Physical Review Letters* **2009**, *102*, 057601.

[36] J. B. Johnson, Thermal agitation of electricity in conductors, *Physical Review* **1928**, *32*, 97.

[37] H. Nyquist, Thermal agitation of electric charge in conductors, *Physical Review* **1928**, *32*, 110.

[38] A. V. Kuhlmann, J. Houel, A. Ludwig, L. Greuter, D. Reuter, A. D. Wieck, M. Poggio, R. J. Warburton, Charge noise and spin noise in a semiconductor quantum device, *Nature Physics* **2013**, *9*, 570.

[39] J. Yoneda, K. Takeda, T. Otsuka, T. Nakajima, M. R. Delbecq, G. Allison, T. Honda, T. Kodera, S. Oda, Y. Hoshi, N. Usami, K. M. Itoh, S. Tarucha, A quantum-dot spin qubit with coherence limited by charge noise and fidelity higher than 99.9%, *Nature Nanotechnology* **2018**, *13*, 102.

[40] C. Spence, B. C. Paz, B. Klemt, E. Chanrion, D. J. Niegemann, B. Jadot, V. Thiney, B. Bertrand, H. Niebojewski, P.-A. Mortemousque, X. Jehl, R. Maurand, S. De Franceschi, M. Vinet, F. Balestro, C. Bäuerle, Y.-M. Niquet, T. Meunier, M. Urdampilleta, Spin-valley coupling anisotropy and noise in CMOS quantum dots, *Physical Review Applied* **2022**, *17*, 034047.

[41] J. Li, B. Venitucci, Y.-M. Niquet, Hole-phonon interactions in quantum dots: Effects of phonon confinement and encapsulation materials on spin-orbit qubits, *Physical Review B* **2020**, *102*, 075415.

[42] L. Bourdet, Y.-M. Niquet, All-electrical manipulation of Silicon spin qubits with tunable spin-valley mixing, *Physical Review B* **2018**, *97*, 155433.

[43] P. Stano, D. Loss, Review of performance metrics of spin qubits in gated semiconducting nanostructures, arXiv:2107.06485, **2021**.

[44] V. Mazzocchi, P. Sennikov, A. Bulanov, M. Churbanov, B. Bertrand, L. Hutin, J. Barnes, M. Drozdov, J. Hartmann, M. Sanquer, 99.992% ^{28}Si CVD-grown epilayer on 300 mm substrates for large scale integration of Silicon spin qubits, *Journal of Crystal Growth* **2019**, *509*, 1.

[45] A. Laucht, F. Hohls, N. Ubbelohde, M. F. Gonzalez-Zalba, D. J. Reilly, S. Stobbe, T. Schröder, P. Scarlino, J. V. Koski, A. Dzurak, C.-H. Yang, J. Yoneda, F. Kuemmeth, H. Bluhm, J. Pla, C. Hill, J. Salfi, A. Oiwa, J. T. Muhonen, E. Verhagen, M. D. LaHaye, H. H. Kim, A. W. Tsen, D. Culcer, A. Geresdi, J. A. Mol, V. Mohan, P. K. Jain, J. Baugh, Roadmap on quantum nanotechnologies, *Nanotechnology* **2021**, *32*, 162003.

[46] D. M. Zajac, A. J. Sigillito, M. Russ, F. Borjans, J. M. Taylor, G. Burkard, J. R. Petta, Resonantly driven CNOT gate for electron spins, *Science* **2018**, *359*, 439.

[47] E. Vahapoglu, J. P. Slack-Smith, R. C. C. Leon, W. H. Lim, F. E. Hudson, T. Day, T. Tanttu, C. H. Yang, A. Laucht, A. S. Dzurak, J. J. Pla, Single-electron spin resonance in a nanoelectronic device using a global field, *Science Advances* **2021**, *7*, eabg9158.

[48] K. Eng, T. D. Ladd, A. Smith, M. G. Borselli, A. A. Kiselev, B. H. Fong, K. S. Holabird, T. M. Hazard, B. Huang, P. W. Deelman, I. Milosavljevic, A. E. Schmitz, R. S. Ross, M. F. Gyure, A. T. Hunter, Isotopically enhanced triple-quantum-dot qubit, *Science Advances* **2015**, *1*, e1500214.

[49] J. M. Elzerman, R. Hanson, L. H. Willems van Beveren, B. Witkamp, L. M. K. Vandersypen, L. P. Kouwenhoven, Single-shot read-out of an individual electron spin in a quantum dot, *Nature* **2004**, *430*, 431.

[50] B. Weber, Y. H. M. Tan, S. Mahapatra, T. F. Watson, H. Ryu, R. Rahman, L. C. L. Hollenberg, G. Klimeck, M. Y. Simmons, Spin blockade and exchange in Coulomb-confined Silicon double quantum dots, *Nature Nanotechnology* **2014**, *9*, 430.

[51] A. C. Betz, R. Wacquez, M. Vinet, X. Jehl, A. L. Saraiva, M. Sanquer, A. J. Ferguson, M. F. Gonzalez-Zalba, Dispersively detected Pauli spin-blockade in a Silicon nanowire field-effect transistor, *Nano Letters* **2015**, *15*, 4622.

[52] A. Crippa, R. Maurand, D. Kotekar-Patil, A. Corna, H. Bohuslavskyi, A. O. Orlov, P. Fay, R. Laviéville, S. Barraud, M. Vinet, M. Sanquer, S. De Franceschi, X. Jehl, Level spectrum and charge relaxation in a Silicon double quantum dot probed by dual-gate reflectometry, *Nano Letters* **2017**, *17*, 1001.

[53] R. Ezzouch, S. Zihlmann, V. P. Michal, J. Li, A. Aprá, B. Bertrand, L. Hutin, M. Vinet, M. Urdampilleta, T. Meunier, X. Jehl, Y.-M. Niquet, M. Sanquer, S. De Franceschi, R. Maurand, Dispersively probed microwave spectroscopy of a Silicon hole double quantum dot, *Physical Review Applied* **2021**, *16*, 034031.

[54] A. M. J. Zwerver, T. Krähenmann, T. F. Watson, L. Lampert, H. C. George, R. Pillarisetty, S. A. Bojarski, P. Amin, S. V. Amitonov, J. M. Boter, R. Caudillo, D. Corras-Serrano, J. P. Dehollain, G. Droulers, E. M. Henry, R. Kotlyar, M. Lodari, F. Lüthi, D. J. Michalak, B. K. Mueller, S. Neyens, J. Roberts, N. Samkharadze, G. Zheng, O. K. Zietz, G. Scappucci, M. Veldhorst, L. M. K. Vandersypen, J. S. Clarke, Qubits made by advanced semiconductor manufacturing, *Nature Electronics* **2022**, *5*, 184.

[55] S. De Franceschi, L. Hutin, R. Maurand, L. Bourdet, H. Bohuslavskyi, A. Corna, D. Kotekar-Patil, S. Barraud, X. Jehl, Y.-M. Niquet, M. Sanquer, M. Vinet in 2016 IEEE International Electron Devices Meeting (IEDM), SOI technology for quantum information processing, **2016**, p. 13.4.1.

[56] N. Piot, B. Brun, V. Schmitt, S. Zihlmann, V. P. Michal, A. Apra, J. C. Abadillo-Uriel, X. Jehl, B. Bertrand, H. Niebojewski, L. Hutin, M. Vinet, M. Urdampilleta, T. Meunier, Y. .-. Niquet, R. Maurand, S. De Franceschi, A single hole spin with enhanced coherence in natural Silicon, arXiv:2201.08637, **2022**.

[57] A. Crippa, R. Maurand, L. Bourdet, D. Kotekar-Patil, A. Amisse, X. Jehl, M. Sanquer, R. Laviéville, H. Bohuslavskyi, L. Hutin, S. Barraud, M. Vinet, Y.-M. Niquet, S. De Franceschi, Electrical spin driving by g-matrix modulation in spin-orbit qubits, *Physical Review Letters* **2018**, *120*, 137702.

[58] B. Venitucci, L. Bourdet, D. Pouzada, Y.-M. Niquet, Electrical manipulation of semiconductor spin qubits within the g-matrix formalism, *Physical Review B* **2018**, *98*, 155319.

[59] B. Venitucci, Y.-M. Niquet, Simple model for electrical hole spin manipulation in semiconductor quantum dots: Impact of dot material and orientation, *Physical Review B* **2019**, *99*, 115317.

[60] V. P. Michal, B. Venitucci, Y.-M. Niquet, Longitudinal and transverse electric field manipulation of hole spin-orbit qubits in one-dimensional channels, *Physical Review B* **2021**, *103*, 045305.

[61] M. Urdampilleta, D. J. Niegemann, E. Chanrion, B. Jadot, C. Spence, P.-A. Mortemousque, C. Bäuerle, L. Hutin, B. Bertrand, S. Barraud, R. Maurand, M. Sanquer, X. Jehl, S. De Franceschi, M. Vinet, T. Meunier, Gate-based high fidelity spin readout in a CMOS device, *Nature Nanotechnology* **2019**, *14*, 737.

[62] E. Chanrion, D. J. Niegemann, B. Bertrand, C. Spence, B. Jadot, J. Li, P.-A. Mortemousque, L. Hutin, R. Maurand, X. Jehl, M. Sanquer, S. De Franceschi, C. Bäuerle, F. Balestro, Y.-M. Niquet, M. Vinet, T. Meunier, M. Urdampilleta, Charge detection in an array of CMOS quantum dots, *Physical Review Applied* **2020**, *14*, 024066.

[63] A. Corna, L. Bourdet, R. Maurand, A. Crippa, D. Kotekar-Patil, H. Bohuslavskyi, R. Laviéville, L. Hutin, S. Barraud, X. Jehl, M. Vinet, S. De Franceschi, Y.-M. Niquet, M. Sanquer, Electrically driven electron spin resonance mediated by spin–valley–orbit coupling in a Silicon quantum dot, *npj Quantum Information* **2018**, *4*, 6.

[64] M. Veldhorst, R. Ruskov, C. H. Yang, J. C. C. Hwang, F. E. Hudson, M. E. Flatté, C. Tahan, K. M. Itoh, A. Morello, A. S. Dzurak, Spin-orbit coupling and operation of multivalley spin qubits, *Physical Review B* **2015**, *92*, 201401.

[65] W. Huang, C. H. Yang, K. W. Chan, T. Tanttu, B. Hensen, R. C. C. Leon, M. A. Fogarty, J. C. C. Hwang, F. E. Hudson, K. M. Itoh, A. Morello, A. Laucht, A. S. Dzurak, Fidelity benchmarks for two-qubit gates in Silicon, *Nature* **2019**, *569*, 532.

[66] T. F. Watson, S. G. J. Philips, E. Kawakami, D. R. Ward, P. Scarlino, M. Veldhorst, D. E. Savage, M. G. Lagally, M. Friesen, S. N. Coppersmith, M. A. Eriksson, L. M. K. Vandersypen, A programmable two-qubit quantum processor in Silicon, *Nature* **2018**, *555*, 633.

[67] L. M. K. Vandersypen, H. Bluhm, J. S. Clarke, A. S. Dzurak, R. Ishihara, A. Morello, D. J. Reilly, L. R. Schreiber, M. Veldhorst, Interfacing spin qubits in quantum dots and donors—hot, dense, and coherent, *npj Quantum Information* **2017**, *3*, 34.

[68] M. Veldhorst, H. G. J. Eenink, C. H. Yang, A. S. Dzurak, Silicon CMOS architecture for a spin-based quantum computer, *Nature Communications* **2017**, *8*, 1766.

[69] M. Vinet, L. Hutin, B. Bertrand, S. Barraud, J.-M. Hartmann, Y.-J. Kim, V. Mazzocchi, A. Amisse, H. Bohuslavskyi, L. Bourdet, A. Crippa, X. Jehl, R. Maurand, Y.-M. Niquet, M. Sanquer, B. Venitucci, B. Jadot, E. Chanrion, P.-A. Mortemousque, C. Spence, M. Urdampilleta, S. De Franceschi, T. Meunier in 2018 IEEE International Electron Devices Meeting (IEDM), Towards scalable Silicon quantum computing, **2018**, p. 6.5.1.

[70] M. Vinet, The path to scalable quantum computing with Silicon spin qubits, *Nature Nanotechnology* **2021**, *16*, 1296.

[71] A. Peres, Reversible logic and quantum computers, *Physical Review A* **1985**, *32*, 3266.

[72] P. W. Shor, Scheme for reducing decoherence in quantum computer memory, *Physical Review A* **1995**, *52*, R2493.

[73] R. Li, L. Petit, D. P. Franke, J. P. Dehollain, J. Helsen, M. Steudtner, N. K. Thomas, Z. R. Yoscovits, K. J. Singh, S. Wehner, L. M. K. Vandersypen, J. S. Clarke, M. Veldhorst, A crossbar network for Silicon quantum dot qubits, *Science Advances* **2018**, *4*, eaar3960.

[74] K. Singh, J. S. Clarke, M. Veldhorst, L. M. K. Vandersypen, US20210296473A1, **2021**.

[75] Semiconductors, (Ed.: O. Madelung), Springer Berlin Heidelberg, **1991**.

[76] G. Dresselhaus, A. F. Kip, C. Kittel, Cyclotron resonance of electrons and holes in Silicon and Germanium crystals, *Physical Review* **1955**, *98*, 368.

[77] R. Winkler, Spin-orbit coupling effects in two-dimensional electron and hole systems, Springer, **2011**.

[78] P.-O. Löwdin, A note on the quantum-mechanical perturbation theory, *The Journal of Chemical Physics* **1951**, *19*, 1396.

[79] J. M. Luttinger, W. Kohn, Motion of electrons and holes in perturbed periodic fields, *Physical Review* **1955**, *97*, 869.

[80] J. K. Asbóth, L. Oroszlány, A. Pályi, A short course on topological insulators, Springer International Publishing, **2016**.

[81] J. C. Abadillo-Uriel, B. Thorgrimsson, D. Kim, L. W. Smith, C. B. Simmons, D. R. Ward, R. H. Foote, J. Corrigan, D. E. Savage, M. G. Lagally, M. J. Calderón, S. N. Coppersmith, M. A. Eriksson, M. Friesen, Signatures of atomic-scale structure in the energy dispersion and coherence of a Si quantum-dot qubit, *Physical Review B* **2018**, *98*, 165438.

[82] J. M. Taylor, V. Srinivasa, J. Medford, Electrically protected resonant exchange qubits in triple quantum dots, *Physical Review Letters* **2013**, *111*, 050502.

[83] J. Medford, J. Beil, J. M. Taylor, E. I. Rashba, H. Lu, A. C. Gossard, C. M. Marcus, Quantum-dot-based resonant exchange qubit, *Physical Review Letters* **2013**, *111*, 050501.

[84] M. Graf, P. Vogl, Electromagnetic fields and dielectric response in empirical tight-binding theory, *Physical Review B* **1995**, *51*, 4940.

[85] J. C. Slater, The theory of complex spectra, *Physical Review* **1929**, *34*, 1293.

[86] E. U. Condon, The theory of complex spectra, *Physical Review* **1930**, *36*, 1121.

[87] J. C. Slater, Molecular energy levels and valence bonds, *Physical Review* **1931**, *38*, 1109.

[88] G. L. G. Sleijpen, H. A. Van der Vorst, A Jacobi–Davidson iteration method for linear eigenvalue problems, *SIAM Review* **2000**, *42*, 267.

[89] S. Bosco, M. Benito, C. Adelsberger, D. Loss, Squeezed hole spin qubits in Ge quantum dots with ultrafast gates at low power, *Physical Review B* **2021**, *104*, 115425.

[90] G. Burkard, D. Loss, D. P. DiVincenzo, Coupled quantum dots as quantum gates, *Physical Review B* **1999**, *59*, 2070.

[91] C. H. Yang, R. C. C. Leon, J. C. C. Hwang, A. Saraiva, T. Tanttu, W. Huang, J. Camirand Lemyre, K. W. Chan, K. Y. Tan, F. E. Hudson, K. M. Itoh, A. Morello, M. Pioro-Ladrière, A. Laucht, A. S. Dzurak, Operation of a Silicon quantum processor unit cell above one kelvin, *Nature* **2020**, *580*, 350.

[92] K. Takeda, A. Noiri, T. Nakajima, T. Kobayashi, S. Tarucha, Quantum error correction with silicon spin qubits, *Nature* **2022**, *608*, 682–686.

[93] L. C. Camenzind, S. Geyer, A. Fuhrer, R. J. Warburton, D. M. Zumbühl, A. V. Kuhlmann, A hole spin qubit in a fin field-effect transistor above 4 kelvin, *Nature Electronics* **2022**, *5*, 178.

[94] C. X. Yu, S. Zihlmann, J. C. Abadillo-Uriel, V. P. Michal, N. Rambal, H. Niebojewski, T. Bedecarrats, M. Vinet, E. Dumur, M. Filippone, B. Bertrand, S. De Franceschi, Y.-M. Niquet, R. Maurand, Strong coupling between a photon and a hole spin in Silicon, arXiv:2206.14082, **2022**.

[95] S. M. Goodnick, D. K. Ferry, C. W. Wilmsen, Z. Liliental, D. Fathy, O. L. Krivanek, Surface roughness at the Si(100)-SiO_2 interface, *Physical Review B* **1985**, *32*, 8171.

[96] C. Buran, M. G. Pala, M. Bescond, M. Dubois, M. Mouis, Three-dimensional real-space simulation of surface roughness in Silicon nanowire FETs, *IEEE Transactions on Electron Devices* **2009**, *56*, 2186.

[97] A. Pirovano, A. Lacaita, G. Ghidini, G. Tallarida, On the correlation between surface roughness and inversion layer mobility in Si-MOSFETs, *IEEE Electron Device Letters* **2000**, *21*, 34.

[98] D. Esseni, A. Abramo, L. Selmi, E. Sangiorgi, Physically based modeling of low field electron mobility in ultrathin single- and double-gate SOI n-MOSFETs, *IEEE Transactions on Electron Devices* **2003**, *50*, 2445.

[99] L. Bourdet, J. Li, J. Pelloux-Prayer, F. Triozon, M. Cassé, S. Barraud, S. Martinie, D. Rideau, Y.-M. Niquet, Contact resistances in trigate and FinFET devices in a non-equilibrium Green's functions approach, *Journal of Applied Physics* **2016**, *119*, 084503.

[100] V.-H. Nguyen, Y.-M. Niquet, F. Triozon, I. Duchemin, O. Nier, D. Rideau, Quantum modeling of the carrier mobility in FDSOI devices, *IEEE Transactions on Electron Devices* **2014**, *61*, 3096.

[101] L. Pirro, I. Ionica, G. Ghibaudo, X. Mescot, L. Faraone, S. Cristoloveanu, Interface trap density evaluation on bare Silicon-On-Insulator wafers using the quasi-static capacitance technique, *Journal of Applied Physics* **2016**, *119*, 175702.

[102] L. Brunet, X. Garros, F. Andrieu, G. Reimbold, E. Vincent, A. Bravaix, F. Boulanger in 2009 IEEE International SOI Conference, New method to extract interface states density at the back and the front gate interfaces of FDSOI transistors from CV-GV measurements, **2009**, p. 1.

[103] M. L. Vermeer, R. J. E. Hueting, L. Pirro, J. Hoentschel, J. Schmitz, Interface states characterization of UTB SOI MOSFETs from the subthreshold current, *IEEE Transactions on Electron Devices* **2021**, *68*, 497.

[104] N. I. Dumoulin Stuyck, F. A. Mohiyaddin, R. Li, M. Heyns, B. Govoreanu, I. P. Radu, Low dephasing and robust micromagnet designs for Silicon spin qubits, *Applied Physics Letters* **2021**, *119*, 094001.

[105] J. Yoneda, T. Otsuka, T. Takakura, M. Pioro-Ladrière, R. Brunner, H. Lu, T. Nakajima, T. Obata, A. Noiri, C. J. Palmstrøm, A. C. Gossard, S. Tarucha, Robust micromagnet design for fast electrical manipulations of single spins in quantum dots, *Applied Physics Express* **2015**, *8*, 084401.

[106] A. C. Davison, D. V. Hinkley, Bootstrap methods and their application, Cambridge University Press, **1997**.

[107] H. Sakaki, T. Noda, K. Hirakawa, M. Tanaka, T. Matsusue, Interface roughness scattering in GaAs/AlAs quantum wells, *Applied Physics Letters* **1987**, *51*, 1934.

[108] K. Uchida, S. Takagi, Carrier scattering induced by thickness fluctuation of Silicon-On-Insulator film in ultrathin-body metal–oxide–semiconductor field-effect transistors, *Applied Physics Letters* **2003**, *82*, 2916.

[109] S. Jin, M. V. Fischetti, T.-W. Tang, Modeling of surface-roughness scattering in ultrathin-body SOI MOSFETs, *IEEE Transactions on Electron Devices* **2007**, *54*, 2191.

[110] B. Martinez, Y.-M. Niquet, Variability of electron and hole spin qubits due to interface roughness and charge traps, *Physical Review Applied* **2022**, *17*, 024022.

[111] J. Stark, Beobachtungen über den Effekt des elektrischen Feldes auf Spektrallinien. I. Quereffekt, *Annalen der Physik* **1914**, *348*, 965.

[112] D. Culcer, X. Hu, S. Das Sarma, Interface roughness, valley-orbit coupling, and valley manipulation in quantum dots, *Physical Review B* **2010**, *82*, 205315.

[113] R. Ruskov, M. Veldhorst, A. S. Dzurak, C. Tahan, Electron g-factor of valley states in realistic Silicon quantum dots, *Physical Review B* **2018**, *98*, 245424.

[114] Ferdous Rifat, Kawakami Erika, Scarlino Pasquale, Nowak Michał P., Ward D. R., Savage D. E., Lagally M. G., Coppersmith S. N., Friesen Mark, Eriksson Mark A., Vandersypen Lieven M. K., Rahman Rajib, Valley dependent anisotropic spin splitting in Silicon quantum dots, *npj Quantum Information* **2018**, *4*, 26.

[115] T. Tanttu, B. Hensen, K. W. Chan, C. H. Yang, W. W. Huang, M. Fogarty, F. Hudson, K. Itoh, D. Culcer, A. Laucht, A. Morello, A. Dzurak, Controlling spin-orbit interactions in Silicon quantum dots using magnetic field direction, *Physical Review X* **2019**, *9*, 021028.

[116] G. Simion, F. A. Mohiyaddin, R. Li, M. Shehata, N. I. Dumoulin Stuyck, A. Elsayed, F. Ciubotaru, S. Kubicek, J. Jussot, B. Chan, T. Ivanov, C. Godfrin, A. Spessot, P. Matagne, B. Govoreanu, I. P. Radu in 2020 IEEE International Electron Devices Meeting (IEDM), A scalable one dimensional Silicon qubit array with nanomagnets, **2020**, p. 30.2.1.

[117] E. Paladino, Y. M. Galperin, G. Falci, B. L. Altshuler, $1/f$ noise: Implications for solid-state quantum information, *Review of Modern Physics* **2014**, *86*, 361.

[118] C. Tahan, R. Joynt, Relaxation of excited spin, orbital, and valley qubit states in ideal Silicon quantum dots, *Physical Review B* **2014**, *89*, 075302.

[119] P. Huang, X. Hu, Spin relaxation in a Si quantum dot due to spin-valley mixing, *Physical Review B* **2014**, *90*, 235315.

[120] O. E. Dial, M. D. Shulman, S. P. Harvey, H. Bluhm, V. Umansky, A. Yacoby, Charge noise spectroscopy using coherent exchange oscillations in a singlet-triplet qubit, *Physical Review Letters* **2013**, *110*, 146804.

[121] R. C. C. Leon, C. H. Yang, J. C. C. Hwang, J. C. Lemyre, T. Tanttu, W. Huang, K. W. Chan, K. Y. Tan, F. E. Hudson, K. M. Itoh, A. Morello, A. Laucht, M. Pioro-Ladrière, A. Saraiva, A. S. Dzurak, Coherent spin control of *s*-, *p*-, *d*- and *f*-electrons in a Silicon quantum dot, *Nature Communications* **2020**, *11*, 797.

[122] R. J. Luyken, A. Lorke, A. O. Govorov, J. P. Kotthaus, G. Medeiros-Ribeiro, P. M. Petroff, The dynamics of tunneling into self-assembled InAs dots, *Applied Physics Letters* **1999**, *74*, 2486.

[123] S. Bosco, D. Loss, Hole spin qubits in thin curved quantum wells, arXiv:2204.08212, **2022**.

[124] A. Sammak, D. Sabbagh, N. W. Hendrickx, M. Lodari, B. Paquelet Wuetz, A. Tosato, L. Yeoh, M. Bollani, M. Virgilio, M. A. Schubert, P. Zaumseil, G. Capellini, M. Veldhorst, G. Scappucci, Shallow and undoped Germanium quantum wells: A playground for spin and hybrid quantum technology, *Advanced Functional Materials* **2019**, *29*, 1807613.

[125] N. W. Hendrickx, D. P. Franke, A. Sammak, M. Kouwenhoven, D. Sabbagh, L. Yeoh, R. Li, M. L. V. Tagliaferri, M. Virgilio, G. Capellini, G. Scappucci, M. Veldhorst, Gate-controlled quantum dots and superconductivity in planar Germanium, *Nature Communications* **2018**, *9*, 2835.

[126] M. Choi, A. Janotti, C. G. Van de Walle, Native point defects and dangling bonds in α-Al_2O_3, *Journal of Applied Physics* **2013**, *113*, 044501.

[127] G. Scappucci, P. J. Taylor, J. R. Williams, T. Ginley, S. Law, Crystalline materials for quantum computing: Semiconductor heterostructures and topological insulators exemplars, *MRS Bulletin* **2021**, *46*, 596.

[128] N. W. Hendrickx, W. I. L. Lawrie, L. Petit, A. Sammak, G. Scappucci, M. Veldhorst, A single-hole spin qubit, *Nature Communications* **2020**, *11*, 3478.

[129] R. Mizokuchi, R. Maurand, F. Vigneau, M. Myronov, S. De Franceschi, Ballistic one-dimensional holes with strong g-factor anisotropy in Germanium, *Nano Letters* **2018**, *18*, PMID: 29995419, 4861.

[130] Z. Wang, E. Marcellina, A. R. Hamilton, J. H. Cullen, S. Rogge, J. Salfi, D. Culcer, Optimal operation points for ultrafast, highly coherent Ge hole spin-orbit qubits, *npj Quantum Information* **2021**, *7*, 54.

[131] W. I. L. Lawrie, M. Russ, F. van Riggelen, N. W. Hendrickx, S. L. de Snoo, A. Sammak, G. Scappucci, M. Veldhorst, Simultaneous driving of semiconductor spin qubits at the fault-tolerant threshold, arXiv:2109.07837, **2021**.

[132] C. X. Yu, S. Zihlmann, G. Troncoso Fernández-Bada, J.-L. Thomassin, F. Gustavo, E. Dumur, R. Maurand, Magnetic field resilient high kinetic inductance superconducting niobium nitride coplanar waveguide resonators, *Applied Physics Letters* **2021**, *118*, 054001.

[133] B. Martinez, J. C. Abadillo-Uriel, E. Rodríguez, Y.-M. Niquet, In preparation.

[134] P. M. Jordan, D. K. Simon, T. Mikolajick, I. Dirnstorfer, Trapped charge densities in Al_2O_3-based Silicon surface passivation layers, *Journal of Applied Physics* **2016**, *119*, 215306.

[135] E. Wigner, On the interaction of electrons in metals, *Physical Review* **1934**, *46*, 1002.

[136] B. Tanatar, D. M. Ceperley, Ground state of the two-dimensional electron gas, *Physical Review B* **1989**, *39*, 5005.

[137] G. W. Bryant, Electronic structure of ultrasmall quantum-well boxes, *Physical Review Letters* **1987**, *59*, 1140.

[138] Observation and spectroscopy of a two-electron Wigner molecule in an ultraclean carbon nanotube, *Nature Physics* **2013**, *9*, 576.

[139] L. H. Kristinsdóttir, J. C. Cremon, H. A. Nilsson, H. Q. Xu, L. Samuelson, H. Linke, A. Wacker, S. M. Reimann, Signatures of Wigner localization in epitaxially grown nanowires, *Physical Review B* **2011**, *83*, 041101(R).

[140] S. Kalliakos, M. Rontani, V. Pellegrini, C. P. Garcıa, A. Pinczuk, G. Goldoni, E. Molinari, L. N. Pfeiffer, K. W. West, A molecular state of correlated electrons in a quantum dot, *Nature Physics* **2008**, *4*, 467.

[141] B. Reusch, W. Häusler, H. Grabert, Wigner molecules in quantum dots, *Physical Review B* **2001**, *63*, 113313.

[142] S. M. Reimann, M. Koskinen, M. Manninen, Formation of Wigner molecules in small quantum dots, *Physical Review B* **2000**, *62*, 8108.

[143] R. Egger, W. Häusler, C. H. Mak, H. Grabert, Crossover from Fermi liquid to Wigner molecule behavior in quantum dots, *Physical Review Letters* **1999**, *82*, 3320.

[144] A. Singha, V. Pellegrini, A. Pinczuk, L. N. Pfeiffer, K. W. West, M. Rontani, Correlated electrons in optically tunable quantum dots: Building an electron dimer molecule, *Physical Review Letters* **2010**, *104*, 246802.

[145] C. Ellenberger, T. Ihn, C. Yannouleas, U. Landman, K. Ensslin, D. Driscoll, A. C. Gossard, Excitation spectrum of two correlated electrons in a lateral quantum dot with negligible Zeeman splitting, *Physical Review Letters* **2006**, *96*, 126806.

[146] L. P. Kouwenhoven, D. G. Austing, S. Tarucha, Few-electron quantum dots, *Reports on Progress in Physics* **2001**, *64*, 701.

[147] R. Hanson, L. P. Kouwenhoven, J. R. Petta, S. Tarucha, L. M. K. Vandersypen, Spins in few-electron quantum dots, *Rev. Mod. Phys.* **2007**, *79*, 1217.

[148] T. Lundberg, J. Li, L. Hutin, B. Bertrand, D. J. Ibberson, C.-M. Lee, D. J. Niegemann, M. Urdampilleta, N. Stelmashenko, T. Meunier, J. W. A. Robinson, L. Ibberson, M. Vinet, Y.-M. Niquet, M. F. Gonzalez-Zalba, Spin quintet in a Silicon double quantum dot: Spin blockade and relaxation, *Physical Review X* **2020**, *10*, 041010.

[149] J. Corrigan, J. P. Dodson, H. E. Ercan, J. C. Abadillo-Uriel, B. Thorgrimsson, T. J. Knapp, N. Holman, T. McJunkin, S. F. Neyens, E. R. MacQuarrie, R. H. Foote, L. F. Edge, M. Friesen, S. N. Coppersmith, M. A. Eriksson, Coherent control and spectroscopy of a semiconductor quantum dot Wigner molecule, *Physical Review Letters* **2021**, *127*, 127701.

[150] H. E. Ercan, M. Friesen, S. N. Coppersmith, Charge-Noise Resilience of Two-Electron Quantum Dots in Si/SiGe Heterostructures, *Phys. Rev. Lett.* **2022**, *128*, 247701.

[151] H. E. Ercan, S. N. Coppersmith, M. Friesen, Strong electron-electron interactions in Si/SiGe quantum dots, *Physical Review B* **2021**, *104*, 235302.

[152] D. Miserev, O. P. Sushkov, Prediction of the spin triplet two-electron quantum dots in Si: Towards controlled quantum simulations of magnetic systems, *Physical Review B* **2019**, *100*, 205129.

[153] Y. Hada, M. Eto, Electronic states in Silicon quantum dots: Multivalley artificial atoms, *Physical Review B* **2003**, *68*, 155322.

[154] Z. Liu, L. Wang, K. Shen, Energy spectra of three electrons in Si/SiGe single and vertically coupled double quantum dots, *Physical Review B* **2012**, *85*, 045311.

[155] N. R. Kestner, O. Sinanoğlu, Study of electron correlation in helium-like systems using an exactly soluble model, *Physical Review* **1962**, *128*, 2687.

[156] S. Kais, D. Herschbach, N. Handy, C. Murray, G. Laming, Density functionals and dimensional renormalization for an exactly solvable model, *The Journal of Chemical Physics* **1993**, *99*, 417–425.

[157] M. G. Borselli, K. Eng, R. S. Ross, T. M. Hazard, K. S. Holabird, B. Huang, A. A. Kiselev, P. W. Deelman, L. D. Warren, I. Milosavljevic, A. E. Schmitz, M. Sokolich, M. F. Gyure, A. T. Hunter, Undoped accumulation-mode Si/SiGe quantum dots, *Nanotechnology* **2015**, *26*, 375202.

[158] Y. M. Niquet, D. Rideau, C. Tavernier, H. Jaouen, X. Blase, Onsite matrix elements of the tight-binding Hamiltonian of a strained crystal: Application to Silicon, Germanium, and their alloys, *Physical Review B* **2009**, *79*, 245201.

[159] Z. Zeng, F. Triozon, Y.-M. Niquet, Carrier scattering in high-κ/metal gate stacks, *Journal of Applied Physics* **2017**, *121*, 114503.